



HAL
open science

Advanced imaging of transient and spectral luminescence for optoelectronic characterization of photovoltaic materials

Marie Legrand

► **To cite this version:**

Marie Legrand. Advanced imaging of transient and spectral luminescence for optoelectronic characterization of photovoltaic materials. Electric power. Sorbonne Université, 2023. English. NNT : 2023SORUS066 . tel-04213622

HAL Id: tel-04213622

<https://theses.hal.science/tel-04213622v1>

Submitted on 21 Sep 2023

HAL is a multi-disciplinary open access archive for the deposit and dissemination of scientific research documents, whether they are published or not. The documents may come from teaching and research institutions in France or abroad, or from public or private research centers.

L'archive ouverte pluridisciplinaire **HAL**, est destinée au dépôt et à la diffusion de documents scientifiques de niveau recherche, publiés ou non, émanant des établissements d'enseignement et de recherche français ou étrangers, des laboratoires publics ou privés.

Sorbonne Université

Ecole doctorale ED397

Institut Photovoltaïque d'Ile de France (IPVF)

**Advanced imaging of transient and spectral luminescence
for optoelectronic characterization of photovoltaic
materials**

Par Marie LEGRAND

Thèse de doctorat de Physique et Chimie des Matériaux

Dirigée par Jean-François Guillemoles,

Présentée et soutenue publiquement le 06/02/2023

Devant un jury composé de :

Dr Xavier MARIE
Dr Emmanuel BEAUREPAIRE
Pr James BLAKESLEY
Dr Elsa CASSETTE
Pr Alexandra FRAGOLA
Dr Jean-François GUILLEMOLES
Dr Daniel ORY

Rapporteur
Rapporteur
Examineur
Examinatrice
Examinatrice
Directeur de thèse
Encadrant



Remerciements

Un grand merci à Daniel, surnommé Master of the cameras à son insu, d'avoir partagé son engouement pour le travail technique, de s'être énormément impliqué et de toujours faire découvrir de nouvelles expressions. À Jean-François pour ses innombrables idées, avec qui chaque discussion est une source d'inspiration et de motivation. À Adrien et Laurent, qui ont initié ce projet un peu fou d'imagerie 4D et m'y ont plongée.

À l'équipe photoluminescence, dont les membres ont les yeux qui brillent pour des mots qui semblent sortis tout droit d'un livre de science-fiction ! À Baptiste, fournisseur officiel de boîtes Thorlabs et d'écoute attentive, Guillaume et Thomas, pour leurs discussions passionnées et leurs projets inspirants, à Alexandra, Stefania, Daniel S., Géraud, Mahyar et Nao de communiquer leurs motivations à leur façon. Aux membres occasionnels de la réunion PL, Alexandre Py et Arthur Julien, toujours curieux et partants pour discuter loi de Planck généralisée. À Daniel M., Maxime et Thomas C. qui ont pourvu échantillons et inspiration ! Mille mercis à Claire et Eva, mes stagiaires curieuses et enthousiastes, véritables dresseurs de Python !

Ces trois années ont été riches en rencontres. On passe d'étudiant apprivoisant le vocabulaire des semiconducteurs à expérimentateur expérimenté qui pense que les stagiaires font bien jeunes cette année. De même, on voit ceux qui nous côtoient gagner en assurance, maîtriser le français quand ils débutaient aux premiers jours au labo, grandir à leur manière (voir se marier !). Je tiens à remercier ceux qui ont commencé en même temps que moi, et avec lesquels les échanges sur les débuts en recherche m'ont porté. Javid, Claire, Elisa, Salim, ainsi que d'autres sus mentionnés, j'étais heureuse de partager cet apprentissage avec vous. À ceux plus expérimentés, qui racontent leurs propres périple et écoutent nos déboires de rédactions, en particulier à Pilar et Alexandre. Merci du fond du cœur au bureau de la bienveillance, Celia, Sunny Sun, Salim, Mirrella, Minjin, Gurleen et aux nouvelles recrues Lauriane et Estelle, qui accueillent toute initiative avec un grand sourire, des pauses thé aux soirées jeu de société ! Merci aux peintres, grimpeurs, danseurs ou skieurs, et professeurs en cuisine d'un jour avec qui je partage de beaux souvenirs, que ce soit à l'IPVF, à Paris ou dans d'autres pays.

À mes amis proches, pour les respirations comme les moments de réflexions : aux guitaristes et aux fans de jeux de société, à celles que je côtoie depuis plus de 15 ans qui m'ont tellement apporté qu'une thèse entière ne suffirait à résumer. À la famille Legrand, pour l'indéfectible refuge qu'elle offre et sa bonne humeur volubile. À mes colocataires

humains et félins, pour la très belle convivialité et la solidarité des uns et les ronronnements des autres. Ils ont tous été un soutien salvateur dans cette aventure.

Enfin, merci au lecteur pour l'intérêt porté à cette thèse !

Table of contents

Remerciements	iii
Table of contents	v
Index of symbols	viii
Index of abbreviations	x
Introduction	1
Abstract	1
Outline	3
Chapter 1 - Luminescence of semiconductors	5
1.I Energy conversion in photovoltaic devices	6
1.I.1 Absorption of the incident light	6
1.I.2 Recombination	11
1.I.3 Transport of charge carriers	13
1.I.4 Inside-out.....	14
1.II On the importance of the different dimensions	15
1.II.1 Luminescence spectra	15
1.II.2 Time-resolved photoluminescence.....	19
1.III Types of materials for photovoltaic conversion.....	22
1.III.1 Overview of photovoltaic absorbers	22
1.III.2 III-V semiconductors.....	23
1.III.3 Perovskite	24
1.III.4 Fluorophores.....	25
Conclusion.....	25
Chapter 2 - Characterization imaging techniques	27
2.I How to build an image?.....	28
2.I.1 Imaging approaches.....	28
2.I.2 Introduction to multidimensional imaging.....	31
2.I.3 Principle of Single-Pixel Imaging	32
2.I.4 Application of Single-Pixel Imaging: State of the art	40
2.II Methods for hyperspectral and time-resolved PL imaging	44
2.II.1 Illumination for PL imaging.....	44
2.II.2 Hyperspectral imaging	45
2.II.3 Time-resolved imaging techniques	49
2.III Towards mixed techniques	53
2.III.1 4D data	53
2.III.2 Various possibilities for 4D imaging	54
2.III.3 Outlook on multidimensional imaging.....	57
Conclusion.....	60
Chapter 3 - 4D-PL technique	61
3.I Experimental setup	62
3.I.1 4D-PL in the landscape of multidimensional imaging.....	62

3.I.2	Streak camera technology	63
3.I.3	TRPL spectroscopy for semiconductor characterization	64
3.I.4	Principle of the 4D-PL setup developed	69
3.II	Imaging by SPI: practical implementation	72
3.II.1	Time scales of the 4D-PL setup	72
3.II.2	Challenges	74
3.II.3	Choice of the collecting optic.....	78
3.II.4	Investigation and correction of SPI artifact.....	79
3.III	Variations of 4D-PL workflow	87
3.III.1	2x3D – Parallel hyperspectral by SPI and TRFLIM	87
3.III.2	Pixel clustering applied to the 4D-PL acquisition.....	90
	Conclusion.....	93
Chapter 4 - Demonstration of 4D-PL and its variations on photovoltaic devices.....		95
4.I	Application of 2x3D to perovskite light-soaking study.....	96
4.I.1	Perovskites, a photosensitive photovoltaic material	96
4.I.2	Experimental protocol	97
4.I.3	Results and discussion.....	98
4.I.4	Perspective: How can we compare steady-state and transient experiments?... 103	
4.II	4D-PL imaging	106
4.II.1	Acquiring PL profile on GaAs sample	106
4.II.2	Results	108
4.II.3	Discussion	110
4.III	Application to different samples	118
4.III.1	Gallium arsenide	118
4.III.2	Fluorophores.....	122
4.III.3	Perovskites	124
	Conclusion.....	126
Chapter 5 - Photoluminescence excitation spectroscopy		127
5.I	Context and frame of the study.....	128
5.I.1	Why employ PL to investigate absorption properties?	128
5.I.2	PLE definition and applications in the literature.....	129
5.II	Methods for PLE	132
5.II.1	Theoretical models	132
5.II.2	PLE Optical setup.....	138
5.III	PLE experiments for perovskite absorptivity investigation.....	142
5.III.1	Sample and method	142
5.III.2	Result and discussion	144
5.III.3	Can we reach the absorption coefficient?	149
5.III.4	Prospects for data acquisition.....	153
5.IV	PLE on a full cell: beyond uniform carrier concentration	153
5.IV.1	Experimental details	153
5.IV.2	Results	154
5.IV.3	Comparison with drift-diffusion simulations	156
	Conclusion.....	160
Conclusion and perspectives		163
	Key outcomes.....	163
	Open questions	165
	How can we compare steady-state and transient experiments?	165

What strategies can we implement to treat the 4D data?	166
What setup and experiment should we use?.....	168
Conclusion's conclusion	168
Bibliography.....	171
References – Chapter 1	171
References – Chapter 2	172
References – Chapter 3	176
References – Chapter 4	178
References – Chapter 5	179
References – Conclusion.....	181
Appendices.....	I
A. Consideration for calibrations	II
From raw data to relative intensity.....	II
From relative to absolute intensity	III
B. Noise and artifacts consequences on basis scan with Hadamard	VI
C. Generalization of diffraction artifact to 2D	XI
D. Improvements for the pixel clustering setup	XIII
E. Filtering out the laser reflection by polarization	XIV
Résumé étendu en français.....	XV

Index of symbols

A_{meas}/A	\square	Absorptivity
$A = (a_{i,k})_{\substack{1 \leq i \leq m \\ 1 \leq k \leq n}}$	\square	Pattern matrix for m measurements and n pixels
α	cm^{-1}	Absorption coefficient
B	cm^3/s	Coefficient for radiative recombination
$b = (b_i)_{1 \leq i \leq m}$	\square	Measurement vector
C_n, C_p	cm^6/s	Auger coefficients
c	cm/s	Speed of light in vacuum
D, D_n, D_p	cm^2/s	Diffusion coefficient of electrons and holes
D_e, D_h	cm^{-3}	Electron/hole density of states
d	cm	Absorber thickness
$\Delta\mu$	eV	Quasi-Fermi level splitting
\vec{E}	V/cm	Applied electric field
E_C, E_V	eV	Conduction band min. energy and valence band max.
E_{FC}, E_{FV}	eV	Fermi energies for electron and hole distribution
E_G	eV	Bandgap energy
f	\square	Occupation function
φ_{BB}	$\#/cm^2/s/eV/sr$	Blackbody radiation
Φ_{em}, Φ_{exc}	$\#/cm^2/s$	Emitted and excitation light flux
G	$\#/cm^3/s$	Generation rate
h, \hbar	$eV.s$	Planck's constant and reduced Planck's constant
$\gamma_{int}, \gamma_{ext}$	\square	Internal/external photoluminescence quantum yields
$\vec{J}_{n,diff}$	$C/cm/s$	Diffusion current
$\vec{J}_{n,drift}$	$C/cm/s$	Drift current
j_γ	$ph/cm^2/s$	Photon flux
μ, μ_n, μ_p	$cm^2/V/s$	Electron and hole mobility
k_B	eV/K	Boltzmann constant

L_n, L_p	cm	Diffusion length
n	cm^{-3}	Electron density
n_{A-}, n_{D+}	cm^{-3}	Acceptor and donors concentration
NA	\square	Numerical aperture
n_i	cm^{-3}	Intrinsic carrier concentration
n_r	\square	Refractive index
p	cm^{-3}	Hole density
p_e, p_h	$kg/cm/s$	Electron and hole momentum
q_e	C	Elementary charge
q	eV	Electron volt
R, R_{meas}	\square	Reflectivity, Reflectance
R_{A-M}	cm^{-3}/s	Auger-Meitner recombination rate
R_{rad}	cm^{-3}/s	Radiative recombination rate
R_{SRH}	cm^{-3}/s	Shockley-Read-Hall recombination rate
R_{surf}	cm^{-2}/s	Surface recombination rate
S, S_n, S_p	cm/s	Surface recombination velocities
T	K	Temperature
T_{meas}	\square	Transmittance
τ_n, τ_p	s	Shockley-Read-Hall lifetime
τ_{eff}	s	Effective lifetime of first order recombination
$x = (x_k)_{1 \leq k \leq n}$	\square	Image vector
$\Omega, d\Omega$	sr	(Elemental) Solid angle

Index of abbreviations

ARC	Anti-reflective coating
CdTe	Cadmium telluride
CCD	Charged coupled devices
CMOS	Complementary metal-oxide-semiconductor
CW	Continuous wave
DOS	Density of States
DMD	Digital Micromirror device
EASLM	Electrically addressed spatial light modulators
EQE	External quantum efficiency
FFT	Fast Fourier Transform
FOV	Field of view
FPA	Focal plane arrays
GaAs	Gallium Arsenide
HI	Hyperspectra imager
MCP	Micro-channel Plate
NA	Numerical aperture
OPL	Optical path length
PLQY	Photoluminescence Quantum Yield
QW	Quantum wells
SRH	Shockley-Read-Hall
SNR	Signal-to-noise ratio
SPAD	Single Photon Avalanche Diode
SPI	Single Pixel Imaging
TRPL	Time resolved photoluminescence
TCSPC	Time-correlated single photon counting
TRFLIM	Time-resolved fluorescence imaging
TRPPL	Time-resolved photoluminescence
TMM	Transfer matrix method

Introduction

This last decade has seen an exponential growth of the installed solar photovoltaics capacity, which has risen from 63.8TWh in 2011 to eventually overcome the 1000TWh symbolic value in 2021¹. Net zero emission scenarii expect this trend to continue in the coming years. Indeed, solar photovoltaic constitutes one of the energy sources with the lowest carbon footprints, along with nuclear, hydro, and wind. Also, it offers a renewable and universal energy source that can greatly help access energy worldwide. One hundred eighty-three years after the discovery of the photovoltaic effect, solar cells provide direct conversion of solar to electric power with efficiencies of 20%. This figure is high compared to the 1% solar to chemical achieved by plants!

Yet, photovoltaic technologies have room for improvement. The following challenges motivate the development of new structures and materials. Higher efficiencies are pursued to require less surface. Indeed, the need for the available area constitutes a major lock, recently tackled through agrivoltaics. It would also allow fewer materials and infrastructures to be employed, reducing maintenance costs and waste. Otherwise, the energy pay-back time of silicon cells is of the order of the year, and emerging technologies such as perovskite could decrease it to the scale of the month. The degradation of mature technologies such as silicon must be investigated to improve their reliability. For all these issues, advanced characterization can play a supportive role.

In this context, this work focuses on developing new photoluminescence imaging methods for characterizing photovoltaic devices and helping their improvements. It was carried out in the frame of CIFRE N° 2019/0780 at EDF R&D and was hosted by the UMR IPVF.

Abstract

Photoluminescence characterization of photovoltaic absorbers provides the charge transport phenomena and the optoelectronic properties on which their performance relies. However, their obtention is based on physical models and may require uncontrolled assumptions and unknown parameters. This thesis explores how acquiring spectrally resolved

¹ <https://www.iea.org/reports/solar-pv>

maps of photoluminescence in pulsed excitation can contribute to material characterization while limiting the necessary prior knowledge and controlling underlying hypotheses and models. On the one hand, we developed imaging systems describing the emitted intensity in four dimensions: 2D spatial, temporal and spectral. On the other hand, we performed excitation wavelength variation studies and investigated their relationship with light absorption.

Maps of intensity can be acquired by pixelated detectors or non-imaging detectors, as in Single-pixel imaging. This approach employs spatial light modulation to reconstruct images and is particularly relevant to obtain multidimensional images. It is thus of interest for photoluminescence as each dimension brings information, as demonstrated by the setups already in use. A hyperspectral imager, providing the spectrum in each pixel, allows the characterization of material properties and the charge carriers generated. Complementarily, time-resolved imaging gives an insight into the transport mechanisms. We review and propose different techniques to obtain 4D data corresponding to the temporal evolution of the spectrum in each pixel of an image $I_{PL}(x, y, energy, time)$. It provides the correlation between temporal and spectral dimensions, which was not available in the lab previously.

Three measurement approaches were developed based on the principle of single-pixel imaging. They correspond to different sampling schemes in the 4D space, focusing on temporal and spectral dimensions that are reached with high resolutions. Their implementation was challenging as photoluminescence corresponds to low light conditions, and the higher the resolutions, the lower the sensitivity. Each dimension of light involved must be accurately reconstructed while entangled in the acquisition process. Particularly, the impact of diffraction and interferences due to the spatial light modulator has been investigated.

This instrumental work allowed, first of all, combined time and spectrally resolved imaging (2x3D) of perovskite. It allowed monitoring of light-induced mechanisms that modify the photoluminescence spectrum and dynamics. Secondly, it has led to the characterization in 4D of the emission of a gallium arsenide wafer. The joint evolution of the signal in temporal, spatial, and spectral dimensions is observed due to band-filling and diffusion. At last, a workflow based on pixel clustering algorithms is proposed. A spatial map is obtained by single-pixel imaging, from which areas of interest are determined before the decay is obtained with high temporal and spectral resolutions. It allows an original sampling of photoluminescence with a high signal-to-noise ratio enabling its application to various samples and injection conditions. These last two approaches are unique to the best of our knowledge and provide photoluminescence variation in the combined spatial, temporal, and spectral domains.

In addition, we have set up a methodology to perform excitation wavelength studies on the hyperspectral imager. It was demonstrated on an inhomogeneous perovskite sample from which the local relative absorptivity is obtained on a wide spectral range by combined analysis of the emission and excitation spectra. Reflectivity measurements completing this study provide optical and topological information allowing us to refine the interpretation of photoluminescence maps.

Outline

This dissertation comprises five chapters describing the background, experimental methods, and results obtained. We first recall notions of material science in **Chapter 1**: a framework for describing light absorption, electronic transport, and recombination is set. Classical models for spectral and transient photoluminescence analysis are provided, and the different types of material characterized are introduced. **Chapter 2** presents imaging technics for multidimensional acquisitions. We review the literature and focus on the techniques applied in this work to capture photoluminescence.

The development of the 4D-PL setup and its variation is explained in **Chapter 3**. The challenges this novel architecture raises and possible ways to address them are discussed. **Chapter 4** presents the experimental results obtained with the different technics implemented. Gallium arsenide and perovskite samples are simultaneously characterized in spectral, temporal and spatial dimensions.

Chapter 5 explores the additional information brought by the excitation wavelength dependence of photoluminescence. The link of photoluminescence with absorption properties and charge carrier profile is illustrated with experiments on a perovskite stack and a gallium arsenide cell, respectively.

Finally, the main outcomes of this work are summarized, along with questions raising short and long-term perspectives for the newly developed methods.

Chapter 1 - Luminescence of semiconductors

“Des rayons qui accompagnent les rayons les plus réfrangibles de la lumière solaire, font éprouver à des lames métalliques plongées dans un liquide, une action telle, qu’il en résulte des effets électriques auxquels on ne peut attribuer une origine calorifique.”

— **Edmond Becquerel**, *Mémoire sur les effets électriques produits sous l’influence des rayons solaires*, 1839

As an introduction, this chapter reviews the notions of material sciences on which this thesis relies. The luminescence of semiconductors is contextualized and described along different dimensions.

First, section 1.I places luminescence in an energy conversion process. The absorbed light generates excited electron-holes pairs. Their energy can be transferred to the lattice, extracted, or lost by recombination. The later process happens partly with the emission of photons by photoluminescence. These energy exchanges take place concomitantly with optical and electronic transport.

Section 1.II questions what light luminescence can bring on semiconductors. The focus will be on the steady-state spectral emission and the transient regime. Physical models that describe them, such as Planck Generalized law and rates equations, are introduced. They lead to the fit of complementary optoelectronic properties.

Finally, the materials families employed for photovoltaic conversion are introduced. Among them, highly efficient III-V and emerging perovskites are further described, as Chapters 1 and 5 present the characterization of such samples.

1.I Energy conversion in photovoltaic devices

Solar cells convert the energy radiated by the sun into electric work. It relies on the absorption of photons generating electron and holes later extracted. A fraction recombines, releasing heat or light. In parallel, the energy is transported by charge carriers or photons.

1.I.1 Absorption of the incident light

Light absorption is described at the device and in the absorber materials' depths, and physical models relate the two scales. It corresponds to the generation of electron-hole pairs following Fermi distributions.

1.I.1.a Quantities describing light absorption

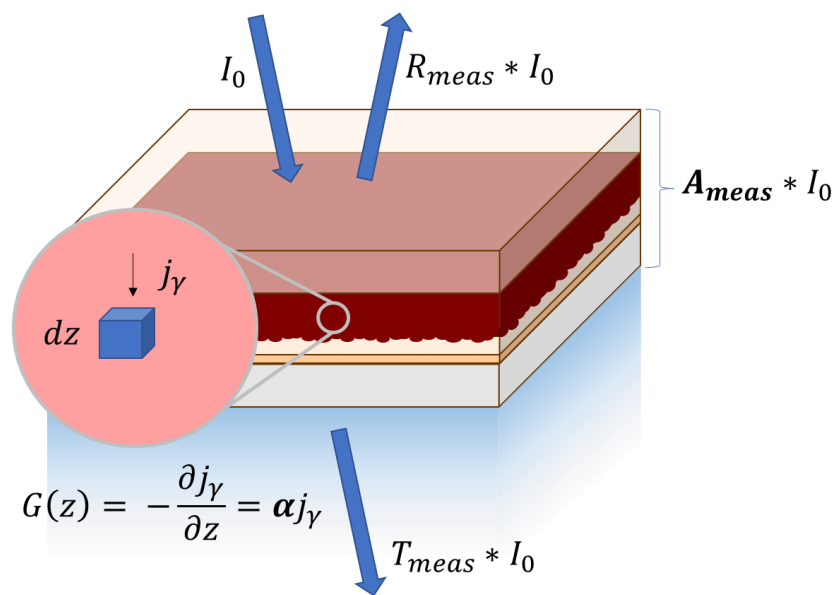


Figure 1-1: Light absorption in a photovoltaic device – from the macro to the microscale. The incident flux I_0 is reflected, transmitted or absorbed in proportion described by the reflectance R_{meas} , transmittance T_{meas} , and absorbance A_{meas} . The absorption coefficient α is a material property characterizing the share of the photons flux j_γ absorbed by an elemental volume. At the microscale, it results in the generation of an electron-hole pair with the rate $g(z)$.

The light absorbed in the photovoltaic device generates electron holes within the semiconductors. High absorption is, therefore, crucial for developing devices that convert efficiently solar energy. At the system scale illustrated in Figure 1-1, incident light flux $I_0 [ph/cm^2/s]$ is either reflected, transmitted, or absorbed in fractions corresponding to reflectance R_{meas} , transmittance T_{meas} , absorbance A_{meas} , so that for all energy E :

$$A_{meas}(E) + T_{meas}(E) + R_{meas}(E) = 1 \quad (1-1)$$

These quantities take into account various light-matter interactions that can happen within the device, such as multiple reflections, interferences, or plasmonic resonances. They are fundamentally different from properties describing materials, as the reflectivity (or reflection coefficient), denoted R , and characteristic of the air-material interface. Likewise, the absorbance (or absorptivity) traduces the optimization of the whole device, and the absorption coefficient is its material counterpart. For a one-dimensional model, the capacity of bulk to absorb light depends on its thickness; the absorption coefficient $\alpha [cm^{-1}]$ is defined for a small volume on which impinges the photon flux $j_\gamma [ph/cm^2/s]$ along the axis z , as shown in Figure 1-1, following the Beer-Lambert law:

$$-\frac{\partial j_\gamma}{\partial z} = \alpha(z)j_\gamma \quad (1-2)$$

Optical models linked this quantity to the absorptivity that we note A for the rest of this report for simplicity. The following paragraph presents the conventional models connecting these two quantities.

1.1.1.b Absorptivity and absorption coefficient

By assuming the absorption coefficient is homogeneous, the solution to the differential equation (1-2) provides the photon flux in-depth. For a slab of thickness d and top surface reflectivity R , neglecting all internal reflection, it comes:

$$j_\gamma(z) = (1 - R)I_0 e^{-\alpha z} \quad (1-3)$$

The transmitted flux can be evaluated in $z = d$, and combined with equation (1-1), leads to:

$$A(E) = (1 - R)(1 - \exp(-\alpha d)) \quad (1-4)$$

This equation is commonly employed to estimate the absorption coefficient from the absorptivity. Literature provides more detailed analytical solutions by taking more mechanisms into account to gain accuracy. Therefore, multiple reflections or the difference between reflectance and reflectivity can be included¹. Numerical solutions are available to model systems of various complexity by implementing geometric or wave optics. Ray tracing, transfer matrix method, or coupled-wave analysis can be combined to have an extensive view of light-matter interactions in a solar cell².

1.1.1.c Generation of electron-holes pairs

The rate of electron-hole pairs generated $G [ph/cm^3/s]$, equals the one of photons absorbed via band-to-band transitions. For one-dimensional systems, it reads:

$$G(z) = \alpha j_{\gamma}(z) \quad (1-5)$$

It leads to a generation that varies with the absorption coefficient and, therefore, with the incident photon wavelength. Together with the model of equation (1-3), one can estimate the variation of the generated carrier profile as follow, known as the Hovel model³:

$$G(z) = \alpha(1 - R)I_0 e^{-\alpha z} \quad (1-5b)$$

The exponential dependence on the absorption coefficient induces considerable changes in the generation profile across the solar spectrum.

The absorption is linked to the material's electronic **density of states (DOS)**. As a reminder, in isolated atoms, electrons occupy discrete energy levels. When n atoms interact, similar energy levels split into n values permitted for electrons. In a bulk material, this mechanism creates bands that are continuum of states charge carriers can occupy. Those determining the optoelectronic properties are the last filled and first empty, namely the valence and conduction bands. They are respectively characterized by their upper energy E_v and lower one E_c , defining bandgap E_g of the material.

The **electronic density of states $D_e[cm^{-3}]$** is defined as the energetic distribution of the number of states N_e per volume unit V :

$$D_e(E) = \frac{1}{V} \frac{dN_e}{dE} \quad (1-6)$$

The occupation function $f(E)$ describes the repartition of the electrons in these levels so that the electronic density $n[cm^{-3}]$ reads as:

$$dn = D_e(E)f(E)dE \quad (1-7)$$

As fermions, electrons follow a Fermi-Dirac statistic:

$$f(E) = \frac{1}{1 + \exp((E - E_F)/k_B T)} \quad (1-8)$$

Where E_F is a characteristic quantity called the Fermi energy, k_B denotes Boltzmann constant, in energy per kelvin, and T represents the system's temperature. These equations for electrons also hold for holes. That is also the case for the other equations written in this manuscript unless specified. In the following, we note p the density of holes, with indices p or h the quantities relating to them, and with indices e or n the electron ones. No subscript is used for properties assumed equal for electrons and holes. This statistic defines the charge

carrier densities at equilibrium, which product corresponds to the squared intrinsic carrier concentration n_i^2 .

In bulk materials, the higher the density of states available, the higher the absorption coefficient. This principle can be intuited from a system with two discrete energy levels. The net absorption rate corresponds to the upward transition from an energy ϵ_1 to a higher energy ϵ_2 to which the stimulated emission is subtracted. This mechanism has a higher chance of taking place when electronic states at ϵ_1 are more numerous and more filled, and ϵ_2 is emptier. The complete derivation leads to the expression of the absorption coefficient for this two-level system as⁴:

$$\alpha_{12}(E) = |M|^2 D_{12} [f(\epsilon_1) - f(\epsilon_2)] \quad (1-9)$$

Where M corresponds to the matrix element for the transition, D_{12} is the joint density of states, i.e., a quantity taking into account the DOS at the two energy levels and selection rules. This expression could be generalized to any system by integrating the energies ϵ_1 and ϵ_2 , to highlight the dependency of the absorption coefficient on a combined DOS.

Several schemes can be followed depending on the nature of the semiconductor, as illustrated in Figure 1-2. Contrarily to direct semiconductors, the absorption of a photon in an indirect semiconductor requires the absorption or the emission of a phonon, so the momentum balance is respected. Therefore, their absorption coefficient is smaller than in direct ones, so the thicknesses to reach a good absorptivity are higher, typically by hundreds of microns. The following paragraph describes the energies at stake in this absorption process.

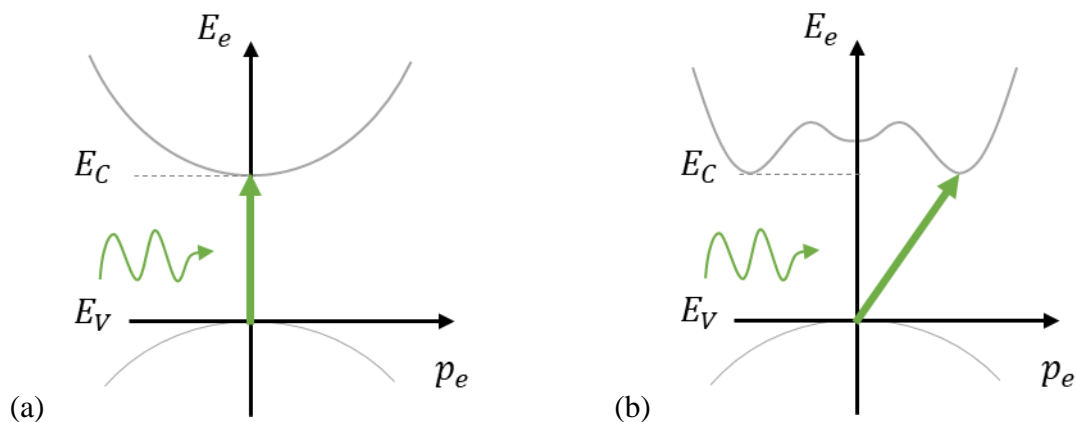


Figure 1-2: Schematic of absorption in direct (a) and indirect (b) semiconductors. In the first case, the conduction band minimum is attained for a null momentum p_e and the photon can be absorbed directly. Conversely, indirect semiconductors absorption requires momentum exchange through phonons.

1.1.1.d Energy conversion

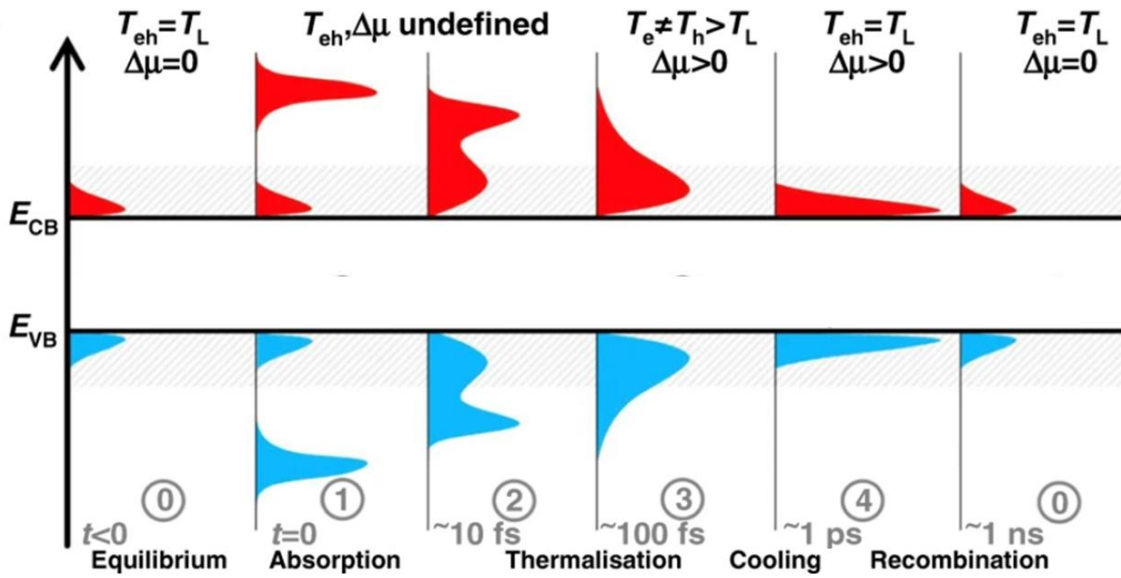


Figure 1-3: Energy distribution of the carriers after the absorption of a light pulse above bandgap (adapted from Ahmed et al.⁵). (0) At equilibrium, it follows a Fermi-Dirac distribution with characteristic temperatures $T_e = T_h$ equal to lattice one T_L . (1) Photoexcitation: electron-hole pairs are generated with an excess energy. (2-3) Collisions with the lattice lead to a thermal distribution. (4) The temperature of the distribution decreases to match the lattice one before the carriers recombine. The reader can note that the scheme is not linearly scaled and the population of charge carriers at equilibrium is usually neglected.

After the photons are absorbed, their energy is redistributed, as shown through the example of pulsed excitation in Figure 1-3. The electron-hole pairs are generated with the energy of the absorbed photon: above the bandgap, it results in an energy in excess of the equilibrium. By carrier-carrier and phonon-carrier collisions, it is quickly redistributed to adopt Fermi-Dirac distributions in a thermalization mechanism. Then, the distribution temperature is cooled until it matches the lattice one. During these processes, the excess energy is transferred to the lattice in the form of vibrations quantified as phonons.

In quasi-equilibrium, both electrons and holes stabilize with Fermi distributions of different energies, denoted E_{Fc} and E_{Fv} . The overall charge carrier number system is then characterized by a difference in Fermi energies called the **quasi-Fermi level splitting $\Delta\mu$** . It corresponds to the maximal energy potential that can be extracted from the system, hence the approximation $\Delta\mu \sim V_{OC}$. For intrinsic concentration n_i and a temperature T , the product of charge carriers densities reads:

$$np = n_i^2 \exp\left(\frac{\Delta\mu}{k_B T}\right) \quad (1-10)$$

These energy redistribution processes take place at short times before the charge carriers recombine through the mechanisms described in the following paragraph.

1.1.2 Recombination

Once the electron-hole pairs are generated, the charge carriers tend to recombine to return to their equilibrium state. It can be achieved by radiative or nonradiative channels, as introduced in the following.

1.1.2.a Recombination via defects

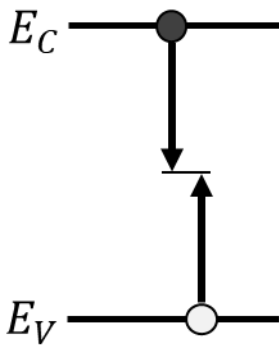


Figure 1-4: Trap-assisted recombination mechanism.

This mechanism is often considered the predominant recombination source in solar cells. As illustrated in Figure 1-4, impurities in the lattice can lead to the creation of energy states lying between the bands. An electron (hole) is trapped by this energy state and constitutes a route for holes (electrons) to recombine. The influence of the defects is all the more important as their energy level is deep and close to the middle of the gap. Indeed, this configuration maximizes the chances for both carriers to occupy the defective state. These defects are characterized by the **Shockley-Read-Hall (SRH) lifetime**, denoted τ_n , which determines their recombination rate R_{SRH} :

$$R_{SRH} = \frac{np - n_i^2}{n\tau_p + p\tau_n} \quad (1-11)$$

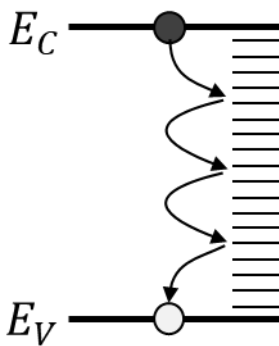


Figure 1-5: Recombination via surface states.

The presence of dangling bonds on the material interface is also a vector for defects-mediated recombination. Indeed, they can create continuous energy states within the gap, serving as a way for excited electrons to release their energy through heat, as shown in Figure 1-5. It is modeled by a **surface recombination velocity**, denoted S_n [cm/s]. This quantity is related to the diffusion coefficient D . In a one-dimensional model, it serves as a boundary condition⁶ and leads to a surface recombination rate R_{surf} [cm⁻²/s]:

$$S_n = \pm \frac{D}{n} \frac{dn}{dz} (z = 0 / d) \quad (1-12)$$

$$R_{surf} = \frac{np - n_i^2}{n/S_p + p/S_n} \quad (1 - 12b)$$

For this recombination, the electron-hole pair energy dissipates as heat in the form of phonons.

1.I.2.b Radiative recombination

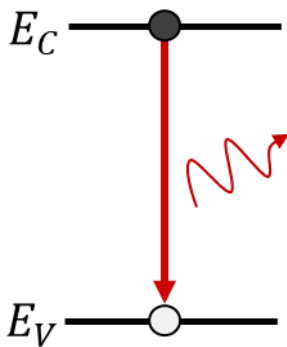


Figure 1-6: Schematic of radiative recombination.

The recombination of an electron-hole pair can lead to photon emission through luminescence, as schematized in Figure 1-6. As a two-body interaction, the rate of radiative recombination is directly proportional to the electron and holes densities:

$$R_{rad} = B(np - n_i^2) \quad (1-13)$$

Where B is the coefficient for radiative recombination. The higher this recombination rate is, the higher the charge carrier densities within the photovoltaic material. The **internal photoluminescence quantum yield** γ_{int} (PLQY) describes the proportion of radiative recombination taking place within the bulk material:

$$\gamma_{int} = \frac{R_{rad}}{(R_{rad} + R_{nonrad})} \quad (1-14)$$

It is an indicator of the material quality, as a high emission is considered a sign of low nonradiative recombination. This mechanism is named photoluminescence (PL) when the carriers are generated by light absorption, and electroluminescence (EL) when they are injected through contacts.

1.I.2.c Auger-Meitner recombination

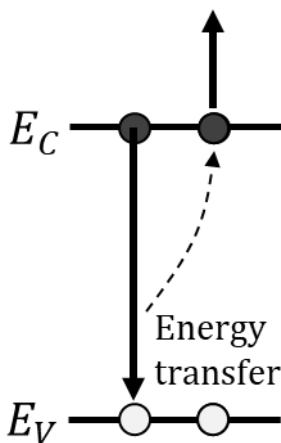


Figure 1-7: Auger-Meitner recombination

As illustrated in Figure 1-7, when electron-hole pairs recombine, they can release the energy through transfer to another charge carrier. The latter gains kinetic energy and is then lost as heat. This three-carrier recombination is predominant in high injection conditions or doping. The corresponding recombination rate reads:

$$R_{A-M} = np(C_n n + C_p p) \quad (1-15)$$

Where C_n and C_p are constants called Auger coefficients traducing the recombination probabilities.

The different recombination mechanisms impact the charge carrier lifetime, which is the average duration before a generated carrier recombines. The characteristic times associated with each process, as the SRH lifetime, set a higher limit. In the following, we'll consider the approximation $np - n_i^2 \sim np$.

1.1.3 Transport of charge carriers

The transport of charge carriers happens simultaneously with their recombination. It tends to homogenize their distribution and charge density.

1.1.3.a Electronic drift and diffusion

Electrons are moved by the action of charges or particle gradients by drift and diffusion⁷. For a semiconductor in which electrons and holes have the mobilities μ_n and μ_p , an applied electric field \vec{E} leads to the drift charge current:

$$\vec{J}_{drift} = q_e(\mu_n n + \mu_p p)\vec{E} \quad (1-16)$$

By diffusion, electrons go towards low-concentration areas, as described by Fick's law:

$$\vec{J}_{n,diff} = q_e D_n g \vec{r} \vec{a} dn \quad (1-17)$$

Where q is the elementary charge, and D is the diffusion coefficient. The associated diffusion length is the mean distance traveled by charge carriers:

$$L_n = \sqrt{D_n \tau_n} \quad (1-18)$$

The diffusion length must be long enough to extract the electrons efficiently through the contacts. In particular, it must be higher than the absorption length. The diffusion coefficient is further linked to the mobility by the Einstein relation:

$$D_n = \frac{k_B T}{q_e} \mu_n \quad (1-19)$$

These relations result in the **drift-diffusion equation**, which can be written for electrons as:

$$\vec{J}_n = q_e(-D_n g \vec{r} \vec{a} dn - n \mu_n \vec{E}) \quad (1-20)$$

$$\frac{\partial n}{\partial t} = \frac{1}{q_e} \text{div}(\vec{J}_n) + G - R \quad (1-20b)$$

They can be solved numerically together with the Poisson equation that describes charges potential φ induced by the charge density ρ in a medium of dielectric permittivity ϵ , reading:

$$\nabla^2\varphi = -\frac{\rho}{\epsilon} \quad (1-21)$$

In which, in the absence of charged defects, charge density can be expressed from acceptors and donors concentration, respectively denoted n_{A-} and n_{D+} , leading to:

$$\rho = q_e * (n_{D+} + p - n_{A-} - n) \quad (1-22)$$

1.I.3.b Photonic transport

The energy carried by charges can also be transported optically when converted to photons by luminescence and reabsorbed elsewhere in the material. The mean distance traveled corresponds to the inverse of the absorption coefficient for each photon energy. This mechanism, denoted **photon recycling**, also leads to a homogenization of the carrier distribution as areas with higher concentrations act more as a source than as a receiver of photons. Its contribution is mainly visible for highly radiative material and, particularly, in cases where electronic transport is negligible, for low electronic diffusion length, or far from the excitation.

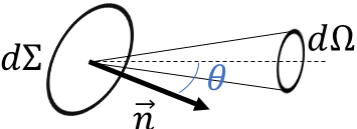
1.I.4 Inside-out

Among the recombination mechanisms, luminescence is the only one that eventually leads to the escape of the energy in a form other than heat. Considerations of photons escaping the system rely on radiometric quantities, such as étendue and solid angles.

As a reminder, solid angles generalize the notion of angle in space. The elemental solid angle $d\Omega$ of surface area dS seen from a reference point at a distance r is:

$$d\Omega = \frac{dS}{r^2} \quad (1-23)$$

The optical étendue characterizes light beam propagation. If a surface element $d\Sigma$ emits in an elemental solid angle $d\Omega$ at an angle θ to its normal, the infinitesimal étendue reads:



$$d^2G = n_r^2 d\Sigma \cos\theta d\Omega \quad (1-24)$$

where n_r is the refractive index of the medium, it can be integrated over a solid angle and surface to retrieve the optical étendue.

Luminescence emission has no favored direction and hence is isotropic. In a specular model, photons reaching the surface with an angle smaller than a critical value go out of the material, defining an escape cone. The others are guided through total internal reflection and can propagate over long distances in the material.

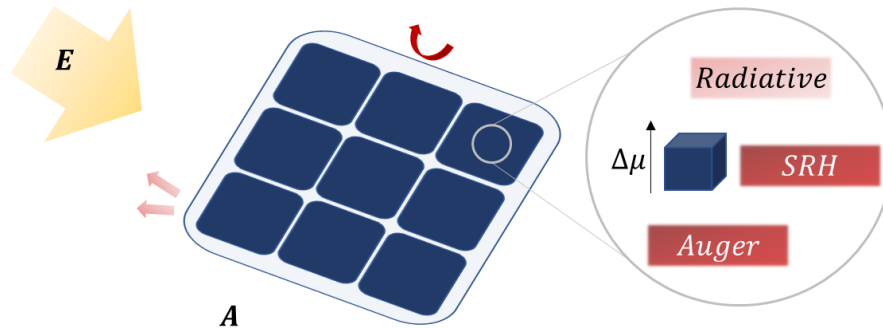


Figure 1-8: Schematic of the energy exchanges between solar irradiation, photovoltaic absorber, and its environment. Absorbed energy can be stored as a potential $\Delta\mu$, or lost radiatively or thermally.

In summary, the photovoltaic devices absorb a fraction A of the incident energy. At the microscale, it is rather described by the absorption coefficient α . Generated charges contribute potential energy or recombine, inducing thermal and radiative losses. They are transported throughout the material by key mechanisms for extraction to the external circuit. The emission of light by luminescence depends on the carrier density and thus offers a way to access the optoelectronic properties of the absorber directly.

1.II On the importance of the different dimensions

This section describes the essential character of luminescence through the model of spectral emission. The information conveyed by the spectrum is explained, as well as what can be deduced from the transient analysis.

1.II.1 Luminescence spectra

The emitted spectrum reveals the energy distribution of charge carriers and provides a way to access the material's intrinsic properties. The collected spectrum is the integration over an emission profile and is further affected by optical and transport properties, thus offering a way to characterize them.

1.II.1.a Emissivity and absorptivity

In steady-state, each body must emit as much as it absorbs radiation. One can derive the Kirchhoff law from the particular case of thermal equilibrium. Good absorbers are also good emitters, characterized by their emissivity $\epsilon(E)$:

$$A(E) = \epsilon(E) \quad (1-25)$$

This relation is one of the three reciprocities in semiconductor luminescence. The two others deal with charge carrier transport: in-depth extraction matches injection, and lateral series resistance affects the current in both ways.

1.II.1.b Internal emission: revealing the electronic energies

Similarly to electrons, the energy distribution of photons can be deduced from an occupation function – Bose-Einstein one - and a density of states. For perfectly absorbing material, it results in the blackbody emission φ_{BB} [*photons/surface/energy/solid angle*]:

$$\varphi_{BB}(E) = \frac{n_r^2}{4\hbar^3 c^2} E^2 * \frac{1}{\exp\left(\frac{E}{k_B T}\right) - 1} \quad (1-26)$$

Where \hbar is the reduced Planck constant and c the speed of light in In 1954, Van Roosbroeck and Shockley⁸ showed that the spontaneous emission from the band transition is related to the blackbody emission. Luminescence internal emission rate [*photons/volume/time*] from a semiconductor at thermal equilibrium, which comprises the emission over the total solid angle $\Omega = 4\pi$, is linked to the absorption coefficient:

$$R_{SP}(E) = \alpha(E)\varphi_{BB}(E)\Omega = \frac{8\pi n_r^2}{\hbar^3 c^2} E^2 \alpha(E) \frac{1}{\exp\left(\frac{E}{k_B T}\right) - 1} \quad (1-27)$$

$\alpha(E)$ increases close to the bandgap energy, whereas the blackbody radiation decays exponentially. Assuming a root-squared absorption coefficient, this leads to a luminescence spectrum with a peak close at $E_G + 2k_B T$. This relation was later generalized to semiconductors in steady-state, at quasi-Fermi level $\Delta\mu$, corresponding to the Lasher-Stern-Wurfel equation:

$$R_{rad}(E) = \frac{8\pi n_r^2}{\hbar^3 c^2} E^2 \alpha(E) \frac{1}{\exp\left(\frac{E - \Delta\mu}{k_B T}\right) - 1} \quad (1-28)$$

In the operating cell conditions $E_g - \Delta\mu > k_B T$, thus Boltzmann approximation is often made, leading to the Lasher-Stern-Würfel equation:

$$R_{PL}(E) = \alpha(E)\varphi_{BB}(E)\Omega e^{\frac{\Delta\mu}{k_B T}} \quad (1-29)$$

Hence, the quasi-Fermi level splitting mainly determines the intensity of emission. The equations of this paragraph focus on the internal emission rate. Rather than this 'pure' spectrum, the quantity measured experimentally is affected by the whole device. In the following, the external emission is described.

1.II.1.c Planck Generalized law and model inversion

Planck generalized law⁹ was derived in 1995 based on reciprocity between the absorbed light flux and the one escaping from the device. It provides the luminescence intensity emitted from the device in [*photons/(area.time.energy)*]:

$$I_{PL}(E) = A(E) \frac{2\pi}{h^3 c^2} \frac{E^2}{\exp\left(\frac{E - \Delta\mu}{k_B T}\right) - 1} \quad (1-30)$$

One can note that this expression writes the luminescence spectrum as a product of the density of states and electronic distributions. It can thus describe the occupation function of the carriers and provide information on the material itself, as illustrated in the following paragraph.

The *linear fit* method provides a simple way to obtain optoelectronic properties from this relation. The exponential term $\exp\left(-\frac{E}{k_B T}\right)$ defines the asymptotic behavior of the luminescence spectrum at high energies. Hence the following relation between the high energy slope and charge carrier temperature provides a way to assess their heating:

$$\ln(I_{PL}(E)) \sim -\frac{E}{k_B T} + ct \quad (1-31)$$

Conversely, at low energies, the curve shape is dominated by the exponential increase in absorptivity due to tail states. In this energy range where the semiconductor is almost transparent, the absorptivity scales with the absorption coefficient, which shape can often be described by an exponential rise characterized by an energy E_U called the Urbach energy:

$$\ln(I_{PL}(E)) \sim \ln(\alpha) + ct = \frac{E}{E_U} + ct' \quad (1-32)$$

E_U is a material property obtained through the DOS dependence of the luminescence emission.

Planck's generalized law can also be fully fitted, requiring a material absorptivity model. For this purpose, Katahara et Hillhouse¹⁰ have developed a unified model of the absorption coefficient as a convolution of the ideal square root above the bandgap with tail states $T(E)$:

$$\alpha = \alpha_0 \sqrt{E - E_1} \quad (1-33)$$

$$T(E) = N \exp\left(-\left|\frac{E - E_1}{\gamma}\right|^\theta\right) \quad (1-33b)$$

Where α_0 scales the absorption coefficient, E_1 is a characteristic energy corresponding to the bandgap for band-to-band transitions. γ and θ are additional parameters describing the exponential absorption rise. In the particular case $\theta = 1$, γ corresponds to the Urbach energy.

Other models of absorption coefficient might be required depending on the transition mechanisms involved. Many of them are listed by Jimenez et Tomm¹¹. Among other things, we can mention the excitonic phenomena described by Elliott¹². The following paragraph introduces the band-filling induced by high injection conditions, as encountered in the experimental work. As shown in Figure 1-9, the energy states close to the band edges are filled when increasing the carrier concentration. Even after cooling, the newly generated carrier will keep higher energies as lower states are saturated, leading to a blue shift of the emitted spectrum.

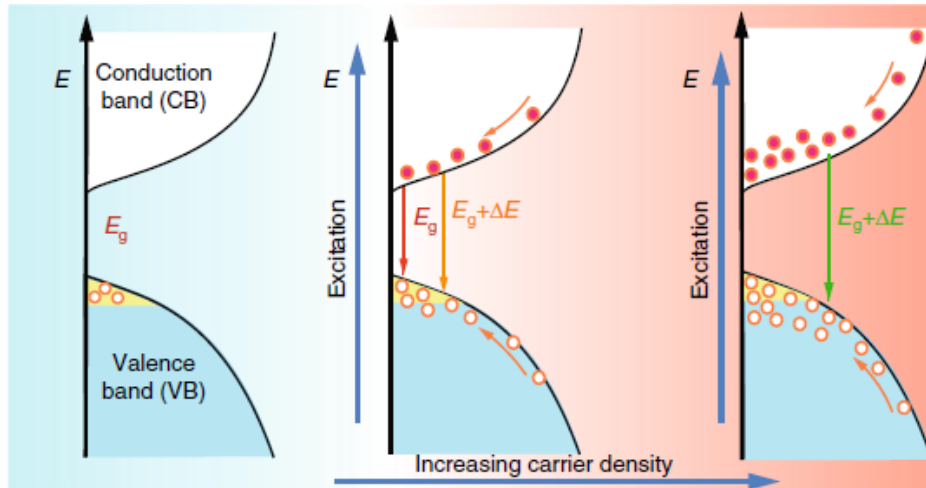


Figure 1-9: Schematic of the band-filling mechanism leading to an energy increase in the emitted spectrum (source Fang et al.¹³).

This effect corresponds to an absorption coefficient varying with the quasi-Fermi level splitting:

$$\alpha(E, \Delta\mu) = BF(E, \Delta\mu) * \alpha_{ref}(E) \quad (1-34)$$

α_{ref} is a reference absorption coefficient corresponding to the limit case of null excess carrier density, and $BF(E, \Delta\mu)$ accounts for the band-filling effect according¹⁴:

$$BF(E) = \frac{\sinh\left(\frac{E - \Delta\mu}{2k_B T}\right)}{\cosh\left(\frac{E - \Delta\mu}{2k_B T}\right) + \cosh\left(\frac{m_h - m_e}{m_h + m_e} * \frac{E - E_g}{2k_B T} - \frac{D}{4} \ln\left(\frac{m_h}{m_e}\right)\right)} \quad (1-35)$$

Where D represents the dimensionality of the absorber, m_h and m_e are holes and electrons effective masses.

1.II.1.d Luminescence ratio method

The emitted spectrum is affected differently by reabsorption at high and at low energies. Hence, it has a varying dependence on the charge carrier profile. For a well-known structure such as silicon cells, it is possible to model accurately the influence of the diffusion coefficient and surface recombination on the carrier profile and thus on spectrum intensity^{15,16}. It leads to a bijection between an effective diffusion length, a function of S , τ_n and D , and the contrast between images at high and low energies. Such analysis requires a good knowledge of the absorption coefficient to determine the lengths probed by each wavelength range. Thus, the steady-state spectral signal also depends on recombination and transport properties, which can be further characterized by transient luminescence analysis.

1.II.2 Time-resolved photoluminescence

The transient regime of photoluminescence provides insight into the charge carrier dynamics relying on various phenomena. These are classically modeled by continuity and rate equations.

1.II.2.a Competing phenomena in the transient regime

Photoluminescence after a pulsed excitation can be probed down to subpicosecond resolution and up to the millisecond. Different mechanisms take place at these time scales in photovoltaic absorbers, and their number grows when considering full devices. Ultrafast processes such as thermalization and carrier cooling can be observed typically at a sub-picosecond scale, as illustrated in Figure 1-3. Charge carriers will recombine with characteristic times of the nanosecond, and at the same time, their density is homogenized through transport. They also can be trapped or extracted to other layers. Figure 1-10 provides examples of characteristic times of diffusion and non-radiative recombination for different materials. It illustrates the diversity of orders of magnitude depending on the materials. For structures as multiple quantum well (MQW), it is also possible to observe thermal mechanism as cooling time can approach the nanosecond¹⁸. If up-conversion offers a way to obtain PL with femtosecond resolution, the carrier dynamic is usually measured at longer

time scales, relevant for recombination and transport properties characterization. This part discusses their link to the collected signal.

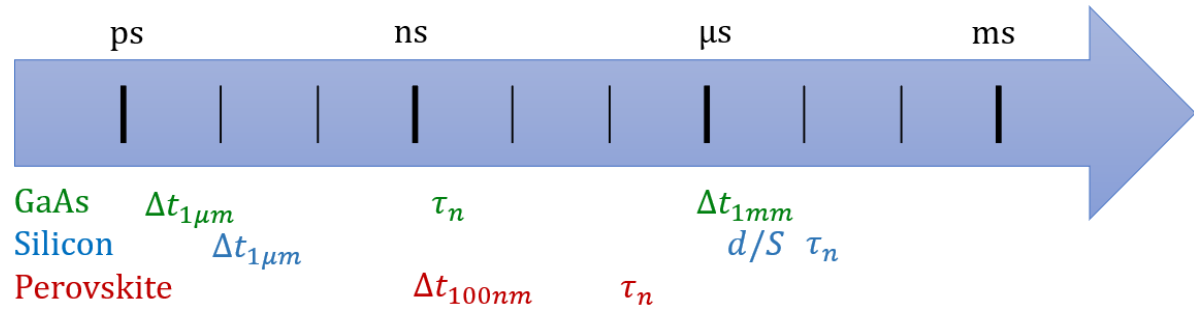


Figure 1-10: Examples of electronic characteristic times reported by the literature. Δt_{dist} represents the duration taken to travel a distance from diffusion $dist^2/D$, d/S is a duration characteristic of surface defects recombination. The characteristic properties of Silicon and Gallium arsenide properties are from the Ioffe database¹⁷, and perovskite's from Kim et al.¹⁹

1.II.2.b Models for photoluminescence decays

Recombination and transport within the bulk can be written as a function of charge carrier density, on which the photoluminescence intensity depends through relation (1-13). It is then possible to fit the decay after pulsed excitation to investigate both recombination and transport parameters. As many mechanisms occur simultaneously, the main challenge is defining the appropriate assumptions to build a model to interpret data accurately.

Indeed, if all the mechanisms previously described are involved, the drift-diffusion equation (1-20) will comprise many terms and can be solved only numerically. In the literature, the influence of drift and diffusion is often neglected^{20,21} to simplify these continuity equations. Indeed, in-depth diffusion typically takes place at a sub-nanosecond time scale. The induced charge homogeneity leads to the absence of electrostatic charge. Thus, when pulsed excitation is over, their following rate equation is often considered:

$$\frac{dn}{dt} = -np(C_n n + C_p p) - Bnp - \frac{np}{n\tau_p + p\tau_n} \quad (1-36)$$

Generally, the main goal is to characterize the absorber quality revealed through the SRH decay times. Krückemeier et al.²¹ present simplifications that can be done for the different structures. In the case of an intrinsic absorber, if injection allows neglect Auger-Meitner recombination and surface recombination is limited by its rate and not the travel to the surface, it leads to:

$$\frac{dn}{dt} = -Bn^2 - \frac{n}{\tau_p + \tau_n} - \frac{Sn}{2d} \quad (1-37)$$

As a consequence, the asymptotic behavior of the decay of charge carrier density is a characteristic exponential time:

$$\tau = \left(\frac{1}{\tau_p + \tau_n} - \frac{S}{2d} \right)^{-1} \quad (1-38)$$

It results in photoluminescence following an exponential decay of characteristic time 2τ , as the emitted intensity scales with the square of the charge carrier density. Relation (1-37) can be used to obtain the sum of SRH lifetimes and the surface recombination velocity from a series of different thicknesses. If the sample is well passivated and surface passivation neglected, SRH lifetimes can be obtained directly. Hence, the direct interpretation of decay time as the SRH lifetime requires two linearities: the one of the rate equation, in which trap-assisted recombination must be dominant, and the one in the photoluminescence intensity with respect to charge carrier density. In practice, the other mechanisms are likely to affect the decay, such as diffusion at a short time²². If first-order recombination prevails, it leads to the definition of an effective carrier lifetime τ_{eff} that encompasses them all. Equation (1-38) provides an example of this, yet its definition varies as a function of mechanisms considered, injection and doping²³.

Based on the rate equation (1-36), one can see that the decay will be highly dependent on the charge carrier density. This parameter will vary the proportions of first, second, or third-order recombination. Thus, shorter decays are observed at higher excitation fluence. The generated carrier density also changes the effects of traps that can be saturated at high injection. It is crucial to consider it in the interpretation of photoluminescence decay, which requires a good absorption coefficient estimation. Furthermore, the emitted intensity dependence on the charge density must be known. If limit cases of high injection ($I_{PL} \propto n^2$) or low injection ($I_{PL} \propto n$) are often assumed, a transition from one regime to the other is possible, as discussed by Krückemeier et al²¹. An intensity-dependent study might be key for a correct interpretation of time-resolved data. Different experimental parameters, such as the excitation wavelength and the repetition rate, must be carefully chosen to avoid affecting the observed decay time.

With time-resolved PL, imaging allows monitoring of the transport of carriers directly. When performing a local excitation, lateral diffusion of the carriers can be observed by the growth of the luminescent spot with time²⁰. Its Gaussian width σ follows diffusion law:

$$\sigma(t) = \sigma_0 + \sqrt{2Dt} \quad (1-39)$$

This is a first example of how spatial dimension, combined with the temporal one, can help determine the optoelectronic properties of materials.

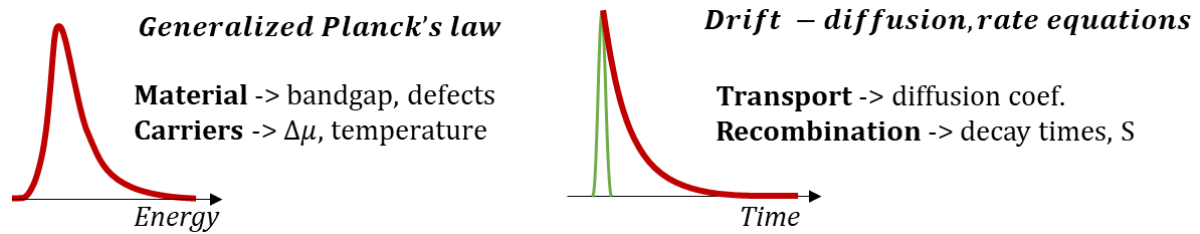


Figure 1-11: Schematic of models and optoelectronic properties at stake for interpretation of spectral and the temporal luminescence.

In summary, spectral emission in quasi-equilibrium and time-resolved photoluminescence depends on complementary quantities they can help to assess. As recalled in Figure 1-11, the interpretation of each dimension relies on physical models to bring new information on the probed material.

1.III Types of materials for photovoltaic conversion

Photoluminescence can be used to characterize samples of families with various characteristics. During this work, we have mainly characterized semiconductor absorbers, such as gallium arsenide and perovskite, and optical concentrators. This section introduces them and places them among the PV application materials.

1.III.1 Overview of photovoltaic absorbers

The design of conventional single-junction solar cells is subject to a fundamental trade-off: only photons with energies higher than the bandgap one (E_g) can be absorbed, and their excess energy ($E - E_g$) dissipates as heat. Thus, materials of high E_g cannot absorb much of the solar spectrum, and low E_g ones owe consequent thermalization losses, as illustrated in Figure 1-12 (a). The losses of radiative recombination and the isothermal ones traducing the decrease between bandgap and extracted electrical work can be added to the model. These four mechanisms result in the efficiency maximum of about 30% under 1sun illumination, known as the Shockley-Queisser limit. This upper bound depends on the bandgap energy, which is therefore a crucial criterion for its application in solar photovoltaics.

Among the semiconductors owing the appropriate bandgap and being implemented in solar cells, crystalline silicon is the majority, representing 95% of the production in 2021²⁴. This mature technology has been optimized to attain efficiencies higher than 80% of their Shockley-Queisser limit, as shown in Figure 1-12(b). This material's relatively low absorption coefficient needs to be compensated by thicknesses of hundreds of microns. Conversely, thin-film technologies are based on few microns thick absorbers, allowing flexible devices. That is the case for CIGS, Cd(Te,Se), or CZTS. Organic materials also provide light and flexible

devices. Compared to their hard counterparts, they provide low efficiencies and stability issues, though they owe low processing costs and are based on widely available materials. Performances achieved by the main materials used in photovoltaics are illustrated in Figure 1-12(b), in which the losses are described with respect to the Shockley-Queisser limit. The pathways and potential for optimization vary greatly. The following paragraphs introduce the materials studied in this thesis.

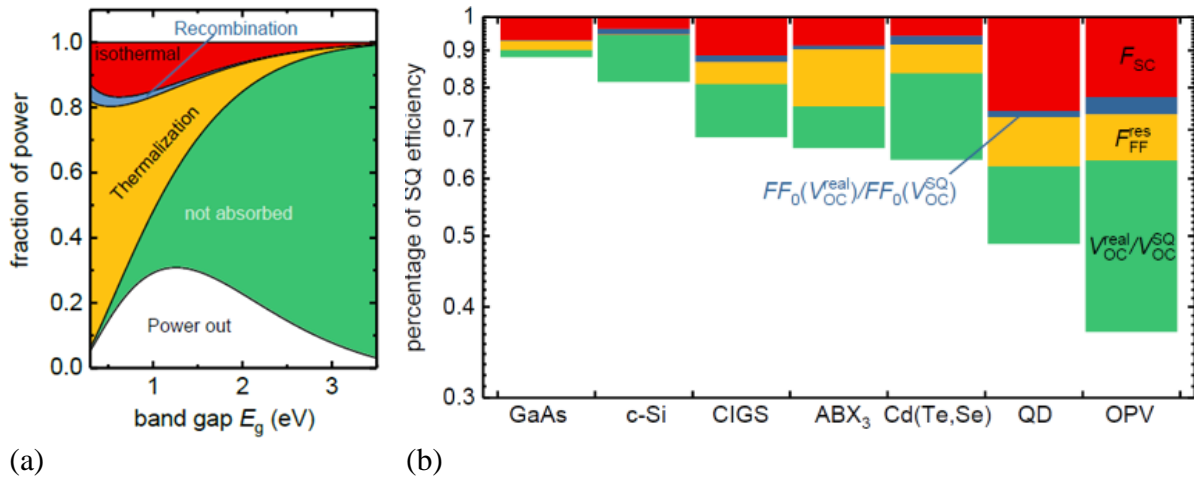


Figure 1-12: (a) Shockley-Queisser limit for the single-junction solar cell under 1 sun illumination, showing the maximal sunlight to electric power conversion as a function of bandgap energy. Four sources of losses are considered: photons with $E < E_g$ are not absorbed and $E - E_g$ will be lost by thermalization. A fraction of the charge carriers undergo radiative recombination. The difference between the electrical work and the bandgap energy is described by the isothermal dissipation. (b) Analysis of the losses in different materials top performing solar cell with respect to the Shockley-Queisser limit for their bandgap energy (source: Guillemoles et al.²⁵).

1.III.2 III-V semiconductors

III	IV	V	VI
5 B Boron	6 C Carbon	7 N Nitrogen	8 O Oxygen
13 Al Aluminum	14 Si Silicon	15 P Phosphorus	16 S Sulfur
31 Ga Gallium	32 Ge Germanium	33 As Arsenic	34 Se Selenium
49 In Indium	50 Sn Tin	51 Sb Antimony	52 Te Tellurium

Figure 1-13: Extract of the periodic table where elements used in III-V semiconductors are highlighted (adapted from source⁹)

III-V semiconductors are alloys of group III elements combined with group V ones, shown in Figure 1-14. Their crystalline structure is based on covalent bonds created from the electron pooling from III-group elements to V ones. They feature high carrier mobilities, large absorption coefficients, and mainly direct bandgap. The shares of elements in the alloys determine the lattice constant and thus allow to tune of the bandgap energy. It turns out that Gallium Arsenide (GaAs) owes a gap energy of 1.424eV, which is optimal with respect to the Shockley-Queisser limit and makes it a common choice for photovoltaic cells. This material allowed the obtention of efficiency as high as 29.1% in thin film crystal²⁶. If III-

V provides the most efficient devices, they are also the most expensive due to a complex and costly fabrication process combined with quite low availability of material. These characteristics and their reliability allowed their use in space, their first historically niche application²⁷.

1.III.3 Perovskite

Originally designing the calcium titanate mineral discovered in the Ural in 1839, perovskite nowadays refers to a class of compounds owing the same crystalline structure. Illustrated in Figure 1-14, their crystal lattices are described by the formula ABX_3 , where A and B design organic and metal cations, respectively, and X represent an anion. Thus, behind this terminology lies a considerable diversity of the materials classified in two subfamilies. Depending on the anion, the material can be an oxide or a halide perovskite. Their structure can ally organic and inorganic compounds and aims at combining their advantages. Indeed, organic structures are characterized by good solubility allowing solution processing, and inorganic ones are associated with high crystallinity levels.

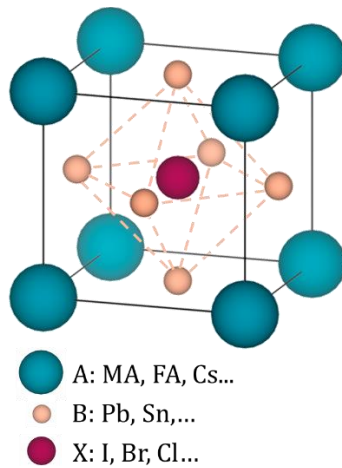


Figure 1-14: Crystal structure of halide perovskites

Their applications in photovoltaic devices have known rapid growth¹⁹ since the first solid-state perovskite solar cell was demonstrated in 2012. Ten years later, state-of-the-art devices achieved a 25.7% efficiency at the lab scale. Indeed, perovskites are attractive for industrial applications: processed in solution, they are tunable, and have low materials and fabrication costs. Otherwise, their energy payback time of the month's order is shorter²⁸ than their counterparts. However, their process upscale and stability improvement must be reached before perovskites are implemented in commercial modules.

The obtention of high-efficiency devices requires the appropriate optical and electronic properties. Organic lead halide perovskite has demonstrated a high absorption coefficient with a sharp edge²⁹. It allows the fabrication of devices with thicknesses below their diffusion length for efficient extraction. Indeed, this diffusion length is of the micrometer order, resulting from mobilities in the range $1 - 100 \text{ cm}^2 / (V.s)$ and relatively long lifetimes ($40\text{ns} - 1\mu\text{s}$) allowed by low non radiative recombination.

1.III.4 Fluorophores

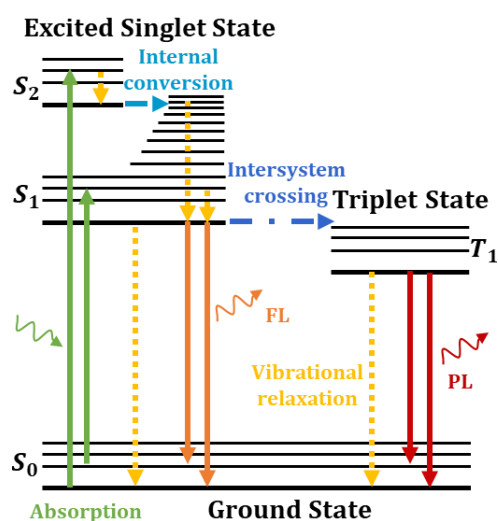


Figure 1-15: Perrin-Jablonski diagram describing fluorescence emission of organic dyes.

Contrarily to the previously introduced materials used to generate and extract the electron-hole pairs, fluorophores are used as light concentrators³⁰. These organic molecules are low-cost and owe high PLQY, making them species of interest for low-concentration photovoltaics. They can be embedded in polymer matrices as PMMA for integration purposes. Their electronic structure is composed of discrete states rather than a continuum, as shown in the Perrin Jablonski diagram in Figure 1-15. Light absorption and emission happen at the scale of one molecule: as a consequence, the absorption depends on the molecular concentration, and no electronic transport is possible. Also, relaxation mechanisms occur before light emission,

leading to a Stokes shift between absorption and emission spectra.

Conclusion

This first chapter has introduced the different notions at stake in the thesis. Luminescence constitutes one of the recombination pathways after the generation of charge carriers in photovoltaic material, which can be done by light absorption. Radiative recombination competes with nonradiative ones and shows the material's quality. It takes place together with charge transport, which plays a major role on the luminescence signal.

Describing the luminescence spectrally and temporally is a way to access these optoelectronic properties. Indeed, corresponding models based on Planck's generalized law and rates equation involve light absorption and charge carrier densities. The interpretation of luminescence relies on many assumptions and requires setting parameters to extract the optoelectronic properties. Notably, the different dimensions of the emitted light have various dependencies on the properties at stake, and their simultaneous acquisition can support their disentanglement. This thesis explores how acquiring spectrally resolved maps of photoluminescence in pulsed excitation can contribute to material characterization while limiting the necessary prior knowledge and controlling underlying hypotheses and models.

Chapter 2 - Characterization imaging techniques

"What makes photography a strange invention is that its primary raw materials are time and light."

— **John Berger**

This chapter focuses on imaging and its use in characterization techniques. Section 2.I set the context by introducing the different ways to acquire images through focal plane arrays or non-imaging detectors, by raster scanning or single-pixel imaging. Far from being limited to 2D, imaging can be multidimensional, a notion that has recently gained in popularity. Single-pixel imaging, a technique implemented during this thesis, is explained in detail, and its applications are reviewed.

Section 2.II addresses multidimensional imaging already in use for the characterization of photoluminescence of photovoltaic materials. After introducing different illumination configurations, hyperspectral and time-resolved imaging are presented. For both techniques, we describe the data at stake, provide a short history of their technology development and current state-of-the-art, and explain how they are performed in the frame of this work.

Section 2.III paves the way for techniques that provide more information than combined hyperspectral and time-resolved imaging. Indeed, 4D data (2D spatial, temporal and spectral) have been or could be reached through different techniques introduced. Such data set raises questions regarding data acquisition, processing, and redundancy.

2.I How to build an image?

Several techniques allow the obtention of images: arrays of photosites can acquire the information in different locations in a snapshot, or one photodetector can take a series of measurements before reconstructing the images. Each pixel represents the intensity of light that can be further resolved across dimensions to provide multidimensional imaging. Single Pixel Imaging will be introduced, as well as its applications.

2.I.1 Imaging approaches

Imaging consists of detecting and spatial mapping a light field and representing it. Hence, its history is inherently linked to developing projection optics and detectors. Technologies have known many revolutions since the first uses of photosensitive resins when Edmond Becquerel obtained "photochromatic" images in 1848. We can distinguish different ways to achieve this intensity mapping, as pictured in Figure 2-1.

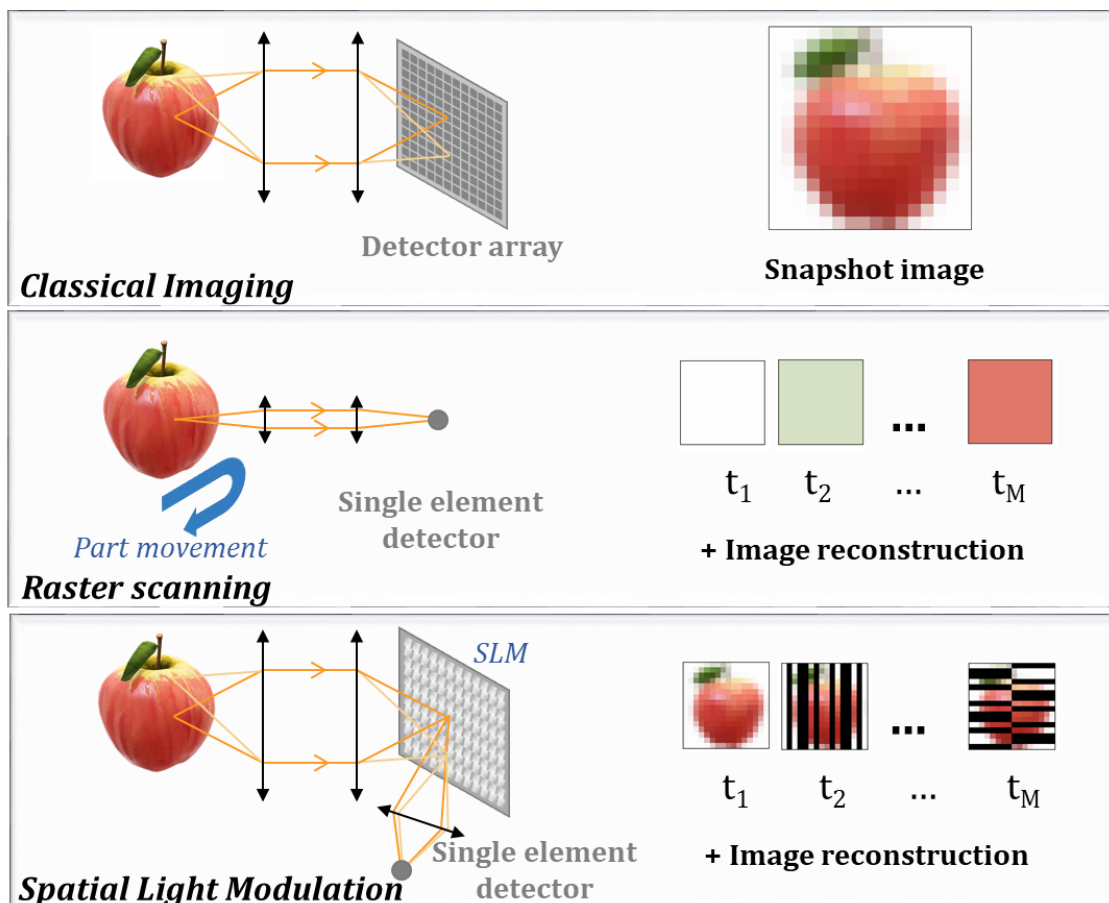


Figure 2-1: Imaging approaches: (top) conventional imaging uses an array of sensors to obtain all spatial information instantaneously, (middle) scanning allows the reconstruction of an image from a single-pixel detector and the movement of an element, detector, (bottom) optical multiplexing employs spatial light modulation (SLM) with a non-imaging sensor.

Classical imaging employs a spatially resolved detector in the focal plane of imaging optics to directly acquire the image of interest projection. Focal plane arrays (FPA) such as charged coupled devices (CCD) and complementary metal-oxide-semiconductor (CMOS) are widespread systems to obtain digital information. Technological advances in the past decades have led to reduced photosite size, as illustrated in Figure 2-2. Notably, light guides or backside illumination optimize light collection. Deep trench isolation optimize light collection. Deep trench isolation has allowed the reduction of dark current and an increase of the photosite capacity, which can store more electrons before saturation. Pixel sizes nowadays reach magnitudes of visible wavelengths; thereby, they can be smaller than the instrumental point spread function, even for high numerical apertures. FPA sensitivity is also improving, and intensified detectors array can now detect at the single photon level¹.

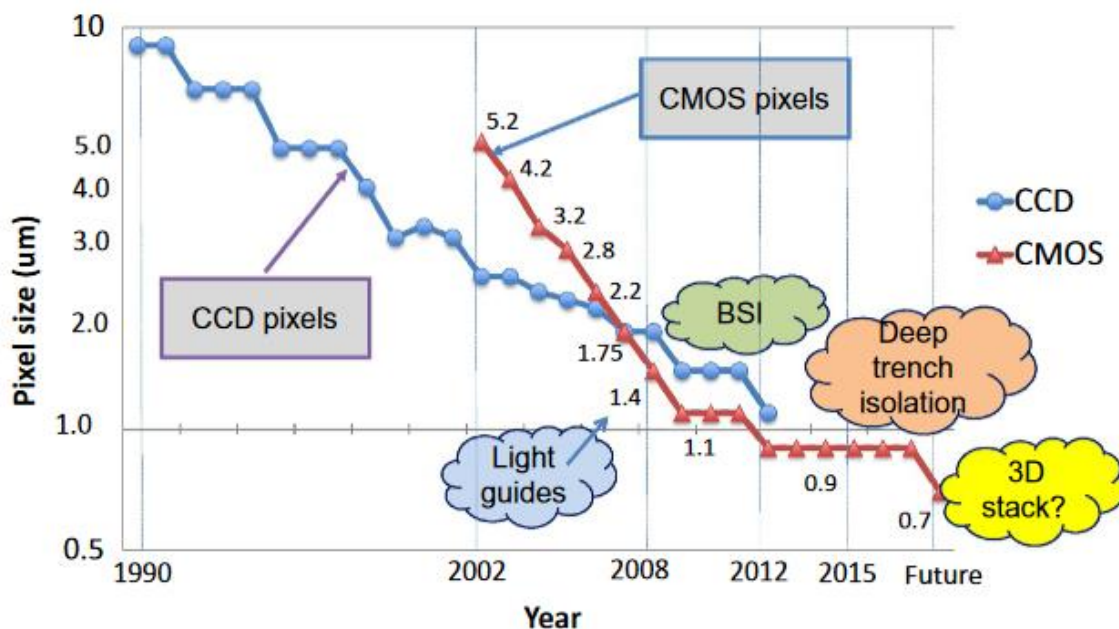


Figure 2-2 Evolution of pixel size of CCD and CMOS detectors source². This decrease has been supported by the technological advances featured by the clouds allowing an increased light collection as the use of light guides or backside illumination (BSI) and the reduction of dark current and photosite capacity by deep trench isolation. Reprinted from *High Performance Silicon Imaging*, ISBN 978-0-08-102434-8, Robert Gove, chap7, p.190, Copyright (2020), with permission from Elsevier.

In terms of signal processing, scanning can be described as the time-sequential acquisition of slices of the final image³. One pixel is seen at a time, and its location changes at each measurement, as pictured in Figure 2-1. It requires the movement of a mechanical part, either illumination, the object under study, or the detector.

To avoid moving critical components in a scanning architecture, some systems used a reticle with holes to select a location in the light field to be mapped, as displayed in Figure 2-3. Such masks dramatically decrease the light throughput by dividing it by the number of pixels

(assuming a homogenous intensity). In 1968, Gottlieb⁴ proposed increasing the number of holes to improve the signal quality. By doing this, he uses spatial light modulation by a set of masks to encode the spatial information temporally. This approach can be qualified as optical multiplexing⁵ or, more recently, Single-Pixel Imaging⁶. The employed terminology varies greatly from year to year and from research field to field. This strategy is often named *coded aperture imaging*⁷ in the X-ray field where lenses cannot be employed, and *Hadamard Transform Imager*⁸ for specific patterns displayed on the masks.

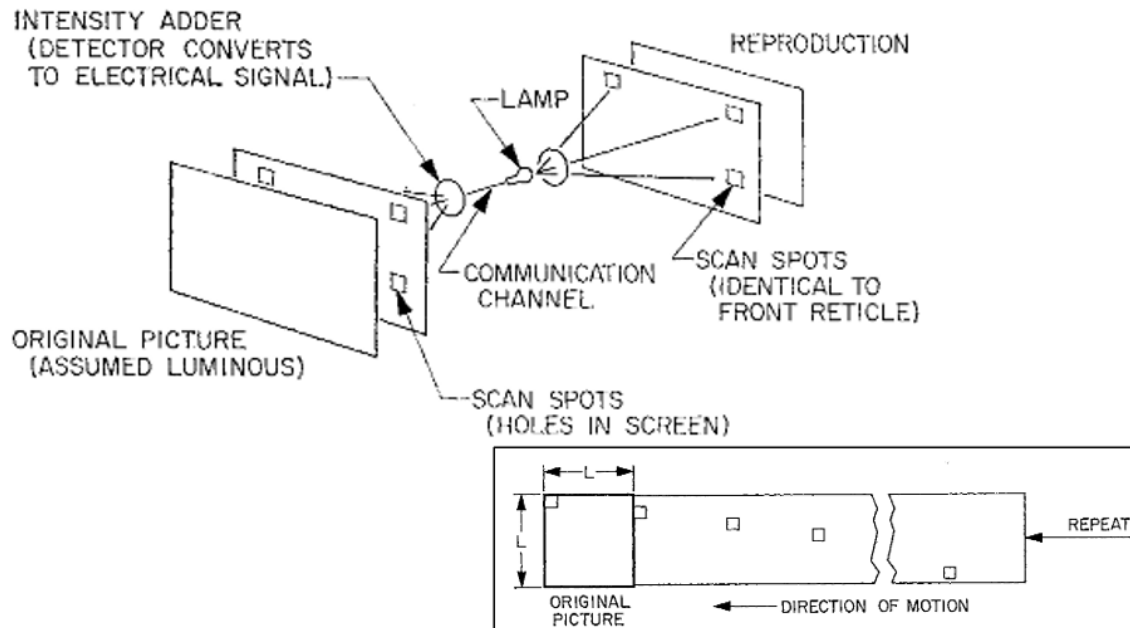


Figure 2-3: Reticle television scanning system employing spatial light modulation developed by Gottlieb⁴ © [1968] IEEE. The detector collects the intensity from a spot of the original image selected by a hole in a reticle. The image can be reproduced by having a similar reticle in motion in front of a lamp whose intensity is determined by the detector signal.

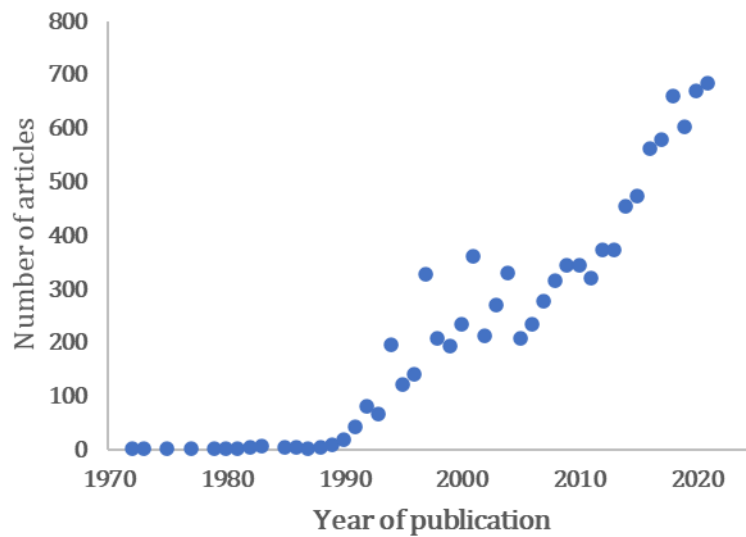
The idea of retrieving a signal through spatial modulating masks had earlier appeared, as demonstrated by the multi-slit spectrometer of Golay⁹ in the late 40s. The choices of holes raise the age-old question of the design of an experiment to perform a measurement effectively. It can be illustrated through the example of a chemist that needs to weigh different objects¹⁰. If he has n times the same compound, he can scale them together to reduce the standard error by a factor \sqrt{n} . Similarly, if he has n different objects to measure, weighing groups of objects together allow to reduce the error. Similarly, optical multiplexing has to find how to group the pixels measured to optimize the signal-to-noise ratio and be competitive to their focal plane array counterparts.

Indeed, as both scan and optical multiplexing rely on a series of measurements, they involve longer acquisition time and assume the system's stability under study. This point will be further discussed later, as some strategies still allow real-time reconstruction. Since they do not require arrays of detectors, they provide a more cost-effective approach. Moreover, they

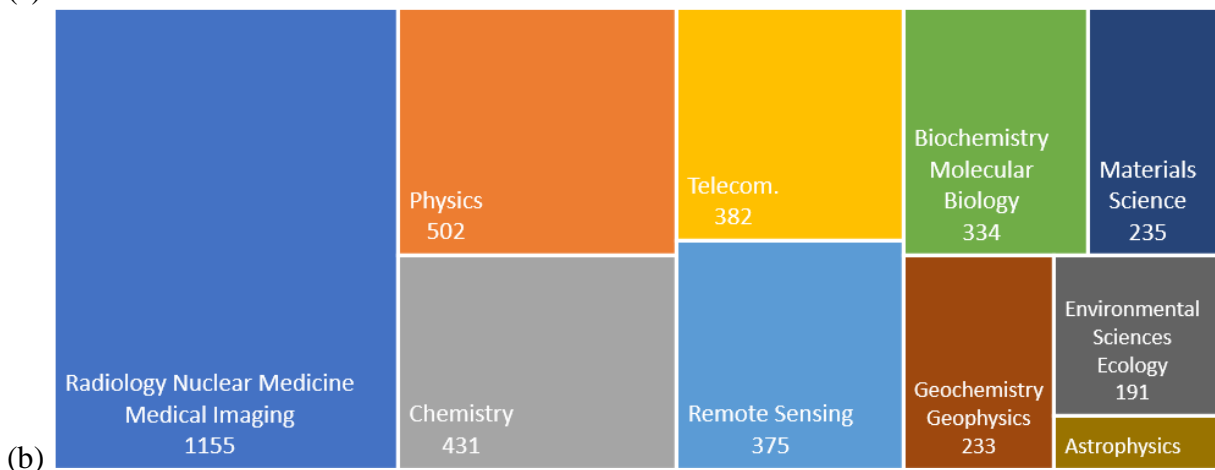
will enable the acquisition of spatial maps in a spectral domain where detector arrays are not available or expensive. Detectors involved can also be far bigger than the spatial resolution and hence more efficient. As detailed in the following sections, it offers the possibility to use sensors sensitive to a specific light characteristic – typically spectrally resolved- thus providing multidimensional imaging.

2.1.2 Introduction to multidimensional imaging

Photons carry information along nine dimensions¹¹. Indeed, geometric optics describes light with three spatial coordinates and two polar propagation angles. Wave and particle models add the notions of wavelength, emission time, polarization orientation, and ellipticity angle. It is possible to add any of the remaining seven dimensions to a spatial map to obtain **multidimensional imaging**.



(a)



(b)

Figure 2-4: Analysis of the scientific articles dealing with multidimensional imaging. (a) Evolution of their number since the first occurrence in 1970, (b) Examples of fields of application referenced by the articles.

However, experimental setups are classically limited to three to five dimensions because of the complexity, costs, and compactness requirements. The development of such systems is pushed forward by progress in focal plane arrays (CCD) and microelectromechanical systems, as well as by the improvement of algorithms and processors. Its popularization can be illustrated by the growing number of articles using this terminology shown in Figure 2-4(a) – although this statistic reflects the employ of the word as much as the techniques. Multidimensional imaging is applied in various fields, including medical, defense, and environment, as illustrated in Figure 2-4(b). It characterizes objects at both macro and micro scales, down to the resolution limit set by Abbe law. Different approaches qualified as super-resolved imaging are investigated to break this fundamental limit, often considered as the main lock of optical imaging¹².

2.I.3 Principle of Single-Pixel Imaging

This part describes Single-Pixel Imaging and the hardware it relies on. Mathematical models and possible reconstruction approaches are introduced. Various modulation patterns can be chosen and implemented in different ways.

2.I.3.a Single-Pixel Imaging hardware implementation

Single-Pixel imaging (SPI) relies on two key components to retrieve the spatial maps of light intensity: one providing the spatial light modulation and a single-point (non-imaging) photodetector.

This term was popularized following the seminal work of Duarte¹³ on compressive sensing in 2009. Due to its novelty, it is often restricted to systems based on electrically addressed spatial light modulators (EASLM) that convert an electric signal into a spatial modulation of light intensity or phase, thus providing computer-controlled masks (or *patterns*). The most commonly employed ones are **Digital Micromirrors Devices (DMD)**: as illustrated in Figure 2-5(a), they consist of millions of micro-mirrors arrays. Each can be set in two positions and reflects the light in directions corresponding to the "on" and "off" states. Consequently, DMD can modulate light following binarized patterns. They can be operated with frequencies as high as a few kHz. They can also offer grey scale levels by subdividing a time interval between on and off states. Video projectors use such devices to create the image sequentially in red, green, and blue colors. As shown in Figure 2-5 (b), DMD are controlled by electronic chips to allow a digital command from pattern loading and storage to display timing.

Other components can achieve intensity light spatial modulation¹⁴. Liquid Crystal Display panels feature more pixels with a higher pitch and lower frame rates than DMD but are generally designed for a specific wavelength and are monochromatic. Liquid crystal

metamaterial absorbers constitute a barely available alternative for modulation in reflection for a small number of pixels. However, they can represent a negative value on the pattern by imposing a destructive phase shift.

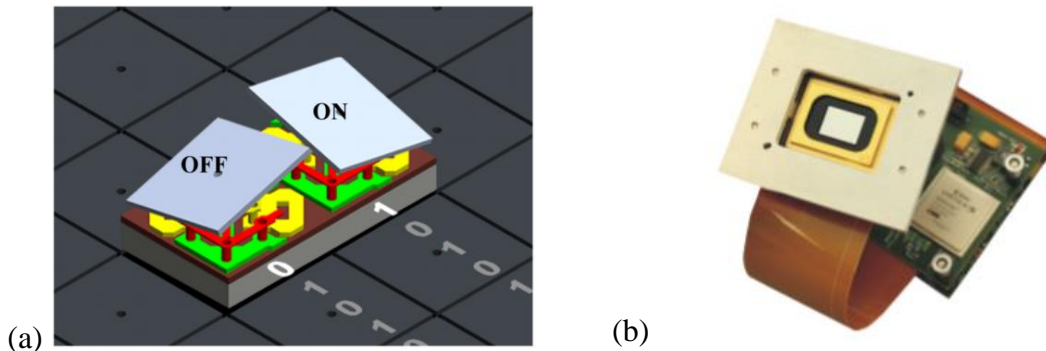


Figure 2-5: (a) DMD microscale structure¹⁵ © [2014] IEEE, (b) DMD module visual (Vialux website)

Two main SPI schemes can be distinguished: structured detection and structured illumination¹⁶. In the former, and as displayed in Figure 2-1, the EASLM is placed in the image plane where the pixelated detector is in classical imaging. Thus, it can be referred to as focal plane modulation¹⁷. Both active and passive imaging (i.e., with and without illumination) is feasible with such a scheme. Whereas in structured illumination, the spatial light modulator projects the patterns on the object. This approach allows using modulated light sources instead of a homogeneous one combined with an EASLM. Literature shows examples of pseudo thermal light sources, rotating ground glass (that can't be controlled), and LED arrays¹⁸. When patterns are unknown, it is possible to map them by placing a beam-splitter before the object and employing an FPA, as shown in Figure 2-6. As the sample is not on the imaging branch, this architecture is known as ghost imaging.

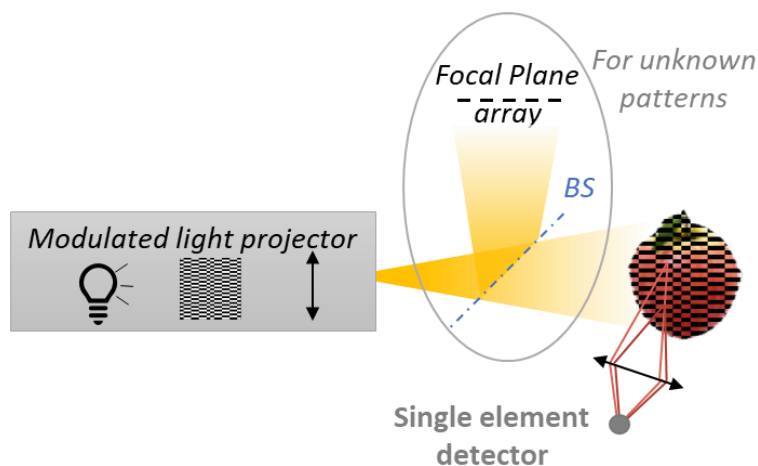


Figure 2-6: Schematic of Single-Pixel Imaging in structured illumination approach. The modulated light projector consists of a modulated light source and projection optics. When the projected pattern is unknown, it can be imaged by a focal plane array after the division of the light by a beam-splitter (BS).

In both structured illumination and detection, the measured signal is higher if the pattern and the scene image are similar. Analysis of this signal and its correlation with the projected patterns allows the intensity map to be reconstructed. With this principle, a photodiode can then be turned into a camera and a spectrometer into a spectrally resolved imager.

2.I.3.b Mathematical view and strategies

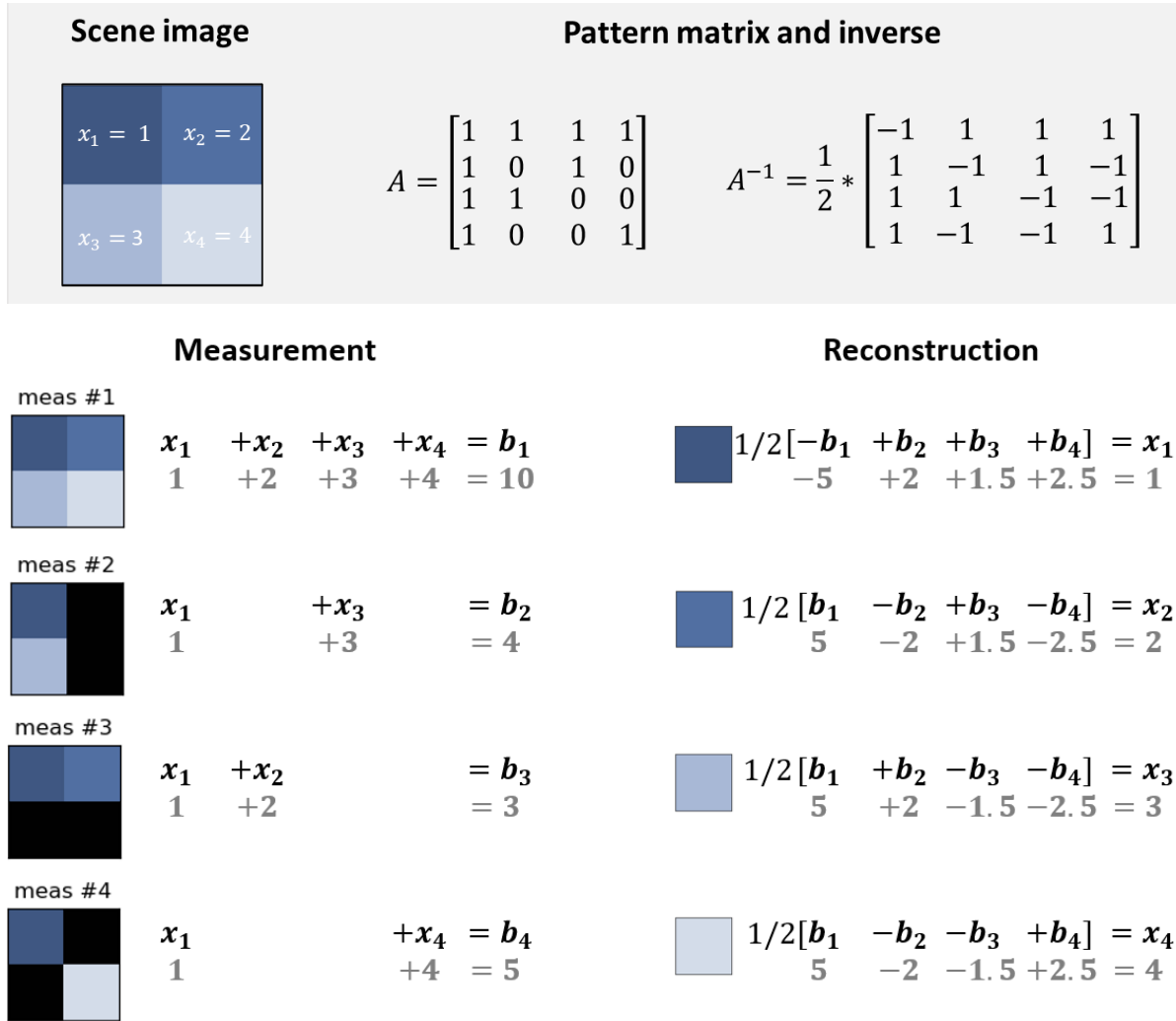


Figure 2-7: Example of single-pixel imaging measurement and basis scan reconstruction on a 2x2 scene image with the numerical application. The scene image is modulated with the invertible matrix A of inverse A^{-1} . The resulting measurement vector is obtained by multiplying A by the vector corresponding to the image, as pictured on the bottom left. Image reconstruction corresponds to the inverse problem, in which A^{-1} multiplies the measurement vector, as shown on the right.

Structured illumination and detection both lead to the detector viewing the image modulated by a pattern and integrating it spatially. In a perfect system (i.e., only the modulator affects the transmission), for each mask displayed i , the corresponding measurement b_i can be obtained from the sum of the transmitted information over the n pixels of the pattern:

$$b_i = \sum_{k=1}^n a_{i,k} * x_k \quad (2-1)$$

Where x_k is the image on the light modulator at pixel k , $a_{i,k}$ is the transmission of the modulator for pixel k of the pattern i , and takes values between 0 and 1. Figure 2-7 presents a practical example of a single-pixel imaging procedure with a 2x2 scene image with a binary mask, taking values of 1 or 0. The scene image on the top left is modulated with four different masks illustrated in the measurement section: the black pixels are obstructed and correspond to zero transmission. The pattern matrix naturally appears when writing the equations corresponding to the spatial integration performed by the detector.

Thus, the set of patterns encoding is provided by the matrix $A = (a_{i,k})_{1 \leq i \leq m, 1 \leq k \leq n}$, where m is the number of measurements performed. An example of a matrix of patterns and pattern extraction is shown in Figure 2-8. One matrix dimension contains the two mapped spatial dimensions: to obtain the spatial mask, values of a matrix line must be "folded into a two-dimensional array, much as the one-dimensional lines of written words are folded into a two-dimensional array of writing on this page"⁸.

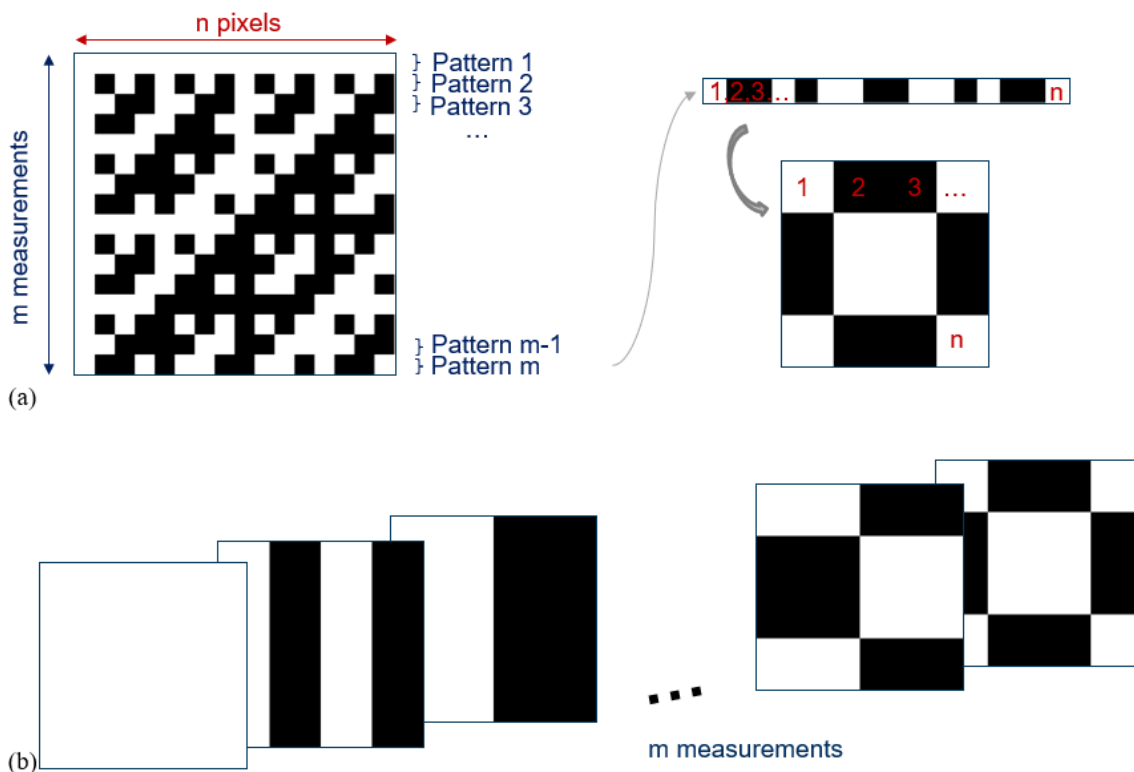


Figure 2-8: (a) Example of the extraction of patterns from a matrix derived from a 16-element Hadamard matrix. White color represents values equal to 1, and black stands for 0. (b) Resulting two-dimensional patterns for a 4x4 image, white thus represents full transmission and black null one.

Hence, the problem of interest can be described mathematically by finding the target image x from the matrix A and the measurement vector b :

$$Ax = b \quad (2-2)$$

One can note that in this model, the measurement is considered equal to the collected intensity. However, detectors return a signal in the form of counts in digital units that require calibration to assess the light intensity, as discussed in the Appendix A. This signal is further affected by various noise sources.

A wide range of approaches^{13,14,19} can be used to solve this inversion problem, as schematized in Figure 2-9. It leads to varied numbers of measurements needed for an efficient reconstruction and the computational complexity of the corresponding algorithm. Some approaches are suitable for uncontrolled masks, whereas DMD allows choosing the matrix A with binary (0,1) or positivity constraint.

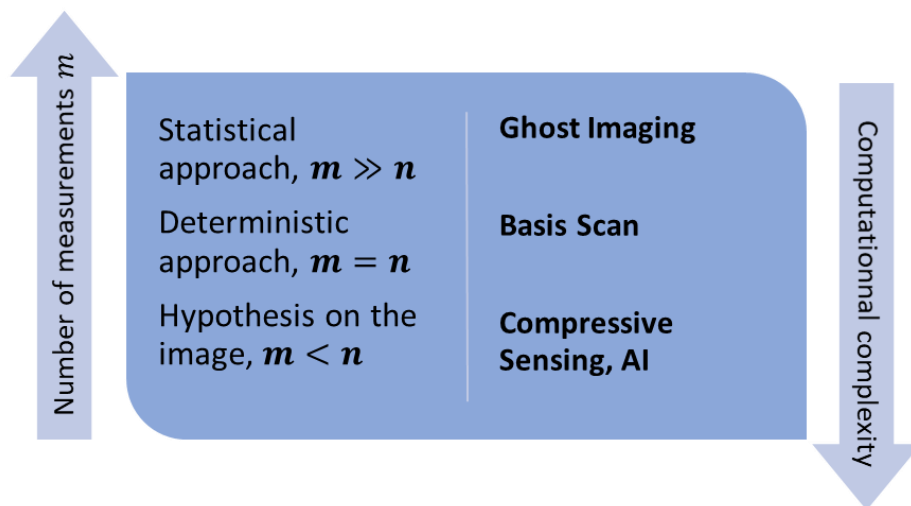


Figure 2-9: Different strategies possible to solve the optimization problem corresponding to image reconstruction with n pixels. Ghost imaging is a statistical approaches requiring more measures m than pixels for satisfactory reconstruction and very low computational complexity. Basis scan relies on matrix inversion requiring as many measurements as pixels. Compressive sensing and artificial intelligence allow imaging with $m < n$.

Ghost imaging: This approach²⁰ is associated with the structured illumination approach with an uncontrolled source imaged through the additional branch pictured in Figure 2-6. It can be employed with pseudo-thermal sourcesⁱ, often consisting of a monochromatic beam passing through a rotating diffuser. It is thus implementable with off the shelves components. In such a case, the number of speckles determines the number of pixels, allowing less control over the

ⁱ Light source with a high temporal coherence length and a low spatial coherence

reconstruction. Its conventional version is essentially a correlation measurement: the reconstruction is obtained from summing the patterns weighted by the output signal. The mean pattern $\langle a_i \rangle$ is further retrieved, though it is sometimes considered homogeneous. It reads:

$$x = \frac{1}{m} \sum_{i=1}^m b_i a_i - \langle b_i \rangle \langle a_i \rangle \quad (2-3)$$

The reconstruction is very elementary in terms of computational complexity. However, it requires a high sampling ratio to recover the image effectively and is statistical. Differential ghost imaging is a variation of this algorithm that considers the fluctuation of the light source intensity, thus improving the signal quality. As a proof of concept, Ferri et al.¹⁹ illustrated its performance in the reconstruction of particles transmission: for 4590 speckles, particles are observable with 10^4 acquisitions by differential ghost imaging, whereas classical ghost imaging still requires more.

Basis scan: The basis scan corresponds to modulating light with a 2D basis set of patterns, owing to as many patterns as pixels in the reconstructed image. Hence, the measurement does not have spatial overlap. This situation is called a Nyquist rate sampling and corresponds to performing $x = A^{-1}b$, as illustrated in Figure 2-7. It allows a perfect reconstruction in a noise-free scheme and is thus deterministic. Similar approaches are often referred to as optical multiplexing⁵ in the literature and have been implemented since the 70s⁸.

Compressive sensing: More recent approaches often aim at lowering the sampling ratio to reduce the acquisition time. An appropriate hypothesis on the image makes it possible to perform sampling at a sub-Nyquist rate. In this frame, compressive sensing limits measurements to the high-weight coefficients in a given basis in which the image is assumed compressible¹³. In other words, the image x can be represented by K coefficients $(\alpha_i)_{1 \leq i \leq K}$ in a basis Ψ , reading $x = \Psi\alpha$. Compressive sensing pursue the obtention of α that minimizes $b - A\Psi\alpha$, an approach that is more efficient than looking for the x that minimizes $b - Ax$. However, this reduction of measurement time goes along with more complex algorithms and longer reconstruction time.

Moore Penrose (pseudo-inverse) can be used to obtain image reconstruction with fewer measurements than pixels. This matrix, denoted A^+ , is defined as the one minimizing $I - A^+A$ and provides a generalization of inverse to rectangular matrix²¹. It is independent of the image, providing an intermediary solution between basis scan and compressive sensing.

The approach of adaptative basis scan²² also aims at acquiring only the major elements of a basis. It relies on the feedback between the detector and the spatial light modulator to predict them and improve acquisition efficiency.

Artificial intelligence: More recently, single-pixel imaging has been performed with deep learning approaches. Achieving real-time acquisitions of compressed video²³, deep neural networks also provide faster reconstructions of the intensity and fluorescence lifetime images²⁴. These algorithms tend to outperform their compressive sensing counterparts in noisy conditions^{25–27}. Indeed, their training can include noise, or they contain a denoising layer²⁸. It is often considered the future of single-pixel imaging.

2.1.3.c Patterns family

The next sections introduce the patterns commonly used in SPI using a controllable modulator and the algorithm used to recover the image.

2.1.3.c.1 *Random*

At first, single-pixel imaging technics have used patterns generated by non-controllable diffusers that were considered random. As well, some pseudo-random patterns can be computationally generated. For instance, they can be provided by binarized variables from a uniform Bernoulli distribution or a white noise²⁹.

The main advantage of modulating light with random patterns is that the object needs no pre-set rules. However, as the information provided by the measurements might overlap, it also requires an increased sampling rate to reach the same reconstruction quality as the other patterns. They also perform well in compressive sensing. Indeed, only the major components are conserved in a chosen compression basis, commonly the wavelet or cosine ones. Consequently, it is better to perform the sampling with patterns that cannot be compressed in these bases, leading to overlapping spatial information, and random patterns avoid this pitfall. According to this principle, Morlet wavelet correlated random patterns with a compression of 4% have been achieved with a competitive signal-to-noise ratio³⁰.

2.1.3.c.2 *Orthogonal patterns*

Orthogonal sets of patterns can be obtained from any two-dimensional basis matrix. They avoid the overlap between the spatial information provided by the different measurements. Therefore, they offer a perfect reconstruction at the Nyquist rate in principle - assuming no noise, for example, and can also be used for compressive sensing³¹.

The most common choice is the Hadamard matrix. They are constructed from the following relation:

$$H_2 = \begin{bmatrix} 1 & 1 \\ 1 & -1 \end{bmatrix} \quad (2-4)$$

$$H_{2^k} = \begin{bmatrix} H_{2^{k-1}} & H_{2^{k-1}} \\ H_{2^{k-1}} & -H_{2^{k-1}} \end{bmatrix}$$

Because they are binary, the Hadamard matrix can be easily used as an entry for DMD and are a widespread choice for SPI. As the -1 elements cannot be retrieved with one photodetector in one acquisition set, different approaches are possible. They are presented in the next paragraph.

A Fourier basis pattern can also be used to acquire the Fourier spectrum of the image. This basis is originally greyscaled and requires fewer measurements than Hadamard patterns but is also more sensitive to noise³². A conversion from greyscale to binary has been achieved³² so that this basis can be adapted to the DMD setup. If the Fourier basis is orthogonal in greyscale, one can note that its implementation with binary matrices removes this property.

2.1.3.d Patterns implementation

As the SLM transmission is comprised between 0 and 1, the physical implementation of patterns, Hadamard ones for instance, requires positive values. Different approaches are feasible to allow their use.

Splitting: The patterns are separated into two sets A_+ and A_- containing the positive and negative values, respectively. For Hadamard, this is equivalent to displaying a first set where one would translate in the 'on' position and -1 in the 'off', followed by complementary patterns. The measure of the second series is subtracted from the first one.

$$b = A_+x - A_-x \quad (2-5)$$

Shifting: This approach slides all the values into the positive realm. In the case of the Hadamard matrix, it consists in replacing the -1 with 0.

$$A' = \frac{A - \min(A)}{\max(A)} \quad (2-6)$$

Doing so with Hadamard, the reconstruction of the first pixel is very sensitive to noise due to the unbalanced coefficients in the matrix inverse. It has led to the definition of the S matrix, in which the first row and column are removed.

Semi-non-negative matrix factorization (SNMF): Rousset et al.³³ proposed this algorithm to determine a transform of the pattern with a positivity constraint that allows their representation and also minimizes dark current (offset) sensitivity. Nevertheless, this algorithm returns greyscale values that are further discretized.

The matrix condition number helps assess the pattern implementation. The closer it is to one, the more homogeneous will be the pattern contributions and the easier the reconstruction is. Shifting is the easiest implementation; however, it decreases problem conditioning. For a 64-element matrix, the shifted Hadamard condition number is 0.0053, whereas the row matrix's one is 0.0156. It can be, therefore, more sensitive to noise.

2.I.4 Application of Single-Pixel Imaging: State of the art

With the democratization of SPI hardware, this technique allowed the development of new optical setups. It is particularly relevant for imaging with unconventional detectors or for implementing both multidimensional and multimodal imaging.

2.I.4.a Unconventional sensors

SPI can employ photodetectors with higher optical etendue than array photo-sites and thus possess a heightened sensitivity allowing imaging in low light conditions. In this vein, Li et al.³⁴ provide an example of an SPI system performing underwater detection based on a 13x13mm² sensor. This surface area is comparable to the size of a classical focal plane array. Photodiodes or photomultiplier tubes also have an increased sensitivity compared to regular sensors³⁵. Therefore they can be employed for imaging in remote sensing, achieving spatial reconstruction of a target at a distance greater than two kilometers^{36,37}.

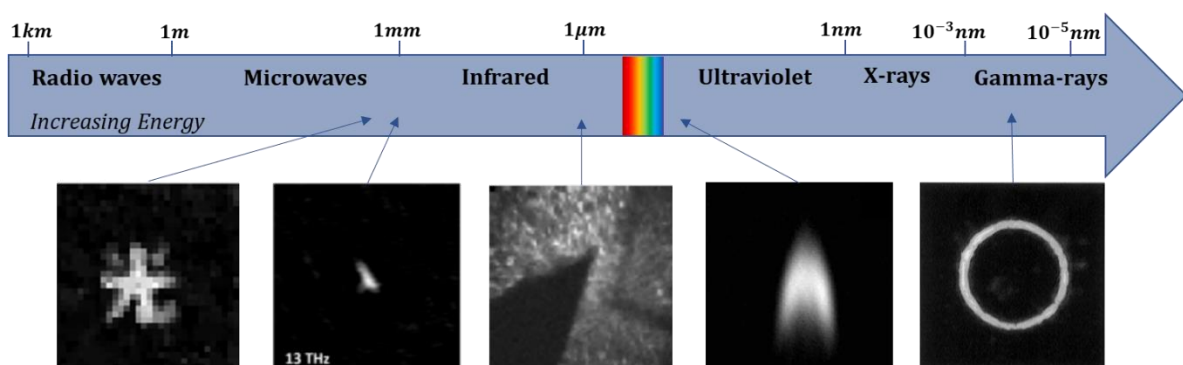


Figure 2-10: Examples of images reconstructed by SPI in different spectral domains outside of visible range. From left to right: 100GHz - Reprinted from Chan et al.³⁸ with the permission of AIP Publishing, 13THZ – Vallés et al.³⁹, 1550nm – Radwell et al.⁴⁰, 230-390nm – Zhang et al.⁴¹, 60keV-1.5MeV -Reprinted from Ivanov et al.⁴² with permission from Elsevier.

SPI allows the design of affordable instruments in ranges where silicon is inefficient and pixelated sensors are costly, as illustrated in Figure 2-10. DMD allows image reconstruction in the infrared, as demonstrated by Radwell et al.⁴⁰, and in the ultraviolet, as shown by Zhang's setup, to study flame chemiluminescence⁴¹. Other modulators are used with the same principle in domains far from the visible. Indeed, spatial modulators owing elements with pitch comparable to the wavelength induce diffraction that hinders SPI implementation, as highlighted by Schmitt⁴³. Moreover, the appropriate coating is required to allow intensity modulation. Thus, examples of coded aperture are many in the X- and gamma-ray ranges with masks made of brass and tantalum^{42,44} with holes of mm diameter. On the opposite side of the spectrum, terahertz imaging also employs metallic masks of comparable sizes³⁹.

2.1.4.b Multidimensional Imaging

Employed with a detector resolved in one of the light dimensions, SPI provides a way to implement multidimensional imaging. Literature is rich in examples of spectrally resolved imagers based on SPI and a spectrometer^{5,8,26,45,46}. They are used with various strategies from basis scan (31 x 33 spatial x 63 spectral)⁸ to the complex neural network (64 x 64 spatial x 2048 spectral). Similarly, time-resolved photodetectors as Time-correlated Single Photon Counting (TCPSC) sensors provide maps of intensity decays once combined with SPI. It has been demonstrated for PL characterization of photovoltaic materials⁴⁷. Moreover, a spectrophotometer based on a 16-channel photomultiplier tube allowed the acquisition of multispectral time-resolved intensity^{48,49}.

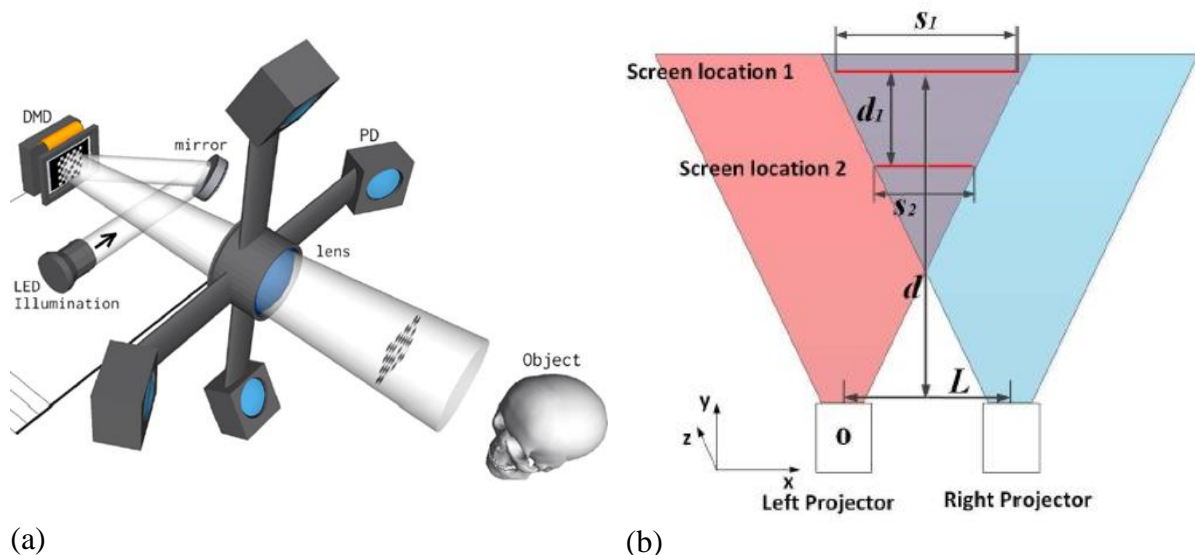


Figure 2-11: (a) Scheme of 3D SPI system based on stereo vision – several detectors capture signal from one illumination (source: Zhang et al.⁵⁰) (b) Scheme of 3D computational ghost imaging based on photometric stereo – the illumination is performed from different angles while measured by a unique detector (source: Yang et al.⁵¹, © [2019] IEEE).

Depth information can be obtained by collecting the images from different angles, known as stereo vision¹⁷, illustrated in Figure 2-11(a). It was demonstrated with SPI by analyzing the patterns with four photodiodes⁵⁰. Alternatively, projecting them from other locations and collecting them with one detector is an approach called photometric stereo⁵¹, shown in Figure 2-11(b). The use of SPI simplifies the pixel correspondences by comparison to classical imaging.

Furthermore, a measured dimension of light can serve to encode another: phase⁵² or time are classically used to obtain the depth information. The Time-of-flight technique uses high-speed detectors to perform three-dimensional imaging. Musara et al.⁵³ have demonstrated this technique with a 30ps-resolved TCSPC for a non-line-of-sight object characterized through its scattered light onto a wall. It translates to a 1.8cm depth resolution instrument, more limited by the variations of light paths for a given pixel than by the temporal resolution itself. A similar approach has been implemented in a direct reflection configuration, providing a depth mean squared error of 2.62mm⁵⁴. The acquisition speed achieved real-time three-dimensional video with a 12Hz frame rate in this case.

2.I.4.c Multimodal Imaging

In SPI, the pixels are determined by the spatial light modulators, not detectors. It is then possible to compare pixel by pixel the reconstruction of a similar scene obtained on different sensors simultaneously, allowing the combination of imaging techniques. It can be performed in structured illumination by capturing the light emitted in different directions or structured detection using the two outputs of a DMD. In both cases, it is possible to add beam splitters and sum up the detectors.

In this frame, Radwell⁴⁰ employs SPI with a detector in the visible and one in the IR⁴⁰. Following this approach, it is possible to increase the spectral range or the number of wavelengths detected simultaneously. Welsh performed RGB acquisitions by combining the signal of four photodetectors as depicted in Figure 2-12.

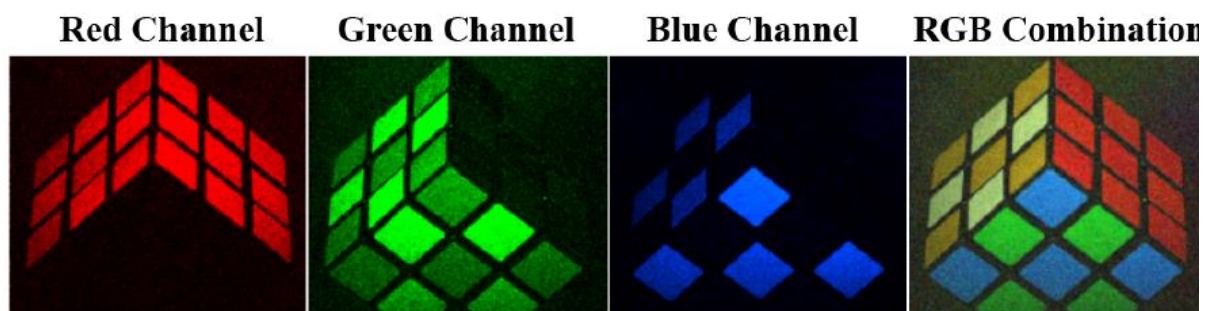


Figure 2-12: RGB acquisition obtained by SPI (source: Welsh³⁶). The measurement is performed by the photodetectors corresponding to the different channels simultaneously.

Positioning the detectors in transmission and in reflection configurations allowed the capture of both data with the same acquisition series, as demonstrated by Rodriguez et al.³⁵. Furthermore, this principle can combine different multidimensional techniques. Klein et al.⁵⁵ thus developed a setup providing hyperspectral transmission and time-resolved photoluminescence. Recently, a multiple SPI multidimensional setup was further combined with a focal plane array⁵⁶. Figure 2-13 shows this system, which provides at the same time multispectral SPI, time-resolved SPI, and a high-resolution map of fluorophores fluorescence. A data fusion algorithm based on regularization combines these three datasets in a 4D matrix resolved spatially, spectrally, and temporally. With this approach, the number of measurements is 0.0003 times the number of reconstructed pixels. Such compression depends on minimizing a cost function that implies a prior assumption on the dataset. It effectively exploits the redundancies of the data; however, it relies on no information for the temporal evolution of the spectrum. The produced 4D matrix is probably valid with assumptions reasonable with fluorophores: an exponential decay owing one lifetime and one spectrum per species.

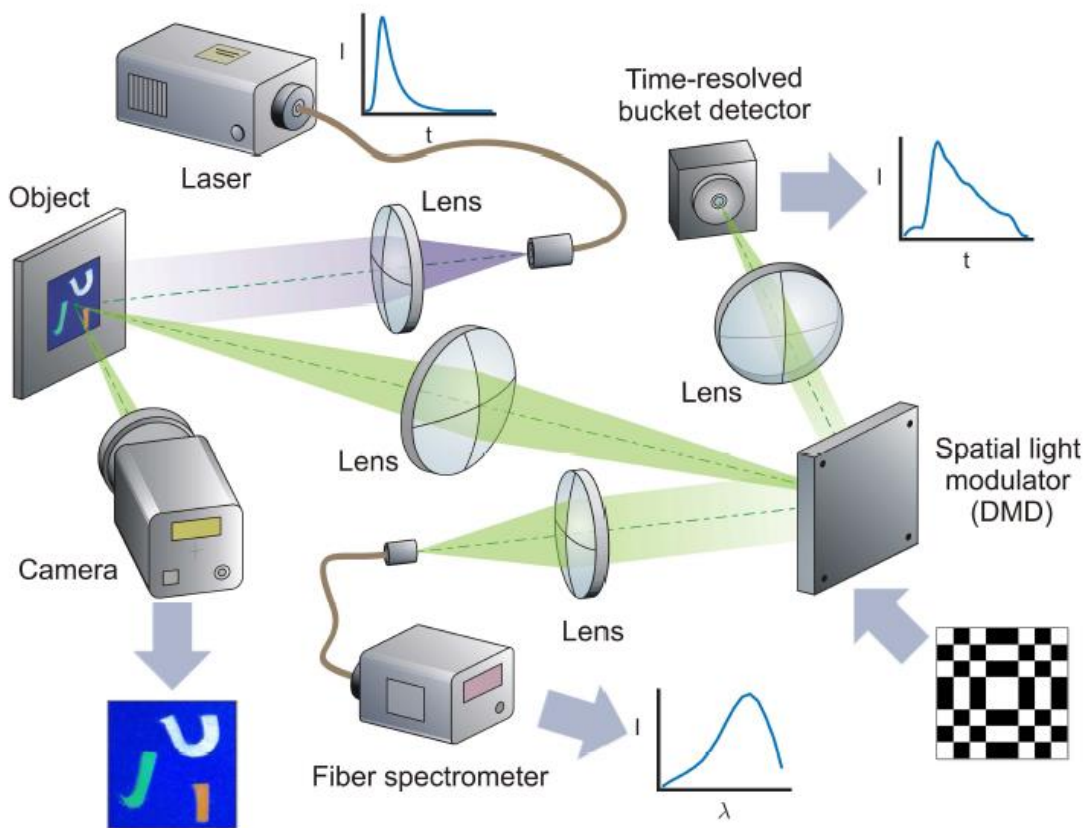


Figure 2-13: Giga Voxel multidimensional fluorescence imaging setup (source: Soldevila et al.⁵⁶). Single Pixel Imaging is performed with a time-resolved detector and a spectrometer simultaneously on the two outputs of the DMD, retrieving $I(x_{SPI}, y_{SPI}, t)$ and $I(x_{SPI}, y_{SPI}, \lambda)$, respectively. At the same time, the sample is imaged with a camera owing higher spatial resolution. Data fusion algorithm combines the different dataset into a 4D matrix $I(x, y, \lambda, t)$.

Another way to perform multimodal SPI involves acquiring different maps by varying the patterns despite the detector. Cox et al.⁵⁷ thus employed patterns modulated in both phase and intensity to obtain a reconstruction of these two quantities. Moreover, Zhang et al.⁵⁸ utilize a single photodiode and different sets of patterns to encrypt simultaneously spatial maps and the object's color and phase. That way, they perform multispectral depth-resolved imaging.

2.II Methods for hyperspectral and time-resolved PL imaging

Developing PL microscopy demands the integration of the imagers in optical setups. First, the different illumination configurations are shortly described. Then, the focus is on the principle of spectrally or temporally resolved imaging and the different approaches possible. In particular, the setups used in this work are described.

2.II.1 Illumination for PL imaging

Several illuminations have been used in this work; they can be sorted into two kinds.

Homogeneous illumination: the goal is to provide uniform conditions across the sample and avoid edge or carrier diffusion effects. Thus, the diameter of the light spot must be far broader than the electronic carrier diffusion length of the material. It allows the characterization of sample inhomogeneities such as grain boundaries or diffusion to contacts. In practice, the laser speckle has to be removed. It was performed by placing a rotating diffuser and extra lenses before the objective or using a square core fiber. The former allows homogenous illumination on relatively large areas at the price of power losses (the laser light is spread in all solid angles) and mechanical movement that might induce a periodicity or a drift on the illumination. On the contrary, the square core fiber limits power losses (when the light source is designed with fibered output) and provides a smaller illumination surface area. The square shape offers better speckle suppression compared to its round counterparts^{59,60}.

Notably, homogeneous illumination is far from flawless for PL characterization. Sample inhomogeneities under study likely cause lateral charge carrier flow that changes PL dynamic and blurs images. Moreover, it can induce different injection levels that should be considered in the analysis. To tackle these issues, the group of Hameiri⁶¹ performs PL imaging under non-uniform illumination to make the PL signal homogeneous.

Concentrated illumination: this strategy is used with the assumption that the material is homogeneous. It allows the investigation of transport mechanisms for high (optical or electronic) diffusion length or an intensity dependant study on the contrary case. Concentrated illumination can be achieved by focusing on a laser. This configuration is "natural" and allows

spot size to be limited by the diffraction limit and the Point Spread Function of the setup. The cleanliness of the illumination is crucial to guarantee an isotropic problem for spatially simplified analysis and might require further spatial filtering depending on the laser quality⁶². Practically, it induces low light flux as the excitation is concentrated on a small spatial fraction of the data. Another strategy consists in implementing linear illumination to increase the signal. It can be performed by diffraction on a slit or by a laser line generator such as Thorlabs FLG10FC-633. Again, a trade-off emerges: the width of the laser line is higher than point-like illumination, and its uniformity is of lesser quality.

2.II.2 Hyperspectral imaging

2.II.2.a Principle of Hyperspectral imaging

Hyperspectral imaging (or imaging spectroscopy) provides the intensity spectrum for each pixel resolved. In other words, the data obtained by **hyperspectral imagers (HI)** has the form of a hypercube $I(x, y, \lambda)$, illustrated in Figure 2-14.

It is said to have started in the 80s in a NASA laboratory⁶³. Its development followed the launch of a multispectral imager on a satellite in the 70s, which captured images of Earth at different wavelengths. It highlighted the need for further spectral information to characterize earth geology. However, SPI provided a similar instrument a few years before⁸! Nowadays, this technic finds applications in various fields, such as art, agriculture, and biology. Examples of its use in semiconductor photoluminescence characterization can be found since the 90s when several groups investigated exciton localized at inhomogeneities in quantum wells^{64,65} by this mean.

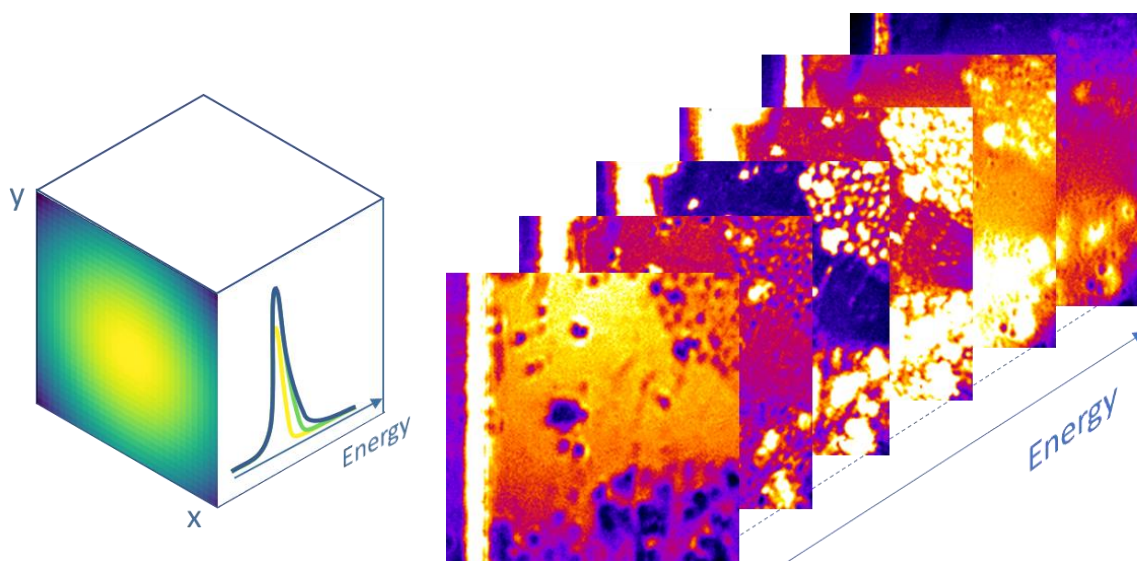


Figure 2-14: HI schematic datacube $I(x, y, \lambda)$ – an intensity spectrum can be obtained at each pixel, and images extracted at each wavelength, as with the example of a sample reflection.

2.II.2.b State-of-the-art in hyperspectral imaging

Strategies to acquire hyperspectral information are diverse and can, to some extent, be generalized to multidimensional imaging, noting that possibilities get more numerous with the additional dimensions.

2.II.2.b.1 Snapshot hyperspectral imaging

Snapshot multidimensional imaging simultaneously acquires all dimensions on a single focal plane array (FPA) within a single exposure. In the case of hyperspectral imaging, various strategies can be implemented to obtain the spectral dimension along with the spatial ones. Figure 2-15 shows two examples of such acquisition schemes. *Imaging spectrometry using a filter stack* is an example of direct acquisition. As illustrated in Figure 2-15(a), wavelengths are reflected in different directions, so their corresponding images are focused onto various areas of the FPA, and obtaining $I(x, y, \lambda)$ is straightforward. Conversely, computed tomography imaging spectrometry is based on acquiring several diffraction-order images, as shown in Figure 2-15(b). It involves an iterative reconstruction to retrieve the hypercube.

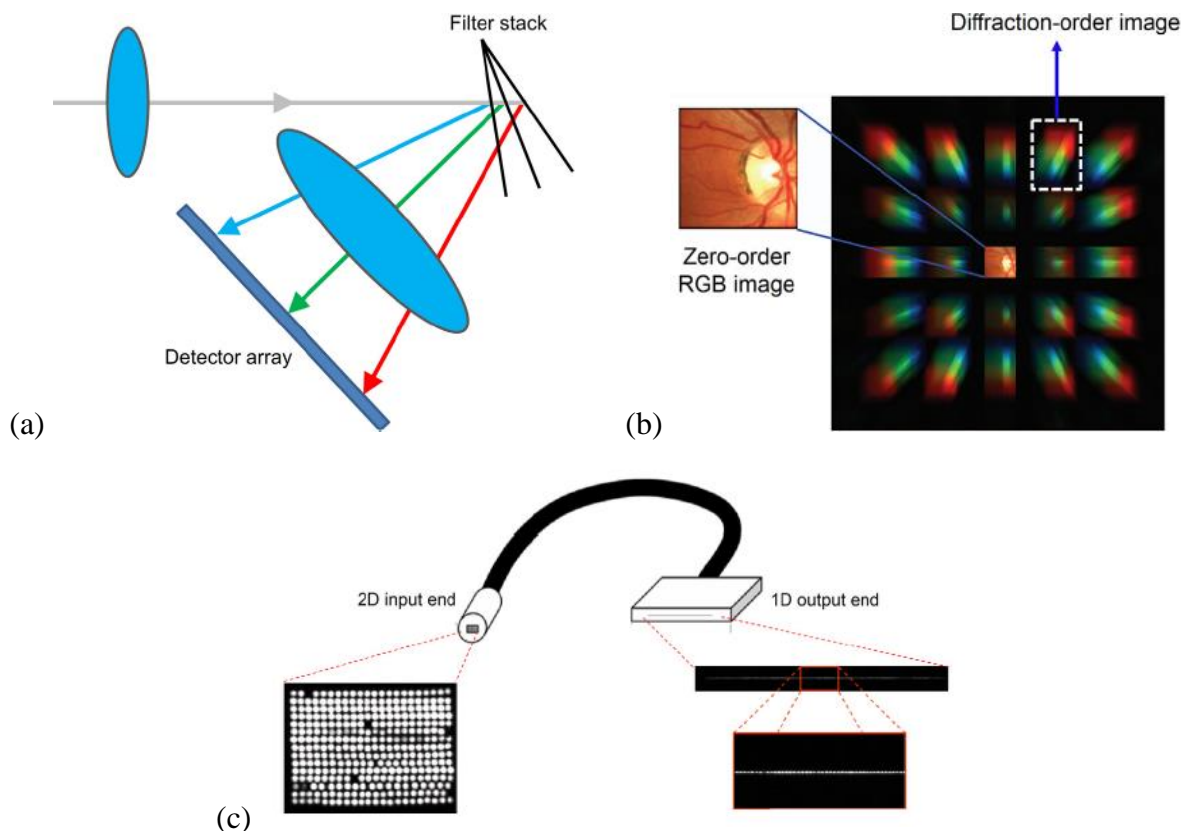


Figure 2-15: Examples of snapshot hyperspectral imaging (a) principle of Imaging spectrometry using a filter stack (IS-FS). Reprinted from Gao et Wang.¹¹, Copyright (2016), with permission from Elsevier (b) Computed tomography imaging spectrometry (CTIS) - Source: Johnson et al.⁶⁶ (c) Principle of the main component of Imaging spectrometry using a fiber bundle (IS-FB) – Source: Gat et al.⁶⁷

These approaches have the advantage of a higher light throughput than in scanning counterparts, referred to as the *snapshot advantage*. In the two examples above, each photon collected is directed toward a spectral channel and allows their parallel measurement. On the other hand, the spectral scanning approach requires rejecting all the wavelengths but the one characterized and dividing the light intensity by an amount comparable to the number of spectral channels.

One can note that snapshot imaging has a limited 'photosites budget' to allocate between the different dimensions. Different architectures will intrinsically promote some over others. *Imaging spectrometry using a filter stack* is limited in terms of spectral channels and can thus give many pixels for the spatial dimensions. Complementarily, *Imaging spectrometry using a fiber bundle* utilizes optical fibers such as the ones presented in Figure 2-15(c) to sample the information spatially. Such a setup can allow the reconstruction of hypercubes of $44 \times 40 \times 300$ (x, y, λ).

2.II.2.b.2 Scanning

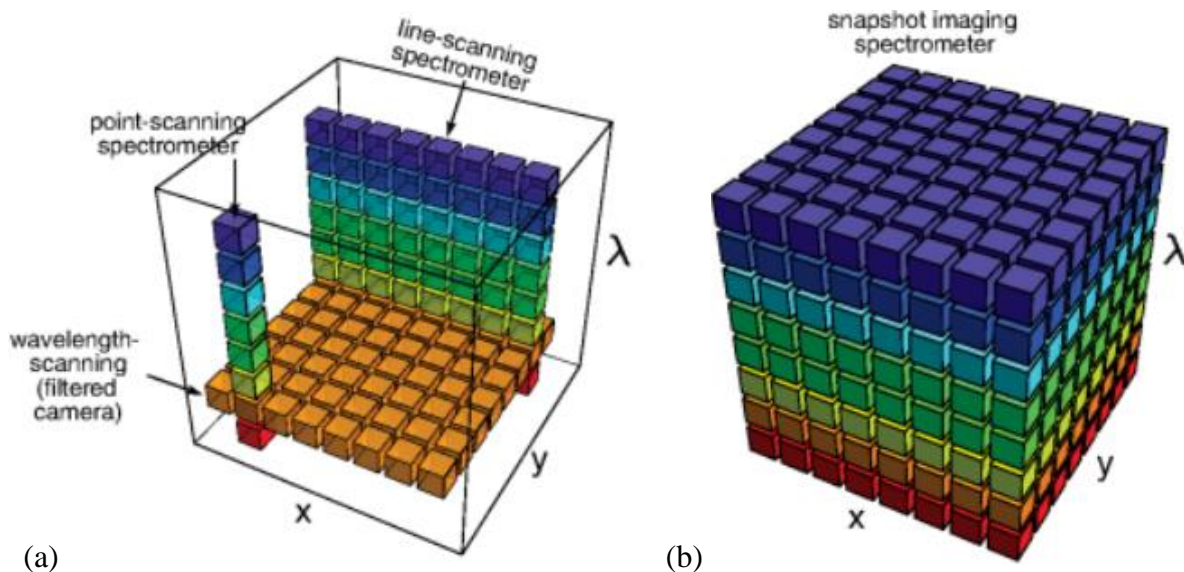


Figure 2-16: (a) Different scanning approaches to retrieve hyperspectral images are possible. The sampling can be spatial, spectral, or spatio-spectral. (b) Conversely, snapshot hyperspectral imaging captures the three dimensions simultaneously³.

As FPA are inherently bi-dimensional, a natural strategy to acquire a hypercube involves scanning across one dimension, as illustrated in Figure 2-16(a). When it comes to hyperspectral imaging, it is possible to browse across the spectral dimension, for instance, by using a camera combined with a variable filter and acquiring a sequence of images at different wavelengths. Otherwise, it is possible to scan along one spatial dimension with a line-scanning spectrometer when the detector retrieves the spectral information on a one-pixel line as classical gratings shear the light along one spatial dimension (known as *push broom* scan). Many spectrometers average spatially the signal to increase its quality and require bi-dimensional spatial scanning

when employed for hyperspectral imaging (also called *whisk broom* scan). In these cases, the hypercube reconstruction is straightforward.

A scan can also be performed in a combination of the dimensions of interest. Thus spatio-spectral scanning offers a way to create hyperspectral images. Each measurement provides a 'rainbow colored' image corresponding to the acquisition of diagonal planes in the above representation⁶⁸. It has the advantage of providing a good resolution in both spatial and spectral dimensions.

2.II.2.b.3 Hyperspectral experimental setup

The photodetector employed in this work results from a volume Bragg grating⁶⁹ and a CMOS camera. For each position of the 2D grating, the CMOS captures the spatial intensity sheared along the x axis by a function of the wavelength. Rotating the grating allows a spectro-spatial scan from which hypercube reconstruction is possible. A subsequent rectification step is necessary to retrieve the images.

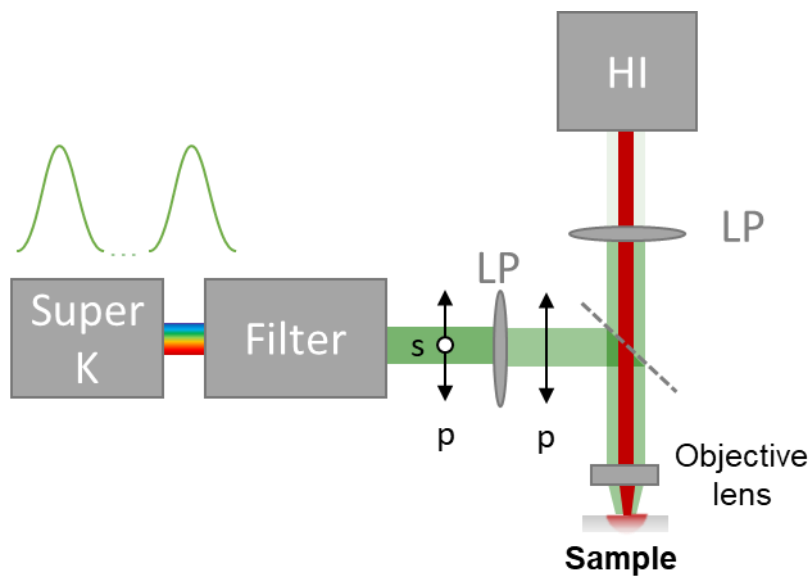


Figure 2-17: Schematic of setup in the configuration used for PLE. A linear polarizer filters the illumination before impinging on the sample, providing a homogeneous illumination. The emitted PL is collected through the objective, further filtered by the second linear polarizer to attenuate the laser reflection, and analyzed by a hyperspectral imager.

In its classical configuration pictured in Figure 2-17, a continuous light source (LED, continuous laser...) illuminates the sample through a microscope objective in a reflection configuration. The reflected and emitted light are filtered through a dichroic long-pass filter so that only the PL is analyzed. In this thesis, we performed Photoluminescence Excitation spectroscopy that required exciting the sample with varying energy close to the emitted spectrum. We used a supercontinuum pulsed laser combined with a variable filter to reach this

goal. The illumination is attenuated by polarization contrarily to the usual spectral filters. The setup at IPVF employs a grating with a 2nm spectral resolution. The spatial scale and resolution depend on the microscope objective and diffraction limit.

The amount of data collected by such a setup can be easily 10^7 pixels. Indeed, hundreds of frames can be acquired in a few minutes. When performing parameter-dependent studies, dozens of Giga have to be processed.

2.II.3 Time-resolved imaging techniques

2.II.3.a Principle

Time-resolved fluorescence imaging (TRFLIM) provides light intensity as a function of time and position. The obtained data cube $I(x, y, t)$, shown in Figure 2-20, is analogous to a movie shot with a very high frame rate.

This technic belongs to the wide family of high-speed imaging that has roots in the late 19th century. Early works demonstrated images of a horse in motion⁷⁰ (1878) or a supersonic bullet⁷¹(1887). Electronic sensors allowed electronic gating faster than their mechanical counterparts and reached 10^5 fps at the end of the 20th century. Now, events can be recorded up to 10^{11} fps⁷² with resolutions of tens of picoseconds. It has been applied to semiconductor characterization since the 80s at least, as illustrated by the images of photoluminescence taken by Greenstein et al.⁷³, shown in Figure 2-18. A raster scanner obtained 100ns-resolved images of anisotropic diffusion in germanium at 2K.

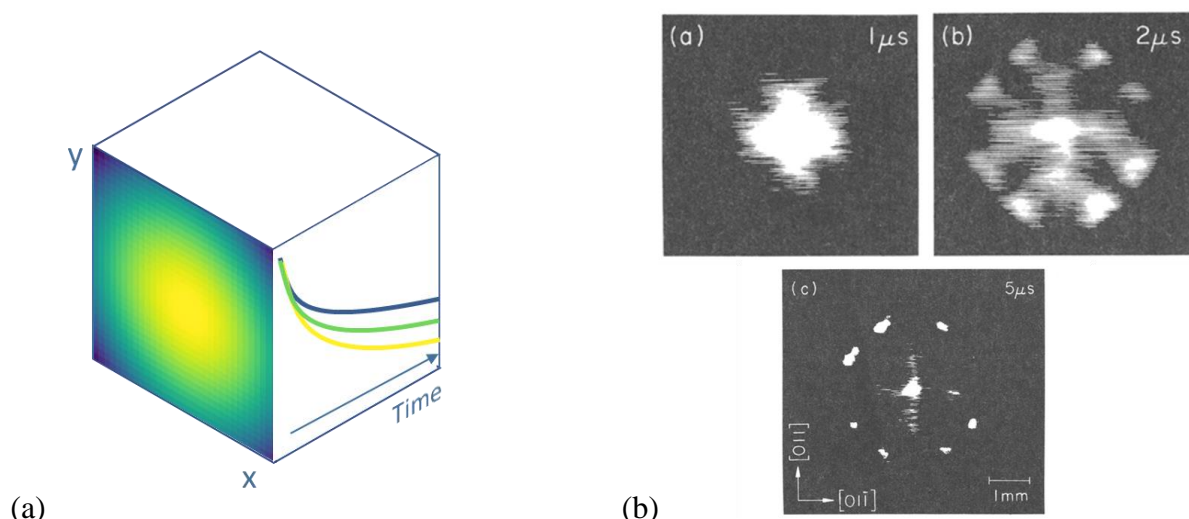


Figure 2-18: (a) Time-resolved imaging data and schematic representation, (b) Example of images obtained 1μs, 2μs, and 5μs after localized pulsed excitation on germanium – Reprinted from Greenstein et al.⁷³, Copyright (1983), with permission from Elsevier.

Photoluminescence decay time typically scales from the nanosecond to the millisecond. Shorter timescales are also of interest for semiconductor characterization: physical phenomena such as thermalization are characterized in the literature with temporal resolution down to the picosecond.

2.II.3.b State-of-the-art in time-resolved imaging

In this paragraph, we focus on technologies that provide temporal resolution below the microsecond and are interesting for semiconductor characterization applications. One can note that the temporal scale is related to the short spatial scale, and observing phenomena at the micrometer length requires ultrafast hardware⁷⁴.

Temporal dependence of the signal can be acquired by different approaches⁷⁵ depicted in Figure 2-19. Time-correlated single photon counting (TCSPC) measures the difference between the time of the laser pulse and the PL photon detection at the picosecond scale. The reconstructed decay corresponds to a histogram of the delay times. However, at high light flux, the detector measures only the first photons arriving due to an intrinsic dead time after their detection. Therefore, it is limited in light intensity and associated with longer experiments. It is also possible to perform time gating: an electronic shutter or an optical gate allows the light to reach the detector for a given time lapse after the trigger. The signal collected is the convolution of the gate and the decay. In this frame, intensified cameras let the light reach an FPA when a bias is applied to a photocathode, providing subnanosecond resolution. Optical gating has the highest resolution with lower efficiency. Lastly, time-domain sampling involves continuous decay sampling by a fast detector. This measurement is direct and allows relatively quick acquisition speed at a high cost and with quite poorly known instrument noise. It is the case for fast detection electronics (nanosecond resolution) and streak cameras (down to picosecond). The latter employs a bias to spread photoelectrons along one spatial dimension and retrieve the intensity $I(x, t)$. They will be further discussed in chapter 3.

Measurement can also be performed in the frequency domain, as illustrated in the photoluminescence characterization of semiconductors by the modulated photoluminescence⁷⁶. It provides a signal corresponding to the Fourier transform of an impulse and can provide insight into similar phenomena without costly pulsed lasers.

Time-gating and TCSPC can be implemented with a focal plane array and provide imaging directly, allowing 'wide field FLIM'. For instance, Micro-channel Plate (MCP) and, more recently, Single Photon Avalanche Diode (SPAD) arrays provide TCSPC⁷⁷. Moreover, intensified cameras provide gating across two spatial dimensions. Non-imaging detector scanning configuration or laser scanning can also achieve spatial reconstruction⁷⁸.

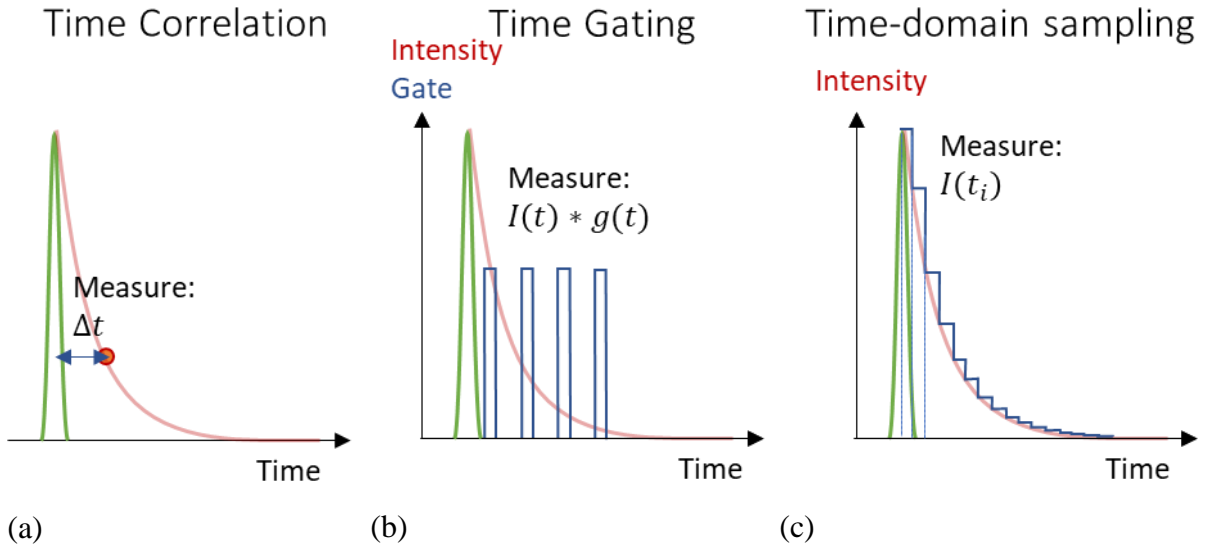


Figure 2-19: Different approaches to retrieve the temporal information of intensity decay. Green and red correspond to laser and PL, respectively. (a) In time correlation, the decline is provided by a histogram of delay time between the trigger and photon count. (b) Time gating lets the light through with a temporal transmission described by the gate function $g(t)$, and the measurement results from the convolution of the gate function and the intensity decay. (c) Time domain sampling consists in measuring a signal proportional to the intensity at different times.

Snapshot imaging has been demonstrated by different strategies¹¹. Active illumination can encode the time of photon reflection spectrally and then be imaged with a snapshot hyperspectral imager (it does not apply to PL). Parallel streak imaging using a tilted array allows the representation of two spatial dimensions on one axis of the photocathode.

In both approaches, experiments can be repeated thousand times to increase the signal quality⁷⁵. One can note that time-resolved information obtained at higher resolution can still be of interest for semiconductor characterization and can be achieved by employing ultrashort light pulses⁷⁴. It is performed in the example of pump-probe technique (e.g., transient absorption), where the delay between two laser pulses sets temporal resolution.

2.II.3.c Experimental setup for time-resolved photoluminescence imaging

The experimental bench employed during this thesis shown in Figure 2-20 allows filming the PL decay after excitation with a 35ps laser pulse (Coherent Talisker). Comparably to HI, the illumination is performed in reflection configuration, and the laser is filtered out from the collected signal. A tube lens focuses the PL onto the focal plane array of a PiMax 4 high-speed intensified camera fabricated by Princeton Instrument. It realizes a temporal scan after the pulse emission by letting the light through during a short duration – down to 480ps. It requires synchronization between the illumination source and the detector. A mechanical shutter would not fit this time scale, and that's why it is performed electronically in high-speed cameras: the light impinges on a photocathode that converts photons into electrons and is

coupled to a microchannel plate (MCP) which multiplies the number of electrons. During the "on" interval, an electrical bias applied to the photocathode and MCP allows electrons extraction. They are converted to photons through a phosphor screen and detected by an electron-multiplying CCD. Therefore, each temporal frame results from the convolution of the PL decay with a gaussian-like temporal gate.

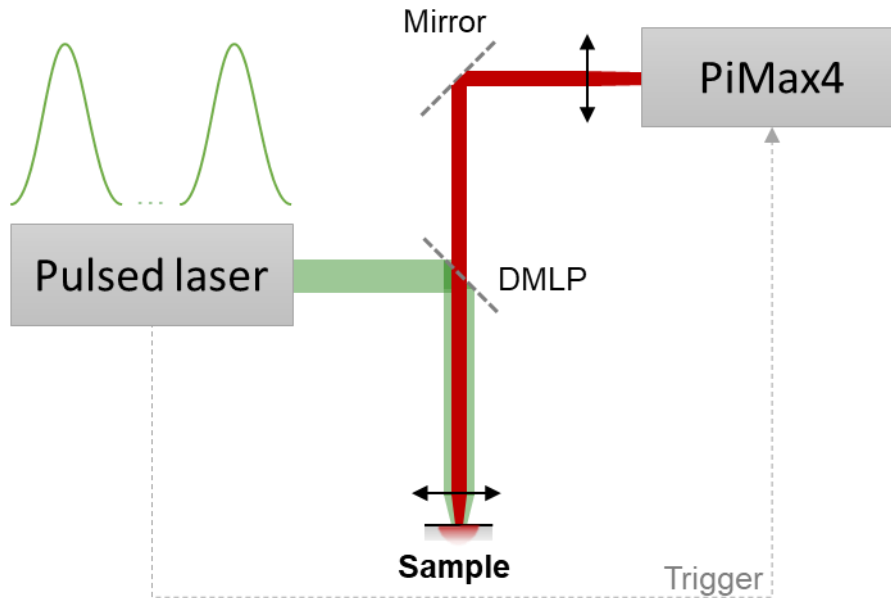


Figure 2-20: TRFLIM setup. A 532nm pulsed laser excites the sample. Its reflection is filtered out by a long pass filter (DMLP), so the PL only is collected by the PiMax4 intensified camera. The latter is synchronized to the laser through an electric trigger.

To obtain enough signal, the experiment is repeated N_{acc} (typically thousands) times per temporal frame. It requires $N_t * N_{acc}$ accumulations where N_t is the number of temporal frames spread over the timescale scanned. TRFLIM thus relies on the assumption that the experiment is repeatable. Attention must be paid to the repetition rate of the laser: to prevent any carrier accumulation in the material, the laser cycle must be at least six times the characteristic decay time as a rule of thumb.

One can note that the PiMax camera has two amplification steps: the first is provided by the MCP intensification, and the second is by the electronic gain in the CCD. They allow reaching the ultralow light detection level required for photoluminescence imaging so the camera can perform single photon detection.

Performances of the TRFLIM are mainly limited by the quantum efficiency (QE) of the photocathode and the amount of signal. Indeed, the GenIII InGaAs intensifier has a nominal QE of about 5-8% in the spectral range of interest, limiting the number of photons detected. Moreover, the shorter the temporal gate width, the lower the number of photons for a given light flux, and they cannot be numerous enough to reconstruct an image. Setting a longer gate

width and realizing an extra deconvolution step may be preferable. Indeed, the delay is precise with a 10ps resolution and can offer a way to increase the temporal resolution. Once more, there is a trade-off between temporal and spatial resolutions. Otherwise, TRFLIM is limited by its on-to-off ratio: the electronic gating doesn't provide total discrimination of the photon time of emission. Indicative values are of $10^6 \sim 10^7:1$ for generation II intensifiers⁷⁹. During the TRFLIM experiment, the decays are exponential-like and inevitably reach values below the detection threshold.

2.III Towards mixed techniques

After having seen how to acquire hyperspectral and time-resolved images, we now discuss ways to increase the size of the collected data in the form of a 4D matrix. The data structure is described, and we introduce different ways of obtaining it and discuss the challenges raised by such a set.

2.III.1 4D data

Analyzing the photoluminescence maps of semiconductors complementarily in time and wavelength allows for deriving their key optoelectronic and transport properties, as detailed in Chapter 1.II. Up to now, separate acquisitions had to be acquired for time and wavelength so that a comprehensive study of the dynamics was out of reach. In particular, the parallel between continuous wave and transient experiments raises interrogations. A multimodal setup providing parallelly $I(x, y, \lambda)$ and $I(x, y, t)$ is the first step to addressing these issues. However, the spectral shape can evolve with time so that $I(\lambda, t) \neq I(\lambda) * I(t)$ and working with the projections may not be sufficient for the material characterization. For instance, the charge carrier density profile can evolve dramatically during the decay. Neglecting surface recombination, PL is first emitted from the top of the sample and then in the depth of the material. The reabsorption increases with time, leading to a red-shifting spectrum. Reasons for the temporal evolution of the PL spectrum are further discussed in the following chapter, justifying the interest in its mapping. A thorough view of photon emission within the material can provide new insights into their physics.

Therefore, we aim at the obtention of the intensity resolved in spatial, spectral, and temporal dimensions, as illustrated in Figure 2-21. In other words, the wanted data consists of a **4D matrix** $I(x, y, \lambda, t)$, simply referred to as 4D data thereafter.

A projection in the spatial domain is represented as well as the information contained in one pixel. In every location, the spectral decay can be pictured as a map presenting intensity as a function of time and energy. Each line corresponds to a spectrum at a given delay after the

laser pulse (red plot), whereas each column provides the temporal decay at a given wavelength (orange line).

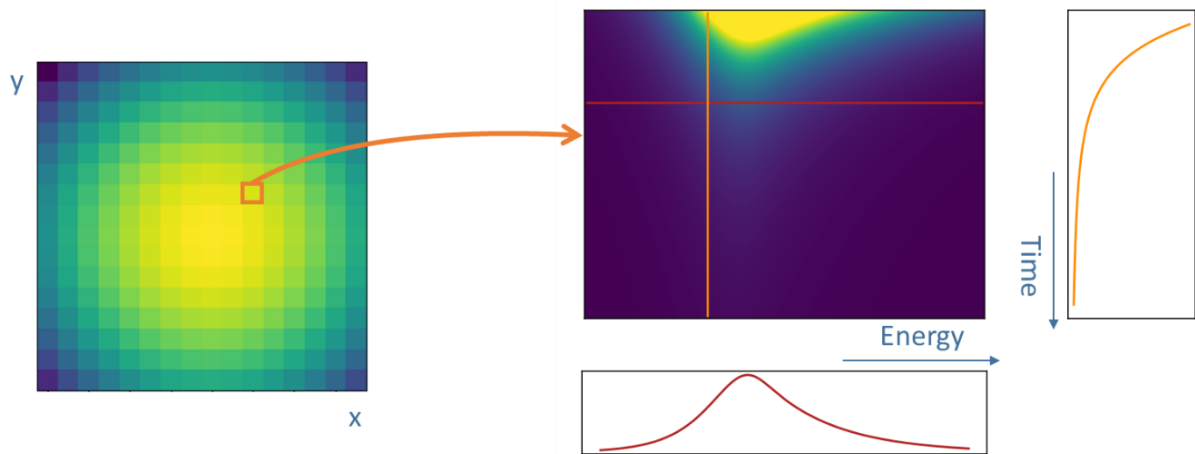


Figure 2-21: Schematic representation of 4D data. On the left, a projection in the spatial domain is presented. Each of the pixels contains the local temporal evolution of the spectrum in the form of an image with columns representing decay at different energies and lines corresponding to the emitted spectrum at various delays.

2.III.2 Various possibilities for 4D imaging

Many principles could have been considered to reach the intensity resolved temporally, spectrally, and spatially. Methods presented in this section rank from applications proved in the literature to mind experiments, which are impossible today.

2.III.2.a Hyperspectrally Compressed Ultrafast Photography (HCUP)

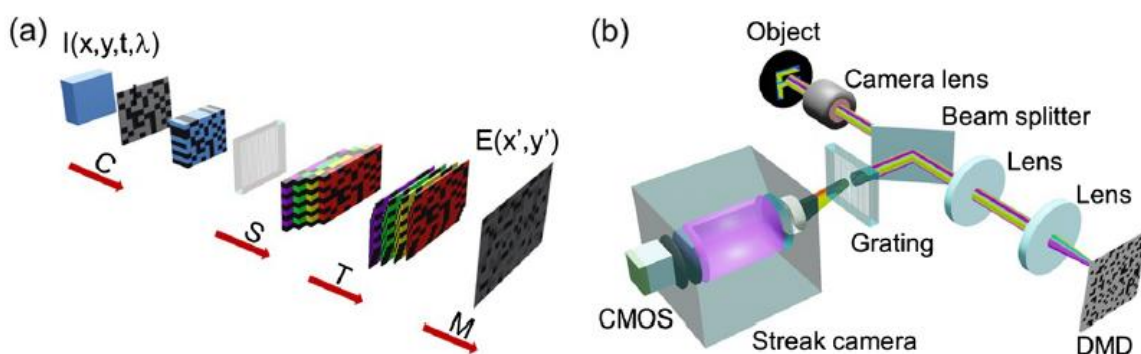


Figure 2-22 : (a) HCUP principle. I : original scene, E : measurement image, encoding operator C , spectral operator S , temporal operator T , multiplexed operator M . (b) HCUP system configuration – Source: Yang et al.⁸⁰

Yang et al.⁸⁰ have demonstrated another way to reach 4D data based on a DMD and a streak camera, providing the decay of the spectrum $I(\lambda, t)$. Based on compressive ultrafast imaging, the light is spatially filtered by a mask, then sheared in temporal and spectral

dimensions and recorded. An iterative reconstruction algorithm allows to retrieval of 4D information from one projection on a focal plane array. This method employs the streak camera with both spectral and temporal slits fully open and uses a large photocathode. This approach collects a high light throughput (thanks to the snapshot advantage) and allows one-shot photography. It is performed at the expense of both temporal and spectral resolutions affected by the reconstruction process. A similar system achieved 240fs temporal and 4.5nm spectral resolutions⁸¹. Compressive ultrafast photography recently allowed 5D imaging by adding the last spatial resolution⁸²!

2.III.2.b Scanning with the streak camera

Krishnan et al.⁸³ have developed a multiphoton TRFLIM system by laser scanning with a streak camera. As no spectrometer is involved, a scan in one spatial direction allows the obtention of $I(x,y,t)$. Generalizing this approach and scanning the two (x,y) spatial dimensions with the streak coupled to a spectrometer would provide the wanted 4D data. One could also consider performing a homogeneous illumination and moving either the sample or the collection fiber (this second option is performed by Sridharan et al. 18 in three sample locations). However, these approaches lose much more light flux than SPI.

2.III.2.c Upgrading the TRFLIM

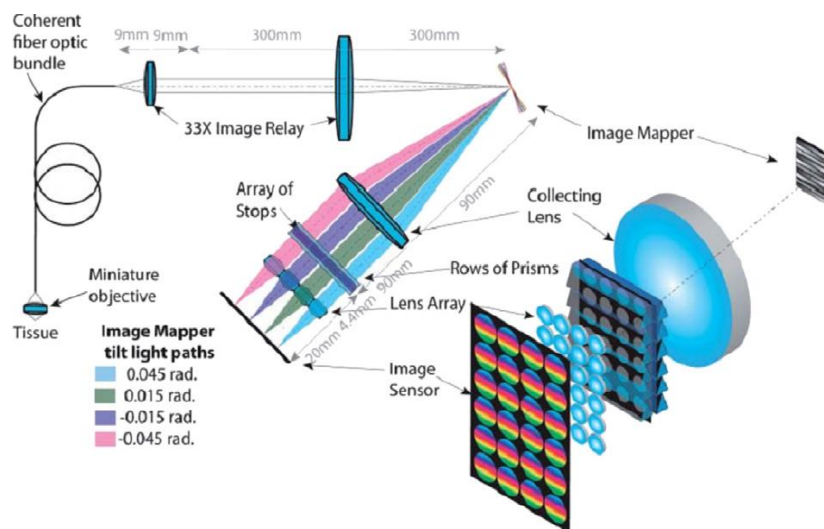


Figure 2-23: Example of snapshot HI technic setup with image division based on an image mapper and spectral dispersion achieved with a row of prisms – Source Kester et al.⁸⁴

One of the most straightforward ways to obtain 4D information would consist in taking TRFLIM acquisitions with a whole set of spectral filters. It would have consequences of drastically reducing the spectral transmission per acquisition (in the range of N_λ). Moreover, a high number of filters would have to be considered if one does not want to be limited to multispectral acquisition. One could also consider directly coupling the hyperspectral and time-

resolved imaging setup: a high-speed camera could replace the focal plane array of HI. It would increase the collected light flux by comparison to the use of a filter set. The reconstruction in the photon counting regime characteristic of time-resolved measurement might not be straightforward and may require advanced data processing.

Furthermore, combining the TRFLIM setup with any hyperspectral snapshot imaging technic would be possible. As a reminder, they aim at dispersing spectral and spatial information onto a focal plane array to allow simultaneous acquisition of these dimensions. Nine of them are presented in the review of snapshot imaging by Gao and Wang¹¹. For instance, Imaging spectrometry using a fiber-bundle⁶⁷ (Figure 2-15(c)) provides hyperspectral information down to the camera acquisition time and demonstrates 4D data acquisition with a microsecond resolution. Figure 2-23 presents an example of Image mapping spectrometry (IMS): the spatial information is divided vertically by an image mapper and further dispersed spectrally with rows of prisms, allowing a direct acquisition of spatial data for different wavelengths. Figure 2-15 b) shows an example of Computed tomography imaging spectrometry (CTIS), in which the light is dispersed spatially by a function of the wavelength. It further requires an iterative reconstruction to retrieve the hypercube. These two technics could be implemented with a high-speed camera instead of a regular focal plane array to provide $I(x, y, \lambda, t)$ with minor light losses.

2.III.2.d Snapshot temporal imaging

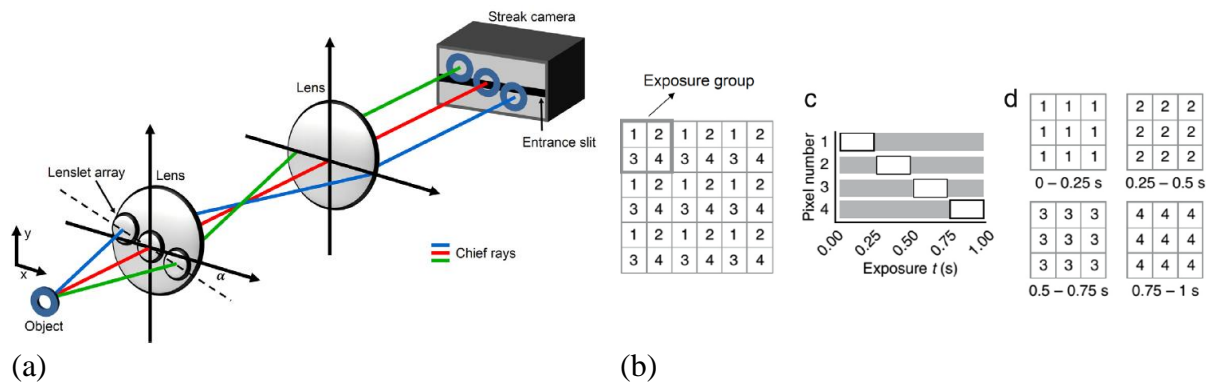


Figure 2-24 : (a) Principle of streak imaging with a tilted lenslet array – Source Heshmat et al.⁸⁵ (b) Principle of the exposure groups for temporal pixels multiplexing (Reprinted by permission from Springer – Source Bub et al.⁸⁶).

The other way around, it is possible to find inspiration from snapshot temporal imaging. Among the methods presented by Gao et Wang¹¹, some encode the temporal information spectrally and would not be suitable. Others, such as streak imaging with a tilted lenslet array, pictured in Figure 2-24, exploit a streak camera and its spatial dimension. Implementing our setup would offer an easy way to obtain $I(y, \lambda, t)$. A further adaptation with a fiber bundle converting 2D spatial dimensions into 1D would allow to reach the 4D data. Another example

suitable for 4D data obtention is the temporal pixel multiplexing that employs a DMD as a temporal modulator: mirrors are divided into exposure groups, as pictured in Figure 2-24 (b). Each mirror per group is attributed a different time delay to split the temporal information spatially. This approach could be implemented with a HI. Provided the typical framerate of DMD (dozens of kHz), the temporal resolution is limited but would suit materials such as silicon.

2.III.2.e With an ideal 4D detector

One can imagine capturing a hypercube with a Foveon-like detector in a snapshot. As displayed in Figure 2-25, this kind of sensor encodes the wavelength at the collection depth. A generalization to more than three wavelengths could be imagined capturing the spectral information without any intensity loss nor reducing the spatial resolution. An ideal detector could also perform temporal multiplexing, dividing the light flux only per factor two and providing the four dimensions by itself.

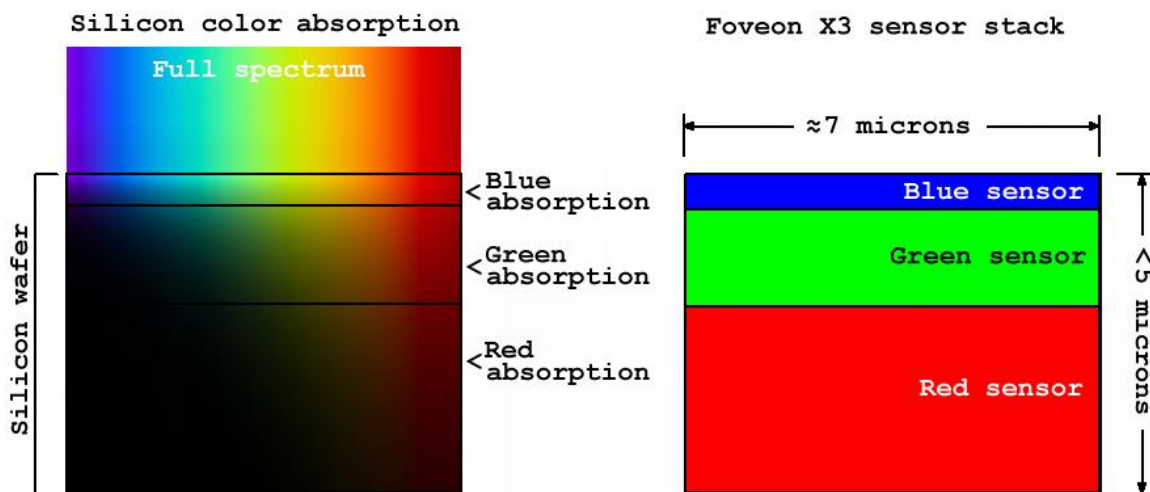


Figure 2-25: Principle of Foveon sensor that retrieves the RGB channels from the depth of photon absorption – Source: English-language Wikipedia, CC BY-SA 3.0.

2.III.3 Outlook on multidimensional imaging

Multidimensional imaging is essentially related to the question of data processing. It can lead to the acquisition of heavy matrices, raising the issues of visualization, exploitation, and possibly compression. Challenges also arise regarding data acquisition, which questions the possibility of sampling the information in 4D differently.

2.III.3.a Considerations on data handling

Data exceeding two dimensions are challenging to represent. Data cubes can be visualized as movies or with a slider on one dimension, as it can be done with ImageJ to prepare for data treatment. The fit of the investigated properties can be performed point per point in the spatial area before looking for correlation. Otherwise, it is possible to study projections of the dataset by selecting a statistical indicator (average, percentile) along one dimension. Another way to proceed is using data clustering algorithms, which groups pixels together based on a chosen metric, as by neighboring intensities. Several methods are available in Python, such as K-means, DB Scan, or OPTICS, as demonstrated in Figure 2-26. This approach is generally less computationally intensive than a point-per-point fitting but relies on the assumption that the pixels binned by the clustering area have similar behavior.

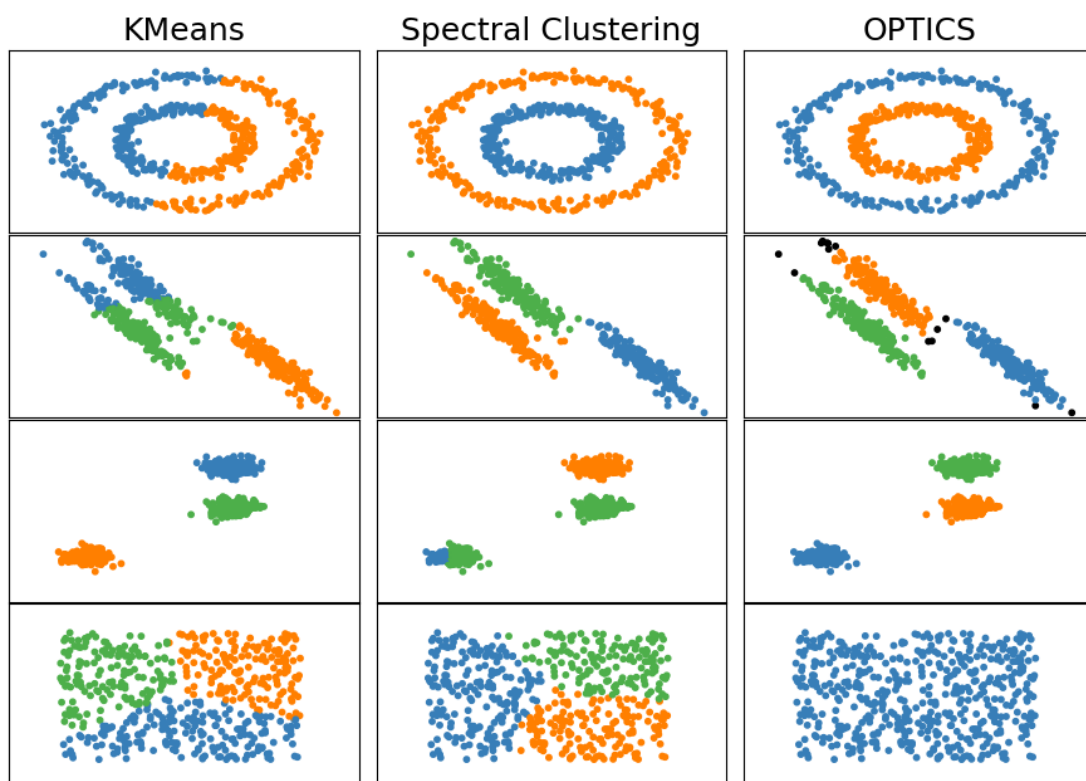


Figure 2-26: Examples of clustering algorithms results for different data sets. Depending on the point distribution, K-means, Spectral Clustering, and OPTICS gather data differently - Adapted from Python documentation⁸⁷.

A huge amount of data can be acquired, but that is not without any flaws. For instance, it is inconvenient to save more gigabits than a classical computer processor can handle (typically 2-4Gbt). It is especially the case if a parameter study as PLE is performed and several data cube needs to be considered simultaneously. This issue can be solved to some extent by data compression as algorithms are more and more efficient in this field. For instance, video compression has grown with the explosion of available cameras. As illustrated by the example

of the European Space Agency SHyLoC compression⁸⁸, scientific progress can also be performed at the price of information and additional processing steps.

2.III.3.b Considerations on data acquisitions

The acquisition schemes presented in the above state-of-the-art underline a few principles. As highlighted by Gao et al.¹¹, the design of a multidimensional device involves a *photon budget* spread across the acquired dimensions. It is determined by the detector's illuminance and the characterized samples' luminance. Moreover, such systems also have a *photosites budget*, corresponding to the number of elements in the focal plane array multiplied by the number of measurements involved in the acquisitions.

How these photons and pixels are allocated to the different dimensions plays a role in the instrument's maximal resolution, signal-to-noise ratio, sampling, and dynamic range. Johnson et al.¹ addressed the question of the number of photons required to reconstruct an image. They suggest that a binary object can be reasonably probed with as many photons as pixels, noted N . With a sparsity constrain, this number could be reduced. Indeed, assuming the image is K -sparse (can be represented by K coefficients on a given basis), allow its reconstruction with $O\left(K \ln\left(\frac{N}{K}\right)\right)$ measures. Smoothing also change the problem by reducing the resolutions to increase the signal-to-noise ratio, resulting in a loss of information.

We could generalize this reasoning to multidimensional images and consider that N is the number of pixels in all dimensions. Probing a grayscale image with a dynamic range of d would lead to the requirement of a higher number of photons, probably multiplying by d the ones required for illumination. In practice, the choice of instrumentation leads to the attribution of photon and photosites budgets that favor some dimension and must suit the problem under study.

2.III.3.c About the 4D data sparsity and other ways to acquire it

The photoluminescence signal is highly redundant in the four dimensions. If the sparsityⁱⁱ of natural images is exploited in compressed imaging, the same idea could apply to each component of the 4D setup. One can imagine a sampling combining all of them: for instance, spectra could be measured at different times in different sample locations. To some extent, this approach is already applied by Soldevila et al.⁵⁶. Their system acquires parallelly high spatial resolution images and hyperspectral and TRFLIM cubes with low spatial resolution. Data fusion algorithms allow to retrieval of a 4D matrix. However, as the spectral

ⁱⁱ Property of a N element vector to be represented by K coefficient in a given basis, with $K \ll N$ non-zero values

information is never acquired at a precise delay time, the temporal evolution of the spectrum seems difficult to guarantee without prior knowledge.

The acquisition design should ideally consider the applications and exploit all the sparsities at stake to avoid wasting light. For 4D, sampling across the four dimensions could be imagined.

Conclusion

Focal plane array, raster scanning, and single-pixel imaging are different strategies to obtain maps of light fields. They can all be applied to multidimensional imaging, which provides extra photon tags such as the wavelength, the time or depth of emission, polarization, or propagation angles.

Single-Pixel Imaging relies on two main components: a non-imaging photodetector and a spatial light modulator. The spatial reconstruction can be retrieved by acquiring the target image modulated by a set of masks. Various approaches are available, providing imaging with different measurements and computational complexity requirements. It has been demonstrated for imaging with unconventional sensors, as well as in the design of multidimensional and multimodal imagers.

Hyperspectral and time-resolved imaging are introduced, and the main strategies to acquire these hypercubes are presented, among which the one adopted at IPVF. Photoluminescence would gain in being more thoroughly characterized, and we explore different methods to obtain it. The following chapter will discuss the chosen setup and its implementation.

Chapter 3 - 4D-PL technique

“Pourquoi faire simple quand on peut faire compliqué?”

— **Les Shadoks**

This work analyses the PL signal in spectral, temporal, and spatial dimensions. To reach this purpose, several photodetectors and optical systems are used and can be combined to investigate the light components of interest.

The setup built at IPVF is described in section 3.I. It employs Single-Pixel Imaging with a streak camera coupled to a monochromator. The working principle of this detector that measures transient spectra $I_{PL}(\lambda, t)$ is depicted and examples of its applications for semiconductor characterization are presented. The properties and particularities of this setup are outlined to contextualize its implementation in the world of imaging.

Section 3.II explains how this setup was implemented. The various time scales at stakes are first clarified. The low light regime and low sensitivity in which 4D operates raise many noises and optical optimization challenges. We detail their incidence and how they are addressed in the choices of optics. Emphasis is given to the effects of diffraction and how it is corrected in acquisitions.

Eventually, section 3.III explains how two variations of this setup were developed. A hyperspectral imager was built in parallel to the existing TRFLIM setup to offer a multimodal 2x3D sampling. As well, a workflow based on a pixel clustering algorithm is detailed. It provides the temporal evolution of the spectrum in specific locations.

3.I Experimental setup

4D-PL is a novel experiment developed during this thesis after the idea protected by patent filling FR19315037.2.^{1,2} It is one of the rare approaches allowing light sampling in the joint spatial, spectral and temporal dimensions. It relies on the combination for the first time of Single Pixel Imaging with a streak camera coupled to a spectrometer. This detector simultaneously brings spectral and temporal data; we describe its principle and applications to semiconductor characterization before presenting the setup and its specifications.

3.I.1 4D-PL in the landscape of multidimensional imaging

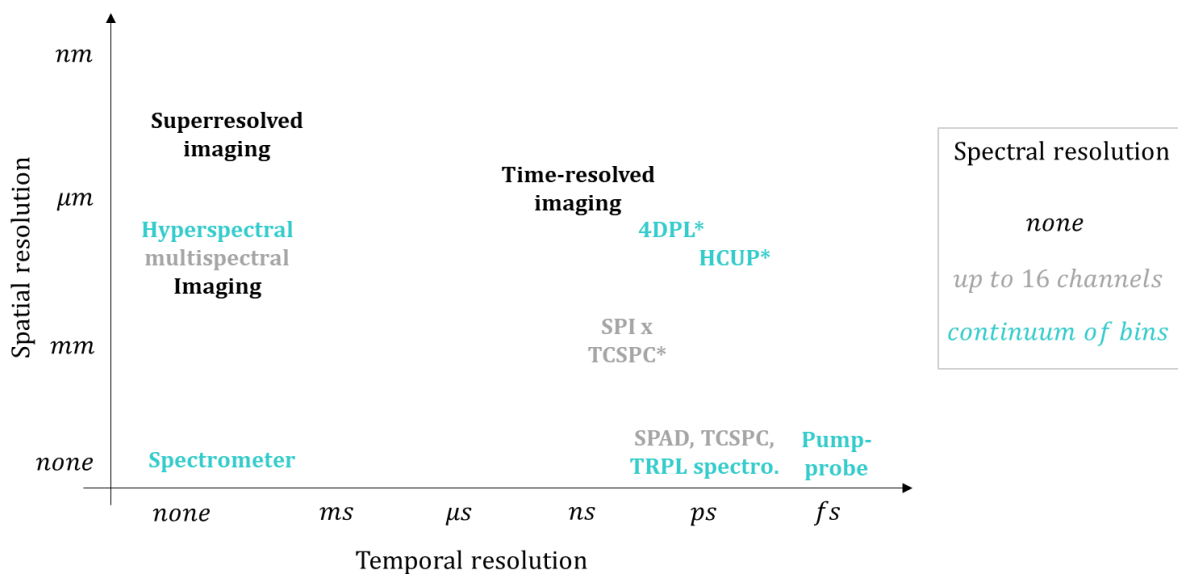


Figure 3-1: Overview of the main photodetectors and multidimensional imaging techniques allowing light analysis in spatial, temporal, or spectral domains. The setups developed in research laboratories feature a star. Commercially-available systems do not provide a way to access the four dimensions simultaneously at our resolutions, while lab systems based on a streak camera or SPI provide approaching data.

4D-PL aims at accessing $I(x, y, \lambda, t)$ at the microscale with nanometric spectral and sub-nanosecond temporal resolutions. Figure 3-1 places it among the commercially available solutions: implemented techniques simultaneously offer up to three dimensions. Imaging $I(x, y)$ or time-resolved photoluminescence (TRPL) spectroscopy $I(\lambda, t)$ characterize two dimensions, whereas hyperspectral and time-resolved imaging capture 3D data cubes. There exists no built-in solution addressing the four dimensions together. Chapter 2 presents examples of the four dimensions at laboratory scale, shown with a star on the figure. Hyperspectrally Compressed Ultrafast Photography (HCUP)³ does achieve 4D in high flux with a high temporal resolution by employing a detector with a wide effective area and complex reconstruction mechanism akin to deconvolution. Also, SPI-based techniques allowed multispectral time-

resolved imaging^{4,5} when used with TCSPS boards with 16 spectral channels. We follow a similar approach with the spectrally and temporally resolved detector.

In our case, the emphasis is put on the temporal and spectral dimensions. A thousand bins are allocated to each, whereas HI and TRFLIM rather dedicate hundreds to them, and thousands for each spatial axis. Thus, for acquisition times and detection capacity comparable to HI and TRFLIM, hundreds of bins can be allocated to the spatial resolution for 4D-PL. Our approach can then be seen as a spatialization of the detector, described in the following paragraph.

3.I.2 Streak camera technology

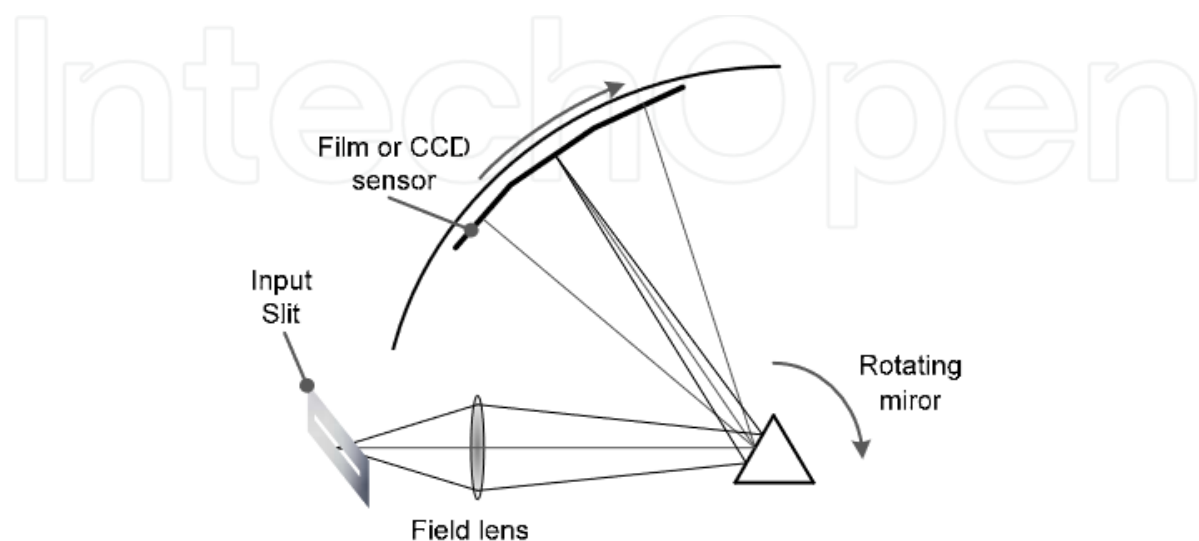


Figure 3-2: Scheme of a mechanical streak camera based on a rotating mirror. Depending on the time of emission, the light will reach different locations on the sensor. The mirror rotation allows encoding the temporal dimension spatially – Source: Uhring and Zlatanski⁷.

Streak cameras capture ultrafast phenomena by a spatial deviation of light. They were first implemented with a rotating mirror in 1834⁶, following the principle illustrated in Figure 3-2. Limited by the mechanical properties, their temporal resolution is of the order of magnitude of the microsecond. From 1950, progress in electronics allowed faster systems to reach 200fs resolution. Optoelectronic streak tubes deviate a photoelectron ripped off from a photocathode with a sweep voltage, as pictured in Figure 3-3. The deviated electron is converted back to a photon by a phosphor screen before being imaged on a focal plane array.

These sensors provide photodetection with the highest temporal resolution⁸. A major demonstration of their capabilities is offered by compressed ultrafast photography: it is thanks to this equipment that Gao et al.⁹ achieved snapshot photography at 10^{11} fps. The captured signal is analyzed as a function of time and one dimension in space. When coupled to a spectrometer, as in our case, the spatial dimension directly conveys the spectral information.

This detector thus provides the temporal evolution of the spectrum by encoding both temporal and spectral dimensions spatially. Other photodetectors can give similar information $I(\lambda, t)$, like monochromators coupled to photomultiplier tubes, with are generally gathered under the term time-resolved spectroscopy.

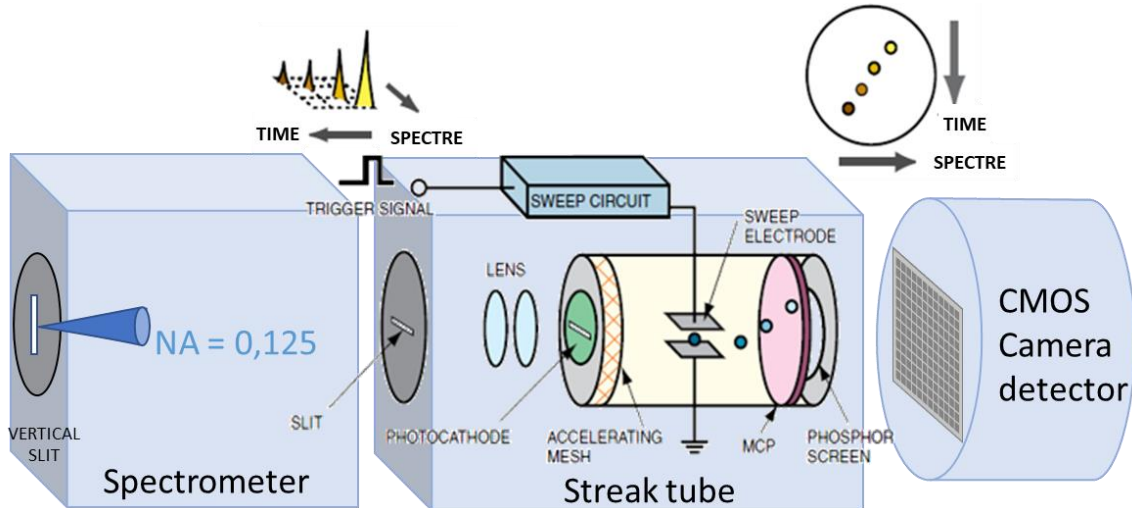


Figure 3-3: Structure of the streak camera detector for TRPL spectroscopy. Photons are deviated horizontally by the spectrometer as a function of their wavelength and arrive on a photocathode. They produce electrons spread vertically by a sweep voltage depending on their arrival time. They hit a phosphor screen, creating green photons imaged by a CMOS camera. Adapted from Hamamatsu⁸.

The photodetector illustrates the intrinsic trade-off between light intensity and resolution. The amount of light collected is determined by the sample emitted light flux and by the collection etendue of the detector, which is a function of the fixed numerical aperture (NA) of the spectrometer (0.125) and the tunable surface area of the photocathode. The latter depends on slits at the spectrometer's entrance and in front of the streak tube. The spectral resolution can be tuned by decreasing the width of the slits at the spectrometer entrance. Similarly, a precise determination of the delay between the laser pulse and the photon emission requires a small vertical fingerprint of the photocathode. That can be performed by closing the horizontal streak slit entrance. Therefore, the better resolution, the lower the etendue¹⁰ of the collected light. As a reminder, this quantity reflects the amount of light impinges on the detector by considering its collection angle and effective surface area. Notably, the etendue is generally in the same order of magnitude as the one collected by one to hundred pixels of a classical focal plane array. Therefore, the light flux is low and leads to shot noise.

3.1.3 TRPL spectroscopy for semiconductor characterization

Such techniques characterize the energy flux by obtaining the temporal evolution of the intensity spectrum. When the density of state (DOS) highlights the presence of different

compounds, it offers a direct insight into the electronic exchanges between them. Light-matter interactions and changes in the electronic occupation function can also be studied.

3.I.3.a Energy transfers between compounds or energy states distributions

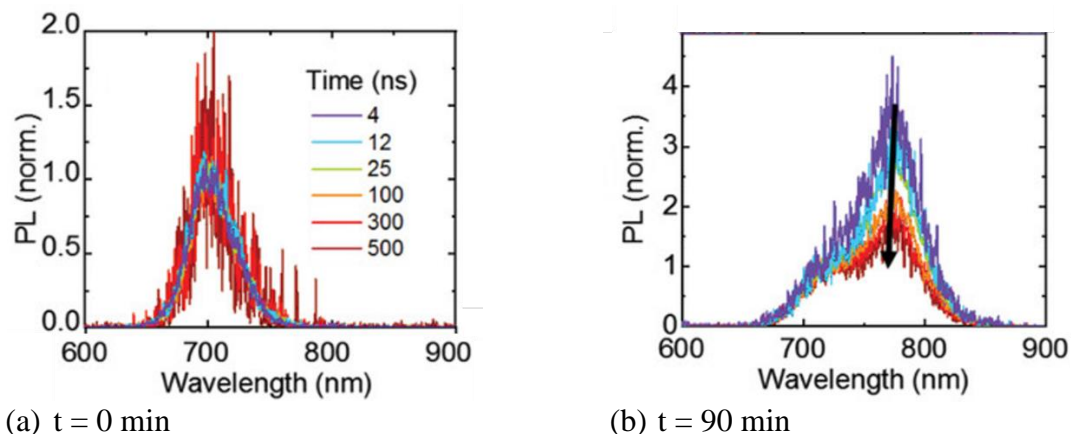


Figure 3-4: Transient photoluminescence spectra from $(\text{Cs}_{0.06}\text{MA}_{0.15}\text{FA}_{0.79})\text{Pb}(\text{Br}_{0.4}\text{I}_{0.6})_3$ films normalized at the wide gap peak at the beginning (a) and after 90 min (b) of illumination – Source: Andaji-Garmaroudi et al.¹¹

When several compounds or electronic states coexist in the absorber, the spectral information allows disentangling of their respective decays. It was illustrated to characterize the phase segregation of mixed halide perovskites. It allowed characterizing energy transfer between two emissive states corresponding to the different states¹¹. Figure 3-4 shows the experimental data before (a) and after (b) phase segregation. The formation of a lower gap energy peak with a shorter decay can be observed. Such reasoning can also be applied to the study of charge injection in the case of electronic exchange between two emissive materials¹². Recently, Dequilettes¹³ used streak data to quantify a bandgap gradient induced by a 2D passivation layer deposited on top of a 3D perovskite.

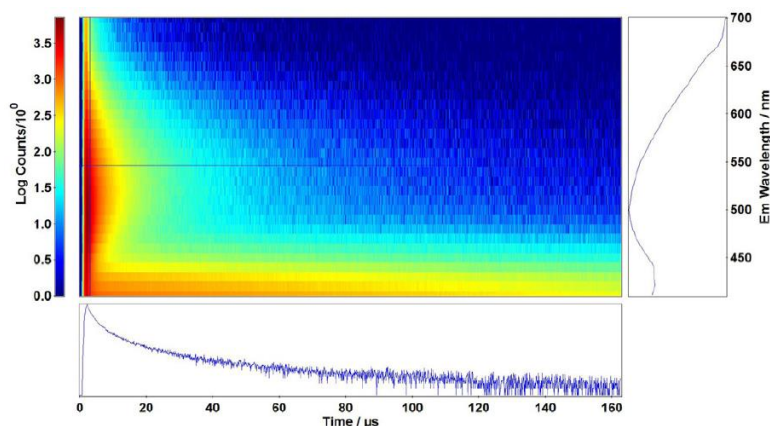


Figure 3-5: TiO_2 transient spectroscopy. Two peaks are visible and attributed to an exciton for lower wavelengths and band-to-band transitions at higher ones. On Cu-N-doped TiO_2 , only the second is seen as doping leads to the suppression of the excitonic signature – Source Arnaoutakis¹⁴.

Decays can also be separated for electronic states within a single chemical compound. In this frame, it allows the observation of excitons. An example is pictured in Figure 3-5: TRPL of pure TiO₂ shows two peaks corresponding to the conduction band and an exciton¹⁴. The latter owes higher peak energy and a longer lifetime; it is not observed for the Cu-N-doped TiO₂ sample.

Electronic transfers can happen within the DOS as electrons at different energy do not necessarily owe the same decay time. It is indeed the case when trap states are present within the DOS, as highlighted by Seitz et al.¹⁵. The streak acquisition shows a red shift of the median energy rather than two clear peaks. However, the steady-state spectrum can be fit by two Voigt functions (Figure 3-6a), orienting the interpretation of this shift as a consequence of two energy distributions. Indeed, it conforms with the sum of two decays of different lifetimes, as highlighted by the plot of the weights of the two spectra fitted along the decay in Figure 3-6b. It is possible to observe a rise time in the trap states occupation. This fit is further supported by analysis of the TRFLIM dataset: the behavior of the FWHM of the PL spot in punctual illumination necessitates the trapping of the carriers, fit with a trap depth of $26 \pm 2meV$.

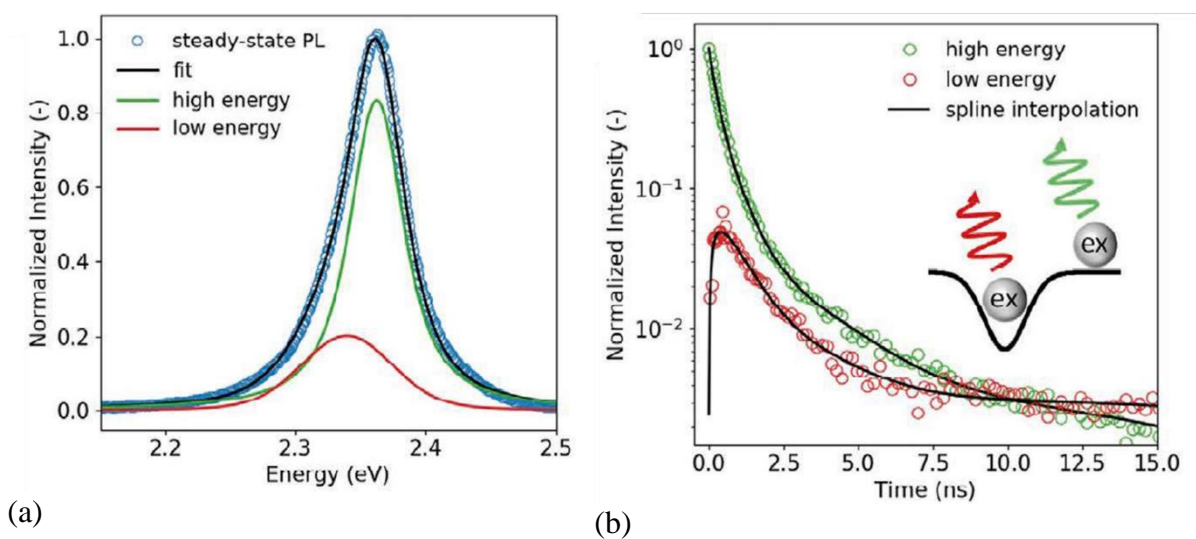


Figure 3-6: Observation of trapped states on the spectroscopy data (a) fit of CW spectrum by a sum of two Voigt functions (b) Spectral weights of the two peaks in the TRPL data. The low energy spectrum corresponding to trapped excitons is associated with the red curve owing to a rise time and longer decay – Source Seitz et al.¹⁵

Similarly, Li et al.¹⁶ have related a blue shift of PL peak with time with the band bending within the absorber. Indeed, for large energy potential and high band bending, the population with lower energy will be relatively more important and recombine first. Conversely, Bleuse et al.¹⁷ observe a red shift attributed to the transfer from highest to lowest energy states within the bands¹⁷.

3.I.3.b Energy transfers between light and matter

PL spectrum depends on the charge carrier profile as it is affected by reabsorption. Indeed, if carrier distribution is close to the surface, the reabsorption will be lesser, and the shape of the PL will be more similar to the one of the spectra emitted in depth. Thus, the spectrum's temporal evolution can characterize the carrier distribution variation by observing the energy transfer between the emitted PL and the sample.

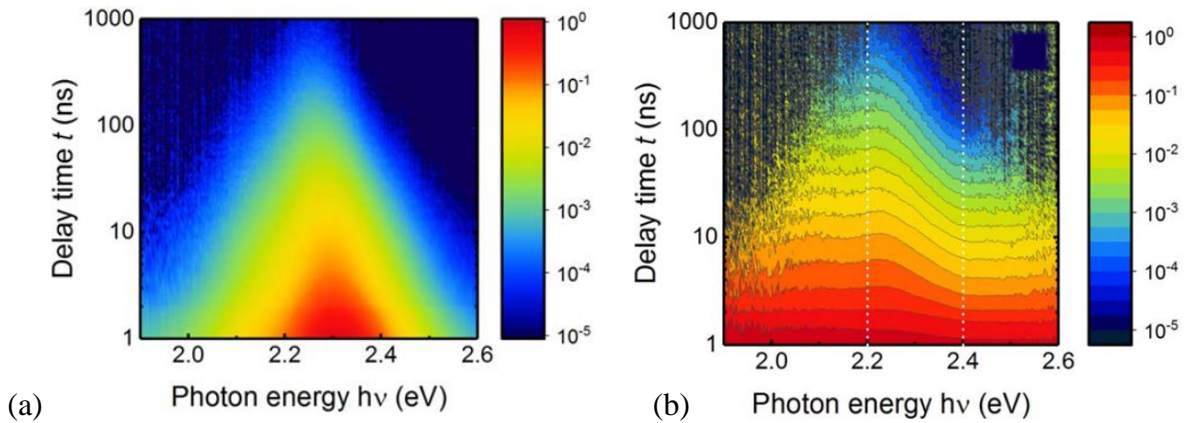


Figure 3-7: Experimental time-resolved spectroscopy of lead-halide perovskite monocrystal, (a) Data normalized to the maximum value, (b) Data normalized to maximum values at $t=0$, energy by energy. This visualization allows the observation of photon reabsorption impact on the collected spectrum with diffusion: higher energies decay quicker – Source: Staub¹⁹.

Yamada et al.¹⁸ use this redshift to fit the diffusion coefficient from a streak acquisition of 2-photons surface excitation on a perovskite single monocrystal. Staub et al.¹⁹ further highlighted the dependence of this shift on surface recombination velocity. Indeed, this quantity greatly influences the carrier profile close to the surface. The spectral shift quantifies the carrier mobility, while the intensity evolution provides surface recombination velocity. One can note that the spectral change is barely visible on the raw PL spectra (Figure 3-7 (a)) whereas it is clear on the spectra normalized by the initial spectrum (Figure 3-7 (b)).

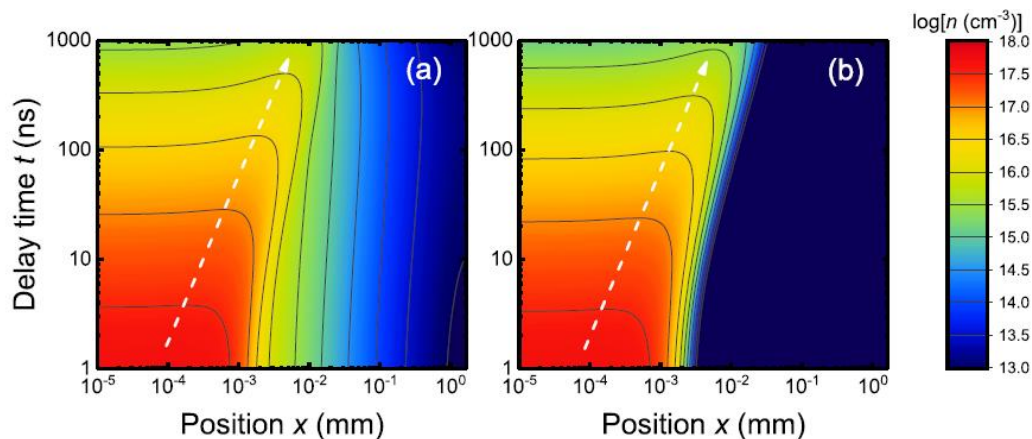


Figure 3-8: Impact of photon recycling on carrier distribution. Evolution of the fitted carrier density in depth and along time, (a) with and (b) without the photon recycling. Its influence is mainly visible at a longer radius or a long time after the pulse – Source: Staub¹⁹.

These datasets support the distinction between photonic and electronic transport. It can be done by fitting time-resolved spectroscopy with models of recombination and transport that include photon recycling^{19,20}. Figure 3-8 provides an example of photon recycling influence on the carrier density along time and in-depth obtained by such approach, by comparison of simulations that takes this mechanism into account or not.

Photon recycling can also be observed more directly. Indeed, PL emission after electronic diffusion and photon recycling owe similar spectra, whereas waveguided ones are redder. The presence of blue photons far from the excitation would then highlight photon recycling events. Moreover, the decay obtained can help quantify its impact. Yamada¹⁸ observes an increase in the effective lifetime and the depth of excitation. It is attributed to the higher number of photon recycling cycles realized before the escape of a photon. The statistical model allows the quantification of PLQY based on this lifetime extension.

3.I.3.c Energy transfers within the electronic distribution

The PL spectra reflect an emission of an electronic distribution occupying a given density of states. In quasi-equilibrium and under assumptions met by most work in PL characterization, this distribution is effectively described by two parameters: the quasi-Fermi level splitting and the carrier temperature.

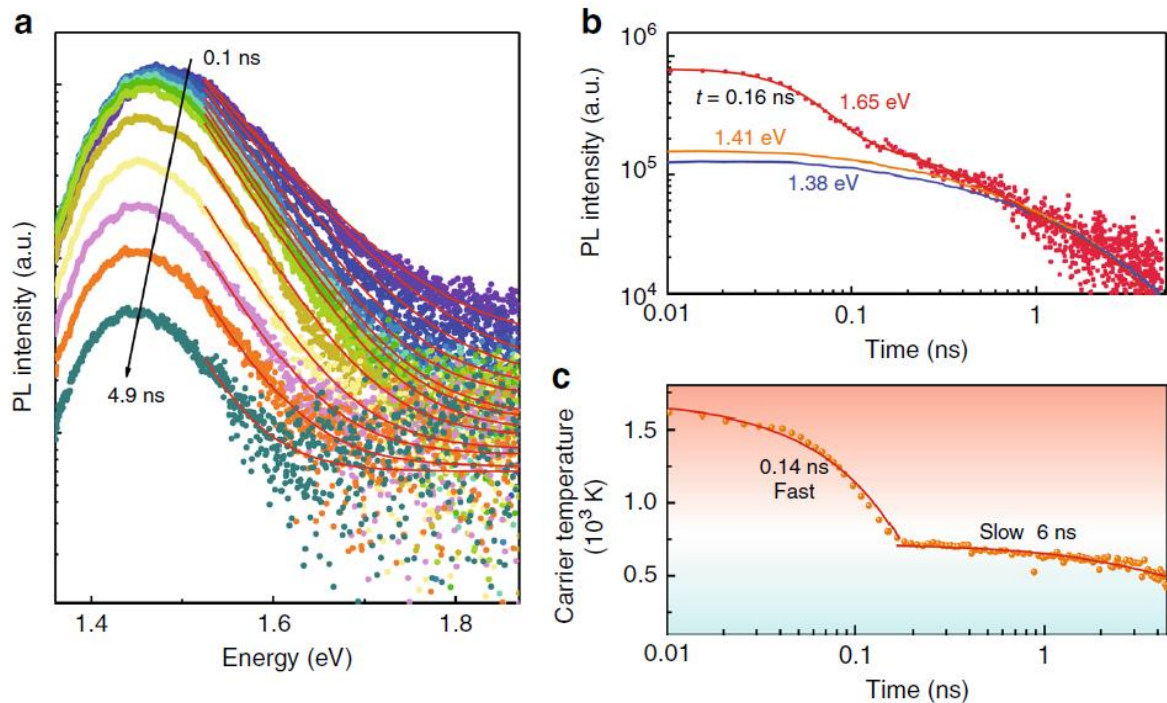


Figure 3-9: Short-time dynamics of FaSnI spectra (a) spectra at different delay times, (b) PL decay at different wavelengths, and (c) temperature obtained by high energy tail fit – Source Fang et al.²⁶

Thus, the distribution temperature change can be observed directly with time-resolved spectroscopy. At short time scales, the carriers cooling can be characterized through the impact of the temperature on the high energy tail of the spectrum²¹. It allowed the description of energy losses through phonons emission and comparison of different structures potential for hot carriers solar cells exceeding the Shockley Queisser limit^{22,23}. If the first studies focused on the presence of hot carriers in quantum wells and bulk III-V, they were also observed in perovskite devices²⁴⁻²⁶. Figure 3-9 shows an example of FaSnI time-resolved spectroscopy acquisition (a) that exhibits a variation of the decay shape with the energy (b). The fit of the high energy spectra provides an interpretation in terms of carrier temperature, shown in (c). Interestingly enough, Bleuse employed hot carriers relaxation as a temperature study to better quantify the density of states by fitting the bandgap and Urbach energies²⁷.

When quasi-Fermi levels splitting difference with the bandgap energy is of the order of magnitude of $k_B T$, the occupation of the bands must be taken into account²⁸. A term of band-filling then reduces the absorption of the lower energy states, as introduced in Chapter 1.II.2. Such a phenomenon can be seen with the streak camera and was also demonstrated on perovskites²⁰. Indeed, the transient regime can be considered a PL intensity study – corresponding to the limit case where transport is negligible. At the beginning of the decline, the spectrum is thus blue-shifted and returns to its reference as the excess carrier densities decrease.

Literature provides examples in which TRPL spectroscopy highlights variation in the externally emitted spectrum over time. They can result from energy transfers between electronic states or changes in the light outcoupling with carrier distribution. All the energy transfers can coexist during experiments, and data provided by the streak can be sufficient to unmix them. Sridharan²⁰ emphasizes the challenge of disentangling different phenomena with the example of redshift along time first attributed to increasing photon reabsorption and eventually mainly ruled by band filling. Therefore, the knowledge of further dimensions can be crucial, and spatial variation helps distinguish them.

One can note that the spectral changes result from mechanisms usually neglected in simple models. Samples behaving like defect-free materials homogeneous in depth and owing constant carrier profile or little reabsorption will have no notable spectral changes in classical injection conditions. They rather fall within the framework of TRFLIM or HI characterization and meet the underlying assumption for their classical data analysis.

3.I.4 Principle of the 4D-PL setup developed

The 4D-PL setup is based on reflection microscope architecture, as illustrated in Figure 3-10. A 35ps pulsed laser (Coherent Talisker) excites the sample in homogeneous or focused

illumination at 532nm up to 1MHz. The emitted photoluminescence is filtered through a long-pass dichroic mirror DMLP650 and a FEL550 long-pass filter. A tube lens focuses it, forming the image of the sample onto a Digital Micromirror Device (DMD, Vialux V7000 module). This component is controlled and synchronized through a python code²⁹. The mirrors in the "on" position reflect the light towards the collection branch, according to the pattern in use. It is then focused into a fiber and analyzed by the single-pixel detector. The latter comprises a Princeton HRS 300 spectrometer combined with a C10910 Hamamatsu streak camera owing a spectral resolution on the order of the nanometer and a temporal resolution below 20 ps.

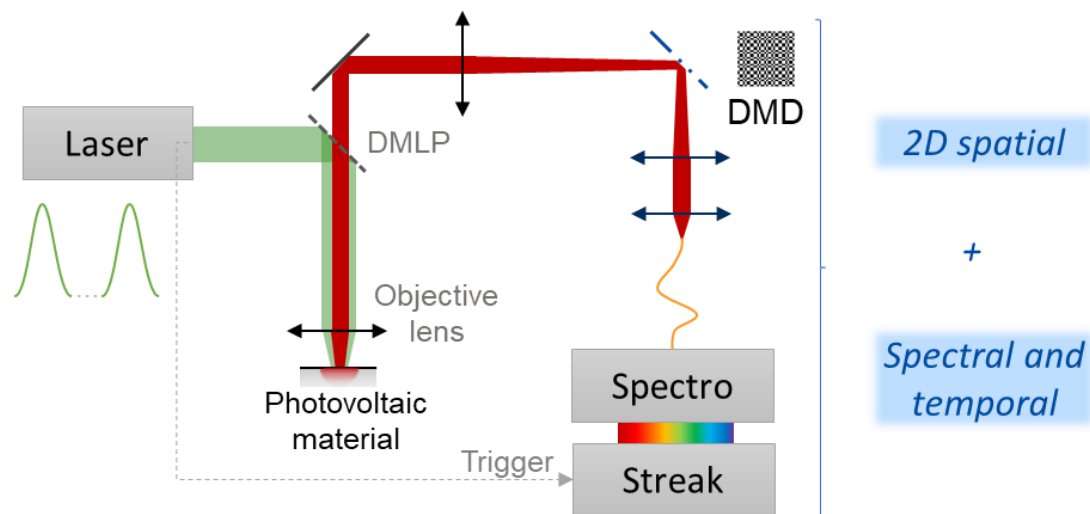


Figure 3-10: Experimental setup of 4DPL. A pulsed laser excites the sample in a reflection configuration. It is then filtered out by the long-pass dichroic mirror (DMLP). PL emission is focused onto the DMD and analyzed with the streak camera.

As the obtained TRPL spectroscopy image is roughly 1000pixelsx1000pixels, the streak sampling camera exceeds its resolution. For instance, the full-width half maximum of the laser on the temporal axis, considered as a point-spread function, is about a dozen pixels, where one would be theoretically enough. The same hold for the spectral dimension. For a high-quality signal, the resolution could then be improved by deconvolution.

As explained in the previous chapter, there are various approaches for SPI implementation. The main possible choices are recalled in Table 3-1. Contrarily to structured illumination, a structured detection scheme allows freely choosing of the lighting. Indeed, going away from homogeneous and concentrated limit cases greatly complexifies the physics under study and transport modeling. Furthermore, we aim to characterize different physical phenomena, among which diffusion, that benefit from the analysis of the PL as a function of the distance from the illumination.

For this architecture, only electrically addressed spatial light modulators (EASLM) can be used for modulation. A DMD was chosen for its speed of response and because it plays on

intensity rather than the phase. We implement a basis scan approach to limit the computational complexity and avoid any prior on our scene image. In other words, we solve the inverse problem and take as many measurements as pixels in the reconstruction. Among the possible basis, we chose to use the Hadamard basis because it is binary, has low noise amplification, and has high light throughput³². As it owes negative values, we must decide on a representation scheme among *shifting*, *splitting*, and *SNMF* (see Chapter 2, section I.3). The first solution is adopted for simplicity, replacing -1 values with 0. As it is developed in Appendix B, it influences the inverse matrix and has implications for the numerical reconstruction of the scene. Notably, the first pixel in the reconstruction is much more sensitive to the noise and is removed in the reconstruction. The others are equally affected by noise.

System architecture	Structured light detection
	Structured illumination
Modulation method	DMD (reflection)
	LCD (transmission)
Acquisition strategies	Basis scan
	Compressive sensing
	Machine learning

Table 3-1: Different SPI approaches possible. The main choices concern the system architecture, modulation method, and acquisition strategy. 4D-PL was implemented in a structured detection configuration with a DMD and performed basis scan reconstruction.

As a reminder, for classical SPI, the physical quantity measured is the intensity of the whole collected light flux. In this case, it can be modeled by the optimization problem $Ax = b$, where x is a 1D vector of n pixels traducing a 2D information, b is a 1D vector of m elements. For our 4D problem, b is 3D and corresponds to the intensity as a function of the wavelength and the time, and x is a 3D vector with the 2D spatial information encoded in one dimension. Its implementation does not limit spatial resolution. It can still be micrometric, as set by the classical diffraction limit. Otherwise, SPI's structured illumination configuration inevitably evokes structured illumination microscopy (SIM) that leads to superresolution imaging.

In summary, we have seen that 4D-PL aims at obtaining information that only a few lab-developed setups can approach. The principle of the streak camera was described as well as its application in semiconductor characterization. In this work, it was combined with SPI to obtain the sought PL dependence. The following section discusses the setup implementation and the constraints it raises.

3.II Imaging by SPI: practical implementation

The following sections address different aspects of SPI implementation: we identify various constraints and challenges and design the system optics and reconstruction method accordingly.

3.II.1 Time scales of the 4D-PL setup

This section explains how the time scales of SPI, detector, and luminescence fit together. The synchronization procedure is described, and the way the DMD oscillations influence it is detailed.

3.II.1.a Streak camera and SPI

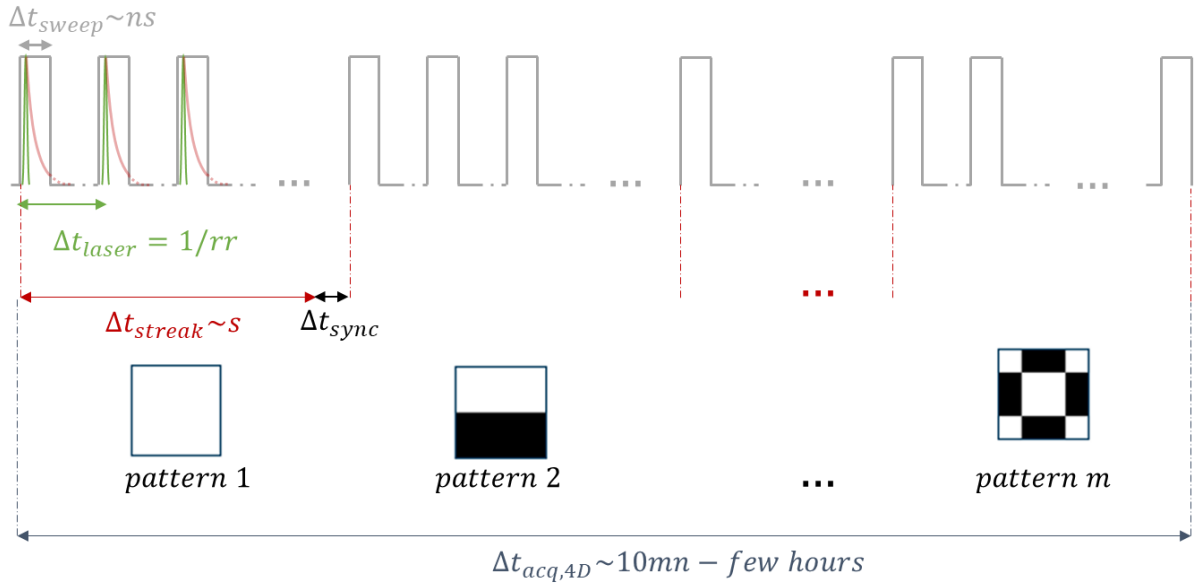


Figure 3-11: Time scales of the 4D-PL setup. Each streak camera acquisition associated with a pattern requires an acquisition time Δt_{streak} . During this period, a large number of accumulations of PL decays are measured every laser cycle Δt_{laser} for a duration Δt_{sweep} .

Figure 3-11 illustrates the different time scales of the setup: the photoluminescence decay has a characteristic time in the nanosecond range and is recorded during the sweep time of the streak camera Δt_{sweep} , which is between 2 ns and 2 ms. For each pattern, the acquisition time corresponds to an accumulation of decays, the number necessary for good signal quality depends on the luminous flux. This time typically ranges from 1 to 100s, resulting in a total acquisition time $\Delta t_{acq,4D}$ of the 4D information of a few minutes to a few hours.

3.II.1.b DMD oscillations

When Vialux DMD is interfaced with Python, mirrors are mobile during the display of each pattern. Indeed, the mirror position is refreshed every *illumination time*, t_{illu} , chosen between $45\mu\text{s}$ and 1s . This name corresponds to the one given in the documentation. After this duration, mirrors are oriented toward the detector for a short duration, inducing some background signal. However, this illumination time also sets the time required by the DMD to display a new pattern. When it detects the corresponding instruction, the iterations are interrupted after t_{illu} , which sets the upper limit to the DMD reaction time Δt_{reac} .

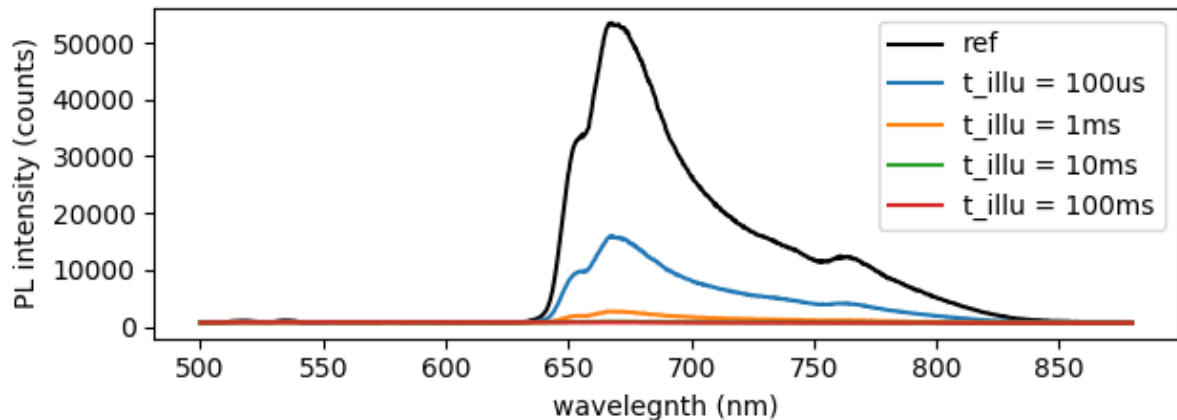


Figure 3-12: Influence of the DMD illumination time on the spectrometer acquisitions. The reference spectrum corresponds to all patterns directed toward the detector. Others are obtained with all mirrors ‘off’ for various illumination times.

Figure 3-12 illustrates signal variations for different illumination times when all mirrors are directed away from the detector, in the ‘off’ state. When the patterns are refreshed at a higher rate, the background signal is increased. We can model this effect by considering that at each actualization, mirrors are directed toward the detector during a short interval t_{on} . For an incident intensity I_0 and dark current of I_{dark} , the collected intensity reads:

$$I(t_{illu}) = \frac{t_{on}}{t_{illu}} * I_0 + I_{dark} \quad (1)$$

By fitting the intensity averaged spectrally for the curve shown in Figure 3-12, we obtain $t_{on} \sim 26\mu\text{s}$, a quantity close to $45\mu\text{s}$ corresponding to the 22kHz maximum refresh rate.

3.II.1.c Synchronization with the detector

The synchronization between the detector and the DMD is carried out digitally: streak camera (or spectrometer) acquisition saving is detected by the python code that triggers the pattern change onto the DMD. As illustrated in Figure 3-13, the detector acquires the signal

during the chosen experimental time Δt_{exp} and is then unavailable during the file-saving time Δt_{save} , before staying idle for a chosen duration $\Delta t_{det,idle}$. The delay time between the spectrometer acquisition and the new pattern display depends on two parameters. First, the output text file must be detected by Python, which questions its writing every Δt_{detec} . Then, a non-negligible reaction time Δt_{reac} is taken by the DMD to display.

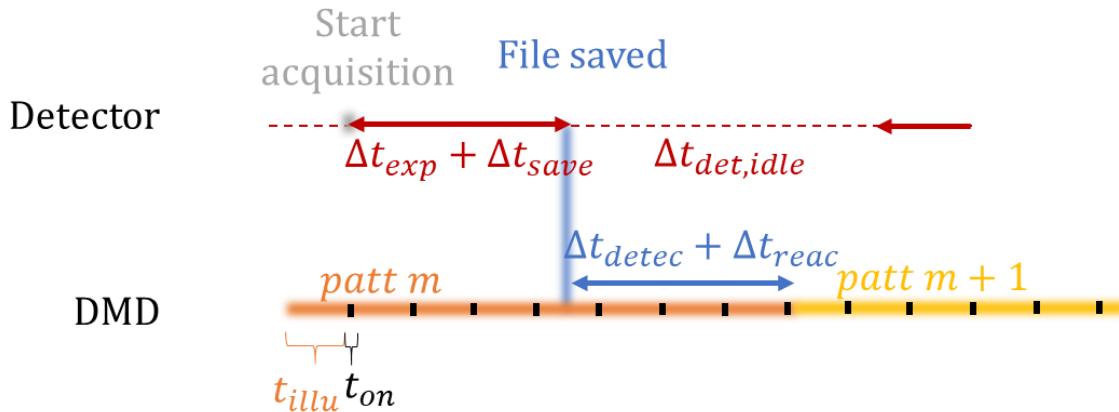


Figure 3-13: Schematic of detector-DMD synchronization. In this configuration, acquisitions are launched sequentially by the detector that is in the master position. The python program detects the saved file and instructs a new pattern display.

Extra care must be taken when setting t_{illu} , Δt_{detec} and $\Delta t_{det,idle}$, and the situation differs with the detector. The typical streak camera acquisition and save time ($\geq 10s$) is longer than DMD characteristic times. The illumination time is defaulted to 100ms, ensuring negligible background noise. Between the acquisitions, a few hundred milliseconds to one second is usually taken as $\Delta t_{det,idle}$. It reduces CMOS heating, sometimes observable on the dark signal, and guarantees synchronization while being negligible. In the case of hyperspectral SPI, the exposure time of the spectrometer is typically short (100ms for photoluminescence, down to 1ms for laser reflection). The temporal settings of $\Delta t_{det,idle}$ must be long enough, so the next pattern is displayed before the next spectrum is acquired. In particular, the time to save the spectrum file Δt_{save} and $\Delta t_{det,idle}$ vary greatly due to the background tasks of Windows, and as a result, a minimum 50ms margin has to be taken in $\Delta t_{det,idle}$. Thus t_{illu} and Δt_{detec} can both be set around 20ms to limit background noise. An improved DMD-spectrometer synchronization can be achieved with a detector with data buffering or controlling the launch of its measurement from Python to ensure a new pattern has been displayed on the DMD.

3.II.2 Challenges

4D-PL setup, as a microscope, is characterized by its field of view and numerical aperture determined by choice of collection optics. The latter also affects the impact of DMD diffraction on the collected signal and the transmission.

3.II.2.a Field of view

The field of view (FOV) is crucial in microscopy as it determines the problem that can be addressed with the setup. A balance has to be found between the FOV and the desired spatial resolution limited by the number of pixels. Moreover, a trade-off between the field of view and DMD collection efficiency per mirror has been highlighted in the literature³⁰.

FOV of an imaging system is provided by the product of the optical magnification times the sensor surface area. In our setup, the effective sensor area is determined by the DMD area viewed by the streak camera. Again, it corresponds to the magnification of the optics coupling the DMD to the streak entrance, multiplied by the surface area characterized by the streak. In free space, the effective surface area is tuned by the width of the entrance slit and varies with the configuration and resolution. These considerations highlight an entanglement of the choice of the FOV with temporal, spectral, and spatial resolutions and collected light intensity.

3.II.2.b Diffraction

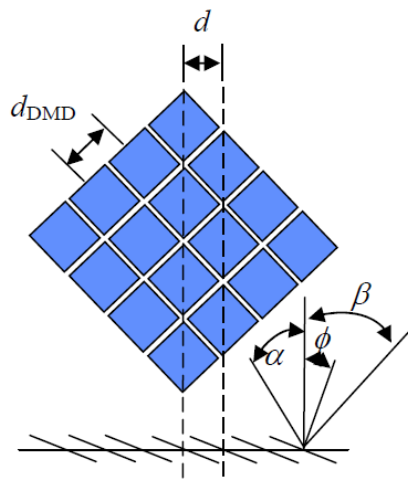


Figure 3-14: DMD periodic structure and blazed grating-like profile. Light impinges on the DMD with an incidence angle α with respect to its normal, and is collected at an angle β . The mirrors are tilted with an angle ϕ . – Source Rice et al.³¹

The DMD has a periodical microstructure and appears to act as a blazed grating³¹. Figure 3-14 shows that the typical sawtooth-shaped cross section associated with this kind of gratings can be seen by taking mirror profiles along their diagonal. A resulting implication is directly observable when a laser is focused on the DMD, leading to a spatial diffraction pattern. Similarly, when illuminated by white light, the DMD appears iridescent.

To better understand the interference created, the spectrum of a halogen lamp is acquired directly and after reflection onto the DMD (all mirrors "on"). As shown in Figure 3-15(a), only certain wavelengths are collected by the spectrometer for the reflected signal (blue curve)

compared to the reference signal (black curve). This phenomenon can be explained by the white light spreading over an arc of 21° in several diffraction orders³¹. The insert of Figure 3-15(b) shows this phenomenon: the visible light is split into orders 5 to 9, which are superimposed in this arc. These characteristics are very different from the blazed gratings used in spectrometers which are sized to reflect light efficiently in 1 or 2 orders. With a fiber that collects only one angle of refraction, only one wavelength is captured per order. This phenomenon induces the five peaks in Figure 3-15 (a).

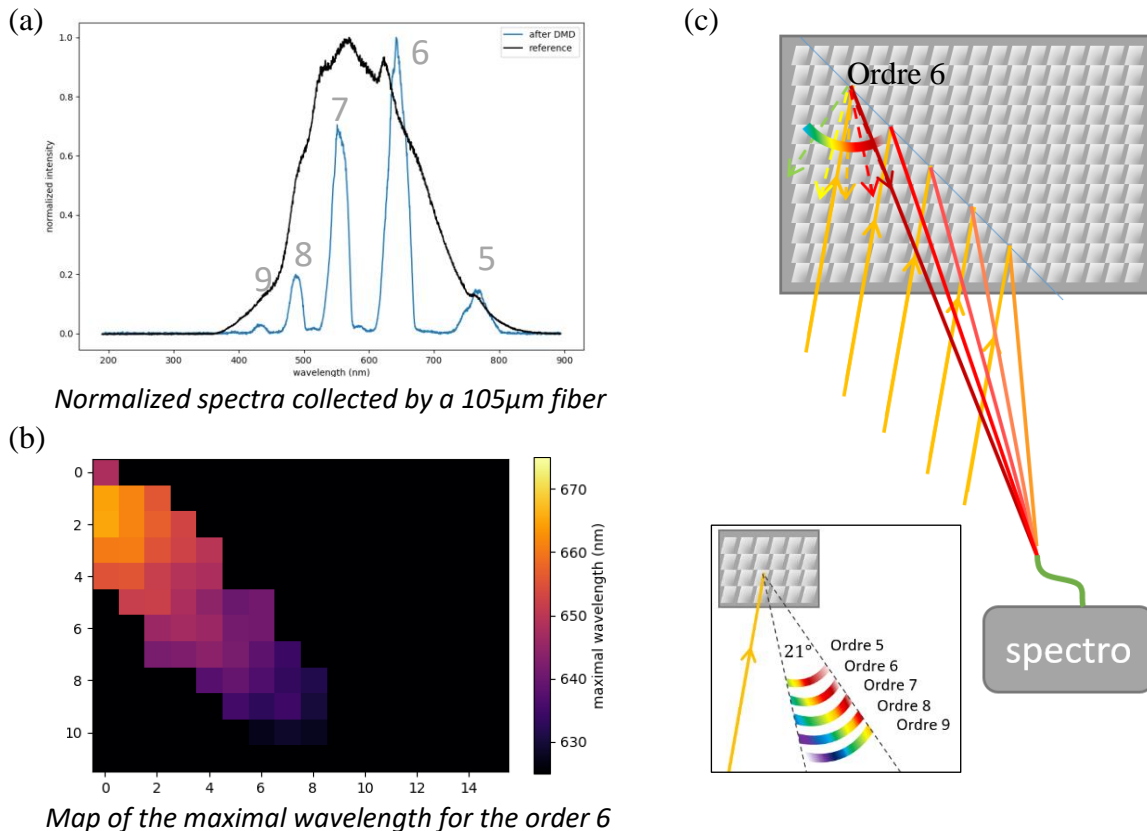


Figure 3-15: Hyperspectral acquisition highlighting the interference created by the DMD. (a) Spectrum obtained when all the mirrors are tilted towards the fiber. (b) Maximum corresponding to order 6 of the spectrum obtained by SPI in each group of pixels. (c) Diagram of the interference phenomenon on the DMD and a collection made directly by the fiber for a single order. The insert shows a schematic representation of diffraction at a mirror for a given order.

By making a Single Pixel Imaging acquisition, we observe that the signal is collected only along a diagonal of the DMD. In each group of pixels of this diagonal, the spectrum presents five peaks corresponding to orders 5 to 9. Depending on the collection angle, their wavelengths vary according to the pixel considered on the DMD. Let's take the example of order 6, centered on 655 nm, which contains the light diffracted efficiently between 487 and 984 nm. The fiber collects the signal in a cone of a few degrees, capturing wavelengths close to the central one. Figure 3-15(b) shows the spectral maximum collected for this order in each

pixel group: it varies with position on the DMD. The pixels at the top left correspond to the largest reflection angles, as shown in Figure 3-15(c). Following the grating formulae, they correspond to the highest wavelengths. In other words, in this configuration, the field of view is not only wavelength-dependent but is reduced to a few mirror groups for a given wavelength.

Diffraction on the DMD highlights a dependence between the angle of refraction of light and its wavelength. To collect a signal containing the entire spectrum of the source, it is, therefore, necessary to use optics that allow the reflected signal to be concentrated in the fiber in a wide angular cone. Consequently, the collection optics must gather a broad angle to characterize the sample in the spectral dimension continuously. Rice et al.³¹ show that these interferences can be considered features in spectral transmission.

Notably, experiments show that the interference influence varies with the impinging wavelength and the pattern displayed. It has proven detrimental in 4DPL experiments, as detailed in Chapter 4. In this section, we restrict the diffraction analysis to the all-on configuration considered for the optical collection.

3.II.2.c Low Light regime and noises

This experiment is performed in a regime approaching photon counting because of the low emission corresponding to PL and the low sensitivity of the detector. This second factor is illustrated by calculating the order of magnitudes of photons collected for an isotropic source, which corresponds to a material with a total photoluminescence conversion in realistic excitation conditions. Setting both slits to a width of $50\mu m$ results in an etendue of:

$$\Omega_{coll} = \pi NA^2 w_{slits}^2 \quad (3-1)$$

Hence, $\Omega_{coll} = 0,0001 \text{ mm}^2 \cdot \text{sr}$. This corresponds to the etendue collected by 5x5 pixels on the TRFLIM camera. By comparison, one mm^2 FOV emitting in a sphere corresponds to $12\text{mm}^2 \cdot \text{sr}$. Thus, as the quantum efficiency of our detector is around 0.15%, about one photon out of 10^8 emitted by a Lambertian source is detected for a one mm^2 FOV (or one photon out of 10^6 for a $100\mu m \times 100\mu m$ FOV). This signal is further spread on the million pixels array. In pulsed experiments, laser fluences of 10^{12} ph/cm^2 would lead to the detection of a hundred photons per pulse.

It results in acquisition with a very low signal-to-noise ratio (SNR). This quantity can be directly estimated by performing a series of similar acquisitions and dividing their mean by standard deviation. For a multidimensional detector like the streak camera, the signal of interest is clearly defined: it can be calculated for each acquisition pixel, providing an SNR per wavelength per delay time or on the intensity averaged spectrally and temporally.

The example of focused illumination on gallium arsenide provides peaks SNR around 5 for one acquisition pixel (10s exposure). For comparison, the SNR of the signal integrated over time and spectrum is about 100. This latter value provides a maximum achievable SNR with smoothing, as it reflects the global variation of the intensity. As seen in the appendix B, SPI is sensitive to multiplicative noise, so collection optimization is crucial.

3.II.3 Choice of the collecting optic

Considering the challenges mentioned above, major issues must be addressed by the light collection: alignment must be as easy as possible, optical losses must be limited and spectral transmission must be representative of the sample.

3.II.3.a Implementing a fiber optic collection

We collect light from the DMD with a multi-mode fiber of 910 μm diameter and a numerical aperture of 0.22. It allows us to capture it over a broad angle to limit the influence of diffraction of the DMD that acts as a blazed grating³¹. One can note a stable field of view is guaranteed by the coupling into the optical fiber serving as a homogenizer. When the streak camera is used in free space, the image modulated by the DMD is focused onto the spectral slit entrance and cropped by it. Moreover, the collection in fiber provides real versatility and allows the detectors to be exchanged easily without further alignment.

3.II.3.b Focusing on the fiber

Parabolic lenses or mirrors focus the light beam to collect the flux at a wider angle than the fiber alone. Different optical configurations have been tested, and the two best-performing ones are shown in Figure 3-16. It can be noted that the results obtained with a single lens in the collection include more pronounced interference and lower intensity. The choice is made to use a parabolic collimator which reduces the complexity of the system alignment.

The first configuration, shown in Figure 3-16(a), uses a diffuser to homogenize the light collected in the fiber. As a result, rays from all the pixels of the DMD are captured, allowing the entire sensor to be imaged. However, the collected intensity is very low, resulting in poor signal quality, as seen in Figure 3-16(b). On the other hand, the second configuration depicted in Figure 3-16(a) provides a very small field corresponding to twice the diameter of the fiber core imaged with good spectral quality shown in Figure 3-16(d). These two examples highlight a compromise between the collection field and spectral resolution. This limit is a consequence of etendue conservation: either a small rays fraction from a large area is collected, or a much higher fraction of the rays reflected from a small area of the DMD.

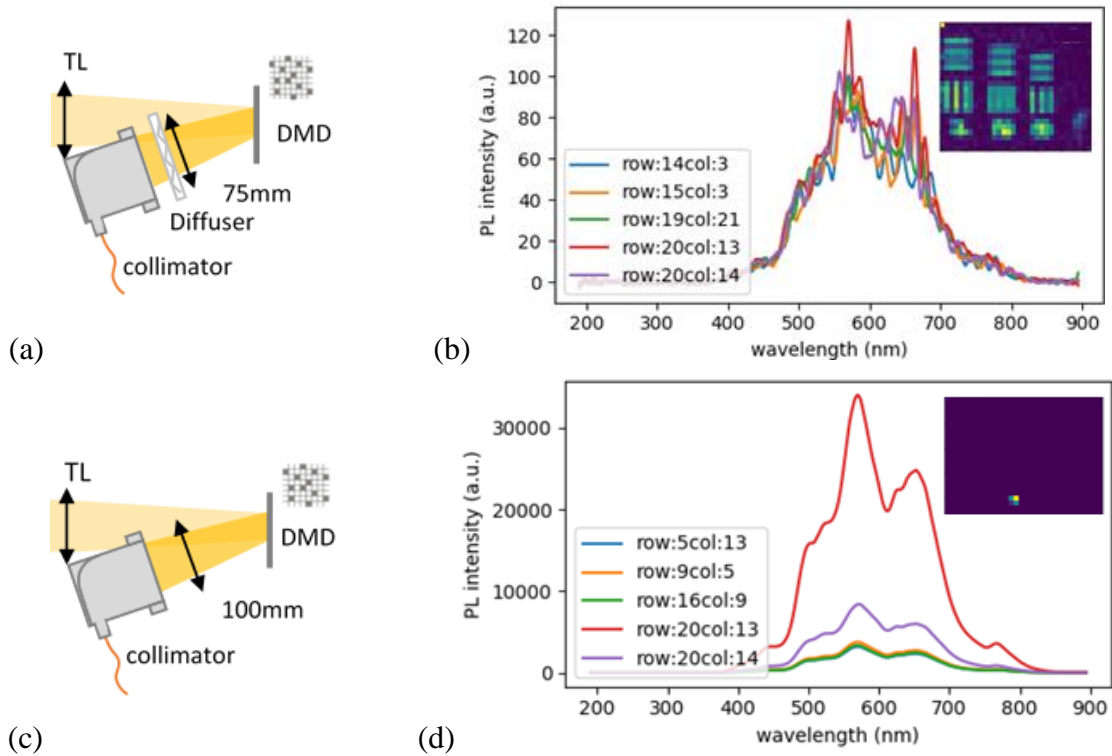


Figure 3-16: (a) and (c) Examples of configurations to focus the light reflected from the DMD into the fiber; the imaged source is the halogen lamp reflected on the USAF target (a standardized test pattern to test the resolution of the microscope), (b) and (d) higher intensity spectra, with spatial reconstruction obtained by SPI with a binning of 64 mirrors in insets.

We chose to maximize the collected light over a small field of view (diameter of 1.8mm on the DMD, corresponding to more than 13 000 micromirrors), given the light intensities at stake. Indeed, by comparison to a diffuser configuration that would image the whole DMD area, the global signal is increased by roughly a factor 5, and by 10^3 in the field of view area, while the FOV is decreased by a factor 60.

3.II.4 Investigation and correction of SPI artifact

Artifacts shown in Figure 3-17 are observed in the reconstruction of the spectralon sample with 64 linear patterns. They can be linked to models of DMD as blazed grating in one or two dimensions. This leads to the definition of a practical correction method.

3.II.4.a Typical artifacts in the reconstruction

Acquisitions performed by SPI with either the spectrometer or the streak camera showed systematic reconstruction artifacts. Some pixels exhibit discontinuities, with either higher or lower values depending on the wavelength. Figure 3-17 shows an example of an artifact on a flatfield acquisition, corresponding to a halogen lamp reflection on a Spectralon diffuser reference. All measurements should have the same values for a perfectly homogeneous object

and transmission, except for the full “on” pattern that collects twice as much light. In practice, pixels referenced $2^n - 1$ (Python count, starting at zero) owes a difference with the average value that scales with n and can't be attributed to regular noise. Indeed, in the simulations presented in the appendix B, except pixel 0, all pixels are affected similarly by additive or multiplicative noise. As in SPI, the values of the different pixels are linked together; the deformations observed in Figure 3-17 may be the visible surface of a more general deformation of the signal. That's why understanding them is important to avoid the spread of errors and may be false correlations in the result.

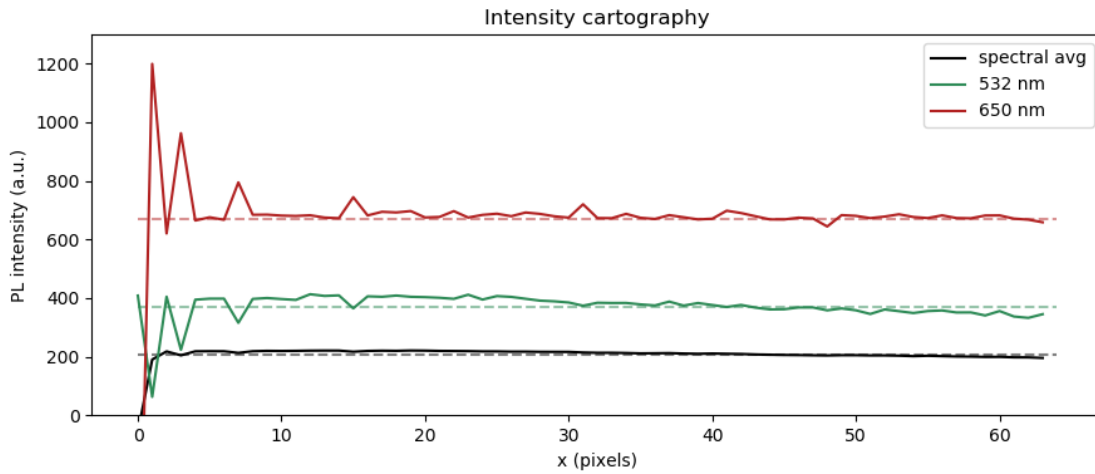


Figure 3-17: Example reconstruction of flatfield acquisition obtained by SPI with 64 linear Hadamard patterns for two different wavelengths and averaged spectrally. The dashed lines guide the eye and correspond to the intensity averaged on all patterns.

Figure 3-18(c) describes the calculation of the distorted pixels, numbered 1, 3, 7, 15, and 31, by showing in white patterns taken into account with a positive coefficient, and in grey that weights negatively. A visible common point is a positive weight on patterns 0 and 32, accompanied by a negative coefficient on patterns 1 and 33. The former owes a low spatial frequency, while the latter is high. Hence the idea of sorting the patterns by their on-to-off transitions number ν , defined as the amount of pixels whose right neighbor has a different value. In the 1D case, it can be obtained from the shifted pattern matrix $(a_{i,k})_{1 \leq i \leq m, 1 \leq k \leq n}$ for each pattern i :

$$\nu_i = \sum_{k=1}^{n-1} (a_{i,k+1} - a_{i,k})^2 \quad (3-2)$$

The normalized measurements sorted this way are plotted in Figure 3-18(b) and display a visible trend. In other words, the number of transitions creates a drift in the collected intensity that can be either positive or negative. It can be quantified by fitting the variation of the normalized intensity with a linear slope, hereafter mentioned as a drift slope. In the different

experiments analyzed, a signal increasing with the number of transitions correspond to negative $2^n - 1$ pixels.

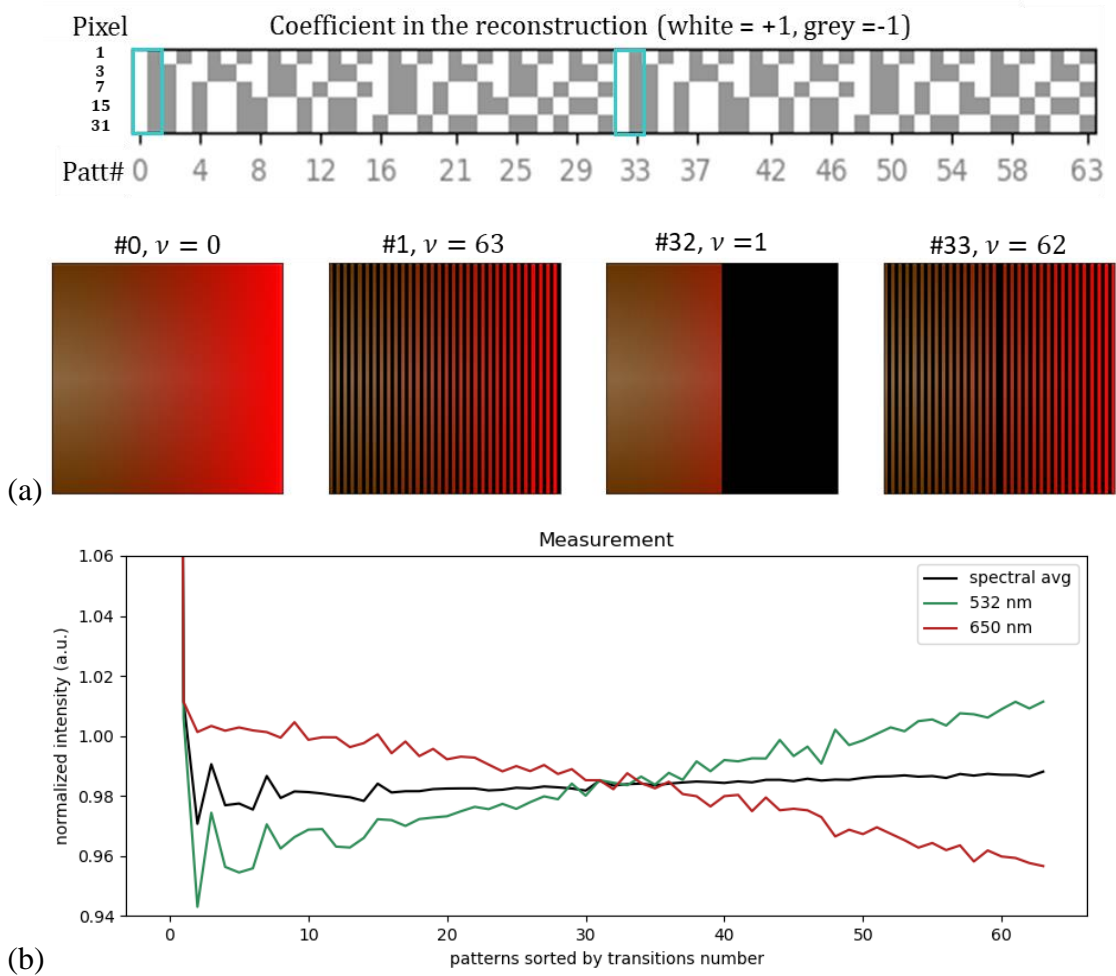


Figure 3-18: (a) Calculation of pixels misestimated 1,3,7, 15, and 31 from the measurement series: white corresponds to a positive factor, and grey to a negative one. They consider patterns #0 and 32 positive and #2 and 33 negative. They are displayed with their transition number ν . (b) Measurements shown in Figure 3-17 arranged by transitions number.

The drift slope $\theta(\lambda)$ can be estimated by fitting the dependence of the collected intensity I_{PL} on the transition number. For each wavelength, it depends linearly on the intensity averaged on the patterns $\langle I_{PL} \rangle_\nu$. Hence, one can define the coefficient traducing this linear dependence, reading:

$$\frac{\partial I_{PL}}{\partial \nu} = \theta(\lambda) \langle I_{PL} \rangle_\nu \quad (3-3)$$

This wavelength dependency, as well as the spatial frequency relation, raises the point of DMD diffraction. In the following, we confront our observation with different models to understand this effect better.

3.II.4.b Modeling and understanding the problem

3.II.4.b.1 Wavelength dependency and 1D diffraction model

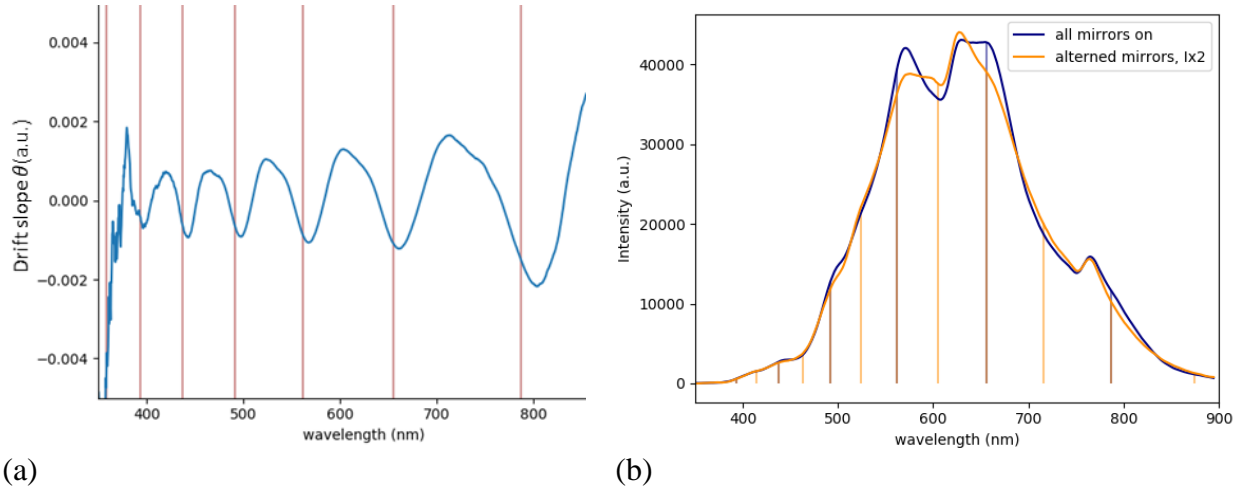


Figure 3-19: (a) Wavelength dependency of the drift slope $\theta(\lambda)$ and DMD blaze wavelengths (b) Measurements corresponding to patterns 0 and 1 superimposed with the blaze wavelengths of the DMD with its physical parameters and with a pitch divided by two (navy and yellow lines respectively).

The normalized patterns slope is plotted in Figure 3-19(a) on the whole spectral range of the spectrometer. It exhibits a sinusoidal dependency on light wavelength. We compare these variations with the blaze wavelengths λ_B obtained for different orders m with the 1D grating formula as done by Rice³¹ (as mentioned in section 3.II.2.b.):

$$\lambda_B = \frac{d}{m} \sin(2\phi) \quad (3-4)$$

Where d is the grating periodicity (DMD half diagonal) and ϕ is the mirror tilt angle. Results are featured by the plot's brown vertical line and show the same periodicity as the normalized pattern slope.

This simple 1D model can also be used to analyze the measurement performed with a pattern of alternating on and off rows and modeling it by a blazed grating of the doubled pitch. Figure 3-19 (b) shows the spectra collected with all mirrors on and in this second configuration, in blue and yellow, respectively. The intensity of the second pattern is multiplied by two as the number of mirrors directed toward the collection is half. The vertical lines of the same shades feature corresponding blaze wavelengths. The 'alternated mirrors' owes the same blaze wavelengths as the 'all on' ones, plus one between them. They correspond to orders 9 to 26 from 300 to 900nm, compared to orders 5 to 12 of 'all on' DMD. The diffraction efficiency is less important for the lower grating pitch, hence the constated effect: in the 'all on' blaze wavelengths, the diffraction leads to a higher collected intensity than in the 'alternated mirrors'

configuration, resulting in a negative drift slope for these particular points. The slight difference between the normalized patterns maxima and the blaze wavelength can be explained by a small variation of the collection angle compared to the ideal one.

3.II.4.b.2 2D diffraction model

A 2D diffraction model is built to assess the influence of the diffraction led by any pixel patterns. It is based on the work of S.Popoff³⁴ as available online and adapted to fit our problem geometry. Figure 15(a) describes a complex transmission function representing the DMD; between two neighboring mirrors a phase shift is introduced:

$$\delta\phi_{DMD} = \frac{2\pi d}{\lambda}(\sin\alpha + \sin\beta) \quad (3-5)$$

Equation (3-5) is written with the notations defined above. The corresponding 2D DMD model is shown in Figure 3-14. It results from the sum of the optical path difference introduced on the incidence δ_i and reflection δ_r . The insert of Figure 15(a) reminds the calculation of this quantity in the case of normal incidence:

$$\delta_r = d\sin\beta \quad (3-6)$$

Far-field intensity images can be obtained by taking the absolute value of Fourier transform of the transmission function. Results of its calculation for patterns 0 and 1 (all “on” and one alternating columns “on” and “off”) are displayed in Figure 3-20(b) and compared to experimental pictures. It succeeds in qualitatively retrieving the shape of the light after diffraction.

This model, however, quickly reaches its limits. It considers only one incident and collection angle, whereas optics integrates a wider angular range. Simulation results do not represent the intensity of the measurement, and a more advanced model is needed to describe the multiple lenses of the collection path.

One can note that diffraction effects and possible correction are more studied in holography³⁵, where DMD is used in projection, than in single-pixel imaging, in which the literature is scarce. Such calibration involves modifying the pattern projected to compensate for the aberrations and does not fit (at least straightforwardly) optical multiplexing as the pursued spatial basis is modified.

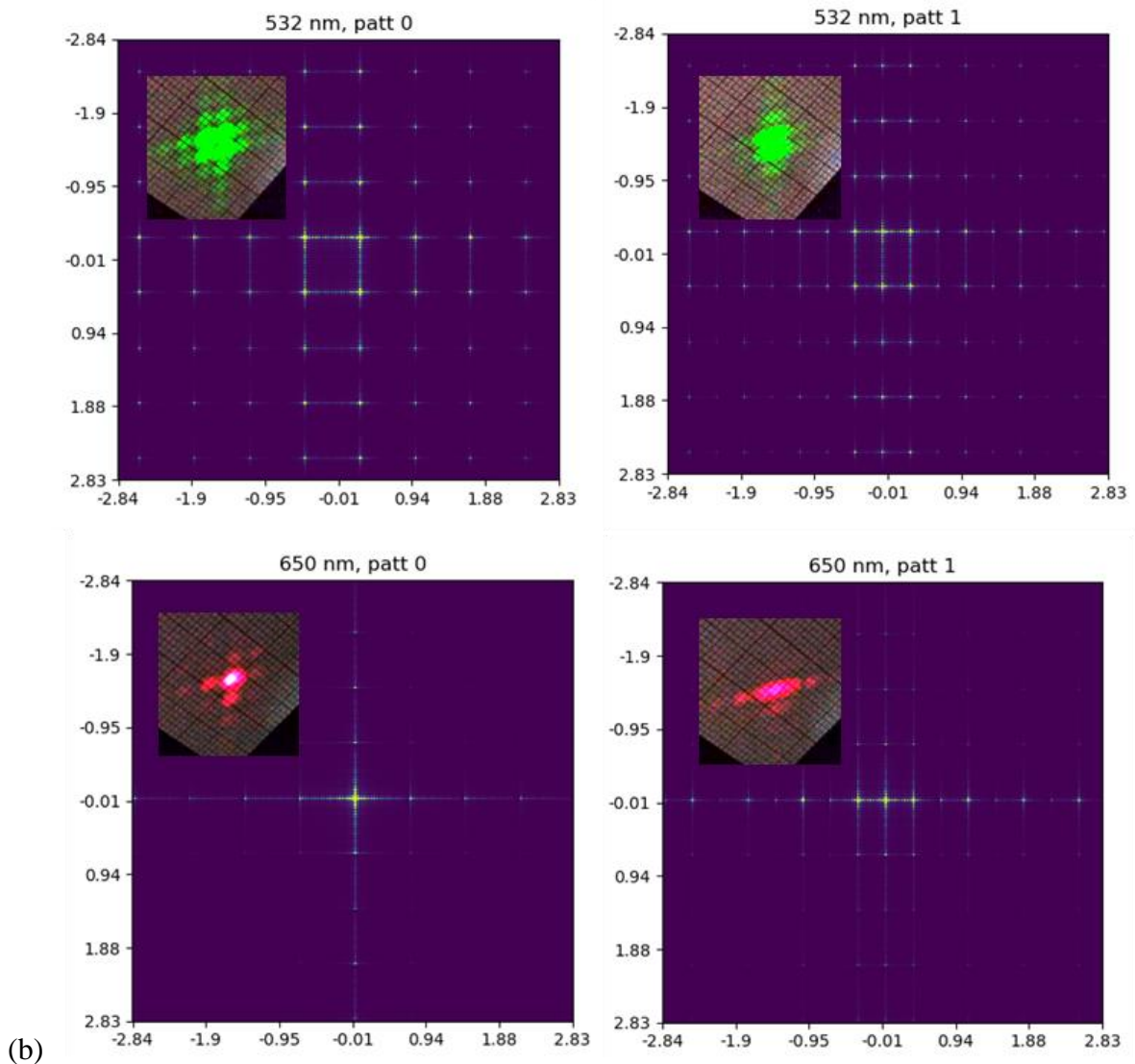
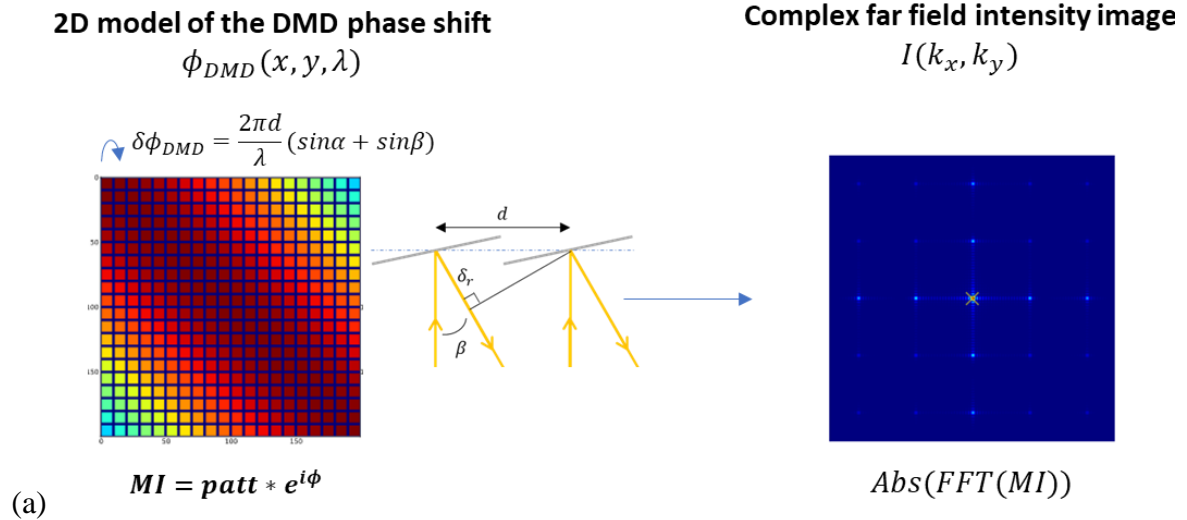


Figure 3-20: (a) DMD model as a complex transmission with a phase shift between all neighboring mirrors and resulting fast Fourier Transform, corresponding to the far field intensity image. (b) Far-field observed on the collection branch for patterns 0 and 1 with excitation at 532 and 650 nm and corresponding simulation.

3.II.4.b.3 Shading

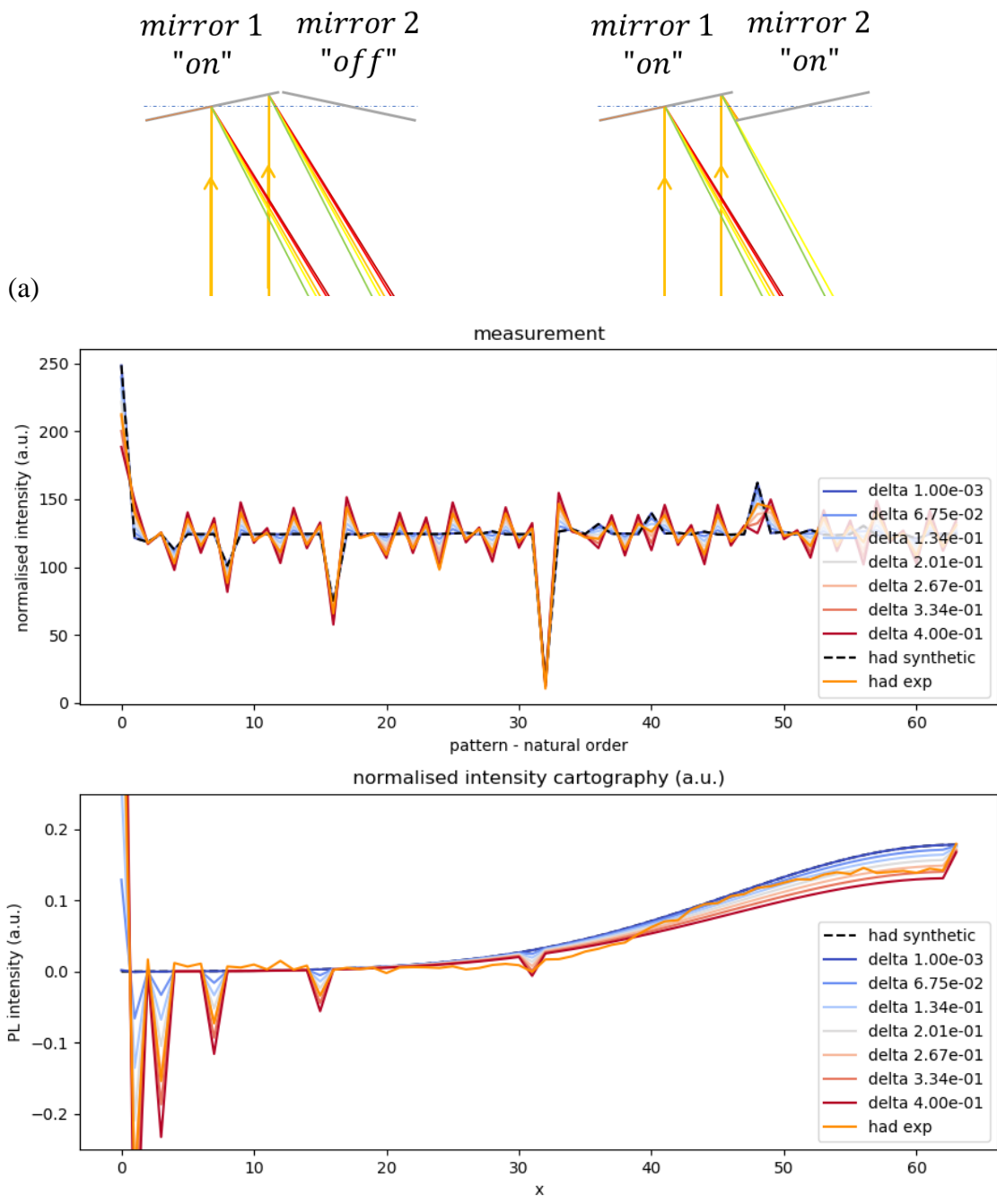


Figure 3-21 (a) Schematic of shading occurring when two neighbors are in the same position (b) Simulation of shading on a simulated data set and comparison with an experimental one.

The importance of transitions number artifact on the SPI reconstructed result has led us to hypothesize that neighboring pixels can affect the others. There is possibly some shading of mirrors, as illustrated in Figure 3-21(a): if consecutive mirrors are in the same direction, a part of it is obscured. On the scheme, colors are associated with the different output directions. Some of them are blocked, and they may avoid destructive interferences. In this way, partial obstruction of the signal would lead to its increase.

This hypothesis was simulated on synthesis data with 1D patterns. For two neighboring 1 in the Hadamard matrix, the second one is replaced by $1-\delta$, to simulate transmission of the second mirror reduced by shading. The synthetic object profile (black) is inspired by the actual streak measurements plot (orange line) for comparison. Synthetic measurements obtained for increasing δ are shown with colors from blue to red. They get closer to the experimental one when approaching $\delta \sim 0.1, 0.2$. The $2^n - 1$ artifacts appear so a shift in the last pixel value is observed on the experimental data. Furthermore, the apparition of negative peaks is concurrent with the global underestimation of the other pixels' values. These results seem to corroborate the presence of shading.

3.II.4.c Practical correction

As the combination of diffraction and shading make it hard to have a proper model of the artifact, a practical and pragmatic correction is implemented by fitting and retrieving the influence of the transition number on the collected intensity. Figure 3-22 shows the comparison between corrected and raw reconstruction. Pixels $2^n - 1$ seem indeed corrected, and pixel 0 remains an outlier.

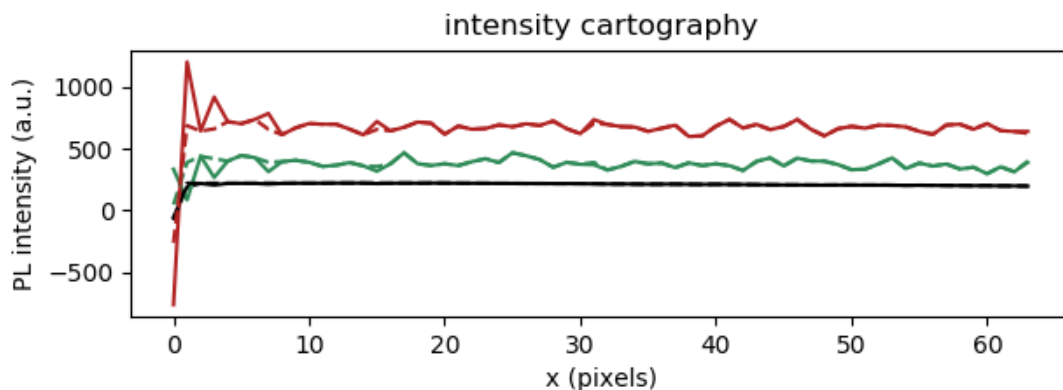


Figure 3-22: Correction of drift slope on 1D measurement. The corrected reconstruction is plotted in dashed lines and the initial in solid lines. Only the $2^n - 1$ pixels are modified.

1D patterns correction was generalized to 2D configuration, as presented in appendix C. If a correlation with the number of transitions is observed, noise is still notable in the associated reconstructions. This generalization is still preliminary, and metrics other than the transition number should be tried out. This work highlights key facts explaining why such a correction is not performed in the literature while it is required to process our data:

- When splitting is implemented, the negative patterns are affected by SPI artifacts similarly to the positive ones, providing compensation.
- In the case of 2D patterns, edge pixels seem mainly affected and are seldom of interest.

- A wider FOV of the DMD is usually employed with mirror binning. Then the number of transitions is closer to the ‘all on’ configuration, and the influence of the interferences is probably lower.
- If SPI is not implemented with a spectrally resolved detector, the sum of positive and negative slopes tends to reduce the artifact.

This correction approach provides an improvement, especially necessary for one-dimensional patterns. Further refinements could still be done to understand this phenomenon better and obtain a validated correction for 2D imaging.

This section describes the 4D-PL technical development, demanding care for each acquired dimension. Temporal encoding of the spatial dimensions is done at a much longer time scale than the detection ones. Oscillations of the mirrors are characterized, and the DMD is controlled, so they don’t impact the collected signal. The main limitations arise from the low sensitivity of the streak camera’s small etendue, which induces both low sensitivity and complex alignment. We implemented a collection into a fiber to ensure a fixed field of view and gain in tunability. Otherwise, the DMD acts as a blazed grating, so the spatial and spectral dimensions are entangled. A wide collection angle is necessary to collect the spectra continuously in all locations. Also, the change of patterns induces interferences varying the transmission. A correction method was developed to suppress their influence on linear patterns. Variations of the 4D SPI acquisitions were designed to allow sampling in the different dimensions at stake for broader light levels.

3.III Variations of 4D-PL workflow

This section introduces the two variations of 4D-PL imaging developed to reduce light sampling while maintaining spatial, spectral, and temporal components. We present the 2x3D approach that acquires hyperspectral and time-resolved images in parallel. SPI can be combined with a pixel clustering workflow to retrieve the temporal evolution of the decay in selected areas.

3.III.1 2x3D – Parallel hyperspectral by SPI and TRFLIM

3.III.1.a Overview

This setup simultaneously performs time-resolved and hyperspectral imaging, providing a faster and easier data acquisition than 4D-PL. It allows for less light dispersion and higher SNR characterization relevant when the spectrum is constant during the decay. The so-called 2x3D setup is shown in Figure 3-23. A 532 nm pulsed laser illuminates the sample. The

outcoming luminescence is filtered by a long-pass dichroic beam splitter and directed to two branches by another beam splitter. On the hyperspectral branch, the beam is focalized onto a DMD. The spatially selected light is collected and focalized into an Ocean Optics USB2000+ spectrometer. The collection into the fiber is performed with the same optics as the 4D-PL configuration. Switching between detectors simply requires plugging the entrance fiber into the connector set in the collection branch.

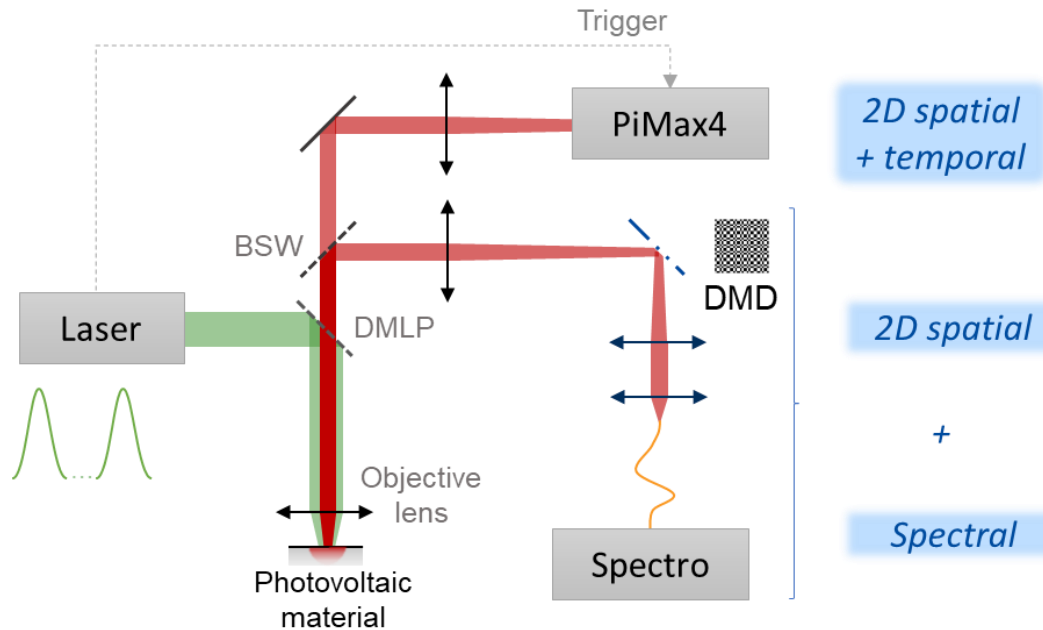


Figure 3-23: Scheme of the optical setup in 2x3D configuration, a TR FLIM branch (PiMax4) is in parallel with a hyperspectral one obtained by combining a DMD and a spectrometer. The laser is filtered out by a long-pass filter (DMLP650). The PL beam is separated into two branches by a beam splitter (BSW).

The ocean optics spectrometer measures the spectra between 200 and 900nm with an 8 nm resolution. Its entrance slits are fixed to a $200\mu\text{m}$ width, which is wider than those of the spectrometer associated with the streak camera (see 3.II.2.c). It has a far higher sensitivity due to a better quantum efficiency and dispersing less light. As a rule of thumb, signals that are not observable (i.e., less than 3000 counts) with this spectrometer at 100ms exposure time will not be detectable with the full 4D-PL configuration using the streak camera. This setup demands extra care about synchronization, as explained above in 3.II.1.c, and for comparing the acquisitions of the two branches.

3.III.1.b Parallelization to TRFLIM

TRFLIM and SPI branches have different fields of view and angles of vision. Indeed, if we note (x, y) the spatial reference frame of the sample, the beam splitter directed toward the TRFLIM creates a rotation to the y -axis. Conversely, the mirror on the DMD path induces a rotation about the x -axis, so the images formed on both branches are rotated relative to each

other. Otherwise, the imaging systems have a similar magnification; thus, the field-of-view ratio can be estimated by dividing the micro-mirror size by the photosite one (taking the eventual binning into account).

Figure 3-24 compares TRFLIM and spectrally averaged SPI images of the USAF-1951 calibration target in transmission. After two rotations and a FOV selection, the two maps show the number 1 featured on the target with a similar orientation and magnification. Indeed, cropping the TRFLIM to the DMD field of view can be done by a rule of three between the photosites and the binned mirror size, confirming the good alignment of the setup. For an easier qualitative comparison of the images captured by the two branches, the TRFLIM map is interpolated to the SPI spatial resolution, as shown in the bottom right. This approach is also used to compare the photoluminescence acquisitions obtained by the detectors. Rather than decreasing the number of pixels in the TRFLIM acquisition, it would be possible to use a data fusion algorithm similarly to Soldevila et al.³⁶ to increase the SPI spatial resolution. Figure 3-24 shows that the TRFLIM has imaged the stripes on the left of the number, whereas SPI didn't. It is due to the fiber collection, which is smaller than the pattern's surface area. The induced effective FOV is scaled from flatfield measurements and pictured by an orange circle. In many acquisitions, the patterns are displayed with a size comparable to the orange circle to avoid collecting unnecessary dark signals.

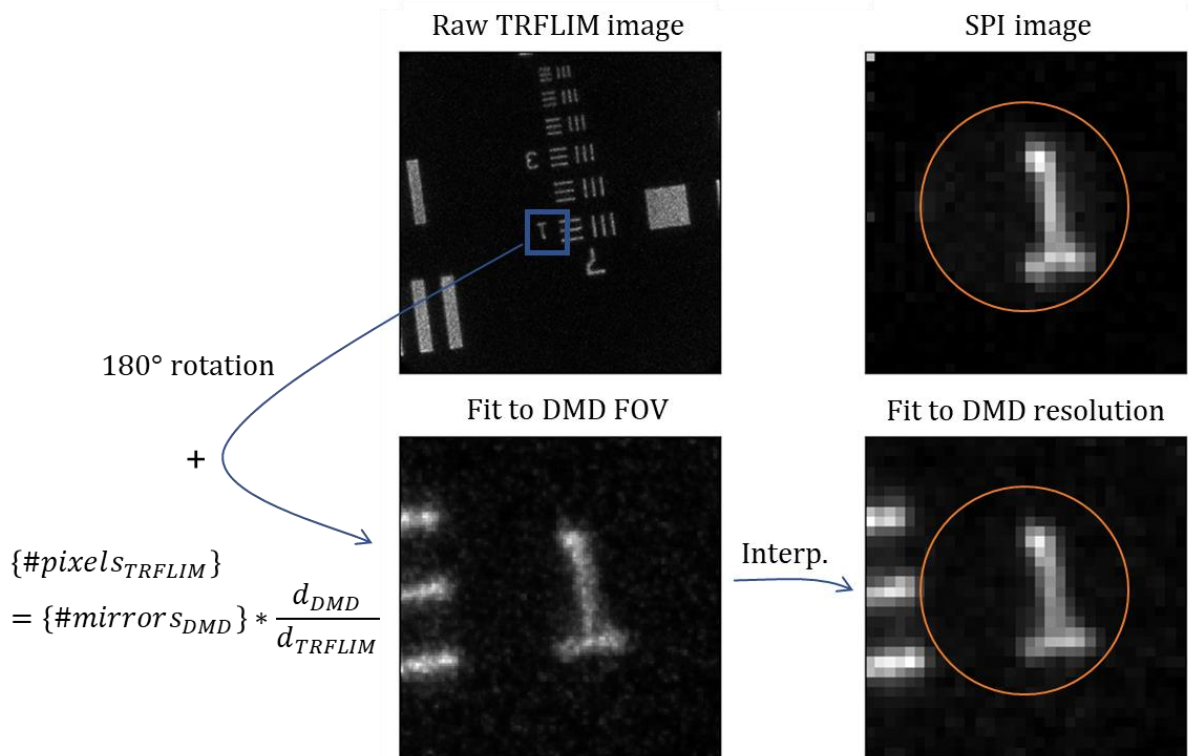


Figure 3-24: Comparison of TRFLIM and Hyperspectral-SPI images. The image obtained on the TRFLIM is rotated twice to the right and cropped to fit the area imaged by SPI. The actual FOV (determined by the fiber diameter) is schematized by the orange circle and extrapolated from a flatfield acquisition.

The setup was sometimes used with a mirror instead of a beam splitter to perform sequential TRFLIM and HI measurements. In such a configuration, the position of the mirror reflecting towards the TRFLIM is not reproducible, and the field-of-view is slightly moved. This shift is enough to be detrimental to the superposition of the two acquisitions and should not be used.

3.III.2 Pixel clustering applied to the 4D-PL acquisition

3.III.2.a Method workflow

This experiment proposes a novel sampling method of PL intensity in the spatial, temporal, and spectral dimensions. It aims to measure both a hyperspectral image and PL's spectral decay in different strategic regions of the sample, as illustrated in Figure 3-25(c), thus improving the signal-to-noise ratio and facilitating analysis. In the following, we will refer to this experiment as 4D clustering, as it relies on clustering algorithms in the spatial dimension. Clustering is also called “segmentation” in the literature or other scientific fields.

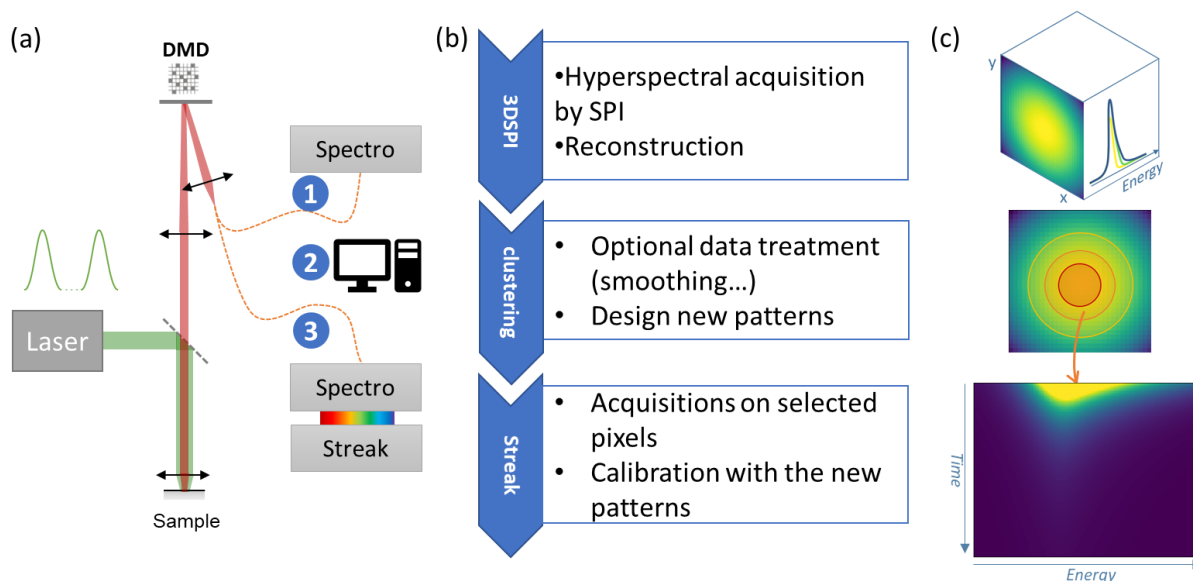


Figure 3-25: (a) Scheme of the 4D-PL setup, (b) Flow of pixel clustering, (c) Associated data. In the first step, the spectrometer is set on the DMD collection to reconstruct a hyperspectral image of the sample by SPI. Clustering algorithms process this acquisition to determine regions of interest. New patterns are generated for each area as the red, orange, and yellow circles shown in (c). They are sequentially displayed, and a streak camera acquisition is performed for each, providing the information without needing reconstruction.

By typically relying on four streak acquisitions instead of 64, clustering allows time-resolved spectroscopy shot noise SNR improvement by a factor higher than 4 for multiplicative noise compared to SPI or an acquisition time reduced by a factor of 16. Thus, it extends the scope of streak spatialization to various samples and makes lower excitations possible. Clustering or binning can be applied during data treatment in multidimensional imaging, and

the following approach allows us to perform it at the acquisition step. If it requires fewer acquisitions, it also questions determining relevant areas. We use focused illumination and group pixel with similar intensities in the following examples. It would also be possible to choose locations with similar spectral shapes and peak maxima or imagine a clustering way to thoroughly exploit the three hyperspectral dimensions.

Figure 3-25(a) shows the associated setup. The sample is illuminated with a 35 ps 532 nm pulsed laser. The outgoing light is filtered by a short pass beamsplitter, magnified with an objective lens, and then focalized onto a digital micro-mirror device that modulates it spatially. The spatially selected light is collected and focalized into a photodetector. It can be either the ocean optics USB2000+ spectrometer or the Princeton HRS300 spectrometer coupled to the Hamamatsu C10910 streak camera used in the previous setups. Thus, the obtained hyperspectral image will have an 8 nm spectral resolution and micrometric spatial resolution. As a reminder, this detector can achieve transient spectroscopy with a sub-nanometer and down to 16ps resolution.

The measurement follows the three steps illustrated in Figure 3-25(b). At first, a hyperspectral acquisition is performed using SPI. Then, the map of PL intensity averaged spectrally is used to determine the new areas by clustering the pixels of similar values. Patterns are generated for each of these areas. For instance, the mask corresponding to the orange area in Figure 13(c) is designed with all the micro-mirrors it covers directed toward the detector and not the others. This new set of masks is sequentially displayed on the DMD and used to acquire spectral decays in the chosen areas.

3.III.2.b Clustering implementation

The implementation of pixel clustering algorithms in the DMD control code was realized by Claire He during her Master 1 internship³⁷. We studied four of the methods available for image clustering: K-Means, DBSCAN, OPTICS, and Spectral Clustering, all based on Scikit learn library. As the K-means provided satisfactory results and was the only one used to obtain experimental data, we refer the reader to Scikit learn documentation for further information on the other algorithms.

The k-means algorithm divides the data into groups of equal variances by minimizing the inertia, i.e., the distance of the elements within the clusters from the cluster mean (called centroid). The number of clusters can be chosen freely or reasonably determined by the "elbow method". This number is generally considered locally optimal when increasing the number of clusters does not significantly improve the segmentation, which would consequently decrease the slope on the distortion curve. This quantity is the sum of the Euclidean distance between pixels' true value and the mean intensity of the cluster. It is illustrated in Figure 3-26 by

clustering the pixels of the reference image (a): in the example output (c), 12 clusters are imposed with a difficult-to-read result. The elbow method actually indicates that fewer clusters are sufficient to segment the image.

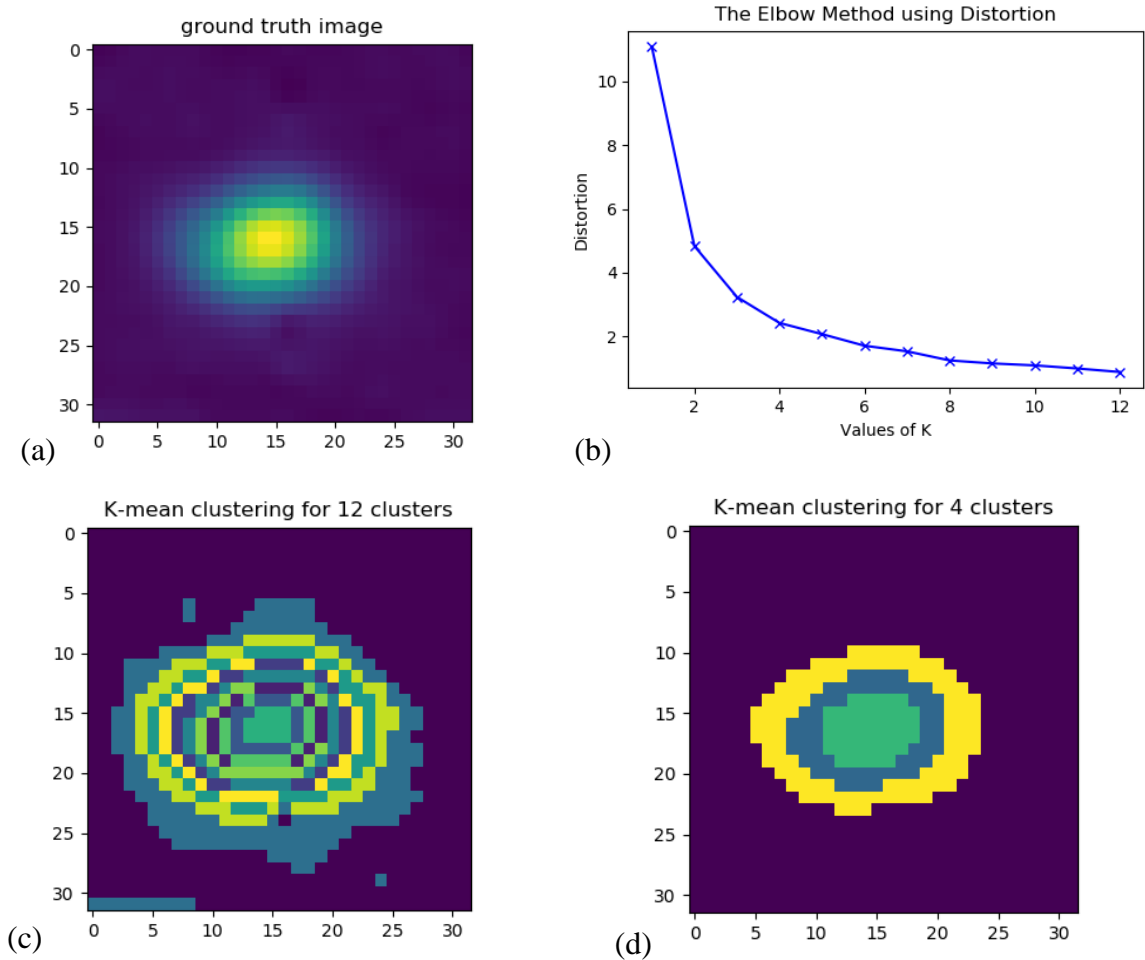


Figure 3-26: Example of clustering on experimental data with a different number of clusters. (a) ground truth image, (b) Elbow figure to determine an appropriate number of groups, (c-d) clusters determined by K-means by imposing 12 and 4 bins, respectively.

One has to remember that from a physical point of view, it can still be interesting to consider more clusters than the number indicated by the elbow method or change the image's dynamic. If more contrast is sought in the high-intensity parts, it is possible to run the clustering algorithm on the squared-intensity image. On the contrary, if low-intensity regions are of major importance, the PL logarithm or root square can be used as a reference. Other works on adaptative patterns were realized, allowing the study of either linear or punctual illumination. Their scope is more limited (as it supposes to be a perfect shape) and not detailed here. Images usually obtained after SPI can present artifacts, as presented in 3.II and due to the absence of calibration. Ways to improve the setup and reduce it are presented in Appendix D, a gaussian smoothing is sufficient to obtain a good representation of the PL intensity.

Conclusion

We have developed a novel characterization that simultaneously measures spectral, temporal, and spatial variations of PL intensity. This 4D-PL bench is based on a high-resolution streak camera coupled to a spectrometer and retrieves spatial information through single-pixel imaging. By construction, it strongly favors spectral and temporal information over spatial one compared to the other possible designs presented in the previous chapter.

Practical implementation of this approach introduces additional constraints and challenges. When it comes to the development of a multidimensional setup, attention must be paid to any component. The system must reconstitute all dimensions at best, and a trade-off between them emerges. Indeed, the spatial information is encoded by a DMD that induces diffraction, mixing the dimensions. The optical design reduces the influence of ‘all on’ mirror configuration, and the impact of the superordinate arrangement of micro-mirrors is empirically corrected.

Furthermore, in turn to the outstanding temporal and spectral resolutions, the detector has low sensitivity, even for an optimized collection. Given the low light intensity at stake in PL measurements and the time constraints associated with them (for stability’s sake), the number of bins in the spatial dimension must be reduced. In practice, it went as high as 64 pixels, corresponding to a spatialization of time-resolved spectroscopy rather than imaging. Variations of the 4D-PL routine, such as pixel clustering, have been proposed to expand its scope to other samples. Both are novel approaches promising for characterizing a wide range of phenomena, from optoelectronic transport of the carriers to transfers to localized states.

Chapter 4 - Demonstration of 4D-PL and its variations on photovoltaic devices

"When performing optical measurement with a limited photon budget, it is important to assure that each detected photon provides as much information as possible."

— Gao, L. & Wang, L. V. **Physics Reports** 616, 1–37 (2016).

Following the explanation of how 4D-PL and its variations are implemented, this chapter presents their application to PV material characterization.

Perovskites optoelectronic are known to evolve under illumination because of ionic migration. Section 4.I present a light-soaking study on a triple cation sample performed by hyperspectral imaging in parallel with TRFLIM. This setup, highly relevant when no temporal spectrum evolution is expected, allows fast acquisitions and monitoring at the minute scale of decay and spectra. The impact of focused illumination is investigated on a wider area thanks to imaging.

Then, section 4.II provides an example of 4D-PL application to a III-V wafer in high injection conditions. Joint variations of the photoluminescence signal are observed in the spatial, temporal, and spectral dimensions. Their correlations and origins are first discussed with a simplistic physical model, then based on the experiment's observables. The effects of carrier and lattice temperatures, band-filling, and optical transport are discussed.

Finally, the pixel clustering-based variation allowing the acquisition of the spectral decay in areas of interest is demonstrated in section 4.III. Examples of diverse samples are shown: III-V wafer, fluorophores, and perovskites are probed. They highlight the broad applicability of this technique and its capacity to characterize various physical mechanisms.

4.I Application of 2x3D to perovskite light-soaking study

The 2*3D setup simultaneously provides PL dynamics and material properties and offers a promising tool for studying light-induced mechanisms in perovskite. They are indeed known to change both properties, as highlighted by a short literature review. This section examines the impact of localized illumination on a broader area for two different fluences. As a perspective, the interpretation of spectral data in the transient regime questions its comparison with the steady-state.

4.I.1 Perovskites, a photosensitive photovoltaic material

Perovskite absorbers are sensitive to external stress and are particularly modified by illumination. Light induces ion migration within the material that can cause either an enhancement or a decrease in device efficiency¹, a phenomenon referred to as **light-soaking**. Indeed, it can lead to segregation, material degradation, and a screening of the electric field within the bulk². However, beneficial defect passivation has also been observed. The effect of light exposure depends dramatically on the experimental conditions¹: factors such as illumination intensity and spectrum, temperature, applied bias³, and atmosphere have shown to play a role. Behaviors also vary with the sample composition and device structure⁴.

Ionic migration is associated with changes in optoelectronic properties modifying PL intensity, spectra, and decays. In-situ PL images can show the local effect of light-soaking, varying between grain and boundaries³. Time-resolved measurements allow monitoring changes in surface or bulk recombination as well as variation of carrier mobility. For instance, they supported the interpretation of light-soaking as a reduction of traps at the interface during the first minutes of illumination in different studies^{3,5}. In the work of Cacovich et al., hyperspectral imaging also highlighted trends on various time scales. It showed a quasi-Fermi level splitting increase during the first dozen minutes of light-soaking followed by a bandgap energy drop during hours⁵. Such measurements highlighted defect healing and subsequent phase segregation induced by illumination. The understanding of light-soaking can be further deepened with streak measurements. The temporal evolution of the emitted spectrum showed different dynamics depending on the phase, revealing an energy transfer to the surface of the emitter⁶.

Thus, PL provides a diagnostic tool and helps identify the light-soaking underlying mechanisms so as strategies to tackle or favor it. Particularly, it was combined with DFT^{1,7} to offer an explanation from the atomic to the macroscopic scale. In that frame, Motti et al.¹ showed that the under-coordinated surface sites act as defect reservoirs, and targeting its passivation paves the way to control the light-soaking effect.

To summarize, light-soaking encompasses many competing phenomena, ranging from the influence of the bias, the chemical reactions, and the temperature increase caused by the illumination. Simultaneously gathering the spectral and time-resolved imaging can help understand the effects at stake.

4.1.2 Experimental protocol

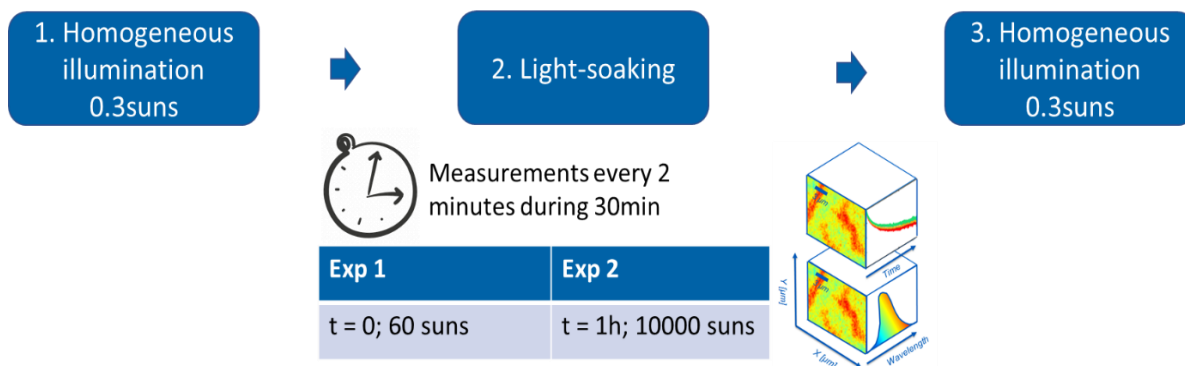


Figure 4-1: Approach followed to monitor perovskite light soaking with the 2x3D setup. In the first step, a reference image of the perovskite is taken under homogeneous illumination. TRFLIM and hyperspectral acquisitions are taken every two minutes in focused illumination at different intensities before taking a new image under homogeneous configuration.

We monitored the effect of laser illumination on a thin layer of mixed lead-halide triple cation perovskite $\text{Cs}_{0.05}(\text{MA}_{0.14}, \text{FA}_{0.86})_{0.95}\text{Pb}(\text{I}_{0.84}, \text{Br}_{0.16})_3$ by experimenting with three steps. A first reference acquisition is performed by both SPI-hyperspectral and TRFLIM imaging in homogeneous illumination at 0.3 sunsⁱ. Then, the sample is set under point-like lighting for 30min and imaged every 2 minutes by the two detection branches. At last, another set of acquisitions is performed under 0.3 suns homogeneous illumination to monitor the changes. We conducted two series of experiments at one-hour intervals on the same sample with point-like illumination at 60 and 10 000 suns to investigate the effect of the fluence. During this process, the perovskite thin film was kept under gaseous nitrogen at 20°C. It is thus possible to observe the influence of the punctual light soaking on a broader area of the perovskite. We will discuss the experimental results in the next section.

ⁱ In this section, the illuminations are expressed in equivalent suns, considering 1sun=1000 kW/m² for the temporally averaged power.

4.I.3 Results and discussion

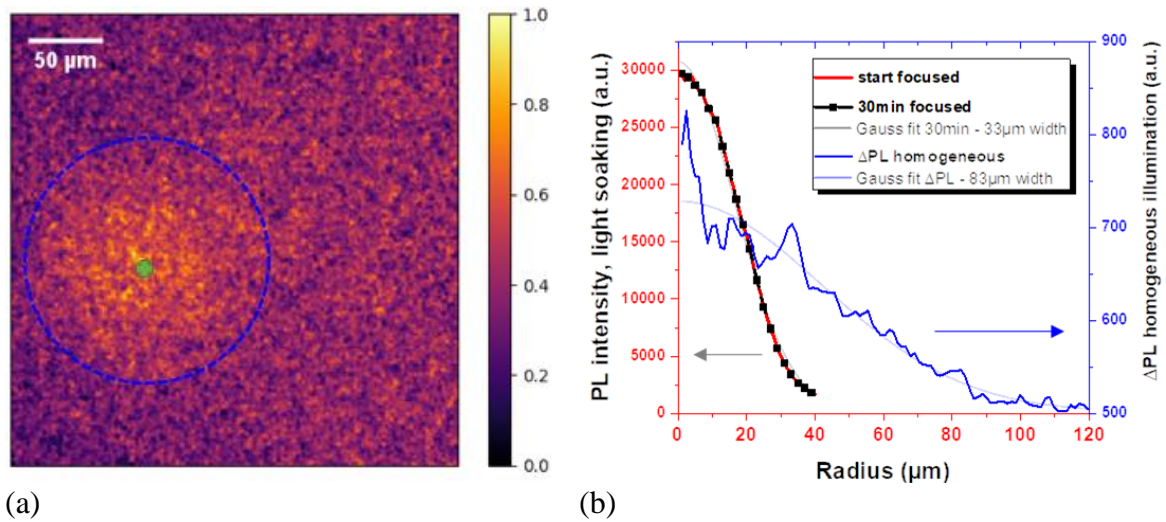


Figure 4-2: (a) ΔPL , normalized variation in PL intensity observed in homogeneous illumination induced by light soaking punctually at 60 suns (averaged on time, after-before). A green spot indicates the focused laser spot, and an indicative radius of PL enhancement is figured in blue. (b) Comparison of PL intensity profiles in punctual illumination with ΔPL (After-Before) averaged radially for homogeneous illumination.

We first look at the global impact of point light-soaking at 60 suns on the material. Figure 4-2(a) shows the evolution in PL intensity obtained on the TRFLIM with a homogeneous illumination (averaged temporally). An increase can be seen on a wide area around the beam pictured by a green cross. The blue circle indicates the region on which the PL intensity is averaged radially. Its variations are shown in Figure 4-2(b), along with the stable PL intensity acquired during the monitoring in punctual illumination. A peak in the center can be observed and is attributed to inhomogeneities of the perovskite sample, as brighter spots can also be seen in Figure 4-3(a). An offset of 500 counts is attributed to a slightly higher incident intensity in the second homogenous measurement rather than a long-scale light-soaking effect. Indeed, homogeneous illumination is obtained by magnifying the laser spot on a rotating diffuser, and the magnification factor highly depends on the element positions. PL intensity may vary greatly because it depends on the squared excitation fluence. The PL intensity increase cannot be quantified; however, its spatial extent can still be measured. Indeed, light-soaking in point-like illumination exacerbated photoluminescence observed later for homogeneous illumination over an 83 μm width gaussian surface. It is much broader than the 33 μm wide one in which carriers are generated. This rise is significant on lengths far longer than the laser radius (below 5 microns) or the carrier diffusion lengths in halide perovskite. Indeed, literature has reported diffusion lengths for halide perovskites up to dozens of micrometers⁸; we rather expect values close to the 1.4 μm reported for the composition characterized in this study⁹.

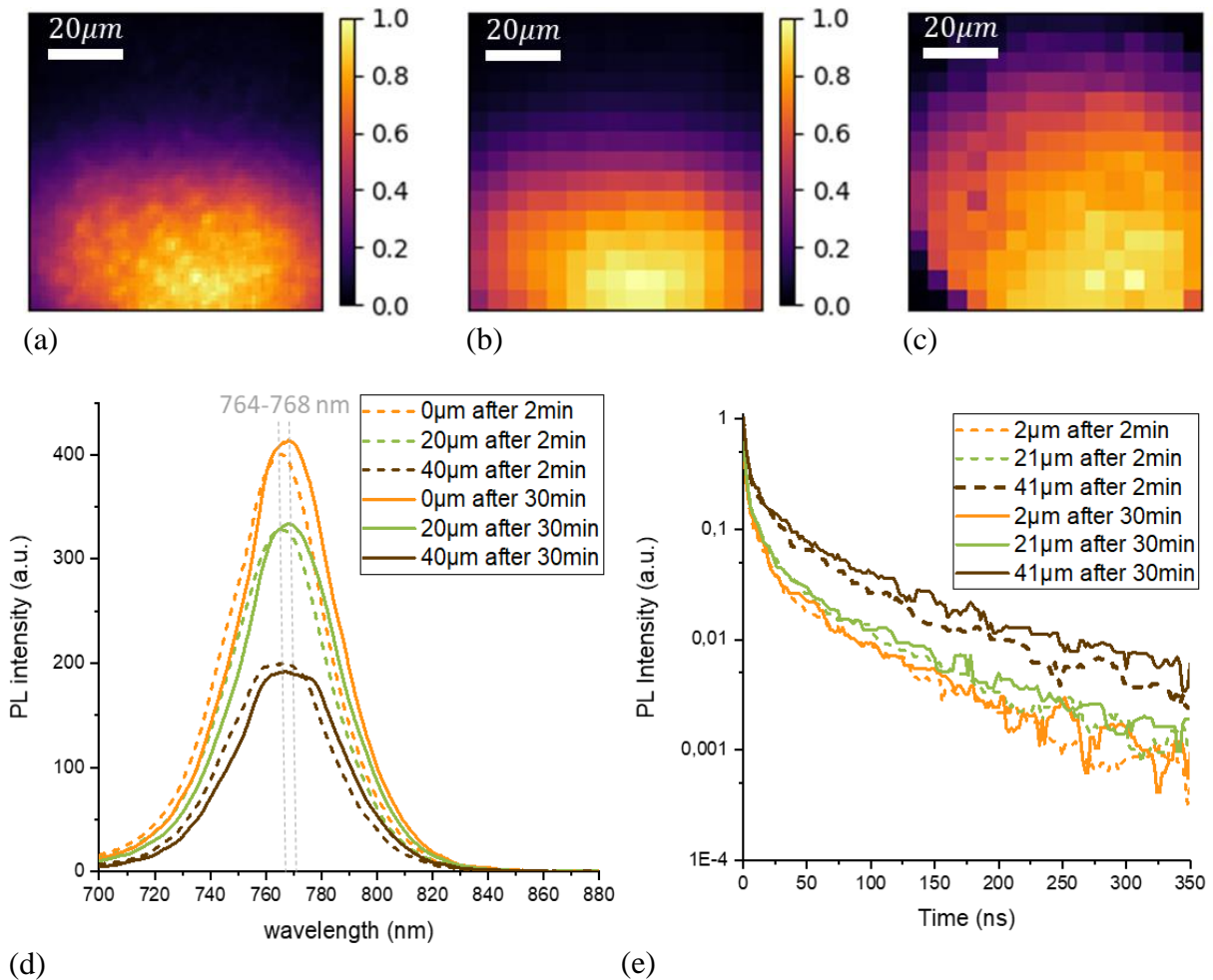


Figure 4-3 : (a) Normalized TRFLIM acquisition averaged on time after 2 min of light-soaking, and (b) Extrapolated to pixels size of the SPI. (c) Normalized hyperspectral by SPI averaged spectrally at 2 min of light-soaking. (d) PL spectra for different radii r from the center at the start (dashed lines) and the end (solid lines) of light soaking under focused illumination at 60 suns, the grey dashed lines are guides for the eye at 764 and 768 nm (e) Normalized PL decays for the same locations and times.

Data from the TRFLIM and HI acquisitions taken along the light soaking are shown in Figure 4-3. Integrating the hyperspectral data obtained by single-pixel imaging is consistent with the time-resolved photoluminescence acquisition averaged over time, as seen in Figure 4-3 (a) and (c). The dark bottom-left corner is a consequence of the circular field of view of the hyperspectral branch. Brighter spots with a few microns width can be identified on the TRFLIM image, which is close to the 4.9 μm pixel size used in SPI and is too large to resolve them. Indeed, the TRFLIM image extrapolated to a 16x16 image illustrated in Figure 4-3(b) does not show these features.

The PL spectrum and decay emitted after 2min of light-soaking under punctual illumination are compared to the one obtained after 30min. Figure 4-3(d) presents the spectra averaged for different radii: at 20 and 40 μm. A similar 3nm-redshift with time is observed in

the three locations. Spectra shapes feature humps that suggest the contribution of different species to photoluminescence, particularly at large radii.

The PL intensity decays were monitored for the same areas and pictured in Figure 4-3(e). Decays have shorter characteristic times in the center than in the external sites, and different factors contribute to this mechanism. By noting 1, the region with a higher carriers density and 2, the lower one, as in Figure 4-4, their dynamic can be estimated through rate equations as introduced in Chapter 1.II. They are considered of equal surfaces and isolated.

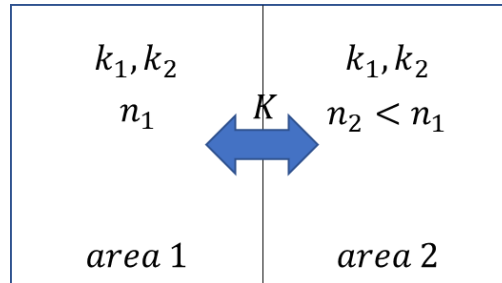


Figure 4-4: System considered for rate equation model

The coefficient for first-order and second-order recombination is considered constant and is written k_1 and k_2 , respectively. We consider that these areas are wide and thus that diffusion between them can be neglected. Indeed, for a similar perovskite composition, Bercegol et al.¹⁰ have measured a diffusion length of $0.54\mu\text{m}$, which is small compared to the radii at stake in this experiment. The further presence of photon recycling within each of these areas can be taken into account by considering k_2^* , the external radiative coefficient. An additional term traduces the share of photons emitted in region 1 which are recycled in area 2. This number is thus proportional to n_1^2 , written with a factor K . By symmetry, this factor also applies for recycling of photons emitted in region 2 in the area 1. It reads:

$$\frac{dn_1}{dt} = -k_1n_1 - k_2^*n_1^2 + Kn_2^2 \quad (4-1)$$

$$\frac{dn_2}{dt} = -k_1n_2 - k_2^*n_2^2 + Kn_1^2 \quad (4-2)$$

By noting the initial carrier concentration $n_{0,1}$ and $n_{0,2}$, decay at $t=0$ are:

$$\tau_0(1) = -n_{0,1} \left(\frac{dn_1}{dt} (t=0) \right)^{-1} = \frac{1}{k_1 + k_2^*n_{0,1} - Kn_{0,2}^2/n_{0,1}} \quad (4-3)$$

So that:

$$\frac{1}{\tau_0(1)} - \frac{1}{\tau_0(2)} = k_2^*(n_{0,1} - n_{0,2}) + \frac{K}{n_{0,1}n_{0,2}} (n_{0,1}^3 - n_{0,2}^3) \quad (4-4)$$

As $n_{0,1} > n_{0,2}$, both terms on the right contributed to having $\tau_0(1) < \tau_0(2)$. Therefore, the difference in the dynamic in the two regions at short time is already expected as a consequence of second order recombination. The additional exchange term increases this disparity, and contributes to the increase in initial decay time with radius shown in Figure 4-5(a).

Decays highlight different trends if the spectral change is witnessed with time in all locations. Indeed, no significant difference in the PL dynamic is observed between 2 min and 30 min of light-soaking for the center of illumination. This suggests that the evolution of the carrier dynamic happens quickly in less than two minutes of lighting in this area. However, we can see a slight improvement in the PL decay time for a longer radius. Different hypotheses can stem from this location-dependent improvement: the relative increase might depend on the charge carrier concentration or gradient. It could also require a time for diffusion of the ions from the center to the exterior of the illuminated area. Also, the healing can be sensitive to either PL intensity or gradient.

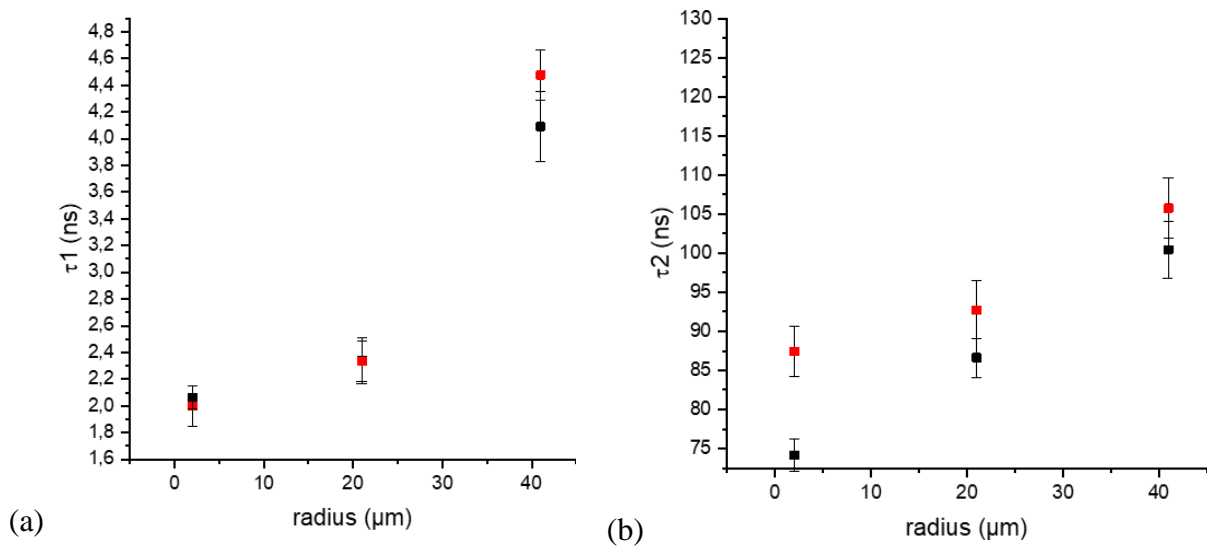


Figure 4-5: Decay times obtained from monoexponential fits at a short time $< 10\text{ns}$ (a), and at a longer time, between 125 and 250ns (b). Dark markers correspond to 2mn of light soaking, and red represent the data obtained after 30min .

When performing light-soaking at $10\,000$ suns, we observed the formation of a darker and a brighter area with different spectrum wavelengths pictured in the insert of Figure 4-6(a). They are created quickly after illumination and are visible from the first TRFLIM acquisition. Interestingly, similar spots were observed on different samples during the preliminary experiments, and the dark one is located aside from the illumination.

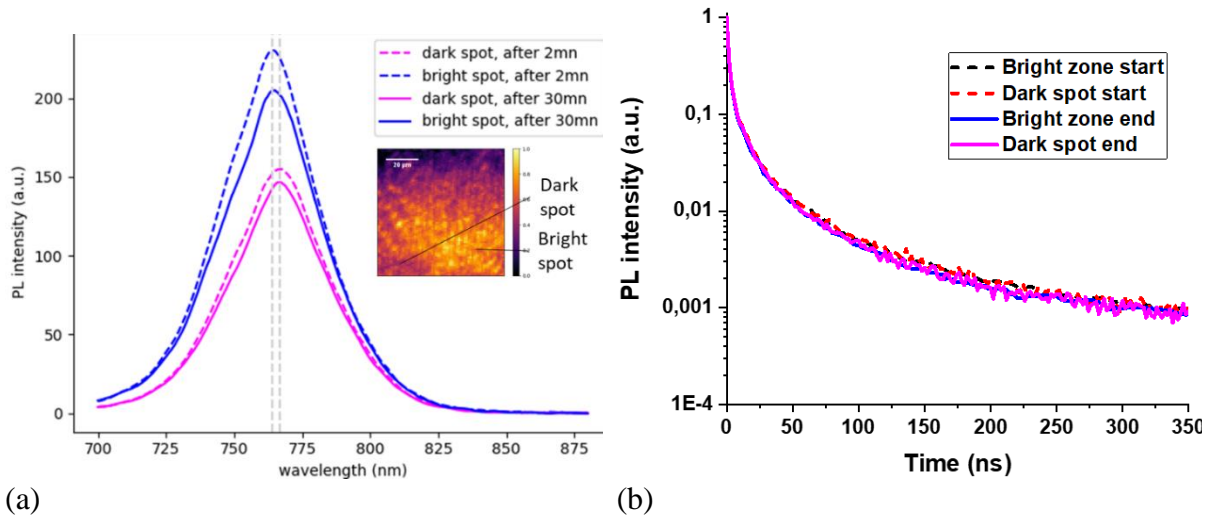


Figure 4-6: (a) PL spectra and (b) decays spatially averaged on the dark spot and the bright one during punctual illumination at 10000 suns.

Contrarily to light-soaking at 60 suns, the PL dynamics stayed stable during the experiment. One can see in Figure 4-6 that the intensity decay is slightly reduced after 30mn illumination. Yet, fitted decay time falls within the same uncertainty interval for $\tau_1 = 2.25 \pm 0.05$ ns. Also, τ_2 is between 120 and 130ns. However, the peak wavelength varies by location: it corresponds to 764 nm and 767 nm in the bright and dark spots, respectively. These two regions have different PL intensities with similar dynamics. Moreover, the PL intensity is lower after light soaking; the sample is degraded at 10000 suns illumination. We can make the hypothesis of spatial phase segregation. Given the illumination intensity, the degradation is relatively low under nitrogen. Indeed, the PL fluctuations can be much higher for other conditions and samples, with the signal divided by two folds in the first minutes of acquisition.¹

In this experiment, single-pixel imaging provides hyperspectral images from a spectrometer. Developed in parallel with a time-resolved photoluminescence imaging setup, it simultaneously opens the way to characterize charge carrier transport and the electronic state distribution. That allows us to investigate light-soaking under focused illumination by obtaining the spectral and temporal PL intensity at different distances from the light spot. Particularly, it can distinguish changes that are not significant on the average intensity but visible in either spectral or temporal dimensions. This experiment is the first step toward 4D-PL imaging by performing single-pixel imaging with a streak camera coupled to a spectrometer as a photodetector. Characterizing light-soaking with 4D-PL would be of interest, as demonstrated by Andaji-Garmaroudi et al.⁶: they observe joint decay time increase and redshift (the same qualitative behavior as in the 60 suns illumination), and streak acquisitions allow them to clearly identify two peaks and characterize energy exchanges between the corresponding phases. However, 4D-PL acquisition time is too long to monitor light-soaking, and the material change

during the experiment would be detrimental to reconstruction. We rather apply this technology to a stable sample.

4.1.4 Perspective: How can we compare steady-state and transient experiments?

If the analysis of spectra emitted in steady-state is well established, how to compare it with the transient one still raises questions. In a transient regime, dynamic phenomena may affect the emitted spectrum, which can thus be characterized by transient spectroscopy or complexify the interpretation. To illustrate the difference between the information brought by photoluminescence intensity in transient and steady-state regimes, we monitored a perovskite sample's photoluminescence signal for about two weeks. The stack under study comprises FTO/TiO₂ compact/TiO₂ mesoporous/Perovskite/PTAA/ITO bilayer and corresponds to a semi-transparent device. Photoluminescence measurements are led in continuous waves (CW) and under pulsed illumination to monitor the sample evolution after the electrode is sputtered. Indeed, IV curves feature an S-shape that disappears within a dozen days. Its resorption allows an increase in the device's efficiency. Along ageing, PL intensity under continuous illumination is almost multiplied by a factor of 10, as shown in Figure 4-7(a).

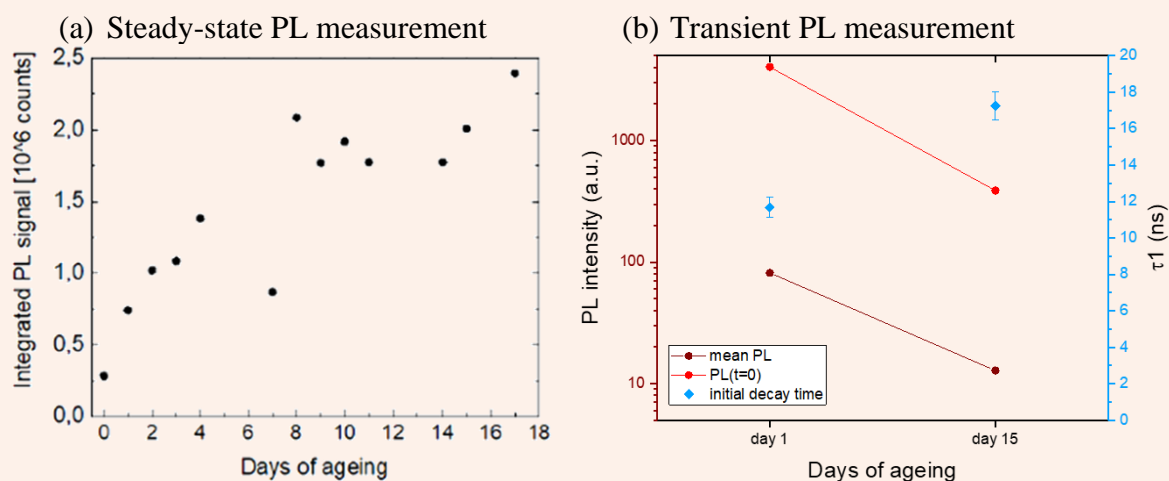


Figure 4-7: (a) Evolution of photoluminescence intensity in steady-state, integrated spectrally (©Alexandra Levtchenko) (b) Variation of indicator in transient regime: mean and initial intensities and decay time obtained by monoexponential fitting of the decay the first 20ns after the laser pulse.

The transient regimes show the reverse trend as initial and temporally averaged intensities are almost divided by the same factor, as illustrated in Figure 4-7(b). Here, these two values bring different information, and the increase in steady-state intensity is likely to be linked to an increase in the decay time τ_1 calculated between the laser pulse and 20ns. One can note that no major change is observed for the decay at long times after the pulse (200-300ns) that stays at 105 ± 18 ns. Indeed, at constant carrier density generation, we expect

the photoluminescence intensity to depend on the decay time. We take the simple model of rate equation with first order recombination described by τ_{eff} , so that:

$$\frac{\partial n}{\partial t} = -\frac{n}{\tau_{eff}} + A\Phi \quad (4-5)$$

The equations integrated over depth are shown in Table 1. We expect the intensity to scale with the squared decay time for intrinsic perovskite absorbers. With $\tau_{eff} = \tau_1$, the initial decay time increase would induce a photoluminescence growth by a factor of $(\tau_1[day15]/\tau_1[day1])^2 \sim 3$. Also, this model suggests similar trends for the intensity in steady-state and with the temporally average time-resolved one. The different evolutions observed experimentally might be due to dynamic phenomena saturated in continuous illumination, as carrier transient trapping by shallow electronic defects¹¹. The joint efficiency improvement leads to the hypothesis of an extraction improvement, which might be caused by the healing of charged defects at the interface. Their mitigation would lower the barrier for extraction and could increase decay time.

Table 1: Comparison of carrier densities integrated over depth in transient and steady-state regimes, Φ names the photon flux [ph/cm²/s] and rr the laser repetition rate

Steady-state	Time-resolved	
n	$n_0 = n(t = 0)$	$n_{avg} = 1/T \int n(t) dt$
$\int n dz = \tau_{eff} A\Phi$	$\int n_0 dz = A\Phi/rr$	$\int n_{avg} dz = \tau_{eff} A\Phi$

Thus, PL intensity in both regimes has a different dependence on dynamic mechanisms. What is the situation with the spectral shape? Transient spectra are obtained with a time-dependent carrier profile and injection, which might not be comparable to the steady-state one. We illustrate this with a drift-diffusion simulation comparing both regimes. It first raises the question of the injection level. Are incident power, photon flux, or energy supposed to be equal? The previous calculation suggests that similar energies would be comparable.

Table 2: Light flux for drift-diffusion simulations, performed with 80ps pulse for TR

Pulsed 80MHz, « reference »	$0,5 * 10^{12} \gamma/pulse$	$4 * 10^7 \gamma/s$
Pulsed 1MHz	$0,5 * 10^{12} \gamma/pulse$	$5 * 10^5 \gamma/s$
CW "low injection."		$4 * 10^7 \gamma/s$
CW "high injection."		$2 * 10^{17} \gamma/s$

The tested parameters are shown in Table 2; we model a sample with inputs similar to Ioffe¹² gallium arsenide except for a low mobility set to $1\text{cm}^2/(\text{V}\cdot\text{s})$. Figure 4-8 shows the resulting carrier profiles: the evolution of transient regimes is displayed by the color line from blue (laser pulse) to red (end of the decay). It is compared to steady-state profiles at injections corresponding to the averaged or peak powers. Resulting carrier profiles are shown in Figure 4-8(a); they depend on the injection level for a steady-state regime and evolve dramatically with time in transient. They have no reason to coincide except in limited cases (for instance, if diffusion is high and surface recombination is negligible, leading to homogeneous profiles). The modification in the photoluminescence emission in-depth induces spectral changes as the contribution of reabsorption varies, as shown in Figure 4-8 (b).

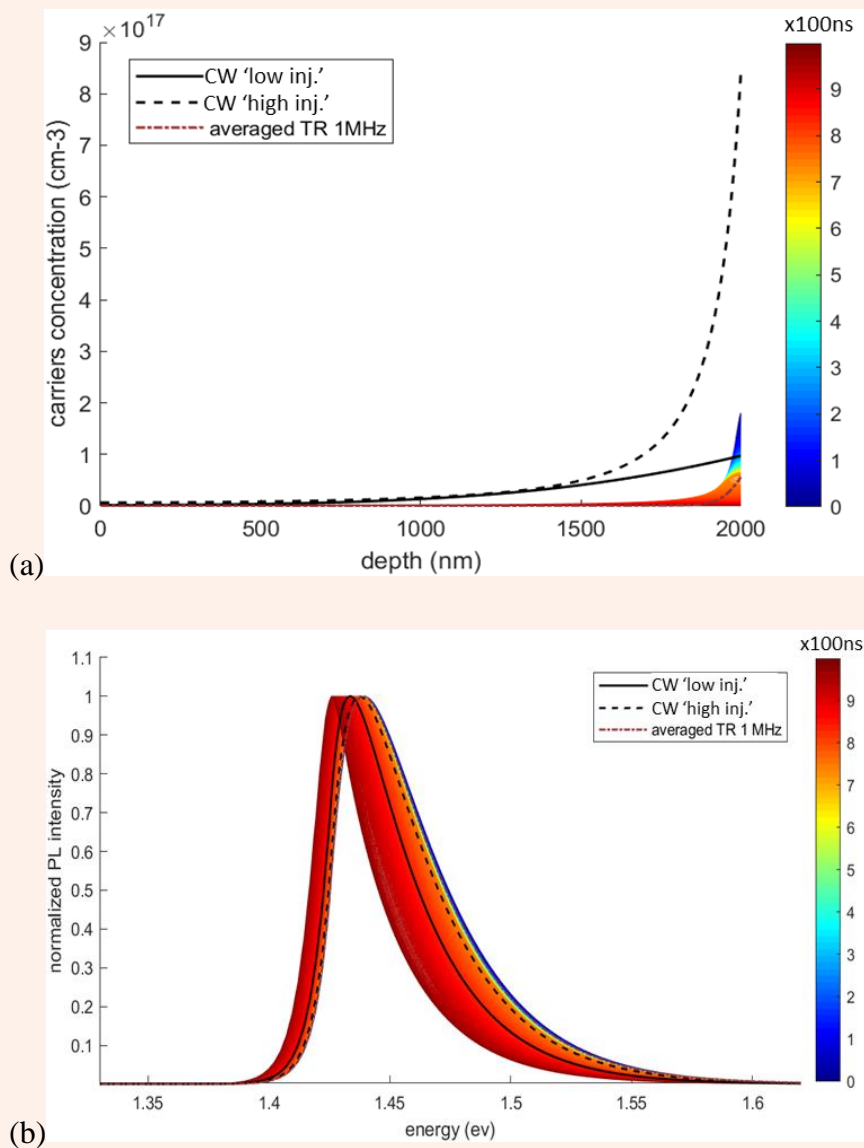


Figure 4-8: (a) Comparison of charge carrier profiles for two injection levels in continuous wave excitation with the temporal evolution of pulsed excitation, and (b) resulting normalized spectra

In summary, the photoluminescence obtained in continuous wave and pulsed excitation thus corresponds to different charge carrier profiles. It leads to both diverse injection conditions, inducing distinct dynamics when the system do not follow linear rate equations. It also impacts the emitted spectrum as the reabsorption contribution varies.

4.II 4D-PL imaging

This section introduces gallium arsenide PL intensity measurements in spectral, temporal, and spatial dimensions together. It is the first time such a dataset has been obtained on hard semiconductors to the best of our knowledge.

4.II.1 Acquiring PL profile on GaAs sample

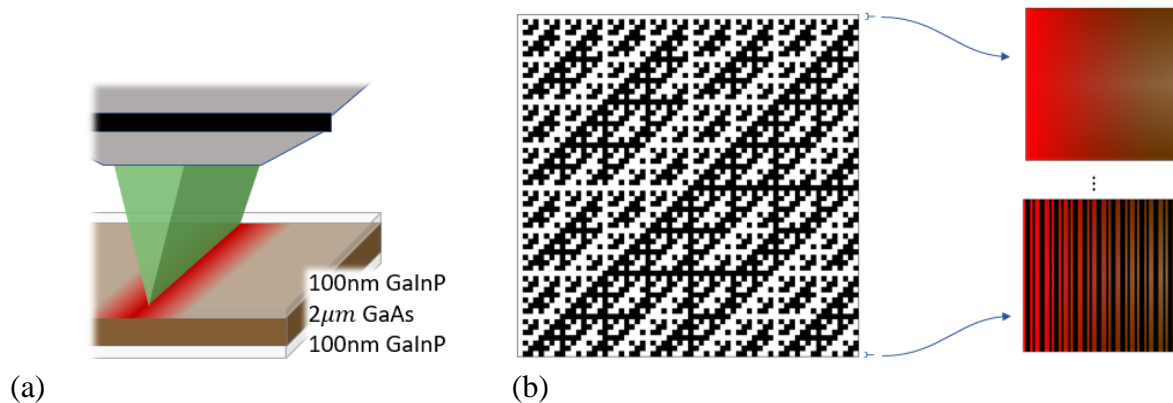


Figure 4-9: (a) Structure of the gallium arsenide sample under study with a schematic representation of the linear illumination. (b) Construction of the linear patterns employed for single-pixel imaging from the 64-element Hadamard matrix: each matrix line corresponds to one pattern displayed on the DMD. Each value of the line determines the position of a column 64 micro-mirrors (white = 'on', black = 'off').

This section provides the experimental details with a reminder of the smoothing and correction procedure. We demonstrate 4D-PL on a 2 micrometers thick gallium arsenide wafer sandwiched between 100nm layers of GaInP. This material provides a stable and well-studied target for this proof of concept. It is placed in a cryostat at 25°C to ensure temperature stability during the experiment. The laser is coupled to a multimode fiber plugged into a laser line generator (Thorlabs FLG10FC) and illuminates the sample with a fluence of $1.6 * 10^{14} \text{ phot/pulse/cm}^2$ and a $23\mu\text{m}$ full width half maximum. In that configuration, the problem under study is symmetric along one spatial direction. Therefore, we use linear patterns to maximize the light flux: the amount of light is multiplied by the number of mirrors in each column. As pictured in Figure 4-9, any mask is still provided by a row of Hadamard matrix. However, each value in the row corresponds to a "linear pixel" composed of a column of 64 DMD mirrors. It results in reconstructing a spatial profile 64x1 of spectral intensity decays. In

this work, it is the only case where the Hadamard rows are not folded into two spatial dimensions.

Streak measurements are dark and spectral transmission corrected. To ensure a high signal-to-noise ratio and monitor the stability, the pattern series is acquired 11 times, with 10s of acquisition per pattern. They are smoothed temporally by taking a rolling average on a window of 60 pixels with a gaussian kernel of 22 pixels full width half maximum. The PL intensity is also processed spectrally with a Savitzky-Golay filter of order 1 on a 101 elements window. As explained in chapter 3, further correction is required to remove the influence of DMD diffraction. Indeed, a linear dependency of the collected intensity is observed depending on the number of transitions ν per pattern, defined in (3-2). The variation of intensity as a function of a number of transitions is plotted in Figure 4-10 (a), with examples of PL intensity 700ps after the laser pulse for different wavelengths.

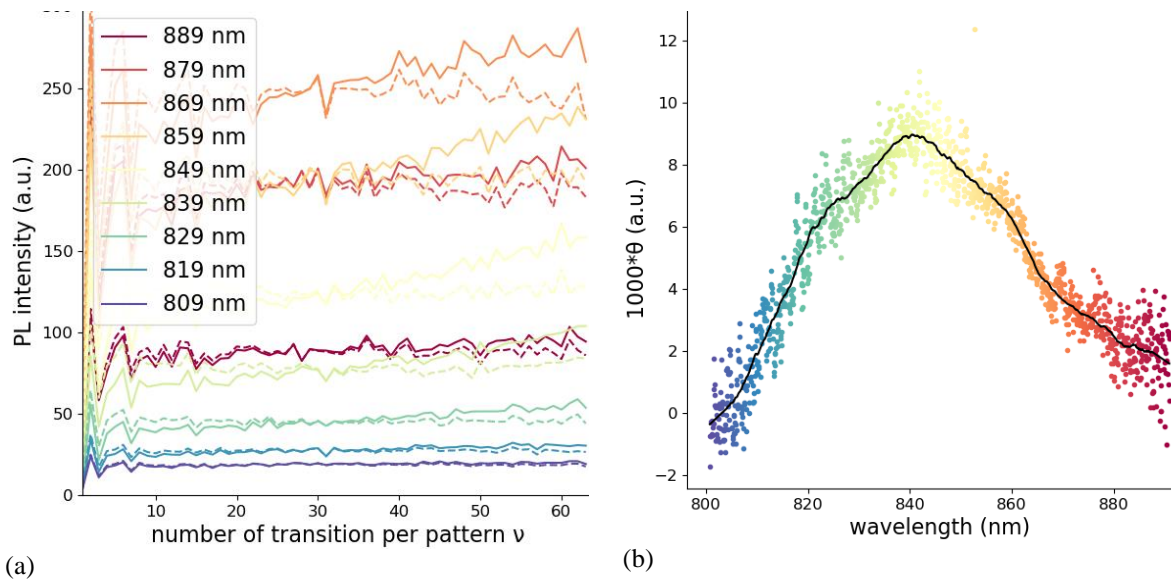


Figure 4-10: (a) PL intensity measured at a specific wavelength and delay as a function of the number of transitions per pattern. Values are shown for different wavelengths 700ps after the laser pulse. The dashed lines correspond to the measurement after the linear drift correction. (b) Correction factor α for each wavelength (colored dot) and Savitzky-Golay filtered extrapolation (black line).

As a reminder, we attribute this artifact to interferences varying with the superordinate arrangements of the pixels. We filter and extrapolate the normalized drift slope θ defined in (3-3) from the raw measurements and correct the smoothed ones. Indeed, raw values already provide a good linear fit while ensuring the correction is not affected by the smoothing required for the reconstruction. This linear drift correction allows for avoiding artificially negative values in the reconstruction. Also, we remove the first and last pixels. The first one does not benefit from the noise reduction characteristic of the Hadamard matrix. Removing it is similar to implementing the S matrix mentioned in optical multiplexing¹³. The outlier in position 64

may be related to diffraction. Indeed, this pixel is outstanding in the reconstruction because it includes all patterns positively with odd numbers of transitions and negatively the even ones. After the reconstruction, the spatial information is fitted with the following Hill equation:

$$f(x, a_1, a_2, x_0, p) = a_1 + \frac{a_2 - a_1}{1 + 10^{((\log x_0 - x) * p)}} \quad (4-6)$$

This fit is not based on a physical model and is employed for denoising purposes and improved data readability. It is performed in two dimensions, for each wavelength and each time delay of the dataset.

4.II.2 Results

The data obtained by this experiment are illustrated in Figure 4-11. Different projections of the 4D data can be extracted: Figure 4-11(a) shows the average intensity profile with $x=0\mu\text{m}$ in the center of illumination. In Figure 4-11(b-d), the spectral decay is plotted at three distances from the center of illumination, both in arbitrary units and normalized at each time. Intensity variation with time, location, and wavelength are visible in the first column. The second visualization highlights the changes in the spectral shape along the return to equilibrium. In all cases, the spectrum redshifts with time and stabilizes with a maximum of 869nm. The closer to the center, the more important the spectral shift is. This is particularly visible when comparing the normalized spectra evolution in the center and the 25 μm . Thus, the PL intensity shows variations in the spatial, spectral, and temporal dimensions.

The 4D data differs from the maps of the spectrum averaged temporally plus the maps of the decay averaged spectrally (provided by the 2x3D setup introduced before). It is possible to observe this by investigating the 4D data averaged spatially $I(\lambda, t)$ shown in Figure 4-12. Indeed, these are different from the product of the intensity averaged spectrally $I(t)$ by the intensity averaged temporally $I(\lambda)$ accessible from the 2x3D setup and illustrated below. The difference between the two quantities highlights the correlation between the two dimensions. The spectrum is clearly blueshifted at short time and redder at longer delays. However, there is no delay time when its shape corresponds to the average spectrum. The other way around, one can see that at higher energies, the intensity is higher at a short time and quickly smaller than it references due to quicker decay. The reverse behavior is observed for the lower energies. Furthermore, it seems that the averaged decay does not correspond to the decay for a given wavelength.

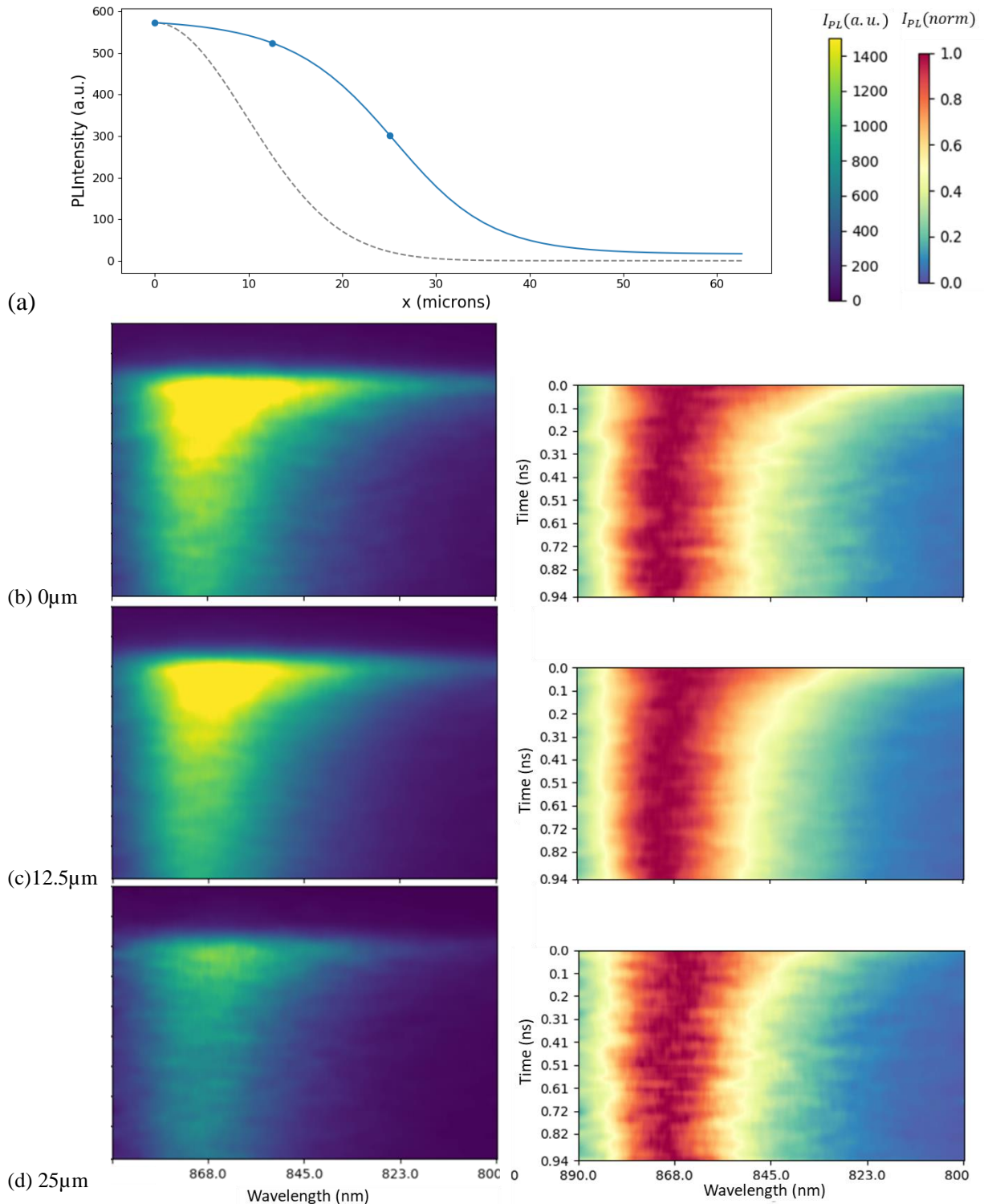


Figure 4-11: Data obtained by 4D-PL on GaAs. (a) The PL intensity profile (averaged spectrally and temporally) is displayed with three markers corresponding to the center of illumination, $12.5\mu m$ and $25\mu m$ away from it. The grey dashed line indicates the illumination profile. (b-d) Evolution of the spectrum in the different locations. The left figures correspond to the decays with the same color map indicated at the top. The right figures show the corresponding spectra normalized at each time after the laser pulse.

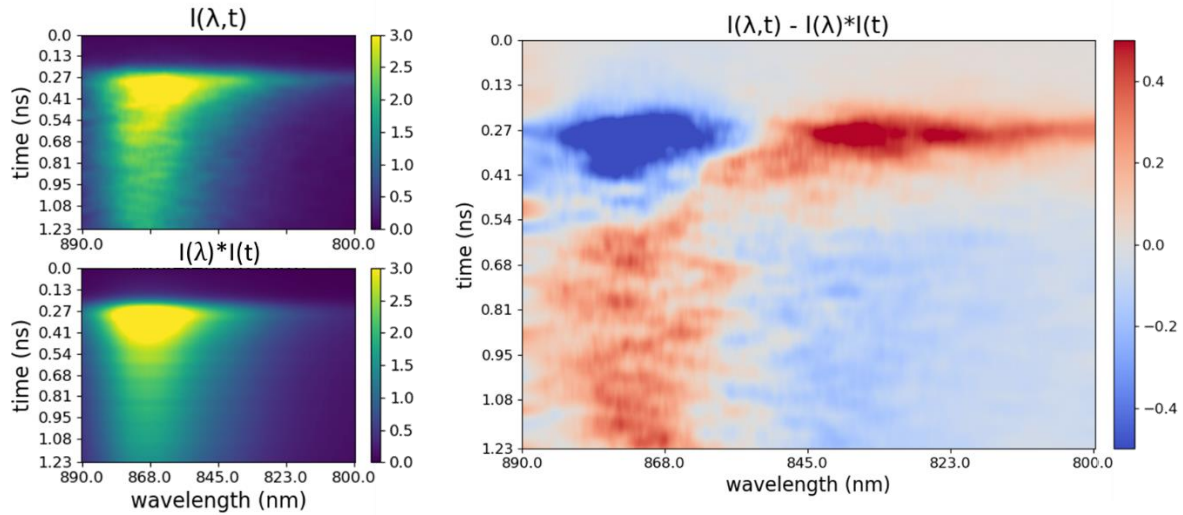


Figure 4-12: Temporal evolution of the spectrum averaged spatially. The product of the spectrum $I(\lambda)$ averaged temporally and the decay $I(t)$ averaged spectrally is shown for comparison. Their difference is illustrated on the right, with visible trends: a short time, the spectrum is bluer than the average, while it is redder at longer delays.

The obtention of $I(\lambda, t)$ from detectors resolved either temporally or spectrally requires the strong assumption that either no temporal evolution of the spectrum is assumed or that it can be extrapolated from the projections on the temporal and spectral axis. It would be interesting to study whether the algorithm proposed by Soldevilla et al.¹⁴ can obtain this kind of temporal evolution.

4.II.3 Discussion

In this section, different ways to interpret the data are exposed. At first, a basic model is employed to obtain the variation of the quasi-Fermi level splitting and temperature, which are the two physical quantities describing a spectrum for constant absorptivity. The obtained results provide far longer cooling rates than the literature, so we propose ways to refine the model.

4.II.3.a Simple model

The illumination intensity, assuming a reflectivity of 0.37 and an absorption coefficient of $8 * 10^4 \text{ cm}^{-1}$ from Aspnes¹⁵, leads to an injection of $8 * 10^{18} \text{ cm}^{-3}$. At such a high carrier density, band-filling and bandgap renormalizationⁱⁱ are expected to modify the shape of the absorptivity and hence the PL spectrum. Otherwise, Auger recombination can influence the beginning of the decay: considering the coefficient provided in the Ioffe database¹², they induce a recombination rate of $5 * 10^{26} \text{ cm}^{-3} \text{ s}^{-1}$, compared to a radiative one of $5 * 10^{28} \text{ cm}^{-3} \text{ s}^{-1}$.

ⁱⁱ Variation of the bandgap energy with the charge carrier density

In this paragraph, the absorptivity is assumed to be independent on the charge carrier density or time to obtain a simplified model that would allow the interpretation of 4D-PL data in elementary cases.

In this framework, the average energy and the logarithm of PL intensity are directly linked to the temperature and the charge carrier concentration by the two relations below:

$$E_{mean} = E_g + c_1 k_B T \quad (4-7)$$

$$I_{PL} = c_2 e^{\frac{\Delta\mu}{k_B T}} \quad (4-8)$$

Where c_1 and c_2 are constant. Equation (4-7) is a generalization of the approximation provided by Wurfel (in 2.7), where the mean energy is obtained with $c_1 \sim 1$. Equation (4-8) is a direct rewriting of equation (1-30) based on Boltzmann approximation. Thus, for a bandgap energy constant with the injection, it reads:

$$T = \frac{E_{mean} - E_g}{c_1 k_B} \quad (4-9)$$

$$\Delta\mu = \frac{(E_{mean} - E_g)}{c_1} \log\left(\frac{I}{c_2}\right) \quad (4-10)$$

By considering $E_g = 1.424eV$ and scaling the temperature at 1ns to 298K, it is possible to obtain a first estimation of the carrier temperature spatially and temporally. This scaling is preferred to the one with respect to the spectra far from the illumination, as the signal is of better quality and leads to $c_1 = 1.67$. As scaling of the intensity would require the knowledge of the injection level, $\Delta\mu$ is known with offset energy. We rather deduce $\Delta\Delta\mu$, the variation in quasi-Fermi level splitting. The corresponding results are presented in Figure 4-13 (a) and (b).

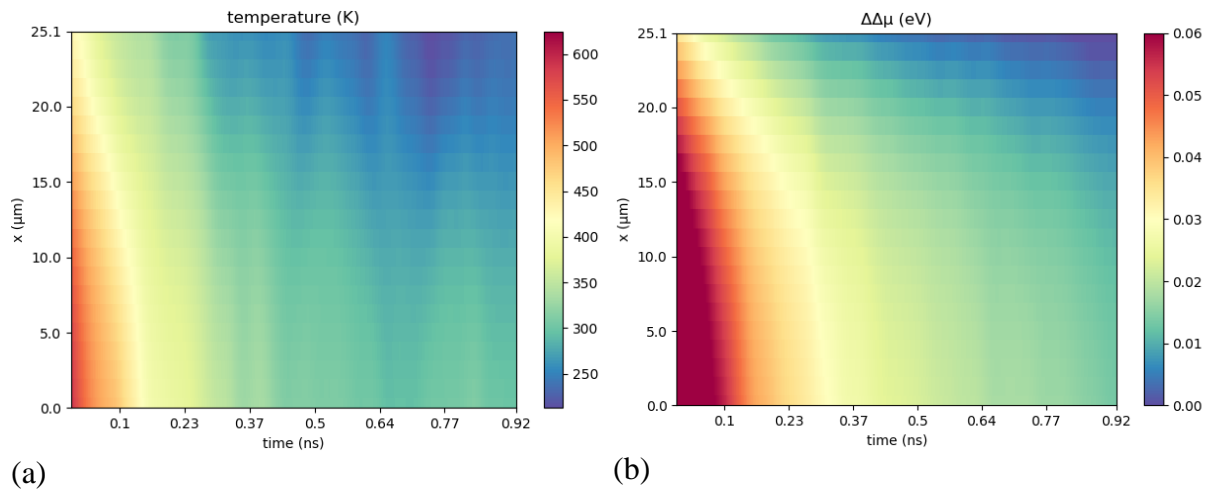


Figure 4-13: Spatial and temporal evolution of (a) the temperature and (b) $\Delta\Delta\mu$ obtained with a simplified model.

The presence of carriers at 600K, though surprising for bulk GaAs, is still a possible scenario. The order of magnitude of the quasi-Fermi level splitting variation is also reasonable. However, Figure 4-13 shows a temperature gradient ($\sim 60K$) at 0.92ns, which is not expected in bulk materials, as detailed later. Otherwise, the maps of temperature and $\Delta\Delta\mu$ have similar feature so there seems to be a correlation between them. To determine if these two values are linked or if there are competing phenomena with different characteristic times and discuss the temperature gradient, we base the following analysis on the intensity and the mean energy. Indeed, these observables are universal as they do not rely on physical assumptions.

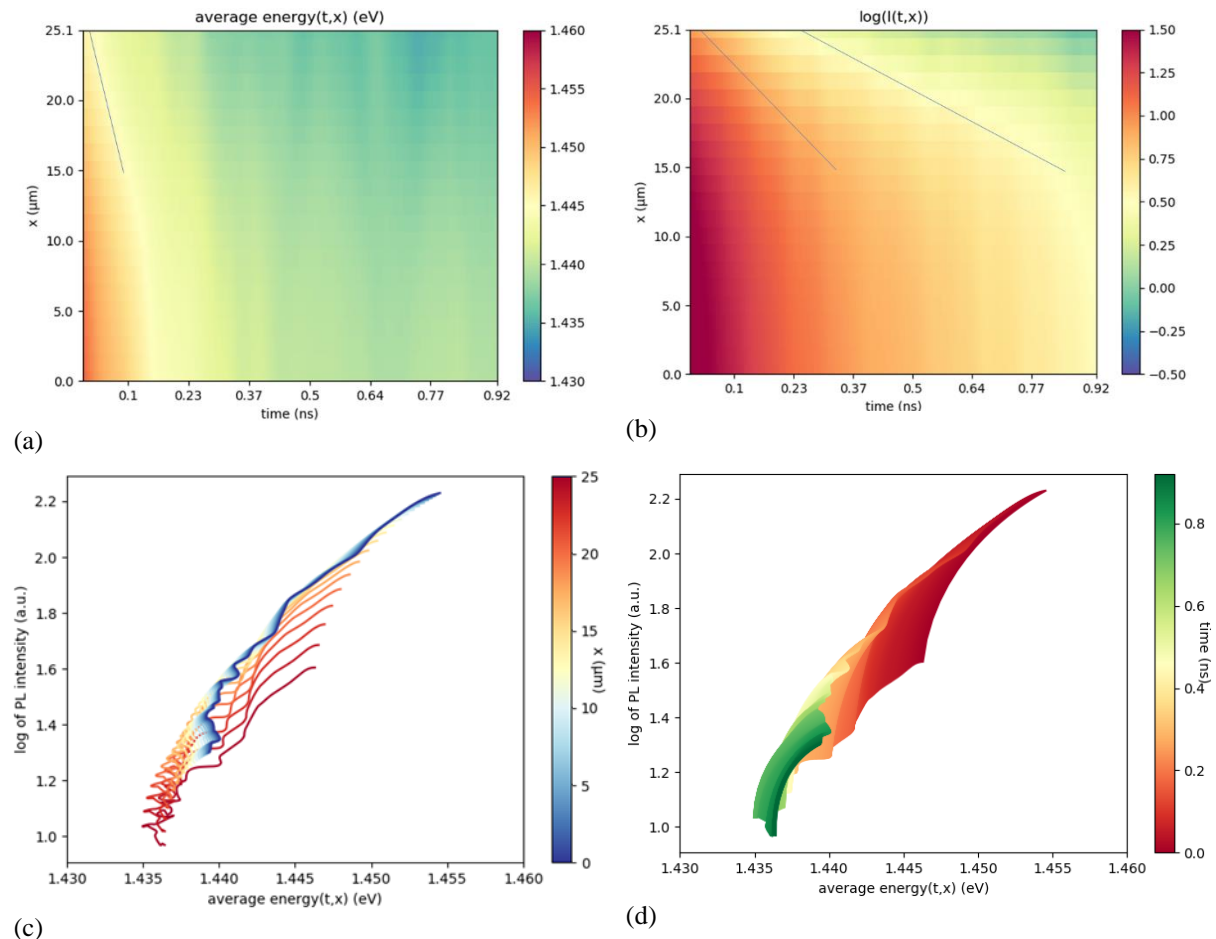


Figure 4-14: Evolution of spectral average energy and intensity as a function of time and location. (a) Average energy during the time at different distances from the center. (b) Corresponding map of the logarithm of the PL intensity. (c-d) Correlation between the logarithm of PL intensity and the average PL energy. The color code highlights the spatial (c) and temporal (d) variations.

PL energy and the average intensity over time in the sample's different locations, as shown in Figure 4-14(a) and (b), respectively. One can see that the variation in average PL energy happens more quickly than variations of the logarithmic PL intensity. Indeed, the energy maps change mainly within the first 200ps, whereas the intensity keeps changing after a nanosecond. Furthermore, for both maps, the isolines are quite parallel in the illumination area

(roughly $0\text{-}10\mu\text{m}$) as the color gradient follows the temporal axis. A slope is observed on the edges of the illumination, as highlighted by the dark lines associated with the propagation mechanisms. The energy propagation owes a higher characteristic speed, determined from the isoline slope about 10^7 cm/s . This value matches the saturation hole velocity obtained by Dalal et al.¹⁶ at room temperature. The intensity logarithm one is slower, about $3 * 10^6\text{ cm/s}$ at the beginning of the decay and $2 * 10^6\text{ cm/s}$ later. PL intensity as a function of mean energy is plotted in Figure 4-14(c) and (d) in the different locations and times, respectively. The expectations for this correlation are described before providing various observations on the experimental results.

4.II.3.b Key considerations to interpret LogI-Emean maps

As a reminder, the spectral shape is provided by the product of the absorptivity and blackbody radiation (see Chapter 1.II.1 for more details). Assuming absorptivity and temperature are stable along the experiment, the shape, and thus the average energy, are fixed along the decay. The associated numerical simulation is presented in Figure 4-15 (a), considering a $2\mu\text{m}$ thick material and by taking an absorption coefficient with an Urbach tail of 10meV and scaled to 12162 cm^{-1} at the gap value of 1.424 eV ¹⁵. This model is valid for $\Delta\mu < E_g - k_B T$, and in this regime the plot confirms that PL E mean energy depends only on the temperature. An incurvation of the logI-Emean plot occurs for $\Delta\mu$ approaching the gap outside the validity range. Once the temperature is determined from the mean energy, $\Delta\mu$ can be obtained based on the PL intensity. It is thus possible to assess the two quantities sequentially, as presented before.

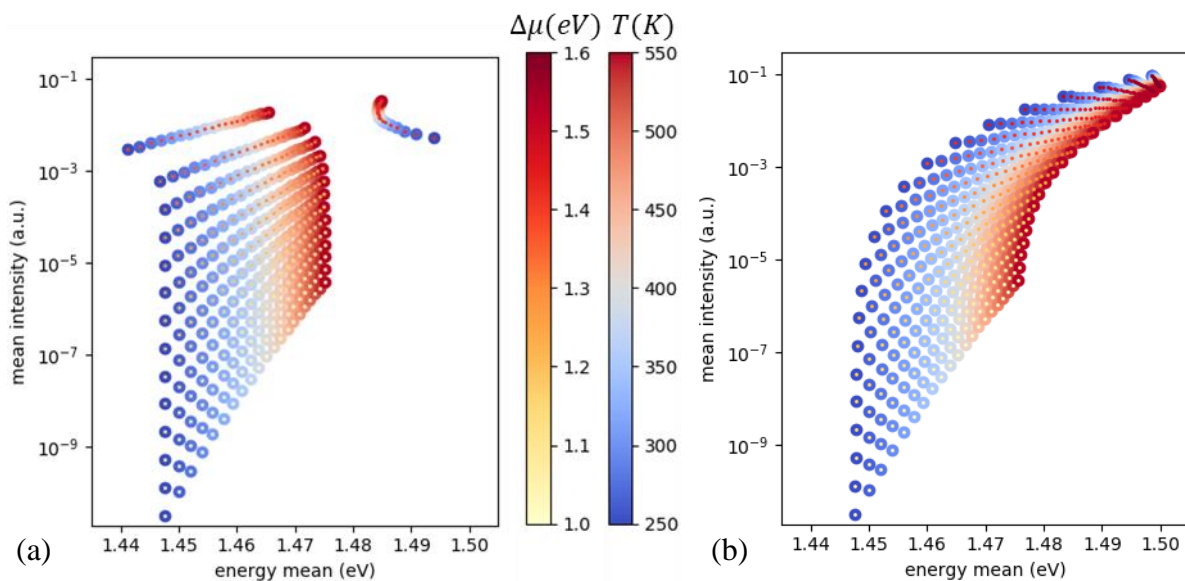


Figure 4-15: Mean PL intensity as a function of mean energy for different temperature and quasi-Fermi levels splitting for (a) model from generalized Planck law, valid for $E_g - \Delta\mu > k_B T$, and band filling is neglected, (b) with band filling model. The external points refer to the temperature, increasing from blue to red, while small dots indicate the quasi-Fermi level splitting.

In a high injection regime such as the one used in this experiment, where the quasi-Fermi level splitting approaches the bandgap energy, the absorptivity dependence on the carrier densities must be considered. All things being equal, both PL intensity and energy mean are bijections of quasi-Fermi levels splitting. We further illustrate the different dependence by simulating the influence of band filling on a similar model material. The variation of the absorptivity with the quasi-Fermi level splitting can be deduced from the variation in the absorption coefficient, following the trend described by equations (1-34) and (1-35).

The results plotted in Figure 4-15(b) are valid on the whole extent of $\Delta\mu$. As expected, the energy mean is a function of both temperature and quasi-Fermi level splitting: accessing the temperature from it can still be done, provided an assumption of low or known $\Delta\mu$. All things being equal and for a given temperature, PL intensity and energy mean are bijections of quasi-Fermi levels splitting. Thus, if the carrier density is the only parameter to vary along time, all points are expected to be on such an elbow trajectory with initial energy depending on the temperature. The inflection intensity is quite stable with the temperature and may provide a way to scale experimental data. Provided the accurate intensity calibration, the mean intensity and energy are observable and adapted to the assessment of these two quantities.

Taking into account the considerations mentioned above, the following observations can be made on the experimental LogI-Emean curve presented in Figure 4-14:

- The experimental data do not follow a straight trajectory in the LogI-Emean plane. The dataset involves more mechanisms than band-filling because it does not show a bijection between the PL intensity and average energy. A combination of carrier cooling and band-filling could explain such behavior.
- The average energy in the experimental dataset ranges from 1.435 to 1.455 eV, whereas the simulated spectrum stabilizes around 1.454 eV for 298K. This discrepancy most likely originates from the difference in absorption of the two materials. A proper investigation of band filling requires working with an experimental absorption coefficient. However, it raises the hypothesis that the redshift is caused by the reabsorption of PL emission distribution going in-depth with diffusion.
- The average energy stabilizes at different values depending on the distance from the illumination: a possible explanation would come from band-filling if the long-term and far from center logI-Emean trajectory is caused by it. Optical transport could also play a role.
- The intensity as a function of average energy seems to follow the same dependence at times approaching the nanosecond and in pixels far from the center.

At least three factors can affect the spectra obtained by 4D-PL: temperature, band-filling, and optical transport. They are further described in the next section. Bandgap renormalization leads to a decrease of E_g in gallium arsenide with increasing charge carrier density¹⁷. It would then induce a blueshift along the decay, which goes against the trend observe in the experimental data. It is then considered as negligible compared to the above-mentioned effects.

4.II.3.c Potential interpretations of LogI-Emean dependence

4.II.3.c.1 Effect of temperature

Several effects can change the average energy and impact the intensity, which may explain this intensity-energy distribution. First, the carrier temperature distribution correlates to the spectral higher energy tail, and hot carriersⁱⁱⁱ increase the average energy, as depicted in Figure 4-15. However, bulk gallium arsenide cooling time is below 10ps for such carrier density^{18,19}. It might be seen at the temporal resolution timescale. In all cases, the hot carrier relaxation is expected to be completed at 1ns. In these conditions, a model with band filling would lead to exponential intensity growth as a function of the energy mean, as seen in Figure 4-15(b).

This temperature could also be related to lattice heating by the laser pulse. Indeed, if all the energy of the laser pulse were converted into heat, it would imply a gain in temperature of:

$$\Delta T_0 \sim \frac{E_0}{c_p S l} \quad (4-11)$$

Where specific heat c_p in the illuminated volume of section S and width l . The heat diffused by the material is then:

$$\Delta T(x, t) \sim f(t) e^{-\frac{x^2}{2Dt}} \quad (4-12)$$

With energy conservation,

$$\int S \rho c_p \Delta T(x) dx = f(t) * S \rho c_p \sqrt{2\pi D t} = E_0 \quad (4-13)$$

After a delay τ , the temperature in the center is thus:

$$\Delta T(x = 0, \tau) = \frac{E_0}{S \rho c_p \sqrt{2\pi D \tau}} \quad (4-14)$$

By assuming a specific heat of 0.33J/g/K and a thermal diffusivity of 0.31cm²/s as provided by the Ioffe database¹², and considering a mass of 0.41mg (23μm*1mm*340μm with a density of 5.32g/cm³), the laser may induce a heating up to 10⁻⁴K in the center area. After the 1μs corresponding to the laser cycle, the temperature increase in the center is about 3 * 10⁻¹⁰K. This second value is negligible compared to initial heat; thus, we do not expect

ⁱⁱⁱ Charge carrier with excess kinetic energies, following a Fermi-Dirac distribution with a temperature superior to the lattice one, as illustrated in Figure 1-3.

accumulation that would induce local heating in the center. As the presence of hot carriers is not likely after hundreds of picoseconds and back of the envelope calculation show that the material should not be heated by the laser, the hypothesis of temperature variation cannot explain the gradient in energy mean at the final time. We might see cooling at times comparable to the laser pulse duration.

4.II.3.c.2 Band-filling

Considering an absorption coefficient of $8 * 10^4/cm$, the maximal quasi-Fermi level splitting expected is 1.54eV, above the gap, based on equation (1.10). If we suppose a reflection coefficient of 0.37 following the values of Aspnes¹⁵ and consider the lateral and in-depth diffusion, it falls to 1.37eV, which is still a value at which the band-filling impacts the above simulation. Also, during the experiments, a clear blueshift at initial times was observed at high fluences. This trend supports the band-filling hypothesis (even though it could be related to the saturation of defective interface states²⁰).

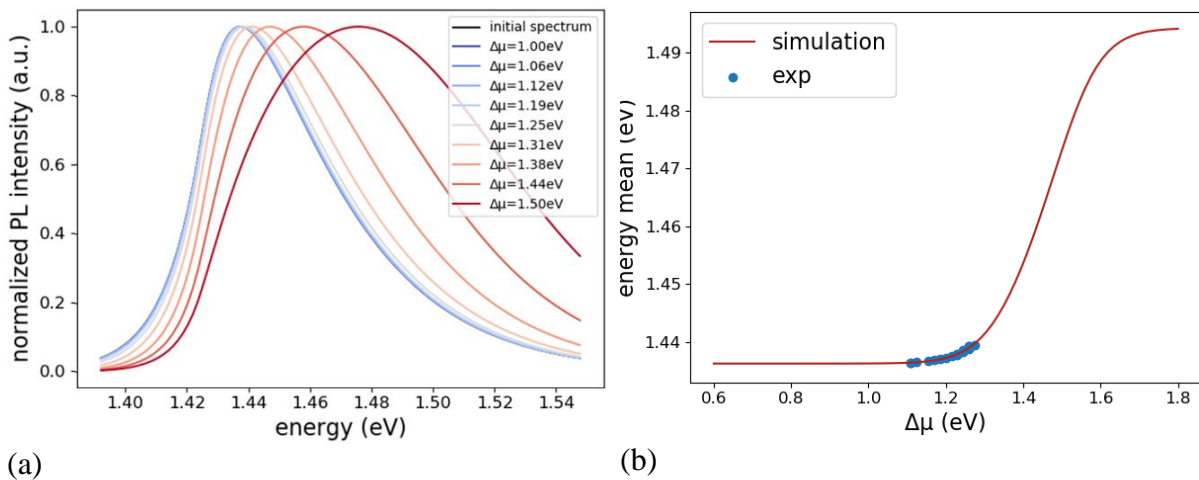


Figure 4-16: (a) Band-filling simulation lead with the absorption coefficient fit from the PL spectrum at 0.9ns. (b) Energy mean as a function of $\Delta\mu$ obtained by simulation. Experimental points are placed as a function of the energy mean to fit $\Delta\mu$.

Band-filling simulation was performed by fitting the absorption coefficient from the photoluminescence spectrum long after the decay. Figure 4-16(a) shows the variation of the spectrum shape induced by different injection levels. Simulations indicate a variation of the low energy tail half maximum superior to 3meV (corresponding to $\Delta\lambda \sim 2nm$) for $\Delta\mu > 1.38eV$. Such variation is not seen on the spectra in Figure 4-11 and corroborates our first estimation of $\Delta\mu$. We further attempt to scale the quasi-Fermi level splitting based on the energy mean obtained from the simulation, as shown in Figure 4-16(b). The experimental data are set on the simulated mean energy curve, corresponding to $\Delta\mu$ from 1.11 to 1.27eV. However, this extent of potential is associated with a PL intensity multiplied by a factor of 100 in the simulation and of 2 for the experimental data, leading to inconsistency.

The discrepancy between simulation and experimental data may result from how the absorption coefficient is estimated: the optical model to retrieve it is very limited. The experimental data are clustered close to the stabilization energy, leading to a badly conditioned problem. Moreover, the mean energy could also be shifted by reabsorption, as explained in the following paragraph.

4.II.3.c.3 Optical transport

The higher energies of the spectrum emitted in the depth of materials are more reabsorbed than the lower ones as a function of the path traveled in the material, as illustrated in Chapter 3 in section I.3b. With this respect, both lateral and in-depth transport could play a role. At the hole saturation velocity mentioned earlier, the $2\mu\text{m}$ would be covered in 50ps and could have an impact at a short time. Also, the temporal evolution of the profile due to different surface recombination velocities cannot be ruled out. Furthermore, if the material roughness is not negligible, photons emitted in a location could be collected outside the collection cone defined by the refraction and the numerical aperture (its diameter is about $0.4\mu\text{m}$ in our case). This leads to a red spectrum shift in the outer regions where the contribution of the photon emitted in the center cannot be neglected¹⁰. Such a mechanism could explain the different average energy at times approaching the nanosecond.

Gallium arsenide is a well-known compound with a bandgap energy of 1.424eV . Hence, with the assumption of a perfect square root absorption coefficient, the PL peak without reabsorption is expected at²¹ $E_g + \frac{1}{2}k_B T = 1.437\text{eV}$. However, the experimental peak goes down to 1.426eV , which tends to confirm that this mechanism play a role in the 4D data. Once more, quantifying this effect would once more require a good estimation of the absorption coefficient.

In this section, we have obtained the spectral, temporal, and spatial dependence of Gallium Arsenide PL emission in high injection conditions. A blue shift is observed and attributed to band-filling with a potential contribution of the carrier temperature. Thus, the classical framework for interpreting spectra does not hold anymore. Furthermore, the characteristic speed of the energy propagation matches the saturation hole velocity, and the corresponding regime is associated with increased carrier-lattice interaction. Strategies have been proposed to interpret the data relying on the energy mean and logarithm of intensity for each time and position, as these two observables are statistical indicators owing to a good resolution. Models taking into account only the band-filling were investigated and were not sufficient to fit the data. It suggests that optical transport and/or charge carrier temperature impact the dataset.

4.III Application to different samples

This section introduces results on different samples to illustrate the variety of physical phenomena this setup can characterize. Signal was obtained on gallium arsenide, perovskite, and fluorophores absorbers.

4.III.1 Gallium arsenide

A sample of gallium arsenide sandwiched between aluminum gallium arsenide layers is characterized by this technique. The sample structure is described in Figure 4-17 (a), along with the intensity image obtained by integrating the single-pixel imaging picture (b) over the spectral dimension. An artifact is visible on the middle line, and gaussian smoothing suppresses it, as shown in picture (c) for a better determination of strategic areas by clustering visualized in (d). The illumination of $\Phi_{exc} = 5 * 10^{14} phot/pulse/cm^2$ whose diameter is of the order of $5\mu m$ is encompassed by the center luminescence cluster.

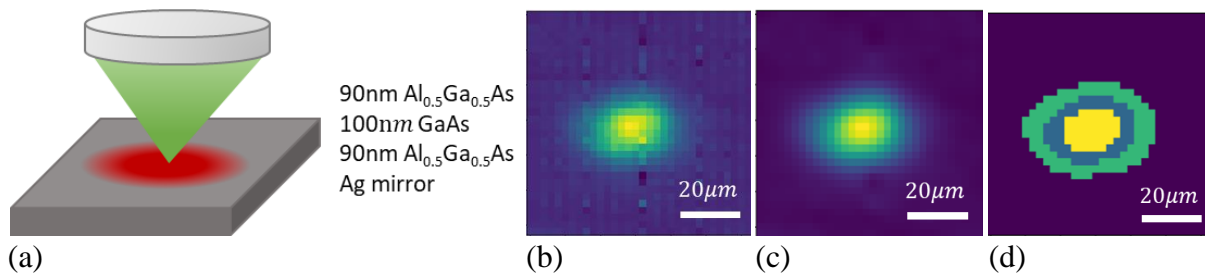


Figure 4-17: (a) Schematic of the GaAs sample, (b) Image obtained by spectral integration of the hyperspectral image, (c) Smoothed image with a gaussian filter, used as a reference for pixel clustering, (d) areas determined by pixel clustering.

The streak acquisitions obtained for the four clusters are depicted in Figure 4-18. Each of them features luminescence spectral changes along the decay: it is particularly visible on the maximum wavelength, shown by the solid red line, that shifts towards higher wavelengths with time. This shift is more important in the center (98nm) and decreases in the inner ring (82nm), the outer ring (59nm), and the external area (38nm). As the maximum of the colormap corresponds to the 98 percentile, one can observe longer decays when going away from the center. The emission of the AlGaAs ($E_g = 2.02eV$ i.e. peak around 614nm) is not comprised in the observed spectral bandwidth.

In classical injection conditions, the maximum wavelength is expected to be close to the bandgap energy of the material, cf Figure 4-19(a). One of the GaAs is about 1.42eV or 870nm. Thus, it corresponds to the spectra a long time after the excitation. Similarly to the 4D-PL experiment, the blueshift with respect to the reference can be related to band-filling due to the high injection levels.

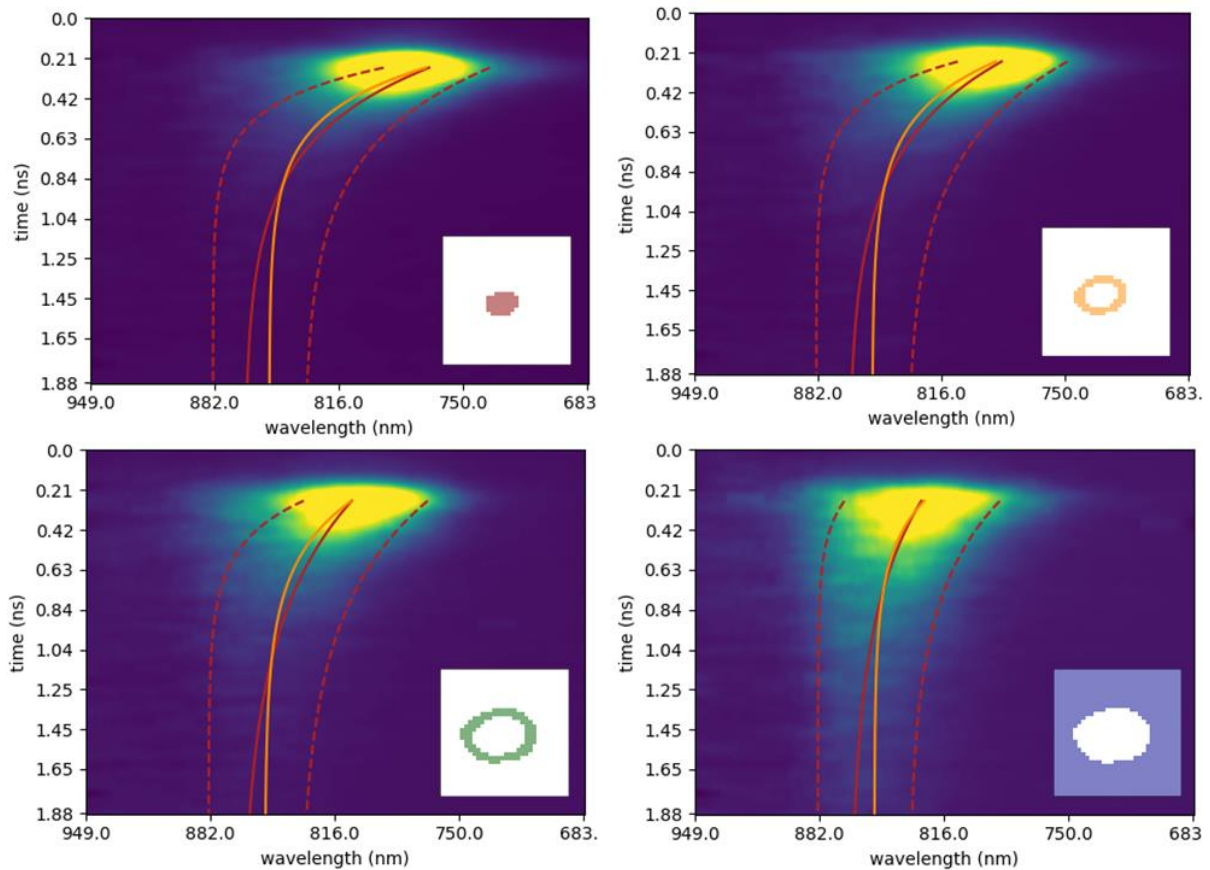


Figure 4-18: Transient photoluminescence spectroscopy acquisitions in the different areas of interest – indicated as an insert. The lines are guided to the eye obtained from the exponential fit of the following quantities: maximum (redbrick solid), averaged wavelength (dark orange), and left and right half maximum (redbrick dashed).

4.III.1.a Characterization of band-filling

When the quasi-Fermi levels splitting approaches the gap, the states in the bands are saturated. Thus, even after carriers cooling, emitted photons will owe higher energy (as further described in Chapter 1, section II.1.c, and depicted in Figure 4-19 (b)). One can approximate this energy with the quasi-Fermi level splitting in a simplistic model. As such, the relation $I_{PL} \propto \exp\left(\frac{\Delta\mu}{k_B T}\right)$ reads $I_{PL} \propto \exp\left(\frac{E_{mean}}{k_B T}\right)$. Therefore, the PL intensity varies roughly as an exponential of the mean energy over $k_B T$. This is quite consistent with what we observe experimentally and is shown in Figure 4-19 (c). Indeed, in all the locations, the PL intensity follows a quite similar correlation to the mean energy, and this trend is quite close to the reference grey line representing $\exp\left(\frac{E_{mean}}{k_B T}\right)$ at 298K. We observe a higher slope that might traduce a higher temperature.

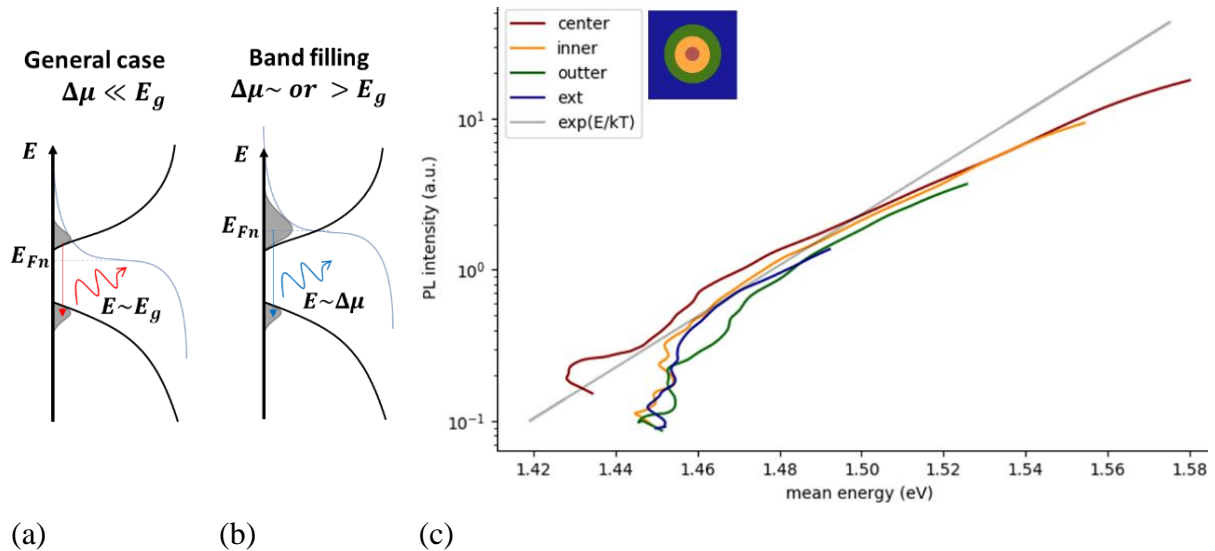


Figure 4-19: Band-filling influence on the emitted photon energy (a) photon energy, the difference between quasi-Fermi levels splitting and the bandgap exceeding few kT , (b) photon energy in presence of band-filling, (c) experimental dependence of the PL intensity on mean energy, the exponential of the mean energy over $k_B T$ is indicated as guide for the eyes at room temperature (298K).

Further attempts were carried out to determine the temperature and band-filling simultaneously. A reference spectrum measured in another project and shown in Figure 4-20 is compared to the time-resolved spectroscopy in different areas. It has been obtained by hyperspectral imaging with a 532nm continuous laser. The long-term behavior of transient spectra seems to match the reference one at 1.35ps. The lower dynamic of the spectra collected by the streak is detrimental. Longer acquisition times are required to capture spectra at the end of the decay with sufficient quality. In this example, 100s acquisitions were performed, and this duration could be multiplied by 10 or 100.

Otherwise, we used the reference spectrum to obtain absorptivity and/or absorption coefficient through the framework described in Chapter 1.II. Adding different levels of band-filling on it didn't allow for reproducing the shape of the spectra a short time and led to spectra owing thinner width. It is probably necessary to consider more mechanisms (diffusion, optical transport...) to obtain a model fitting the measured spectra.

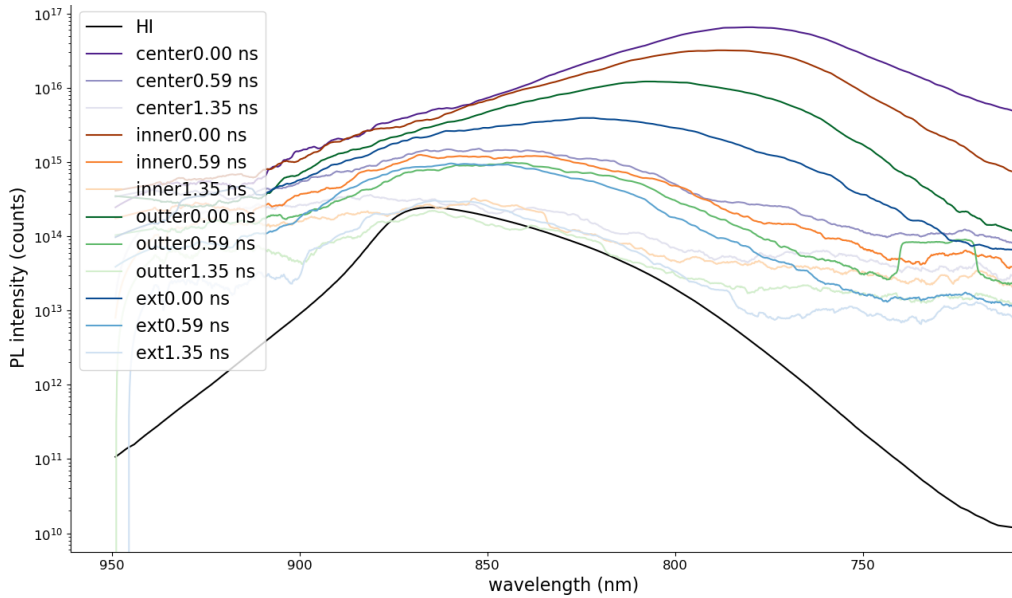


Figure 4-20: Photoluminescence spectra obtained in the different clustering areas at various delays after the laser pulse. They are compared with the reference photoluminescence spectrum measured in lower injection conditions with a 532nm continuous wave excitation. Time-resolved spectroscopy spectra tend to adopt the shape of the reference spectrum at long times.

4.III.1.b Determination of transport properties

Furthermore, one can observe the carrier dynamic through PL decays. Figure 4-21(a) shows that the PL decay time varies with the area of interest for a short time, whereas it is stable for longer. Indeed, provided the characteristic times shown in Chapter 1.II.2, diffusion in gallium arsenide is expected to be far quicker than recombination so that transport prevails at the beginning of the decay. Also, second and third-order recombination will induce quicker decay areas with higher charge carrier concentrations that are brighter. At longer time, PL dynamics are dominated by first-order recombination, and transport can be neglected.

The cumulative plot in Figure 4-21 shows the repartition between the different areas of the emitted intensity over time. The increase in the external sites, as opposed to the decrease in the inner ones, can be interpreted as diffusion of the carrier from the center to the exterior. The non-negligible intensity in the external areas at a short time depends on the temporal resolution of the camera that could not capture PL before lateral diffusion. It might also be a sign of optical (and immediate) transport.

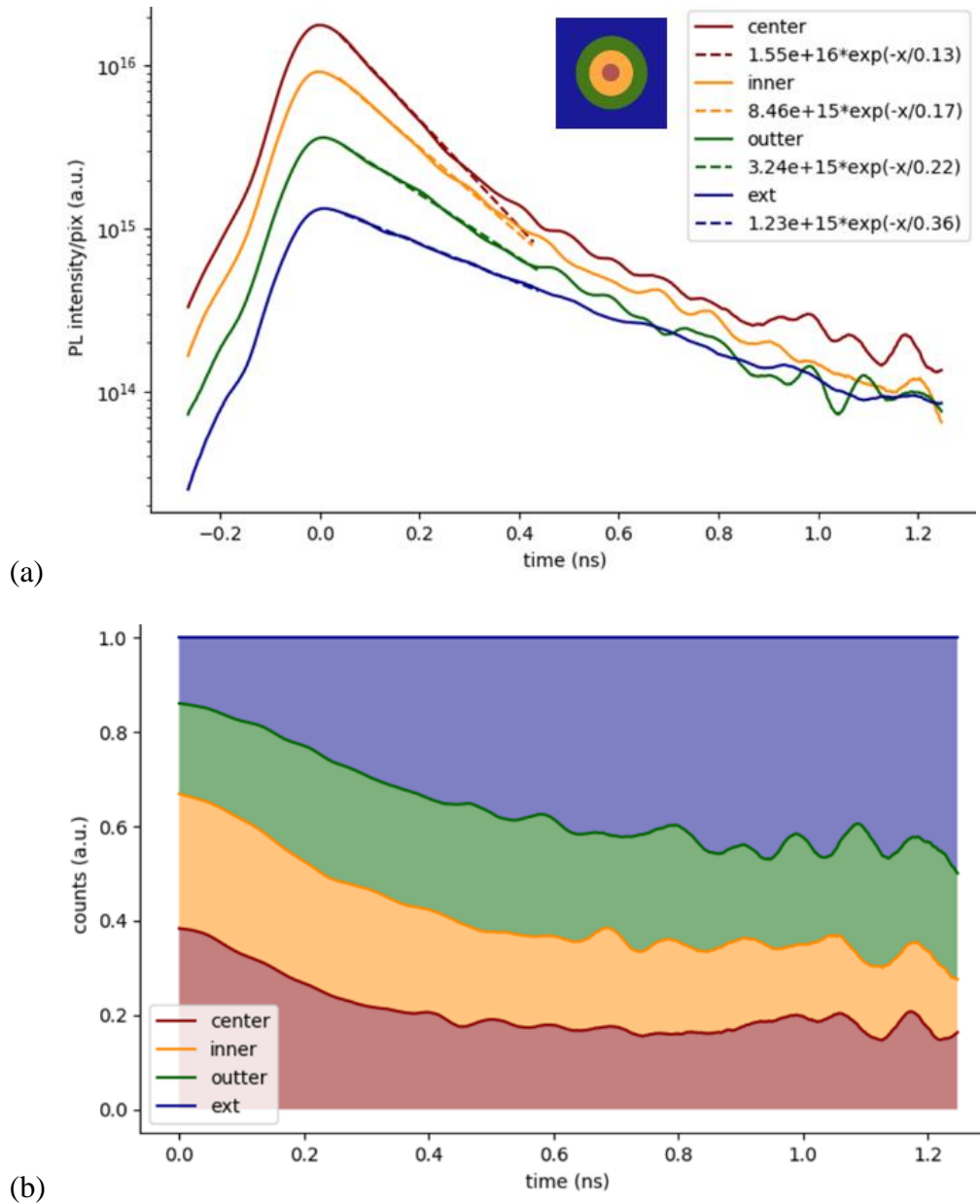


Figure 4-21: Visualization of the charge carrier transport between the different areas of interest. (a) PL decays, and the intensity is divided by the number of pixels in each zone. The short-time characteristic decay time decreases with the distance from the illumination. (b) Cumulative plot of the PL intensity in the areas. PL distribution between the site over time provides an insight into the carrier one, showing a flow from the center zone towards the outer area.

4.III.2 Fluorophores

The measurement of fluorophores in an insulating medium provides validation on a simpler system, as it presents optical transport only. The sample consists of red dyes R305 embedded in a polymer matrix with a thickness of several millimeters and was synthesized in the frame of Florian Proise's thesis²². It is illuminated with the 532nm Talisker laser at a fluence of $\Phi_{exc} = 5 * 10^{13} phot/pulse/cm$.

We do not see any significant shift in the spectral decay, as testified by the isolines in the image of spectra normalized by the initial PL spectrum in Figure 4-22(a). As expected with dyes, the decays in all locations, shown in Figure 19(b), are monoexponential. They owe a characteristic decay time of $\tau_{dec} = 6ns$. As the PLQY is above 95%²², this value is a good approximation of the fluorophore lifetime.

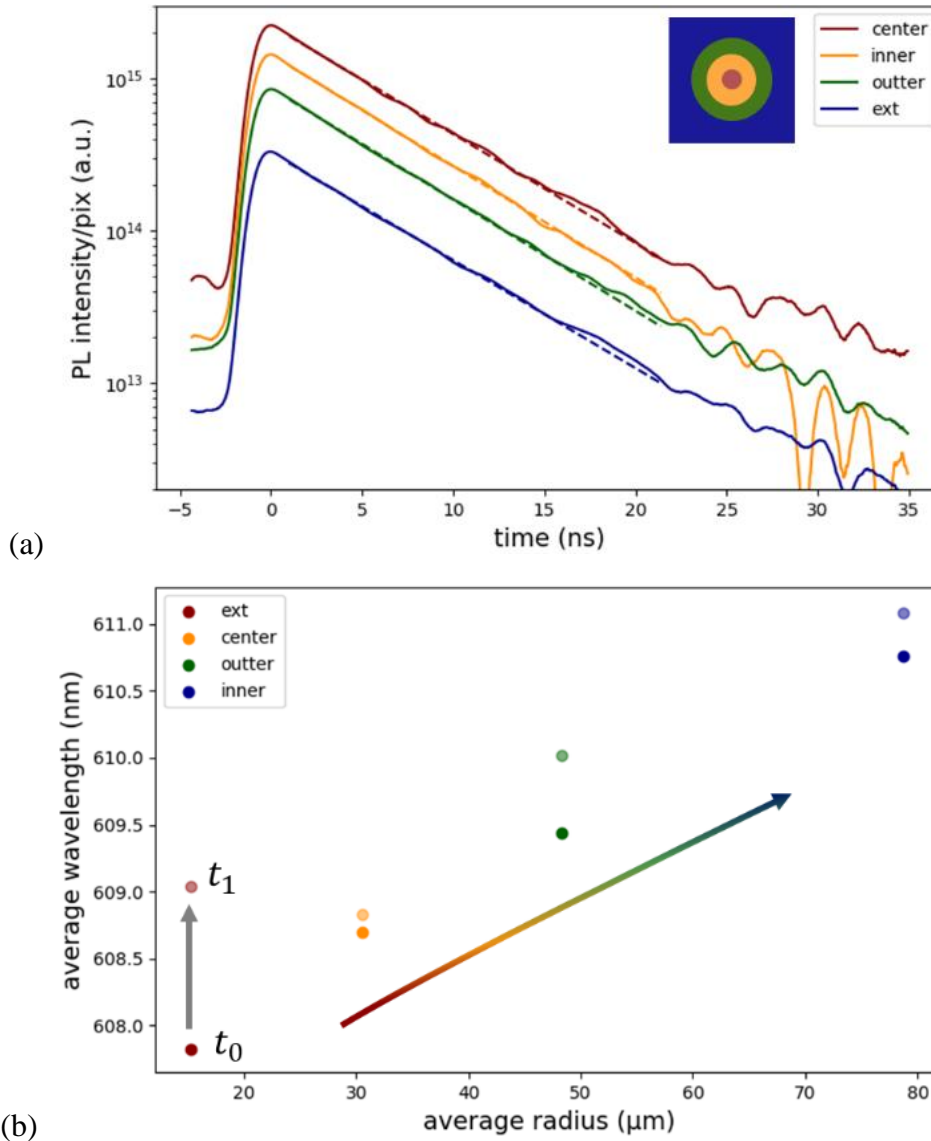


Figure 4-22 (a) Decays in the different areas, they all follow a monoexponential decrease of 6ns characteristic time (b) Average wavelength of the spectra extracted at t_0 and $t_1 = 12ns$, highlighting both temporal and radial redshifts.

The average wavelength shown in Figure 4-22(b) is more sensitive: we observe a spatial and temporal redshift. Far from the center of the illumination, we collect photons emitted close to it that escape due to the surface roughness. They traveled longer within the material, and blue tends to be more reabsorbed, inducing this redshift. It can also be seen temporally as the sample is excited close to the surface, and with time excited states are generated within the material depth by photon recycling.

4.III.3 Perovskites

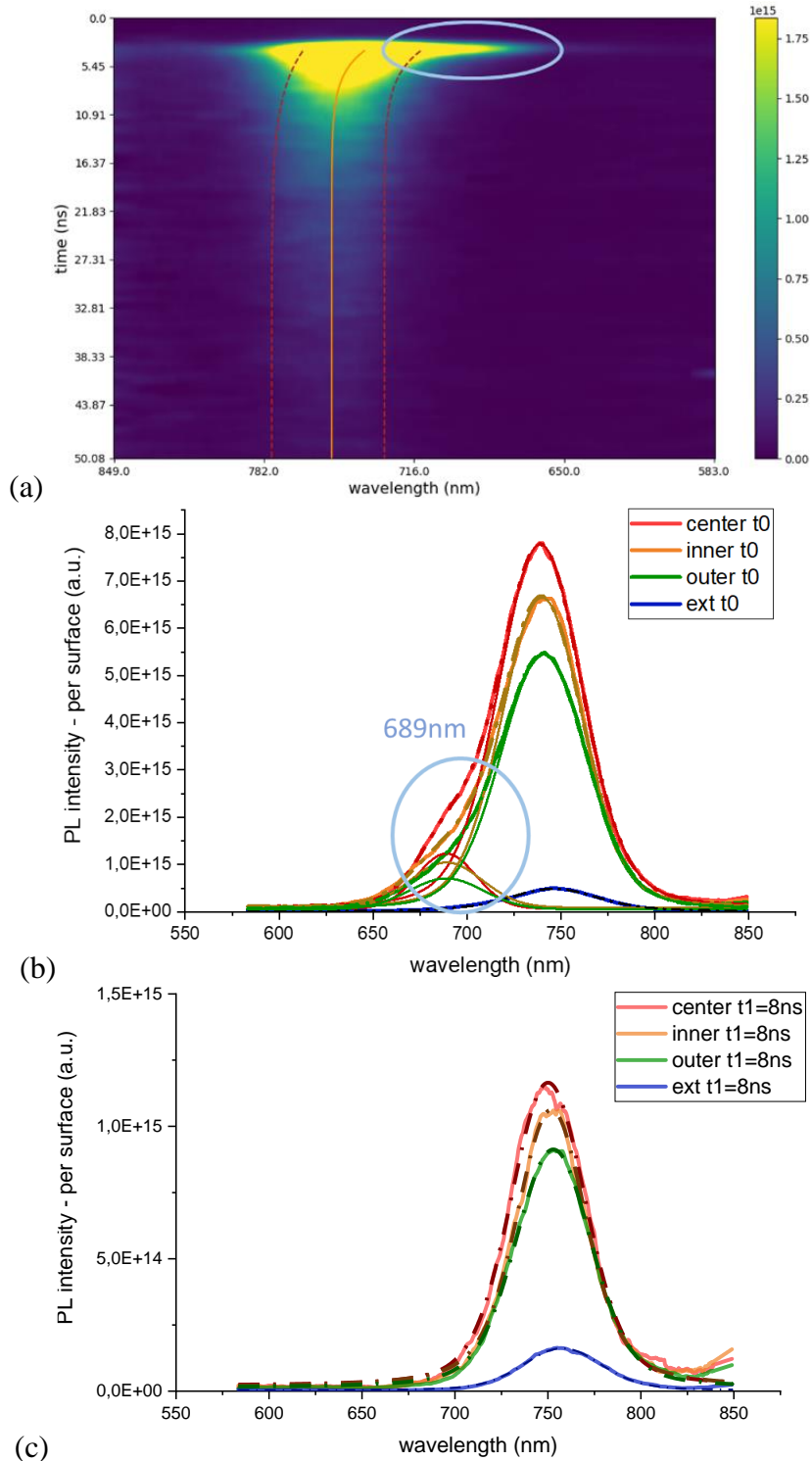


Figure 4-23: (a) Time-resolved photoluminescence intensity in the center area, in arbitrary units. The emitted spectrum shifts during the first nanoseconds and then stabilizes. At a short time a contribution at lower wavelengths is observed. Spectra were extracted in the different areas at the time of the laser pulse (a) and (c) after 8ns. Spectra can be fit by a sum of Voigt function at $t=0$ in the three central locations, with a contribution peaking at 689nm. Fits at $t=8$ ns do not converge for two peaks.

The following paragraph provides a simple illustration of 4D clustering for studying perovskite degradation. The sample characterized was provided by Julia Van der Burgt of the AMOLF institute for a side project. It consists of a 200nm MAPb(Br0.5I0.5)₃ thin film coated with a 15nm aluminum oxide passivating layer. It is observed under point-like illumination with an excitation fluence of $\Phi_{exc} = 3 * 10^{14} phot/pulse/cm^2$. In AMOLF, an initial PL peak was observed at 650nm, that redshifts to 750nm under illumination.

Figure 4-23(a) shows the streak acquisition in the center area, where a hump at high energy can be observed at short times. It can also be distinguished in the inner and outer regions but is not detected in the external ones, as highlighted by the spectra shown in Figure 4-23(b). Indeed, those spectra can be fit by sums of Voigt functions, with a higher energy peak at 689 nm. Due to its location and without prior knowledge, it could be assumed that the peak corresponds to the emission of a second phase induced by the illumination. This segregated phase may have a shorter lifetime and charge carriers transferred to the bulk, as expected due to its higher energy. Another possibility would be that the high injection favors more the photoluminescence in the lower energy phase, that is still present in all locations. It fits better to the prior PL measurements done at AMOLF. Clustering experiments in different injection conditions could help determining the mechanisms at stake.

Spatial and temporal redshifts can also be observed in this sample. Different hypotheses could explain this phenomenon: the optical transport can cause such an effect, as shown in the preceding example; moreover, band-filling or gradient in the composition could explain it. In any case, pixel clustering data can then be useful to observe degradation that is not distinguished by more traditional setups. Indeed, the hump can't be observed on the temporal average of the spectrum. The clustering workflow is then promising to investigate phase segregation.

In summary, pixel clustering workflow allowed observing different evolutions of the time-resolved photoluminescence depending on the material. As well as 4D-PL, it was employed on gallium arsenide at high excitation power. The acquisition duration was much shorter and took ten minutes compared to the dozen hours necessary for acquiring the results presented in 4.III.2. Clear spectra variations with time and location were observed. A higher quality signal would be preferable for quantitative analysis, and longer exposure time would be easily feasible.

Otherwise, fluorophores were used as a model system. The expected monoexponential decays were observed, and redshifts attributed to optical transport can be seen in time and spatially. Pixel clustering was also demonstrated on perovskite: through this technique, local spectral modifications are shown at the beginning of the decay, which can't be accessed with common photoluminescence imaging.

Conclusion

Three different sampling schemes in the spatial, spectral, and temporal domains have been demonstrated in this chapter. They are relevant for various physical problems depending on the data of interest. Single-pixel imaging is the key to accessing the spatial dimension in the different approaches.

Localized light-soaking in triple cations perovskites was monitored by the 2x3D setup at two different injection levels. At the lower one, PL emission is improved over an area wider than the one on which notable excess carriers were generated by the pulse. A redshift of the spectra and location dependent dynamic variation accompanies it. At the higher injection, the properties of the sample are degraded as PL intensity decreases, and lateral spectral variations are observed. In perspective, the issue of comparing spectra acquired in continuous-wave and the transient regime is discussed.

4D-PL imaging allowed the characterization of an III-V wafer under high injection in regimes inducing notable spectral changes attributed to band-filling. In conditions that do not change the absorption shape, temperature and quasi-Fermi level splitting variations could be obtained locally and temporally. Simple models do not hold here, as highlighted by the joint variations of mean energy and intensity. These observables indicate that band-filling, optical transport and probably carrier temperature contribute to the observed trend. A more complex model could be developed as future work to assess the contributions of each.

A variation of 4D-PL allowing a different spatial sampling based on a pixel clustering algorithm is implemented and demonstrated with focused illumination. Its use on gallium arsenide wafer at high fluence illustrates the promises of this approach for band-filling and hot carrier characterization. Measurements on fluorophores show the signature of optical transport. Demonstration on perovskite highlights the presence of degradation that cannot be observed when the spectrum is averaged. In conclusion, it offers a successful generalization of streak spatialization for characterizing various samples and monitoring a wide range of physical phenomena.

Chapter 5 - Photoluminescence excitation spectroscopy

“One very important difference between color and monochromatic photography is this: in black and white you suggest; in color you state. Much can be implied by suggestion, but statement demands certainty... absolute certainty.”

— Paul Outerbridge

This chapter addresses another set of 4D data: rather than further analyzing the light emitted during one experiment, a parametric study is performed. The experiment of varying the excitation wavelength λ_{exc} , known as photoluminescence excitation (PLE) spectroscopy, is performed with a hyperspectral imager. It results in the obtention of the matrix $I(x, y, \lambda_{em}, \lambda_{exc})$ where correlations depend on the probed system.

In the previous chapter, it can be seen that absorption coefficient and absorptivity are involved in the interpretation of photoluminescence data. Section 5.I first develops the motivation to measure these quantities directly through photoluminescence. Particularly, as the emitted light intensity varies with the absorption of the excitation wavelength, PLE offers a potential strategy to reach this goal. We define the quantities at stake and provide a short literature review on this technique. In section 5.II, corresponding theoretical models with different levels of precision are determined. The experimental methods implemented are explained, with highlights on polarization for laser attenuation and calibration of the incident fluence.

A measurement campaign on 3D perovskite coated with a 2D layer is presented in section 5.III. PLE was combined with PL fit to access the relative absorptivity on a wide range and at the local scale. Drift diffusion models support the hypothesis that the regime in which the measurement is performed leads to the same behavior as steady-state. These measures were further completed by local reflectance measurements that provide an insight into the sample topography, which could provide a way to determine the absorption coefficient. Otherwise, section 5.IV illustrates the link of PLE with carrier profile variation on a gallium arsenide cell. PL spectra change as a function of the excitation wavelength in a way which is with a variation of the repartition of charge carriers between layers.

5.I Context and frame of the study

5.I.1 Why employ PL to investigate absorption properties?

Absorption characterization is crucial for understanding material properties and proper PL data interpretation. Accurately measuring the optical properties comes with many issues that PL imaging can address to some extent.

5.I.1.a On the importance of absorption assessment

As detailed in Chapter 1.I, light absorption is described within the material by the absorption coefficient, and at the device scale by the absorptivity. The absorption coefficient is the main material property at stake for photonic transport presented in Chapter 1.II.3. As far as photon absorption induces the generation of an electron-hole pair, it bridges optical and electronic properties. It also reflects the chemical composition of a material through its dependence on the electronic density of states. Assessing it is crucial in optical optimization and defect characterization of photovoltaic devices. Notably, the sub-bandgap absorption coefficient reflects the impurity distribution¹ and may contain the signature of trap states².

However, determining the absorption coefficient comes with many challenges. Indeed, standard techniques measure absorptivity and rely on an optical model to derive it. Also, the absorption coefficient exponential increase in the spectral region of interest is experimentally challenging, as ultralow coefficients need to be measured accurately³. Moreover, it varies with charge carriers' densities⁴ or temperature, and thus with the experimental conditions. A further outcome of its assessment concerns PL imaging, where absorption variation has to be measured for a correct interpretation of PL maps. Indeed, when considering an inhomogeneous PL map, the question arises: are brighter spots emitting more light because they absorbed more, i.e., the number of generated carriers is higher? Or is it due to a superior coefficient for radiative emission? Or lesser non-radiative recombination? One can question the limits of the traditional perfect light absorption assumption. We aim at mapping the absorption properties experimentally rather than assuming its homogeneity.

5.I.1.b Advantages of PL for absorptivity measurements

Absorptivity is classically characterized by transmittance and reflectance measurements. Its accuracy is relative as the thickness of the stack highly influences it. It can also be accessed through ellipsometry, which measures the change in polarization induced by a reflection on the sample. Phase and amplitude changes can then be fitted with models of the dielectric function to obtain thicknesses and refractive indices simultaneously. Yet, these two

approaches are highly dependent on the whole stack structure. Transmittance and reflectance won't have good accuracy when small values are at stake.

PL signal, in which the exponential blackbody law levels the absorption drop around bandgap energy, has been used to determine ultralow absorption coefficient values^{3,5}. Furthermore, PL Imaging techniques are available and provide a way to assess spatial inhomogeneities, whereas classical techniques rarely offer mapping capability.

As pointed out by Jimenez⁶, PL ensures the emitting layer's characterization and avoids the need for complementary ultrathin samples required by absorption measurements of samples as quantum wells. It is also thought to be less affected by interferences and may be useful in case of low absorption that transmission measurements cannot distinguish. One has to keep in mind that PL is still affected by the parasitic absorption of the layers above the emitter⁷. At last, when absorptivity is required in interpreting PL maps, accessing it through PL itself ensures its measurement within the actual experimental conditions. For instance, it considers potential phase segregation in perovskite or the influence of injection that could cause notable band-filling effects.

5.1.2 PLE definition and applications in the literature

The community uses PLE terminology to design different experiments and quantities. This part sets the terminology employed in this chapter. It introduces examples of the literature in which PLE is used to investigate absorption properties or to disentangle the influence of surface and bulk recombination.

5.1.2.a What is PLE?

PLE consists of a parametric experimental approach where the incident wavelength is varied. It also refers to a physical measurement⁸: PLE spectra are defined by the ratio of emitted photons Φ_{em} to the number of photons in the illumination Φ_{exc} for varying excitation wavelengths λ_{exc} . It reads:

$$PLE(\lambda_{exc}) = \frac{\Phi_{em}(\lambda_{exc})}{\Phi_{exc}} \quad (5-1)$$

As shown in Figure 5-1, PLE has to be distinguished from the spectrally resolved PL emission. As a matter of fact, PLE absolute value can be obtained by integrating the spectral emission, as illustrated in Figure 5-1 (a). Iterating this process for each excitation wavelength and normalizing to the incident flux results in the PLE or excitation spectrum pictured in Figure 5-1 (b).

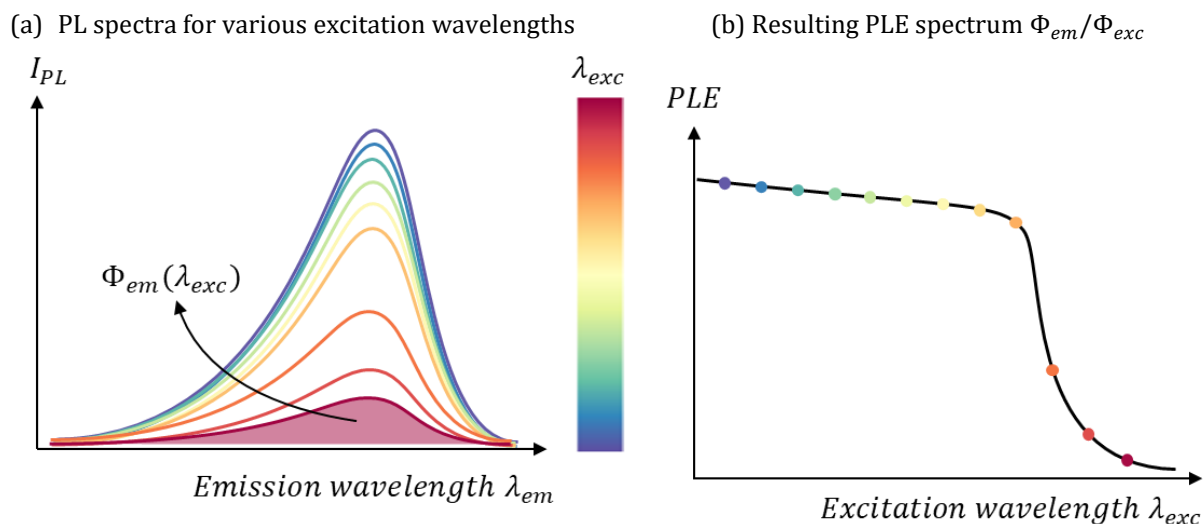


Figure 5-1: Scheme of the obtention of PLE spectra from spectrally resolved PL. The PL spectra obtained for different excitation wavelengths shown in (a) are integrated and normalized to the incident flux to provide the PLE spectrum featured in (b).

In the literature⁶, a variation of this definition can be found, where PLE rather determines the PL intensity at a certain probed wavelength, typically in the low energy part of the spectrum or at the known or expected bandgap energy. The two notions coincide when spectra remain homothetic with the change of excitation wavelength and absolute calibration of the emission is performed. If the terminology PLE applies to both, it is more employed for this second quantity, often assimilated to absorptivity⁹. In this work, we chose to restrict its use to the ratio defined in Equation (5-1) and to name the experiment.

Varying the energy of the excitation changes the quantity and profile of charge carriers generated within the material, see chapter 1.I.1. Higher energies are absorbed more, and in shorter depths, so the PL is dominated by surface recombination⁹, whereas lower energies penetrate deeper. Hence, it offers a way to study material's absorptivity and disentangle bulk and surface contributions.

5.1.2.b PLE for absorptivity measurements

PLE is often considered analogous to absorptivity measurement and serves qualitative reasoning in this frame. Luminescence being emitted close to the surface, identifying species chemisorbed on a semiconductor was performed by measuring the absorption edges of the different materials on the PLE spectrum¹⁰. Classical absorption measurements might be unable to resolve it due to its lower sensitivity. Similar analyses are also especially relevant to investigate nanostructure optical properties. Their absorption spectra feature peaks due to their particular DOS, observable by PLE¹¹, as illustrated in Figure 5-2. Due to their thinness, they are hardly distinguishable in transmission measurements, whereas PL is a way to isolate their signal. In the same way, determining the absorption peak allows for the quantification of Stokes

shift compared to the PL maximum^{12,13}. Therefore, in these different examples, PLE provides only a qualitative assessment of absorptivity.

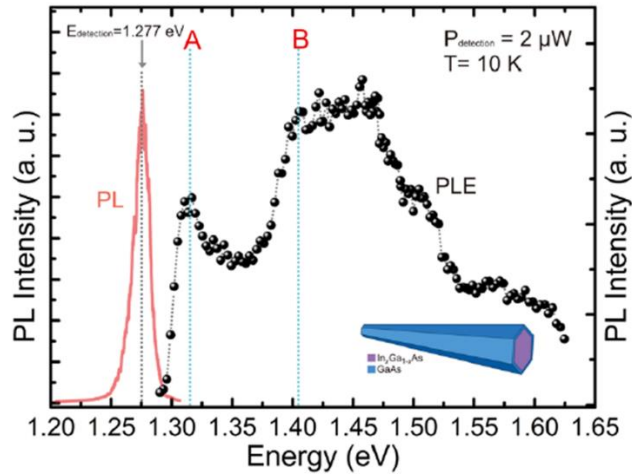


Figure 5-2: Comparison between PL and PLE spectra of wurtzite InGaAs nanoneedles. In such material, the valence band splits into three bands A, B, and C. PLE spectrum features the signature of the absorption in the A and B bands – Source: Wang et al.¹²

5.1.2.c PLE for bulk and surface contribution distinction

As a rule of thumb, the excitation absorption coefficient α_{exc} plays on the depth probed by PL in steady-state d_{PL} as follow⁶:

$$d_{PL} \leq L_d + \frac{1}{\alpha_{exc}} \quad (5-2)$$

Where L_d represents the electronic diffusion length. By changing the bulk and surface contribution ratio to the emitted PL spectrum, PLE provides an insight into their respective properties. Interestingly, this selection of different probed volumes is analogous to two-photon excitation.

Literature shows how PLE can characterize different properties of surfaces. The quality of the CdTe surfaces etched has been assessed in this frame¹⁴: their PL spectra feature several peaks linked to crystalline defects. Invariant spectra with the excitation depth are synonymous with a good-quality surface, whereas relative changes in the peaks indicate the addition of defects by the etching process. In the same vein, PLE can be used to study non-radiative recombination at the surface. Surface defects or band bending can induce a depletion zone close to the interface that can be seen as a 'dead layer' in which PL is bleached. Comparison of PLE spectra allows a direct qualitative assessment of the surface quality, as illustrated in Figure 5-3. Gallium arsenide wafer is known to have a low-quality surface, often passivated by other III-V layers in the form of a double heterostructure. The charge carriers generated close to surface recombine more, increasing PLE with higher excitation wavelengths. In this example¹⁵, a

further drift-simulation fit suggests a reduction of surface recombination velocity of at least two orders of magnitude.

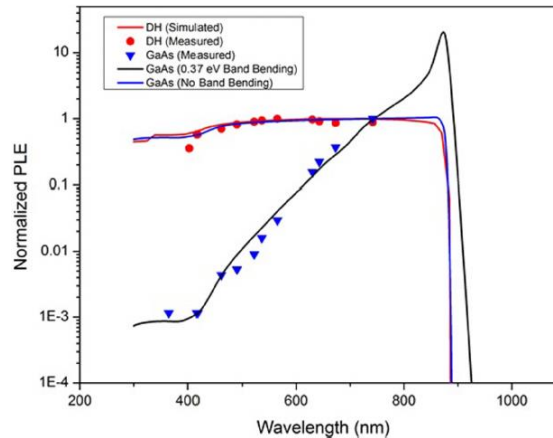


Figure 5-3: Comparison of PLE spectra of GaAs wafer and GaAs double heterostructure (DH), fitted with drift-diffusion simulation – Source Bhosale et al.¹⁵

Moreover, PLE allows the obtention of the dead layer thickness variation by comparing different samples¹⁶. PLE was used jointly with time-resolved photoluminescence to determine simultaneously surface recombination velocity and bulk Shockley-Read-Hall lifetime¹⁷ by fitting with drift-diffusion models.

The two applications mentioned above of PLE involve the characterization of one absorbing layer. It can also be employed on devices by allowing a selective excitation of the different compounds. This method, known as resonant PLE, is often applied to nanostructures. In quantum wells, it enables the distinction of the influence of barriers and wells and characterizes transfers between them. This application is outside the scope of this thesis, and we refer the reader to Jimenez⁶ or Corfdir¹⁸ et al. for further information.

5.II Methods for PLE

This section addresses the theoretical framework and experimental methods used for PLE. Physical models allow us to estimate the emitted light flux from absorption properties and photoluminescence quantum yields. As both photoluminescence and PLE bring information, we use an optical setup that simultaneously captures both.

5.II.1 Theoretical models

The higher the absorptivity of the material at the excitation wavelength $A(\lambda_{exc})$, the more charge carriers are generated in-depth, and the more intense PL is. In this part, we first describe the luminescence intensity based on integrating the radiative recombination rate. Secondly, the notion of spectral emission and outcoupling will be added. At last, the interplay between PL and PLE is detailed.

5.II.1.a PLE estimation

Continuity equations can be written for a given generation function to obtain the charge carrier profiles $n(z)$ and $p(z)$. As stated by Equation (1-13), they allow the obtention of the radiative recombination rate which integration over depth provide the internally emitted light flux. Hence, considering that the internal emission equals the external one, it provides an estimation of the PLE. The whole 5.II.1.a. consider only internal quantities, and notion of outcoupling and reabsorption will be added later. Also, reflection at the front surface are neglected.

Bhosale et al.¹³ determine PLE expression by considering a model in which first-order recombination prevails, characterized with an effective lifetime τ_{eff} . They further assume a generation described by the Hovel model and neglect drift current. Hence, with the notation $\alpha(\lambda_{exc}) = \alpha_{exc}$, the rate equation reads:

$$D_n \frac{d^2 n(z)}{dz^2} - \frac{n(z)}{\tau_{eff}} + \alpha_{exc} \Phi_{exc} e^{-\alpha_{exc} z} = 0 \quad (5-3)$$

We remind the reader that the index of symbols recalls notations and units at the beginning of the manuscript. For a semi-infinite material with diffusion, Bhosale et al. provide the following solution:

$$n(z) = \frac{\alpha_{exc} \Phi_{exc} \tau_{eff}}{1 - \alpha^2 D_n \tau_{eff}} \left(- \frac{S + D_n \alpha_{exc}}{S + \sqrt{\frac{D_n}{\tau_{eff}}}} e^{-\frac{z}{\sqrt{D_n \tau_{eff}}}} + e^{-\alpha_{exc} z} \right) \quad (5-4)$$

For a p-doped material, p is approximated by the acceptor concentration N_A . Approximating the PL emission by the recombination rate (Equation (1-13)) integrated over depth leads to the following PLE expression:

$$PLE(\alpha_{exc}) = BN_A \frac{\alpha_{exc} \Phi_{exc} \tau_{eff}}{1 - \alpha_{exc}^2 D_n \tau_{eff}} \left(- \frac{S + D_n \alpha_{exc}}{S + \sqrt{\frac{D_n}{\tau_{eff}}}} \sqrt{D_n \tau_{eff}} + 1/\alpha_{exc} \right) \quad (5-5)$$

Many hypotheses on the semiconductor are required to obtain this equation, as a more general solution would involve more parameters. A model considering a slab and recombination at both interfaces can be implemented by taking the (long) solutions of rates equations in steady-state.

We refer the reader to the paper by Michl et al.¹⁹ for the analytic expressions of charge carrier densities.

We derive different models following the same reasoning. We assume first-order recombination described by an effective lifetime τ_{eff} is dominant, leading to the same continuity equation as (5-3), and considering negligible surface recombination. A first limit case is derived by assuming that the diffusion coefficient is high so that excess carriers density is constant in-depth on the sample thickness d . It comes:

$$\frac{n}{\tau_{eff}} = \frac{1}{d} \int_0^d \alpha_{exc} \Phi_{exc} e^{-\alpha_{exc} z} dz \quad (5-6)$$

We write $A_{exc} = A(\lambda_{exc})$, reading:

$$n = \tau_{eff} A_{exc} \Phi_{exc} / d \quad (5-7)$$

We assume a slightly p-doped material with an acceptor density N_A , reading $p = n + N_A$. This framework is quite general and allows the obtention of limit cases. Approximating the external PL by the internal one as above, the emitted flux can be obtained from the integration of the radiative rate over depth:

$$\Phi_{em} = \frac{B}{d} (\tau_{eff} A_{exc} \Phi_{exc})^2 + B N_A (\tau_{eff} A_{exc} \Phi_{exc}) \quad (5-8)$$

Leading to the expression of PLE for high and low injection:

$$n \sim p \gg N_A, \quad PLE = B \tau_{eff}^2 A_{exc}^2 \Phi_{exc} / d \quad (5-9a)$$

$$n \ll N_A \sim p, \quad PLE = B N_A \tau_{eff} A_{exc} \quad (5-9b)$$

In high injection, PLE scales with the squared absorptivity and still depends on the excitation fluence, whereas their relation is linear in low injection. These two limit cases alone do not allow the determination of the absolute absorptivity, as it is always multiplied by the unknown τ_{eff} . Yet, these expressions show that PLE offers an easy way to reach the relative absorptivity, provided the sample follows the corresponding assumptions. One can also note that thickness influence results in high injection: increasing it will induce a higher absorptivity and a lower concentration of carriers. In high injection, the emitted flux reduces with thickness in the case of highly absorbing layers.

We can compare this equation to negligible diffusion behavior. Neglecting the diffusion term in Equation (5-3) leads to:

$$n(z) \sim \tau_{eff} \alpha_{exc} \Phi_{exc} e^{-\alpha_{exc} z} \quad (5-10)$$

And its integration leads to:

$$\Phi_{em} = B\tau_{eff}\Phi_{exc} \left(N_A(1 - e^{-\alpha d}) + \frac{\tau_{eff}\Phi_{exc}\alpha}{2}(1 - e^{-2\alpha d}) \right) \quad (5-11)$$

As a result:

$$n \sim p \gg N_A, \quad PLE = \frac{B}{2}\alpha_{exc}\tau_{eff}^2(1 - e^{-2\alpha_{exc}d})\Phi_{exc} \quad (5-12a)$$

$$n \ll N_A \sim p, \quad PLE = BN_A\tau_{eff}A_{exc} \quad (5-12b)$$

The low injection case is similar for high and low carrier diffusion as a consequence of the linearity of the equation in this regime. It allows us to write the relation between *PLE* and absorptivity under the form:

$$PLE(\lambda_{exc}) = A(\lambda_{exc}) * \gamma_{int} \quad (5-13)$$

Where γ_{int} is the internal photoluminescence quantum yield (PLQY). It matches the expression provided by Berdebes et al.⁸, who highlight that this quantity is generally independent of the excitation wavelength. Yet, this result is based on negligible surface recombination contrary to Equation (5-5), which shows that α_{exc} changes the bulk and surface contributions to PL, so that the PLQY depends on the excitation wavelength. High injection leads to different expressions of PLE depending on the diffusion. If large diffusion lengths lead to a PLE varying with A_{exc}^2/d , low ones induce dependence on $\alpha_{exc}(1 - e^{-2\alpha d})$.

PLE is comparable to External Quantum Efficiency (EQE) measurements⁸, which also assess the device's response to different illumination wavelengths, yet through the generated current. It can be written as the product of the absorption and charge carriers' collection efficiency. Thus, in the case of high injection and diffusion, the PLE spectra depend on the squared absorptivity, while the EQE still depends linearly on it.

The theoretical models introduced have focused on the generation of carriers due to different excitation wavelengths. The influence of absorptivity differs with injection regimes: If B , n_d and d are inherently constant with the excitation wavelength, and Φ_{exc} can be kept equal throughout the experiment, solving the continuity equation leads to more advanced models of τ_{eff} that depends on the excitation wavelength through bulk and surface recombination contribution. One should pay attention to the obtained quantity being the internally emitted light flux, which does not consider light transport or reabsorption. Their incidence is discussed in the following paragraph.

5.II.1.b When the light goes out

When integrating the radiative recombination rate over the depth, an internal flux emission is obtained. During the experiment, the measured value is the externally emitted after PL photons are guided towards different directions, experience reabsorption, and recycling. The integration of the photoluminescence emission taking these effects into results in a dependency on the absorptivity expressed by the Planck Generalized law (1-30) rather than on the absorption coefficient. This is a consequence of the reciprocity between emissivity and absorptivity stated by Equation (1-25), which holds for constant quasi-Fermi level splitting as detailed by Araújo et Martí²⁰. This paragraph illustrates the transition from α to A by integrating over depth the spectral emission provided Lasher-Stern-Würfel Equation (1-28) in two simple cases.

We suppose a stable charge carrier profile across the material thickness d , corresponding to a high mobility and low surface recombination, and suppose Boltzmann approximation. **Without reabsorption**, it leads to [*photons/cm²/s/sr/energy*]:

$$I_{PL}(E) = \int_0^d \alpha(E) \varphi_{BB}(E) e^{\Delta\mu/k_B T} dz \quad (5-14)$$

$$I_{PL}(E) = \alpha(E) \varphi_{BB}(E) e^{\Delta\mu/k_B T} d \quad (5-15)$$

This expression corresponds to the Generalized Planck Law within the approximation of low absorptivity $A(E) = \alpha(E) * d$. By comparison, adding a **reabsorption term** $e^{-\alpha z}$ yields:

$$I_{PL}(E) = \int_0^d \alpha(E) e^{-\alpha z} \varphi_{BB}(E) e^{\Delta\mu/k_B T} dz \quad (5-16)$$

$$I_{PL}(E) = (1 - e^{-\alpha d}) \varphi_{BB}(E) e^{\Delta\mu/k_B T} \quad (5-17)$$

This case corresponds to an absorptivity reading $A(E) = 1 - e^{-\alpha(E)d}$. The reflection coefficient at the interface could also be added and still be inscribed in classical absorptivity definitions. However, in actual devices, the carrier profile can be quite different than the homogeneous one required to reach this result. One can note that this model is compatible with the one precedently described. Indeed, with the definition of quasi-Fermi level splitting (1-10) and in case of high injection and diffusion and first-order recombination:

$$e^{\frac{\Delta\mu}{k_B T}} = \frac{1}{n_i^2} * \left(\frac{A(\lambda_{exc}) \Phi_{exc} \tau_{eff}}{d} \right)^2 \quad (5-18)$$

One can write, with the notations of chapter 1:

$$I_{PL}(E) = A(E) \frac{\frac{2n_r^2}{h^3 c^2} E^2}{\exp\left(\frac{E}{kT}\right)} \frac{\left(\frac{A(\lambda_{exc})\Phi_{exc}\tau_{eff}}{d}\right)^2}{n_i^2} \quad (5-19a)$$

$$\Phi_{em} = \Omega \int A(E) \frac{\frac{2n_r^2}{h^3 c^2} E^2}{\exp\left(\frac{E}{kT}\right)} dE \frac{\left(A(\lambda_{exc})\Phi_{exc}\tau_{eff}/d\right)^2}{n_i^2} \quad (5-19b)$$

This relation is analog to equation (5 – 8) with the use of an effective coefficient for radiative recombination B^* that takes reabsorption into account, reading:

$$B^* = \frac{\Omega}{d * n_i^2} \int A(E) \frac{\frac{2n_r^2}{h^3 c^2} E^2}{\exp\left(\frac{E}{kT}\right)} dE \quad (5-20)$$

Similarly, the generation model is very simple and could be refined considering the reflection at the front surface, and replacing the excitation flux by $\Phi_{exc}^* = (1 - R)\Phi_{exc}$.

5.II.1.c Limits of the models

The different models require a strong assumption on the carrier profile: whether constant or expressed with Green's function,ⁱ the analytical solutions might not be sufficient to describe the system. Since the optical profile is 'blurred' depending among others on the diffusion length, as equation (5 – 2) shows, there is no general rule to retrieve the absorption coefficient from the PL signal. Determining absorption properties from PL requires a good knowledge of the material electronic properties or to cross the analysis to determine both simultaneously. The extent of details known about it will define the most precise model we can use to process our data.

The above-mentioned models rely on very simple optical considerations, whereas a more accurate determination of the generation profile can be done with the transfer matrix method (TMM). This methodology relies on both real and imaginary parts of the optical index and thus requires reflectivity as an extra input. Moreover, these models are based on steady-state regime, whereas the experiments were conducted with a pulsed laser, as explained in the following section.

ⁱ Functions solution to partial differential equations owing a Dirac as right term. The solution to more general problems can be written as convolution of Green's functions.

5.II.1.d PL and absorption interplay

When describing PL, light absorption influences the generation function at the excitation wavelength, as seen in the equations (5 – 3), (5 – 8) and (5 – 13). It also plays a role, in a spectral range close to the bandgap energy, on the photonic emission by directly appearing in the coefficient for radiative recombination expressed in equation (5-20). In this domain, propagation and reabsorption are affected as well. This double dependency is summarized in Figure 5-1.

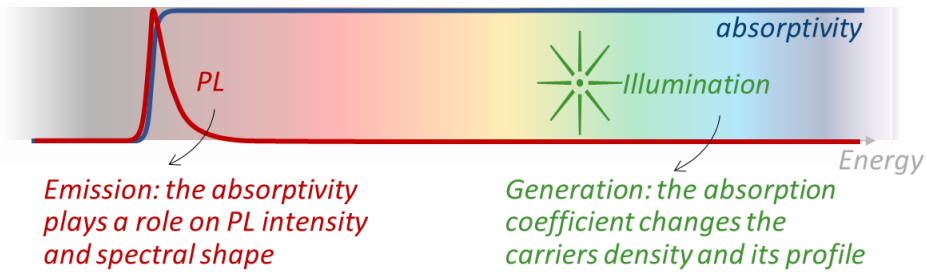


Figure 5-4: Schematic representation of the interplay between PL and absorptivity. The emitted photoluminescence spectrum is shaped by the absorptivity of the device, multiplied by the blackbody radiation. The absorptivity of the illumination varies the number of carriers generated, affecting mainly PL intensity.

In the following, an intrinsic semiconductor is characterized, and in this frame, the equation (5 – 9) shows that PLE allows to access quite easily the relative absorptivity $\tilde{A}(E)$. Posing $A(E) = \chi_A * \tilde{A}(E)$ where χ_A is a scaling factor, and considering the intrinsic semiconductor case described by equations (5 – 19), it reads:

$$\Phi_{em}(E) = \chi_A^3 \tau_{eff}^2 \left[\Omega \int \tilde{A}(E) \frac{2n_r^2 E^2}{h^3 c^2 \exp\left(\frac{E}{kT}\right)} dE \left(\frac{\tilde{A}(\lambda_{exc}) \Phi_{exc}}{dn_i^2} \right)^2 \right] \quad (5-21)$$

Where the quantities at stake in the brackets are often assumed known and independent of the location. Thus, the absolute PLE is sensitive to $\chi_A^3 * \tau_{eff}^2$ and does not provide the scaled absorptivity. If the sample is optically thick enough, a saturation of the absorptivity is expected at high energies E_{sat} . It provides a first way to scale it, assuming $\chi_A * \tilde{A}(E) \sim 1 - R(E_{sat})$. In other case, absolute PLE can provide a lower limit of the effective lifetime.

5.II.2 PLE Optical setup

The setup we employed is described in Chapter 2.II.2 and pictured in Figure 5-5 (a). We chose to vary the excitation wavelength on the hyperspectral imager bench to capture potential spectral changes and simultaneously exploit the spectral emission and PLE. The sample is

illuminated with a supercontinuum pulsed laser NKT SuperK with an 80MHz repetition rate and spectrally filtered by a monochromator. It is set to the maximal repetition rate to approach the continuous regime as much as possible. In this section, we describe the laser attenuation by polarization and the calibration of the excitation flux for PLE. Indeed, these questions were not addressed in the previous use of this characterization bench.

5.II.2.a Laser attenuation by polarization

As shown in Figure 5-5 (a), the laser is attenuated by placing two linear polarizers orthogonally. This configuration allows an attenuation independent of the laser wavelength and is relatively easy to implement. We can assess this configuration by quantifying the minimum external luminescence quantum efficiency γ_{ext} it can measure. Indeed, in the limiting case where the laser reflection saturates the camera, the dynamic range available for PL characterization DR_{PL} can be obtained from the camera dynamic range DR_{cam} as follow:

$$DR_{PL} = DR_{cam} * I_{PL,max}/I_{las,max} \quad (5-22)$$

Where $I_{PL,max}$ and $I_{las,max}$ express the number of counts attributed to the spectral peaks of PL and laser intensities, respectively. These are linked to I_{PL} and I_{las} , the corresponding total counts integrated over the wavelengths. Noting $\Delta\lambda_{PL}$ the spectral full-width half maximum of PL, as a first approximation, the peak number of counts is:

$$I_{PL,max} = \frac{I_{PL}}{\Delta\lambda_{PL}} \quad (5-23)$$

The same hold for laser reflection. For a given laser incident flux Φ_{exc} [photons/cm²/s], a spatially homogeneous problem is assumed, and dark current and noises are neglected. The camera response function $TF(\lambda)$ corresponds to the number of camera intensity counts per photon of a given wavelength collected during the acquisition time on a surface area unit. As highlighted in Figure 5-5 (a) and (b), we consider that the laser is reflected with a reflectivity R , filtered by the beam splitter, and later attenuated by the second linear polarizer by a factor denoted att . Considering a specular model in which all photons reflected are collected, it reads:

$$I_{las} = R * \Phi_{exc} * TF(\lambda)/att/2 \quad (5-24)$$

PL emission is supposed to be Lambertian. As recalled in Figure 5-5(b), the objective collects light in an effective solid angle Ω_{eff} related to its numerical aperture NA , so that:

$$I_{PL} = \gamma_{ext} * NA^2 * \Phi_{exc} * TF(\lambda)/16 \quad (5-25)$$

As the target wavelength for laser attenuation is the same as for emission, the instrumental response function is similar for PL and laser reflection. It comes:

$$DR_{PL} = DR_{cam} * \gamma_{ext} * \frac{NA^2 * att}{8R} * \frac{\Delta\lambda_{las}}{\Delta\lambda_{PL}} \quad (5-26)$$

In a classical configuration, measurements are done with a x10 objective of 0.4 numerical aperture. The laser attenuation experimentally obtained is typically around 1/300 and was measured by comparing the counts when the linear polarizer is orthogonal or parallel. For a 16-bit camera, a PL dynamic range of 100 counts can be obtained for samples where $\gamma_{ext}/R \geq 0.002$.

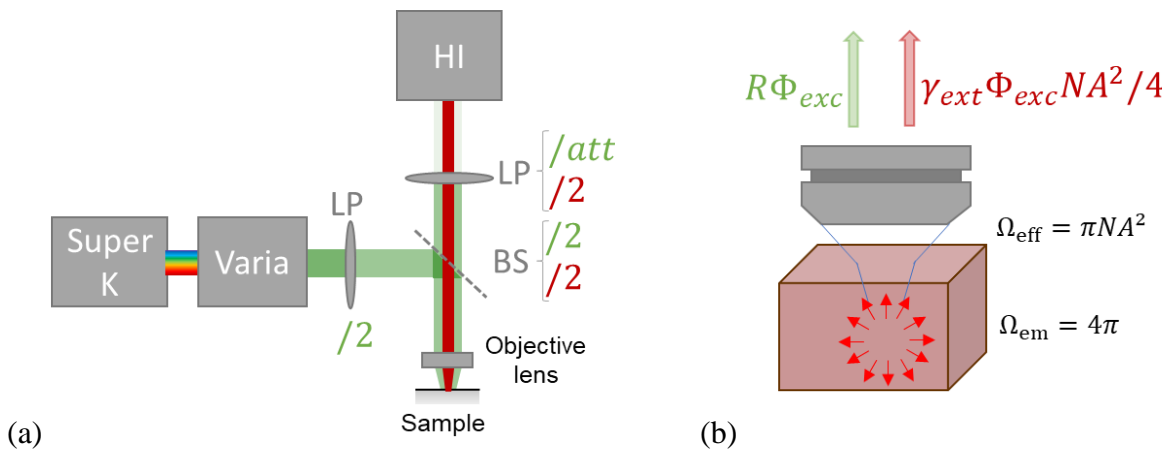


Figure 5-5: (a) Optical setup and losses induced by the components. The excitation wavelength is selected from a supercontinuum pulsed laser by a monochromator (Varia). The output light is polarized linearly (LP), and half of the flux is directed toward the sample by a beam splitter (BS). Reflected illumination and PL collected by a microscope objective go through the beam splitter and a linear polarizer that attenuates the laser up to a factor of 300. (b) Detail of the sample emission and the microscope collection. The PL isotropic emission is collected over an effective solid angle Ω_{eff} characteristic of the objective.

Therefore, this approach is suitable for samples with a relatively high quantum yield compared to reflectivity. It is feasible with perovskites samples, which owe a reflective index of around 0.1 on a wide spectral range, and can be probed with γ_{ext} down to 0.02%. For highly reflective samples, such as gallium arsenide wafers, spectral attenuation of the reflected laser flux is preferred. Experimentally, after being decreased by polarization, the laser reflection was too high compared to the PL signal to perform acquisitions as soon as it is in the [750nm-950nm] range characterized by the camera. This observation holds for preliminary experiments performed with a camera of 12-bit digitization range instead of 16-bit. By comparison, spectral filters typically divide by 10^4 up to 10^7 the transmitted light flux and can be summed. They allow the collection of PL with almost no restriction on the external PL quantum efficiency to the expense of a reduced spectral range. Other setups employing polarization (with polarizing

beam splitter, modified Faraday insulator, or $\lambda/4$ waveplate) have been first considered and are provided in appendix E.

The attenuation of laser reflection can be compared to the one provided by commercial Faraday Isolators. Thorlabs tandem isolator IOT-5-850-VLP offers a 55dB (~ 500) attenuation, along with an 80% transmission. However, such performances are restricted to a 40 nm wide spectral range. IO-5-NIR-LP and IO-5BB-800-HP are efficient on a broader bandwidth, though with reduced attenuations of 35 dB (60) and 30dB (30). The attenuation has to be put in regard to the reflectance of lenses, whose anti-reflective coating is decreased to 1% or 0.5%ⁱⁱ. Using two linear polarizers is a satisfactory compromise to reduce the laser illumination as efficiently as possible on a wide spectrum.

5.II.2.b Calibration of the excitation flux

As mentioned previously, PLQY depends on the charge carrier density. Thus, measuring constant PL would be a way to remove one factor of uncertainty. However, this approach is not straightforward regarding hyperspectral imaging: in case of disparities, in what region and wavelength should the PL intensity be kept constant? To avoid an arbitrary decision, we followed the approach mainly pursued in the literature and set our measurement at a given fluence for all wavelengths.

The fluence calibration is obtained from the light flux estimated with a powermeter and spot size measurements. During the experiment, a powermeter is placed after the beamsplitter in the incident laser beam continuation. Because light is polarized, the beam splitter is not 50%-50% anymore, and the proportion of light sent to the powermeter changes with the wavelength. A prior calibration of this powermeter is necessary, with a second one placed below the objective. The spot surface size is rather constant with wavelength when the laser is homogenized with a squared fiber and collimated with a x20 Olympus objective. However, it varied by 70% when obtained from a defocused round core fiber with different optics. Therefore, this parameter must be paid attention to for reliable results.

This section shows that PL interpretation depends greatly on the material and structure probed. In the following, experiments on perovskites and gallium arsenide structures are demonstrated and allow for highlighting the PLE link to absorptivity and carrier profile, as well as discussing the applicable models.

ⁱⁱ Specifications for AB and B coating as provided by Thorlabs

5.III PLE experiments for perovskite absorptivity investigation

In this section, we investigate the potential of PLE to characterize the absorptivity of perovskite samples. We use PL dependencies on excitation and emission wavelengths to obtain the absorptivity of the bulk material on a wide spectral range. Firstly, we acquire and analyze the PL spectrum of a perovskite sample to get the absorptivity close to the bandgap. Then, PLE is performed to assess it at higher energies. We discuss the validity of our approach based on a drift-diffusion model and consider photon reabsorption. Spatially resolved reflection measurements provide further insights into the sample structure. It brings knowledge key for a potential absorption coefficient determination.

5.III.1 Sample and method

This part presents the sample characterized by hyperspectral PLE. The experimental details for the measurement campaign are presented, as well as the modeling approach allowing us to discuss our results.

5.III.1.a Sample structure and fabrication

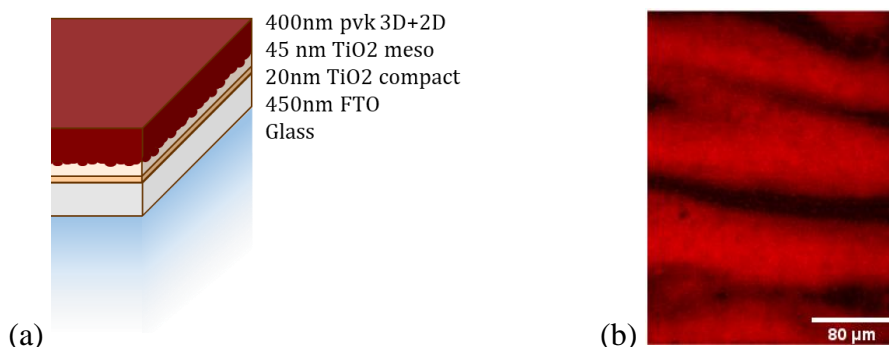


Figure 5-6: (a) Structure of the perovskite stack under study. (b) Image of reflection of white light illumination onto the sample at 810nm.

The sample under study is described in Figure 5-6(a) and fabricated as follows. FTO-coated glass substrates are cleaned, and a compact-TiO₂ electron transport layer (ETL) is synthesized onto it by atomic layer deposition (ALD). Mesoporous TiO₂ is then spin-coated and annealed on top of the c- TiO₂ layer before the Glass/FTO/TiO₂ substrates are treated with UV-Ozone. The triple-cation perovskite solution consists of a mixture of a solution of CsI in DMSO and another solution of MABr, PbBr₂, FAI, and PbI₂ of a DMF and DMSO mix. It is deposited onto the substrates by spin coating resulting in a $Cs_{0.05}(MA_{0.17}FA_{0.83})_{0.95}Pb(I_{0.83}Br_{0.17})_3$ thin film that is annealed. Finally, a 4-FPEAI solution dissolved in IPA at a concentration of $2.5 \text{ mg} \cdot \text{mL}^{-1}$ was then spin-coated onto the 3D perovskite and annealed. Figure 5-6 (b) shows the sample reflection at 810nm: spatial inhomogeneities are visible.

During this experiment campaign, the laser is further filtered with Thorlabs short pass FESH 800nm and FESH 850nm filters to ensure there is no second order. It is homogenized through a square-core optical fiber and concentrated by the x10 objective onto a 400-micrometer side square, with a constant photon flux of 10^{15} photon/s. It corresponds to an average fluence of $6.25 * 10^{17}$ photon/cm²/s (close to 2 suns illumination). Considering the pulse of 80ps FWHM at 78MHz, these values are multiplied by 160 during the burst of light. Eight different wavelengths of excitations are selected between 600 and 780nm, and owe a 10nm spectral FWHM for each.

5.III.1.b PLE experimental details

The experiments are performed by increasing wavelength, and one more acquisition is taken at 600nm at the end of the experiment to assess the repeatability of the experiment and monitor the potential light-soaking. To mitigate this effect, the sample was placed in a cryostat at -10°C in a nitrogen flow and waited to stabilize the spectral peak. Indeed, the first measurements showed a redshift from 670nm to 675nm during 15mn. The data collected are spatial maps of PL spectra that provides a map of PLE. For the sake of simplicity, we performed pixel clustering analysis on an image of reflection at 810nm. It allows us to distinguish five areas of interest in which the spectra are averaged and analyzed. They are shown in the inset of Figure 5-8.

5.III.1.c Simulation

Drift-diffusion simulations of the PLE experiments are conducted in a transient regime with a one-dimensional homemade code. It calculates the emitted PL from the steps described in Figure 5-1: for each wavelength, the generated carriers' profiles are calculated, their transport is obtained by drift-diffusion, and the emitted PL is calculated in-depth and propagated by taking into account reabsorption. For the sake of simplicity, the perovskite sample is modeled as a homogeneous slab 400nm thick.

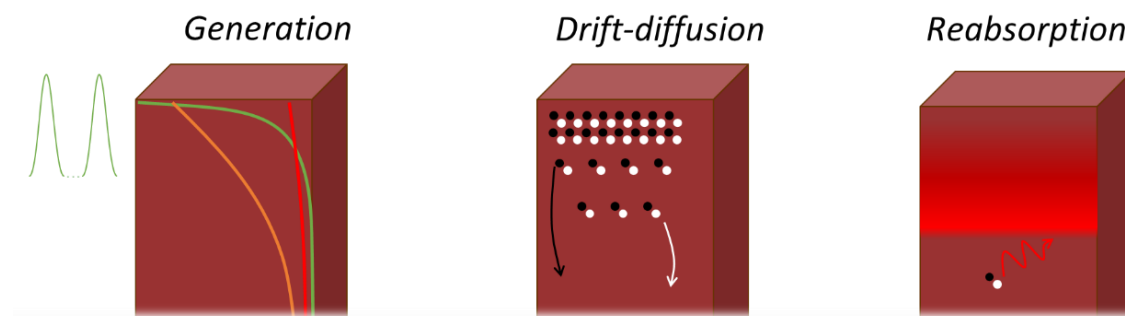


Figure 5-7: Principle of the drift-diffusion model: generation from Beer-Lambert law, drift-diffusion of the carriers, and PL model.

First, the generation profile is modeled from the Beer-Lambert law for an excitation fluence corresponding to the experimental one, leading to $7.8e9$ photons/pulse. The absorption coefficient to estimate this generation profile is based on transmission and reflection measurements carried in a regular spectrometer. It is prolonged above the bandgap wavelength with a straight exponential tail with an Urbach energy of $30meV$ to allow PL modeling.

Second, the drift-diffusion of the generated carriers is computed based on continuity equations for both electrons and holes. They provide the variation of carrier density n due to transport (drift due to the electric field E and diffusion of coefficient D_n), generation and recombination rates (resp. G and R). For electrons, it reads as

$$\frac{\partial n}{\partial t} = \frac{1}{q} \text{div} (J_n) + G - R \quad (5-27)$$

$$J_n = D_n \text{grad}(n) + \mu_n n E_n \quad (5-28)$$

The Poisson equation and boundary conditions complete these. We set the front recombination velocity at $S_{front} = 100cm/s$ and the back one at $S_{rear} = 10cm/s$, taking orders of magnitudes similar to the literature²¹. This assumption is motivated by the presence of 2D perovskite on top that passivates the sample, and the interface perovskite-TiO2 can be considered well passivated and inducing a low surface recombination velocity. Electrons and holes mobility of $1cm^2/(V.s)$ were assumed.

At last, the PL is calculated spectrally along the depth z with Van Roosbroeck-Shockley equation²², i.e., by a function of carrier concentration, weighted by a reabsorption term $\exp(-\alpha(E)z)$. The emitted PL reads

$$I_{pl}(E) \propto \int_0^d \alpha(E) E^2 \exp\left(-\frac{E}{kT}\right) \cdot \exp(-\alpha(E)z) \cdot n(z) \cdot p(z) \cdot dz \quad (5-29)$$

Very notably, this code provides a way to obtain spectral decay and thus simulate streak camera acquisition. This simulation is valid for classical regimes without band-filling, and could highlight spectral changes due to in-depth diffusion.

5.III.2 Result and discussion

PL absorptivity fit, and PLE results are first introduced and then compared. We discuss the difference between the relative variations obtained close to the bandgap energy based on the drift-simulation results.

5.III.2.a Luminescence Spectral Fit

As a consequence of equation (5-21), dividing photoluminescence spectra by the blackbody radiation directly provides the relative absorptivity. When normalizing to the peak intensity, it reads:

$$\frac{A(E)}{A(E_{I_{max}})} = \frac{I(E)}{I(E_{I_{max}})} * \frac{E_{I_{max}}^2}{\exp\left(\frac{E_{I_{max}}}{kT}\right)} * \frac{\exp\left(\frac{E}{kT}\right)}{E^2} \quad (5-30)$$

This calculation is performed with the laser excitation wavelength set at 600nm to ensure the absence of a parasitic peak on the spectrum coming from the illumination. The results are presented in Figure 5-8 in different areas of the sample. In this case, the relative absorptivity is normalized by the peak energy value in each area. One should be careful that the relative intensity values are not directly comparable between locations that might have different peak energy and hence a different normalization. One could also consider normalizing the relative absorptivity by the saturation values at high energies, assuming that it approaches 1-R. It results in almost overlapping curves and does not have incidence for the fit perform afterwards.

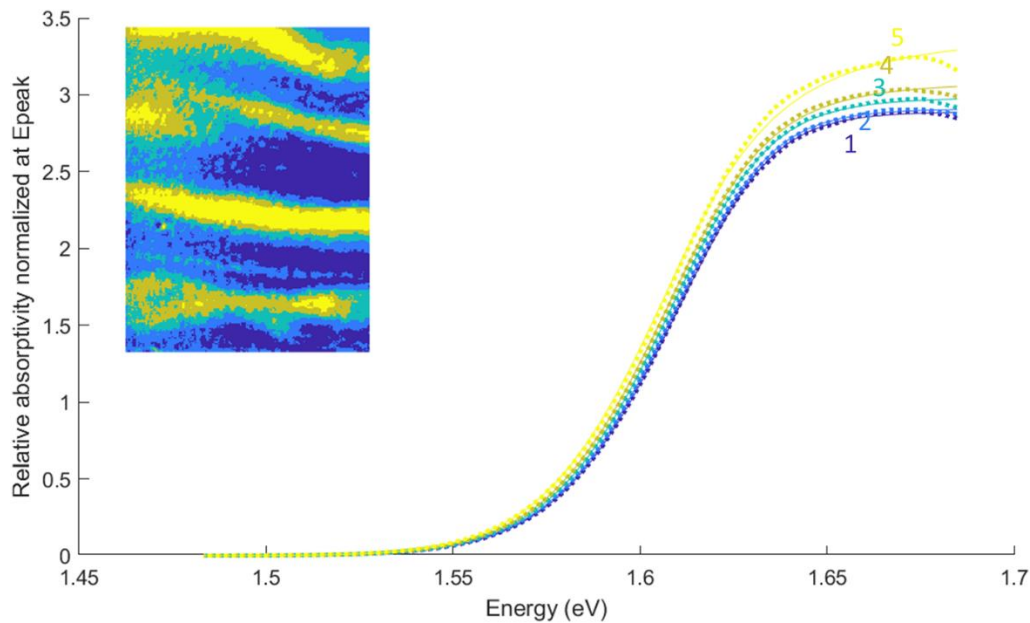


Figure 5-8: Absorptivity normalized at the peak energy (dashed lines) in five sample areas which are determined from pixel clustering on the reflection image and shown in the inset. They are numbered by increasing intensities – the deep blue one being the less emitting. The absorptivities are fit with the Katahara model (solid lines).

As a reminder, the model of Equation (5-33) is based on strong physical assumptions. Indeed, stating that PL spectra can reflect the absorption coefficient of the sample implies that^{3,5} the carriers' densities profile is approximately uniform, and reabsorption and parasitic

absorption of the other layers are negligible. The latter statement is particularly constraining and contradictory with the data, as the relative absorption saturates at high energy. Moreover, P. Fassl et al.²³ have shown that the PL spectra can be greatly distorted by reabsorption in high PLQY perovskites. Furthermore, the case of imaging requires that the influence of lateral carrier diffusion and photon smearing is negligible, which depends on the magnification and instrument resolution.

This relative absorptivity can be further fitted with an absorption coefficient model and assuming a Beer-Lambert law, as introduced in Chapter 1, section II.1. Katahara model¹ described by Equation (1-33) is employed with a fixed parameter θ and for varying tail characteristic energy γ . A further parameter α_0 is considered, that scales the ideal square root absorptivity, and is always multiplied by d . Hence, we fit $A(E) = ct * (1 - \exp(-\alpha(E, E_g, \gamma, \theta)d))$. Our data fit reasonably with $\theta = 1,5$. Results for the bandgap and the tail energies are indicated in the legend of Table 1. The obtained values are very similar in the different areas and suggest that the absorption coefficient of the material is homogeneous for energies below the gap. By performing such a fit, it is possible to retrieve the absorption coefficient multiplied by the absorber depth, which corresponds to the optical thickness and is shown in Table 1. This approach still strongly relies on the optical model and cannot disentangle it from the height of the sample.

Table 1: Katahara fit results in the different areas

area	1	2	3	4	5
E_g (eV)	1.63	1.63	1.63	1.62	1.61
γ (meV)	36	36	35	34	33
$\alpha_0 d$	13.4	23.8	19.1	27.3	28

5.III.2.b PLE

The hyperspectral measurements were absolutely calibrated, so it is possible to obtain the number of photons emitted locally by integrating the signal spectrally. For excitation wavelengths above 675nm, the reflection of the laser is visible on the spectra. To ensure that it is not taken into account in the PLE calculation in such cases, the spectral integration is performed between 800 and 850nm and scaled to the spectrum emitted with an excitation at 600nm. The obtained result presented in Figure 5-9 shows an increase in PL with the excitation energy in all regions of interest. The shape shows a similar trend to the squared absorption of the sample measured with a regular spectrometer plotted in sky blue.

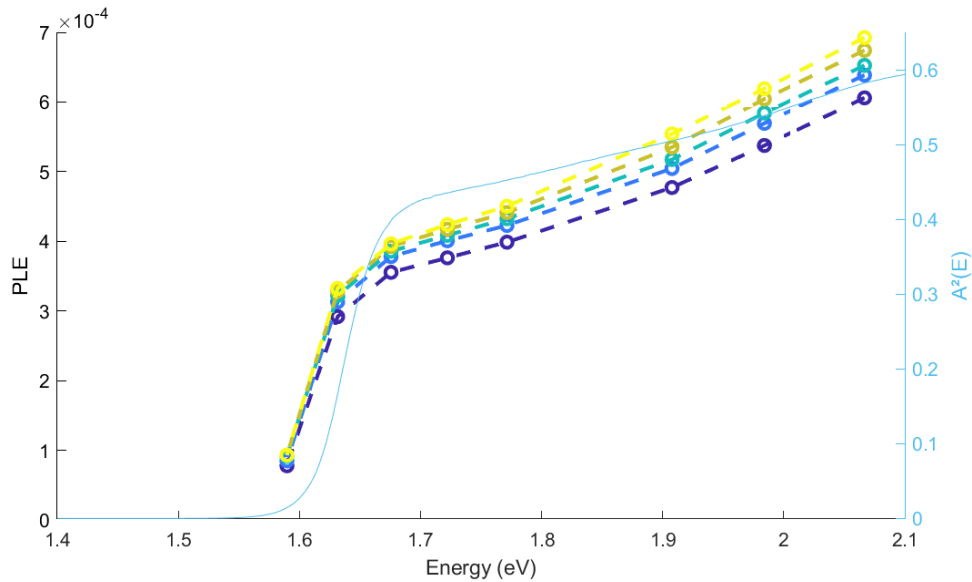


Figure 5-9: PLE spectra for the different areas of the sample (the color code is similar to previous figures). The sky-blue line displays the squared absorptivity obtained with a spectrometer.

The steep increase in PLE happens at energies lower than the absorptivity. This is consistent with the ~ 0.1 eV redshift observed before launching the measurement series and mentioned in 5.III.1. It highlights the dependence of absorptivity on experimental conditions and the need for its measurement simultaneously with the PL experiment. Moreover, the slope of PLE is steeper than the one of absorptivity. It might come once more from a change in absorptivity between the two measurements also induced by light soaking. It could also indicate that the internal PL quantum yield increases with the energy. That would mean that generating close to the surface leads to a relatively higher quasi-Fermi level splitting. It can be explained by a better front interface than the rear one. As indicated by equations (5-8) and (5-9), the PLE varies with $\tau_{eff}^2 A(E_{exc})/d$. Thus, the scaling between areas can come from thickness, effective lifetime or absorptivity variations.

5.III.2.c Combining the results

Figure 5-10 compares the absorptivity values obtained in the two spectral ranges scaled at 1.61eV. The absorptivity obtained by PL fit and the squared PLE both features a rise close to 1.6eV. Yet, the three squared PLE measurement points in the PL fit energy range do not scale with it. The 10nm laser spectral width employed in the experiment corresponds to a minimum horizontal error bar of 20meV, which could greatly contribute to this misalignment as highlighted by the cross marks indicating this spectral width. However, when taking the rolling average to quickly evaluate the impact of a convolution with the laser spectral width, a window of 30nm need to be taken to obtain parallel curves close to the bandgap energy. A change in the injection regime could also contribute to this difference: as shown by Equation (5-8), nonnegligible doping when the light is less absorbed. The PLE maybe scales linearly with the

absorptivity in this particular spectral region. As noted earlier, the relative absorptivity is obtained with different proportionality factors depending on the location for both methods.

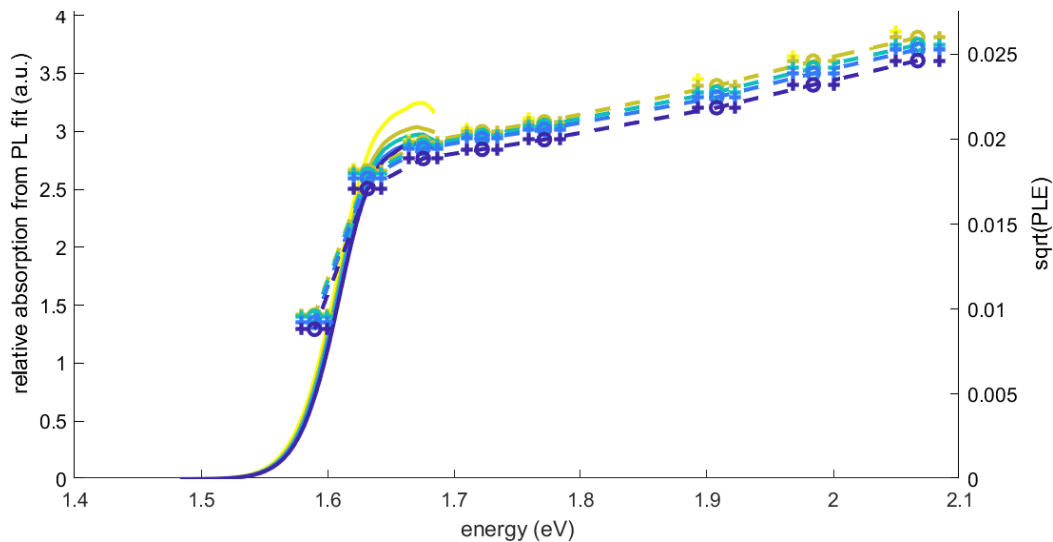


Figure 5-10: Combination of PL fit and PLE. The dashed lines at high energies represent the curves obtained by PLE. The cross markers associated to them correspond to the spectral width of the excitation laser and provide an idea of the error bars induced by it. PL fit is the solid lines and allows the obtention of absorptivity below 1.7eV. The scales are adjusted so that the relative absorption averaged on the different areas matches the averaged squared PLE at 1.61eV.

Furthermore, as we have seen in Chapter 4, PL spectra emitted in continuous-wave and pulsed excitation are fundamentally different. The PLE scaling with absorptivity is studied in the transient regime and determines if it contributes to the difference in the spectra obtained by the two approaches.

5.III.2.d Model validity

Contrary to classical PLE measurements, the excitation source used is pulsed. Drift diffusion calculation tends to support that it is of little consequence, as shown in this paragraph. Indeed, with such a high repetition rate, Figure 5-11(a) shows that the carrier concentration varies a little during the decay: at the front interface, where its variation is maximal, its amount decreases by 15%. Moreover, the carrier profile is quite flat each time: the variation between the front and rear surfaces is less than 5% each time. For an intrinsic semiconductor, PL intensity is proportional to the squared density of carriers. Hence, we expect PLE to scale as the square of absorptivity. That is confirmed by the simulation in Figure 5-11(b). For energies above the bandgap, the absorptivity and square root of PLE differs by less than 2% when scaled at 700nm. This difference is about the setup measurement uncertainty. For higher wavelengths, PLE overestimation of absorptivity keeps increasing, as illustrated in Figure 5-11(c). A potential explanation lies in the fact that generated carrier density is lower and the contribution

of monomolecular recombination increases. For instance, at 900nm, the generated carrier density is of the order of $10^9/cm^3$, and the intrinsic carrier concentration of $7 * 10^7/cm^3$.

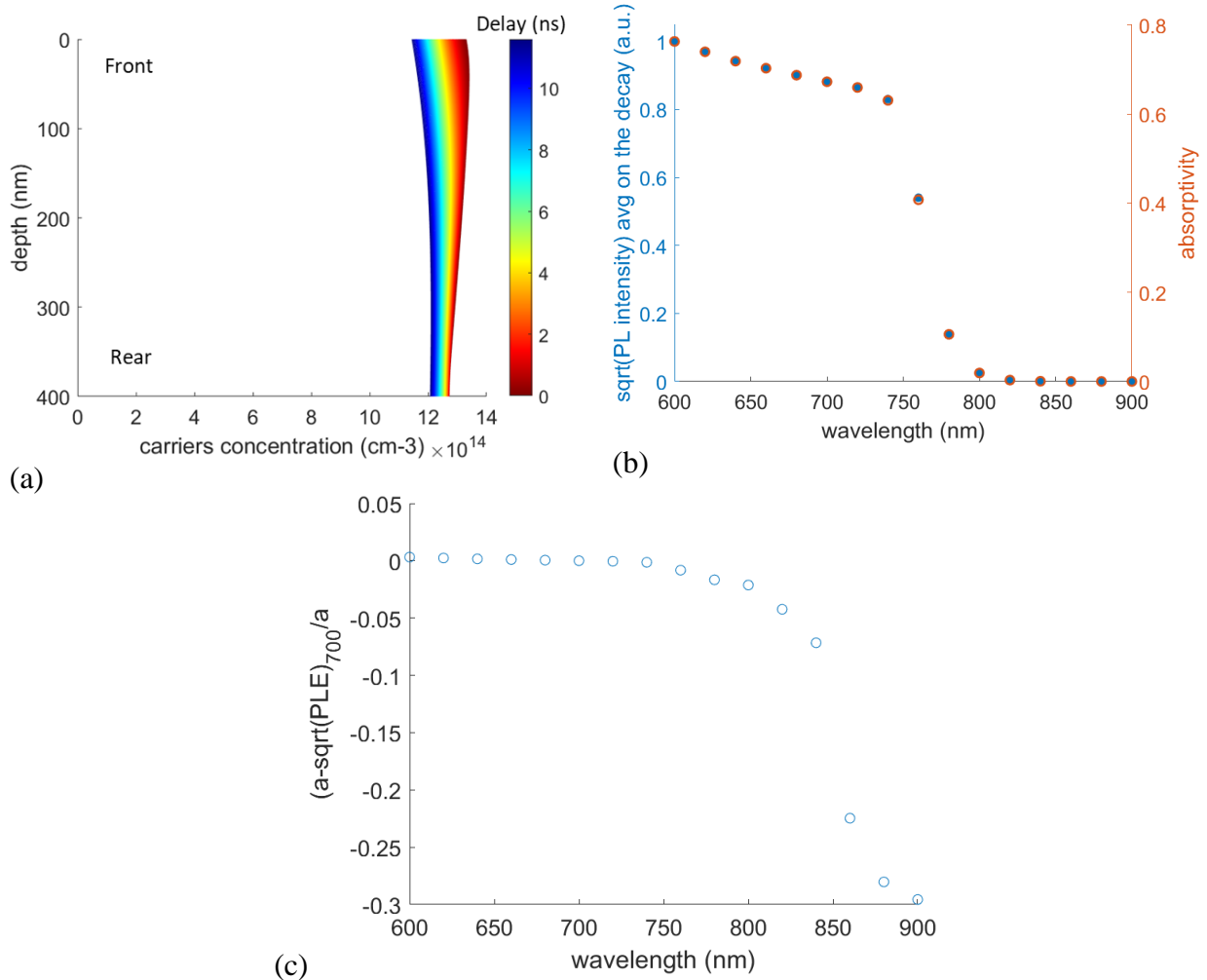


Figure 5-11: Drift diffusion results. (a) Electron densities for different depths and times after the pulse. (b) Comparison between the square root of PL intensity averaged on the decay and the absorptivity (c) Relative difference between the absorptivity and root square of PL scaled at 700nm.

Hence, the simulation suggests that the framework leading to a PLE scaling with the squared absorptivity is still valid in our experimental conditions. High surface recombination or background doping might cause a difference between the absorptivity obtained by PLE and PL fit.

5.III.3 Can we reach the absorption coefficient?

Taking the reflectivity into account is the next step for potentially scaling the absorptivity and determine the absorption coefficient. Local reflectance measurements were performed to gain insight into the sample's optical properties and topography.

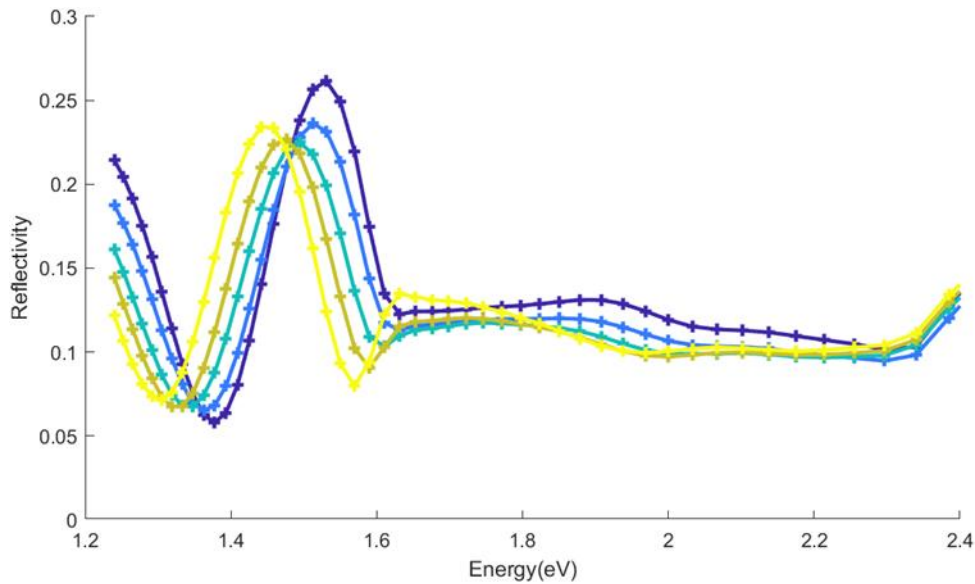


Figure 5-12: Reflectivity of the sample obtained from HI white light reflection measurements ratio. They are shown in the different areas of interest and allow to fit half optical length t fit with equation (5-37).

The reflectance experiment is performed as follows: a halogen light impinging on a diffuser is first focused onto the sample and then onto a mirror to assess the reflectance of the perovskite. Reflected light flux is imaged between 550-950nm with the HI, providing $I_{sample}(x, y, \lambda)$ and $I_{mirror}(x, y, \lambda)$. The reflectivity is assessed through reflectance measurements, reading:

$$R \sim R_{meas} = \frac{I_{sample}(x, y, \lambda)}{I_{mirror}(x, y, \lambda)} * r_{mirror}(\lambda) \quad (5-31)$$

Where the reflectivity of the mirror $r_{mirror}(\lambda)$ provided by Thorlabs is considered to improve measurement accuracy. The result presented in Figure 5-12 shows a similar trend for all areas: the reflectivity varies quite steadily between 550 and 750nm, whereas interferences can be seen for wavelengths above the absorption threshold of perovskite. One can note that the obtained reflectivity value is sensitive to the focus (chromatic aberration) and to the angle of the mirror compared to the optical axis of the setup. The measurement performed in a regular spectrometer provides a curve with a similar shape and higher values, reaching $R = 0.20$ at 2.25eV. Indeed, the incidence and collection angles differs between the two setups so the obtained value are not directly comparable. HI characterizes mainly the specular reflection while the spectrometer also collects diffuse reflectance.

As the glass substrate is thick (3 mm) and therefore optically incoherent, we can suppose that interferences appear between its surface and the top of the perovskite layer. Their characteristics will depend on the optical path length (OPL) traveled when going through the

different layers and being back reflected once by following the contour C . We note t the OPL attributed to one way in the media:

$$t = 1/2 \int_C n_r dl \quad (5-32)$$

Indeed, under normal incidence, by considering the model of a slab of optical path length t and back reflectivity R_b the initial intensity I_0 is modulated as follows:

$$I(\lambda) = I_0 \left(1 + R_b^2 + R_b \cos \left(\frac{4\pi t}{\lambda} \right) \right) \quad (5-33)$$

Hence, the difference in wavelengths between an intensity maximum obtained in λ_c caused by constructive interferences and the following minimum reached in λ_d reads as:

$$t = \frac{1}{4} * \frac{\lambda_c \lambda_d}{\lambda_c - \lambda_d} \quad (5-34)$$

The result of this calculation is close to $2\mu m$, and is consistent with the expected optical path length of the stack from the FTO to the top shown in Table 2.

Table 2: Optical path length calculated in each layer and cumulated on the stack. The refractive indices at 750nm are taken from Raoult et al.²⁴

Layer	Thickness (μm)	n_{750nm}	OPL (μm)	Cumulated OPL (μm)
Perovskite 3D	0,4	2,5	1,000	1,000
TiO2meso	0,045	2,25	0,101	1,101
TiO2	0,02	1,78	0,036	1,137
FTO	0,45	1,68	0,756	1,893

The cosin function can be fit to Equation (5-33) with this OPL as a starting point to gain in accuracy from the use of (5-34). A change of perovskite thickness Δd results in a change of OPL of $\Delta t = n_{pvk} \Delta d$. The hypothesis of a decrease of TiO₂ thickness resulting in an increase in perovskite thickness was also considered. However, the resulting change in the optical index would be $\Delta t = (n_{pvk} - n_{TiO2}) \Delta d$, and would correspond to variation in the absorber thickness up to 250nm, and would have visible impacts on the regular characterization routine. By taking the less emitting area as reference, we obtain the thicknesses variation shown in Figure 5-13. The emitted PL intensity increases with the perovskite thickness obtained this way. Equation (5-9a), on the contrary, predicts a dependency on $\frac{1-e^{-\alpha d}}{d}$ for the internal PL emission for high injection and high diffusivity.

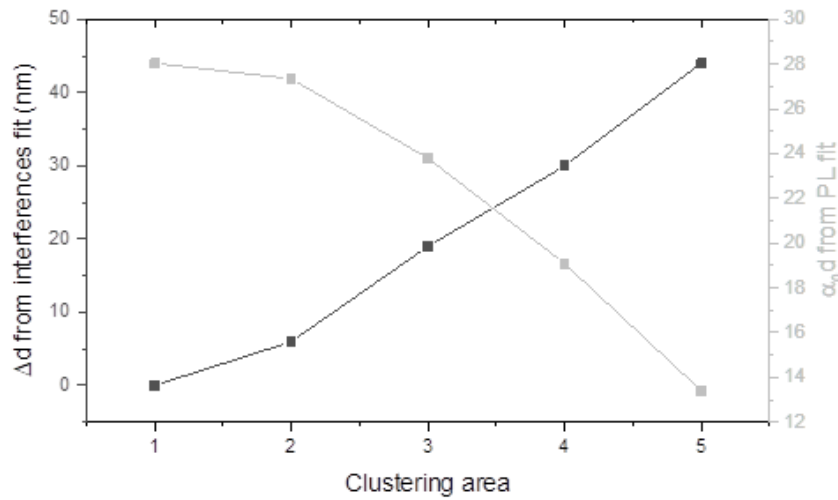


Figure 5-13: Variations of the perovskite layer thickness estimated by fitting the interferences in the clustering areas, increasing with the PL intensity. It is compared to $\alpha_0 d$ obtained by PL fit in the previous section.

The diverging behavior of the thickness obtained by PL and interferences fits probably stems from the impact of reflectivity that depends on the location. Figure 5-14 shows the PL spectra obtained with a 600nm excitation and the reflectivity measured in the same spectral range. The emission is brighter in the less reflective region, that would come from a higher effective coefficient for radiative recombination B^* . Also, the PL spectra tend to overlap in the energy ranges where the reflectivity is similar, around 1.5eV and 1.65eV. This variation of B^* would also provide an explanation to the PL intensity increasing with the thickness of the perovskite layer. It leads to the hypothesis that the material is homogeneous, and only the outcoupling differs depending on the areas.

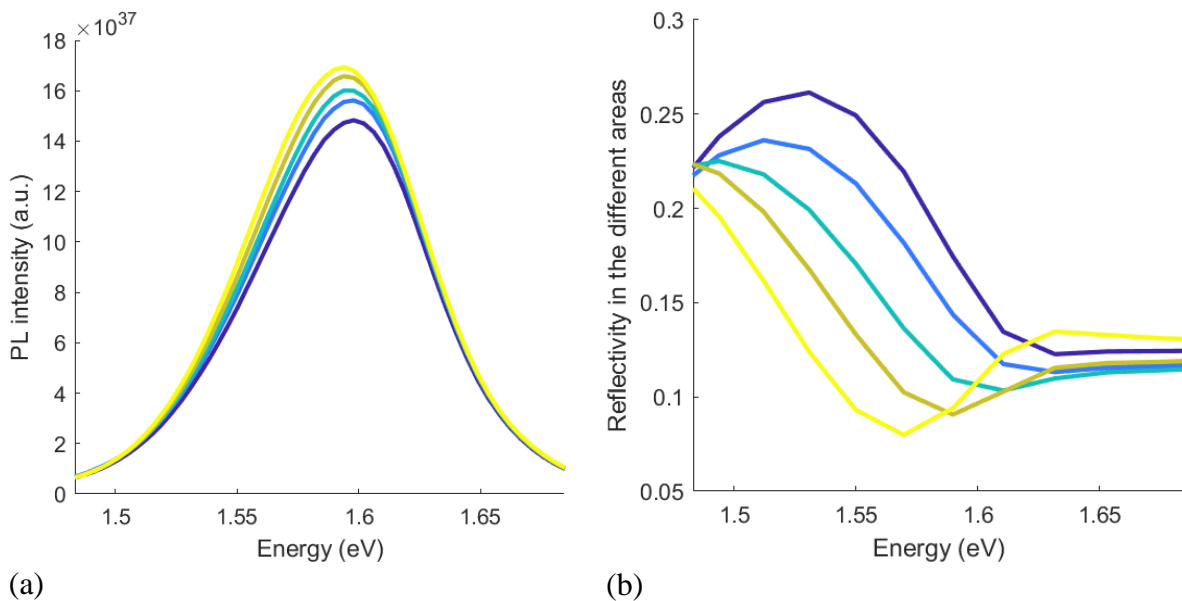


Figure 5-14: Comparison between (a) the PL spectra for a 600nm excitation and (b) the reflectance measured in the same spectral range, for the different areas. The brighter areas are the one in which the reflectivities in the emission spectral range are the lower.

A proper way to scale the reflectance and correcting its impact on the PL shape could be sought as future work. It can be investigated through improved optical models. This step would allow to use the calibration of the data to disentangle the influence of absorptivity and effective lifetime on the PL emission.

5.III.4 Prospects for data acquisition

Data processing employed $I(x, y, \lambda_{em})$ and $I(x, y, \lambda_{exc})$ rather than $I(x, y, \lambda_{em}, \lambda_{exc})$. Indeed, the collected information is very redundant as spectra have similar shapes for different excitation wavelengths. Once this stability has been established by checking the extremal excitations wavelengths, the acquisition of zero-order images with a spectral filter would be preferred. That would match the approach employed in the literature^{10,25} with the spatial dimensions in addition. Indeed, the measurements are far quicker in this configuration, and it would be possible to multiply the number of excitation wavelengths. The automation of laser calibration by establishing a feedback loop between the excitation laser and powermeter would be a plus to limit the risk of errors during the excitation flux calibration procedure. Also, synchronizing the laser and the detector would greatly help speed up the measurement and is all the more crucial with materials evolving with light exposure as perovskites. Absolute calibration of the emitted PL intensity can easily be performed by comparing a calibrated PL spectrum to the collected intensity on a reference zero-order image and applying a rule of three.

5.IV PLE on a full cell: beyond uniform carrier concentration

In this last section, we present results obtained on gallium arsenide structure. A full cell stack characterized by PLE exhibits a notable spectrum emission dependence on the excitation wavelength. With the help of simulation, we show that this behavior can be linked to the variation of the charge carrier profiles.

5.IV.1 Experimental details

The sample is a cell fabricated by the Fraunhofer Institute; its structure is described in Figure 5-15. This cell is characterized as a well-studied material known for its reliability, which has been described before²⁶. The illumination is provided by a defocused fiber and is rather gaussian with an approximative surface of $2 * 10^{-5} \text{cm}^2$. The experiment was led at a constant photon flux of $2.6 * 10^{19} \text{ph/cm}^2/\text{s}$ but with slightly varying photon flux, in the range of flux of $1 - 3 * 10^{15} \text{ph/s}$. Indeed, the calibration of the incident source considers the spot size changes

with the wavelength. However, data treatment was performed by integrating the information spatially. In this experiment, the laser signal was filtered only by linear polarization with no short-pass filter set on the illumination branch.

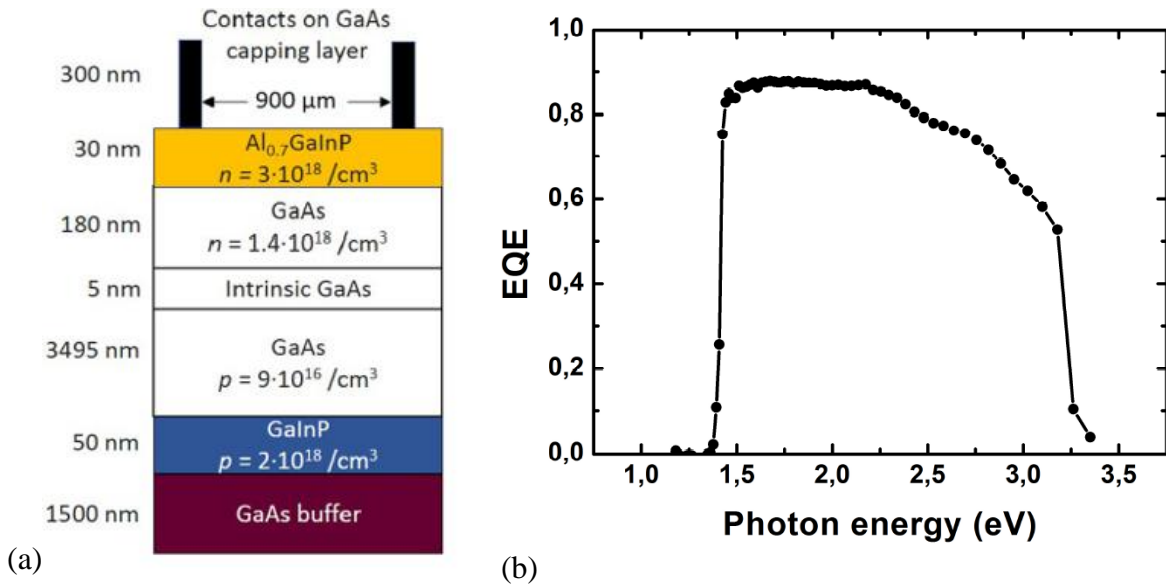


Figure 5-15: (a) Structure of the gallium arsenide cell under characterization, constituted of GaAs buffer, GaInP back surface field, p-doped GaAs base, n-doped emitter, and AlGaAs window layer. (b) Corresponding EQE measurement²⁶.

5.IV.2 Results

In this experiment, the luminescence spectra have the same shape in all locations; they are summed in the region of interest. PL spectra normalized by the incident flux for the different excitation wavelengths are presented in Figure 5-16. A redshift of the emitted spectrum is clearly visible when increasing the excitation wavelength between 550nm and 725nm. The second experiment batch showed that the PL emitted spectrum has a stable shape between 500 and 525nm. The one emitted at 550nm is a bit redder but still provides a satisfactory reference.

By calibrating and integrating these spectra, it is possible to obtain the PLE of the material. Figure 5-16 shows that the limits of integration for the resulting excitation spectrum are critical for the results. For instance, at a probe wavelength of 850nm, the PL intensity decreases with the excitation wavelength increase, as shown with the orange arrow. The reverse trend is observed at 870m.

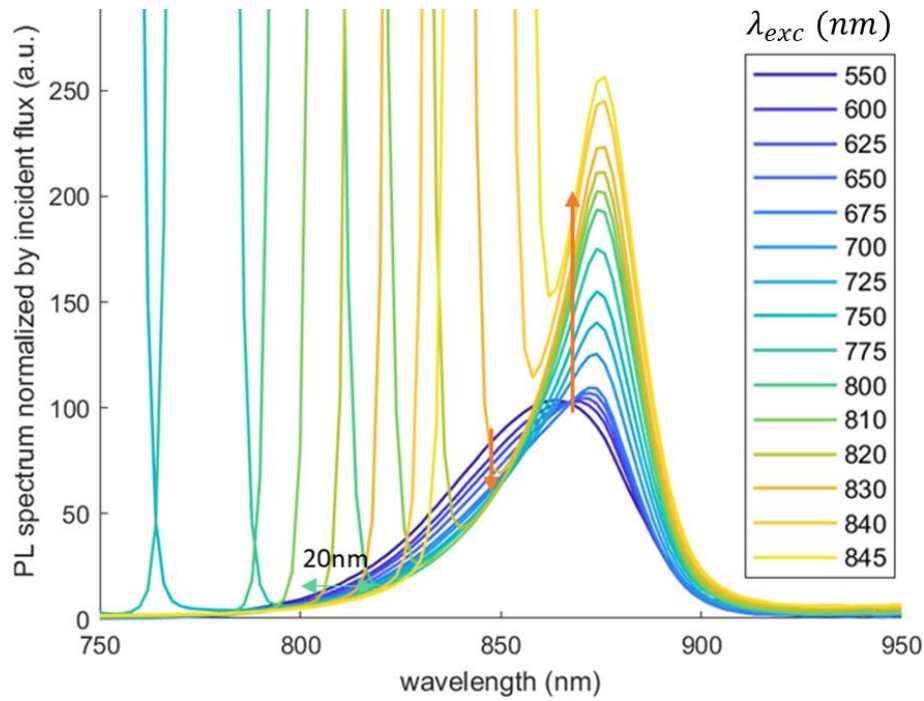


Figure 5-16: PL spectra of GaAs cell emitted for different excitation wavelengths. As highlighted by the orange arrows, PL intensity emitted at 850nm decreases with increasing excitation wavelength, whereas PL emitted at 870nm rises. The laser reflection can also be seen; it has a full-width half maximum of 10nm and a half width at low counts estimated to be 20nm on the illumination at 800nm.

A first PLE spectrum was assessed with the classical protocol by integrating the spectral emission, as illustrated in Figure 5-17 (a). As the emitted photon flux estimation is affected by reabsorption, it is referred to as *surface PLE*. To limit the influence of the laser on the result, spectra with illumination above 750nm were cropped 30nm away from the illumination wavelength. They were further scaled with the spectrum at the 725nm excitation with which they share the shape.

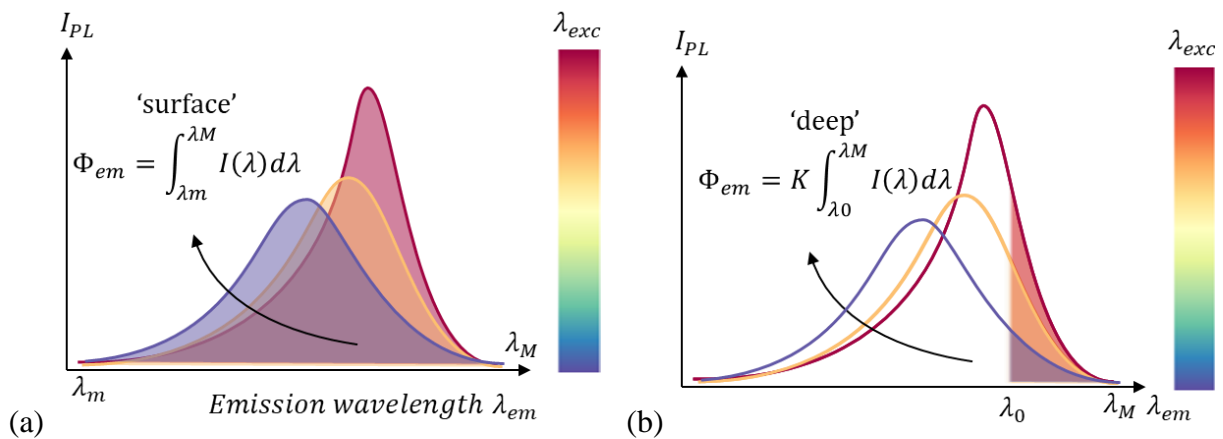


Figure 5-17: Principle of calculating the 'external' PLE (a) and 'internal' one (b). The former corresponds to the spectral integration of the emitted flux, while the latter is based on the poorly reabsorbed lower wavelengths. A proportionality factor K is calculated from the highest excitation energy, assuming the emission is mainly from the surface, with low reabsorption.

A second calculation is made based on the emission at high wavelengths. It can be seen as a way to avoid the influence of reabsorption on the emitted flux estimation, with the underlying hypotheses of emission spectrum being homogeneous in-depth and negligible absorption in the chosen spectral range characterized. Thus it is called *deep PLE* in this work. One can note that this distinction would be similar to the one between internal and external PLQY for simplistic optical models: it would hold if all photons emitted in the collection cone of the objective lens are either collected or reabsorbed, with reflection and scattering being neglected. For internal PLE, the emitted flux is calculated by integrating the emission in the high wavelengths, between 876 and 900nm, and scaling it with the spectrum at 550nm.

As shown in Figure 5-18, both PLE increases with the excitation wavelength. The corresponding EQE shown in Figure 5-15(b) increases with wavelength stabilizing around 650nm and begins to diminish from 775nm. This decrease is not observed here, probably because of the parasitic laser signal that compensates for it. The growing difference between the 'surface' and 'deep' PLE can be linked to an emission that takes deeper bulk and gets increasingly reabsorbed.

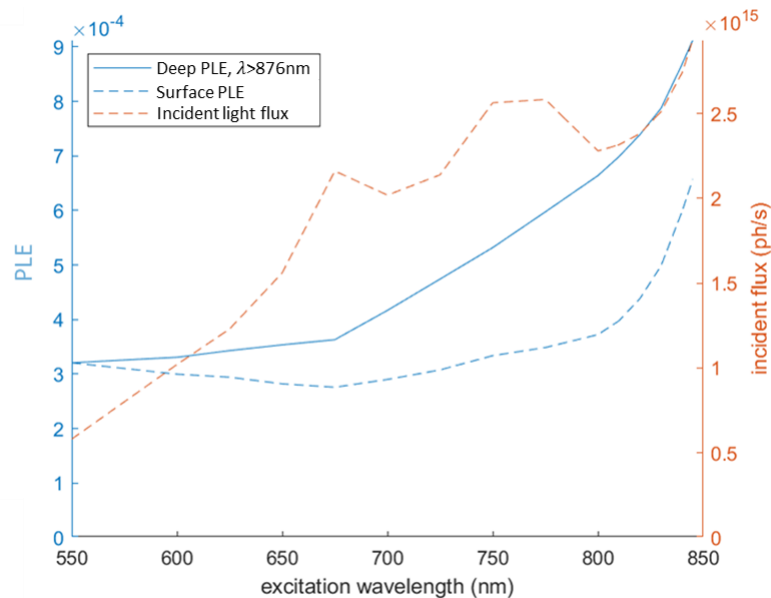


Figure 5-18: Internal and external PLE spectra of the gallium arsenide cell obtained from the extrapolation of the low energies emission (solid line) and by integrating the PL spectra (dashed line), respectively. It is set in regard to the incident light flux.

5.IV.3 Comparison with drift-diffusion simulations

To provide a qualitative understanding of this phenomenon, drift-diffusion was performed in steady-state with the open-source software SCAPS²⁷. We aim to simulate the charge carrier distribution with the different excitation wavelengths to understand what could lead to an increase in the PLE with the excitation depth. A simplified structure consisting of the

three GaAs layers is considered, owing only radiative recombination with coefficient $B = 10^{-10} \text{cm}^{-3}/\text{s}$. The doping is indicated in Figure 5-15, and a simple absorption coefficient with a squared root dependence is employed. The other properties as the effective density of states or mobilities are taken from the Ioffe database²⁸. Different excitations wavelengths are considered between 300 and 1000nm, at a constant fluence of $1.25 * 10^{17} \text{ph/s/cm}^2$ corresponding to pre-defined spectra.

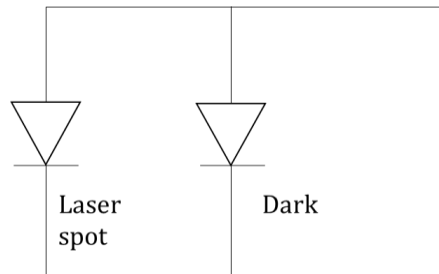


Figure 5-19: Experiment equivalent circuit. As the laser spot illuminates only a fraction of the cell, a contribution of the areas in the dark is expected to reduce the potential observed under the illumination.

Figure 5-19 shows the circuit equivalent to our experiment. The laser spot is roughly $2 * 10^{-5} \text{cm}^2$ for a much larger cell, approximately of 0.03cm^2 . The cell areas in the dark can be modeled by a diode in the dark, which will decrease the potential below the illumination. However, the relative contribution of these two diodes remains unknown, and the experimental function point is between open-circuit and short-circuit. Two batch calculations were led for these limit cases: at short circuit current density J_{sc} and at open circuit voltage $V_{oc} = 1.14 \text{V}$ (calculated by the software and valid for excitation wavelengths up to 860nm where the light flux is almost integrally absorbed).

The resulting electron-hole pairs generation and charge carrier densities product are plotted in Figure 5-20. One can note that at V_{oc} , the charge separation is high: the $n * p$ product is constant within the bulk and approaches $n_i^2 * \exp(V_{oc}/k_B T) \sim 7.2e31 \text{cm}^{-6}$. Thus it leads to a PLE constant in intensity and spectral shape. It would match the constant absorptivity of light in the cell for these energies, yet it cannot explain the experimental results. At J_{sc} , the profile of $n * p$ varies with the generation: higher excitation energies lead to higher PL emissions from the n-doped area, and decreasing it increases the emission from the p-doped region. Such behavior could explain the experimental data qualitatively: at a monitor wavelength of 850nm, reabsorption is high, and we observe mainly what is happening in the top layer. The carrier density at steady-states is diminished with absorptivity. On the contrary, a monitor wavelength of 870nm provides relatively more information on the p-doped layer. In other words, varying reabsorption at the emission wavelength changes the depths probed by photoluminescence. Emission wavelengths offer an insight into different depths so that change in $n * p$ profile will affect the PL spectrum.

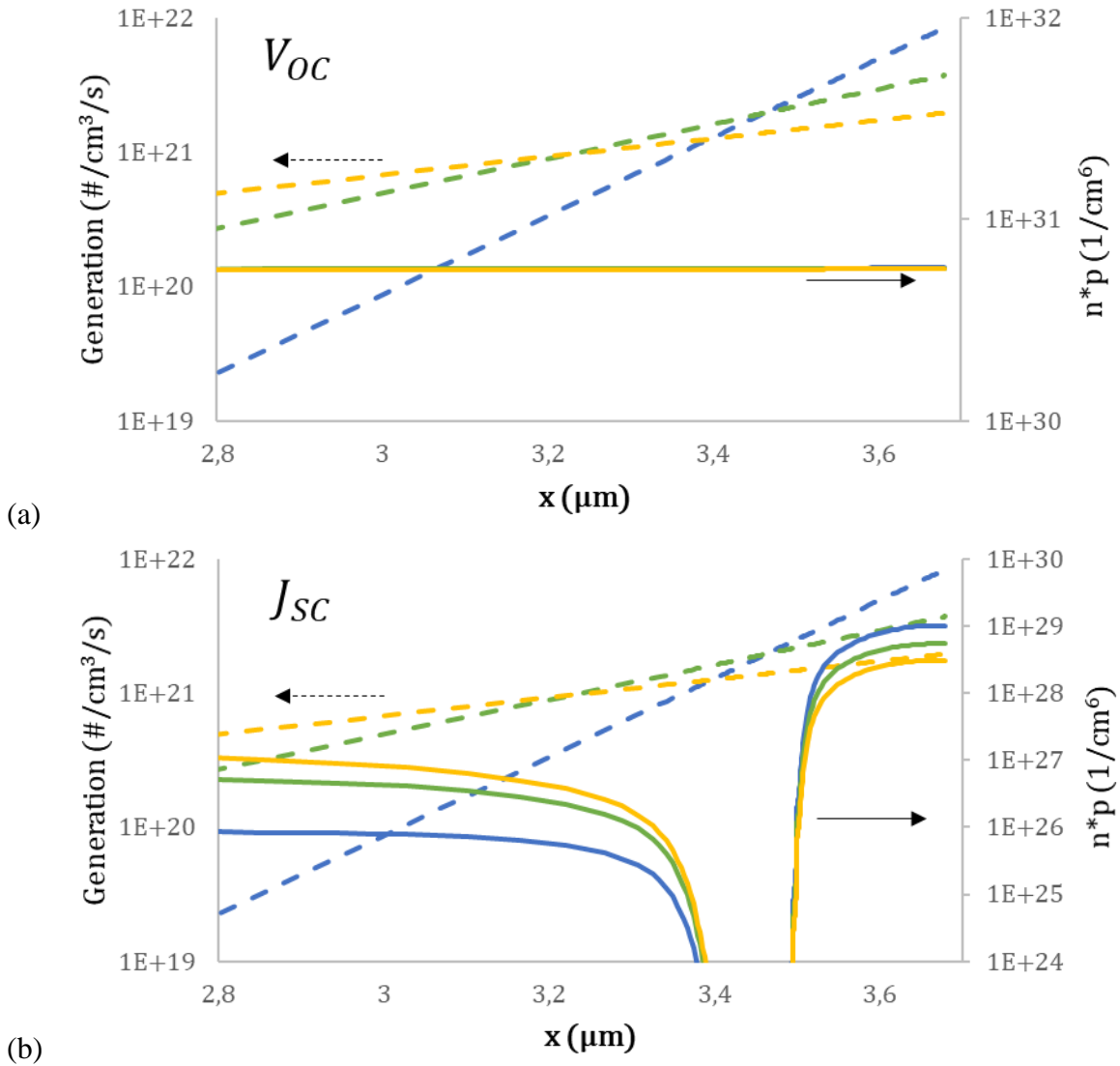


Figure 5-20: Generation rates (dashed lines) and charge carrier density product $n \cdot p$ (solid lines) as a function of depth under continuous wave monochromatic illumination at (a) V_{OC} and (b) J_{SC} . The structure is illuminated from the right side, corresponding to higher abscissa. Results of the simulation are presented for excitation wavelengths of 600nm (blue), 800nm (green), and 850 nm (yellow).

To illustrate this, PLE is calculated with a reabsorption term for different absorption coefficients at the emission wavelength $\alpha(\lambda_{em}) = \alpha_{em}$ as follows:

$$PLE(\alpha_{em}) = \frac{1}{\Phi_{exc}} \int_0^d B n p e^{-\alpha_{em} z} dz \quad (5-35)$$

This relation corresponds to a linearization of Equation (5-32). Indeed, it does not consider the PL intensity variation with the emission wavelength. Thus, it provides the PLE scaled with a probed wavelength inducing reabsorption characterized by α_{em} and follows the same idea as the experimental PLE plotted in the precedent section. The obtained results are shown in Figure 5-21: without reabsorption, an augmentation of PLE is indeed visible close to

the bandgap energy. However, reabsorption terms lead to a continuous decrease in the collected signal as the resulting PLE mainly scales with the absorptivity in the top layer. In the absence of reabsorption, the PLE corresponds to the sum of the decreasing PL from the top n layer with an increase in the excitation wavelength and the subsequent growing one in the bottom p layer. Their contribution is not linear, with the flux impinging on the layers as it depends on the exponential absorptivity, involving different doping and thickness. It results in the black curve whose shape approaches a linear combination of the absorptivities in the top and bottom layers shown in the inset of Figure 5-21.

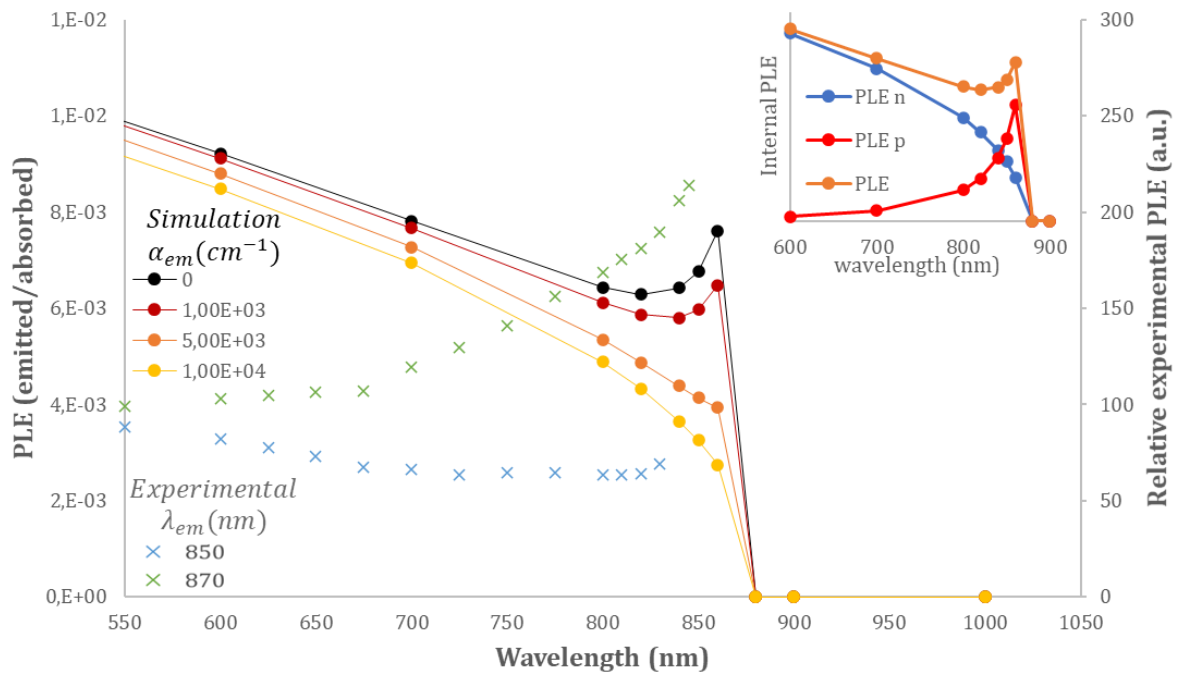


Figure 5-21: PLE at J_{sc} obtained with different reabsorption coefficients. For higher absorption coefficients, the curve has a classical shape of absorptivity. With no reabsorption, it corresponds to the sum of the decrease in the charge carrier densities in the top n layer with the increase in the excitation wavelength and the subsequent growth of these quantities in the bottom p layer. The shape corresponds to a linear combination of the absorptivities in the n and p doped layers as shown in inset for the example of null reabsorption. The simulations are compared to the relative experimental PLE at 850 and 870nm featured by the crosses.

These results are compared to the PLE evaluated in different emission wavelengths corresponding to different reabsorption. One can observe that the decrease of PLE at 850nm in the range 650nm-750nm is much flatter than in the simulation, and PLE at 870nm increases. Qualitatively, the shape of the experimental data seems relatively closer to the one of the p-layer of the simulation. The contribution of the n-layer must be lower in the experiments, that might come from a higher non radiative recombination stemming from a surface to bulk ratio. Moreover, the pulsed illumination probably impacts the spectrum, as following the mobility considered for the model, the electrons take less than 1ns to diffuse over the stack thickness of 4 μ m. This time is short compared to the 12ns laser cycle. It is also possible that the n-doped

and p-doped layers have different spectra due to bandgap narrowing effects with the doping density.

In summary, this experiment illustrates how the excitation wavelength can notably impact the observed PL spectrum of solar cell devices. Redshifting spectra with increasing excitation wavelength can be seen as a consequence of emission from longer depths in the material. Hence, choosing the wavelength of integration allows the obtention of PLE from different regions of the cell. Based on the steady-state drift-diffusion simulation, we attribute the change in PL spectra to varying np profiles. They are the result of experimental conditions comparable to open-circuit. Once more, it raises the question of comparing results in transient and continuous regimes. Otherwise, possibilities to solve the inverse problem in this configuration and get back to the PL emission in different depths could be explored in future work. It would require detailed knowledge of the absorption coefficient and would be a way to access a three-dimensional PLE(x,y,z). Studying PL on the illumination edge could be a way to vary the polarization spatially and obtain a voltage-dependent signal PLE(V,z). Performing the experiments at short-circuit would be a way to get better-conditioned problems than open-circuit.

Conclusion

PLE experiments offer a way to access the absorption properties of the photovoltaic light absorbers, as demonstrated mainly qualitatively in the literature. It is also illustrated as a tool for assessing surface recombination by varying its contribution to PL. Theoretical models describing the link between PLE and absorption properties are introduced. An experimental methodology was put in place to carry out such measurements.

We have presented a proof of principle of a well-resolved spatially and spectrally local absorptivity measurement. We confirmed by simulation that using a pulsed laser should not hinder the absorptivity from PLE in our case. Yet, the absorptivity obtained close to the bandgap energy by PL fit is compatible with the one assessed by PLE. A further measurement by spectroscopy is necessary to scale the measured absorptivity locally, as PLQY and absorptivity cannot be disentangled. Completing the PLE by a spatial reflection measurement provides insight into the optical properties of the device and offers useful information to build a physical model.

A further experiment on a full GaAs cell illustrates how the excitation wavelength can change the observed PL spectrum. Redshifting spectra with increasing excitation wavelength are observed as the charge carrier product is moved towards longer depths. Drift-diffusion simulation suggests that this phenomenon should not occur in open-circuit conditions at steady-

state. However, varying np profiles are obtained in the short circuit model, and calculating the PLE for different reabsorption wavelengths qualitatively fits the experimental behavior. Hence, choosing the wavelength of integration allows the obtention of PLE from various cell regions and could be key to attaining the information in depth.

Conclusion and perspectives

This thesis focused on developing new approaches to characterize the photoluminescence of semiconductors for photovoltaic applications. It has explored different ways of acquiring more comprehensive spectrally-resolved photoluminescence data sets to assess optoelectronic properties by limiting the necessary prior knowledge and controlling assumptions and models. We summarize here the main findings of this work. This exploratory project has raised many questions, providing short and long terms perspectives.

Key outcomes

Photovoltaic devices can be described at different scales, from the macroscopic performances obtained by current-voltage measurement to the nanometric characterization offered by electronic microscopy. Photoluminescence, a contactless technique, plays a major role in linking these two ends. **Chapter 1** explains the different physical phenomena at stake in photoluminescence by describing different paths the energy carried by the incident photons can follow. The information brought by the spectral and temporal dimensions of the emitted light is detailed, highlighting their complementarity. In steady-state, the spectral emission described by Planck's generalized law offers an insight into the material properties, such as bandgap and Urbach energy, and the carrier distribution. Otherwise, continuity equations define carrier dynamics and relate the transient photoluminescence to recombination and transport properties. These characteristics vary greatly depending on the absorber, as highlighted through the description of the type of materials used for the photovoltaic conversion. Thus, obtaining the local photoluminescence spectra and decays is crucial to characterize samples' inhomogeneities or characterize more properties by non-uniform illumination or extraction.

Thus, **Chapter 2** presents the imaging techniques and ways to increase map dimensions to acquire data cubes or matrices of higher dimensionality. In the same way as focal plane arrays or raster scanning, Single-Pixel Imaging retrieves spatial information of light fields. This unconventional technique, particularly relevant for designing multimodal or multidimensional imagers, relies on spatial light modulation and inversion problems to obtain maps with non-imaging photodetectors. It is put in perspective by a state-of-the-art of hyperspectral and time-resolved imaging, with a focus on the imagers available at IPVF laboratory. From all these examples, we discussed optical setups that (would) retrieve light intensity as a function of space, wavelength, and time of emission, hence providing a complete 4D dataset for luminescence intensity as $I(x, y, \lambda, t)$.

A 4D-PL setup was built with high spectral (<1 nm) and temporal (50 ps) resolutions to increase the information gathered within one experiment. Its implementation, described in **Chapter 3**, is based on Single-Pixel Imaging with a streak camera combined with a spectrometer. The novelty of this design, protected by a patent, also came with many challenges as light is scarce in photoluminescence experiments and is spread in the four dimensions of interest. The photon budget and the trade-off between the field of view and collection efficiency drive the choice of optical components and single-pixel imaging approach. The influence of diffraction induced by the spatial light modulator and its model and correction are discussed. The constraints raised by photoluminescence signal and detector efficiency restrict the number of pixels leading to a spatialization of streak camera acquisition rather than imaging. Two variations of this approach are introduced to increase the system's applicability. First, a hyperspectral single-pixel imager is parallelized to the existing time-resolved imaging branch, leading to a $2x3D$ setup, $I(x, y, t) + I(x, y, \lambda)$. Also, a workflow based on pixel *clustering* allows the obtention of time-resolved spectroscopy in different areas of interest $I(\lambda, t)_{r_i}$.

These different samplings of photoluminescence in four dimensions are demonstrated on photovoltaic devices, as shown in **Chapter 4**. The lateral impact of perovskite light-soaking is studied with the $2x3D$ setup mentioned above. Changes in the PL dynamic and spectra are shown in different locations. Trends differ with the injection: lower intensity illumination leads to an increase in the photoluminescence intensity on large areas, which is probably determined by the ionic migration time. Higher injection leads to a degradation visible on the intensity without notable PL transport or recombination property change. An example of *4D-PL* is presented on a Gallium Arsenide wafer in high injection conditions. The emitted light intensity variations are observed along the spatial, temporal, and spectral dimensions. These changes are attributed to band-filling combined with another mechanism, as highlighted by the correlation between mean intensity and energy. Carriers at temperatures higher than the lattice or optical transport could lead to the observed trend. At last, we demonstrate the pixel clustering workflow on gallium arsenide, fluorophore, and perovskite to highlight the successful generalization of streak camera spatialization for a broad range of samples.

On the other hand, it is possible to obtain more data by performing parametric studies. **Chapter 5** presents photoluminescence experiments in which the excitation wavelength is varied. Performed with hyperspectral imaging, they result in a $I(x, y, \lambda_{em}, \lambda_{exc})$ data, which is another 4D matrix. Associated models are derived, and the dependence on the material probed is highlighted through different limit cases. The corresponding experimental methodology requires careful calibration. As detailed, the workflow relies on polarization to filter out the reflected laser light, which allows exciting low-reflective samples close to their bandgap energy. PLE was demonstrated on a perovskite inhomogeneous sample and combined with PL fit to determine the relative absorptivity on a large spectral range. The two result in variations

Conclusion and perspectives

close to the bandgap to which laser spectral width contributes. We highlighted that reflection measurements contain information on the sample topography, which is useful for photoluminescence maps interpretation and obtained at a low experimental cost. Otherwise, PLE can bear the signature of notable carrier profile variation when spectral shape varies with the excitation wavelength.

This thesis has laid the foundation for sampling photoluminescence in four dimensions. As such, it touched on crucial questions that would be worth being investigated.

Open questions

Key questions remain at the core of the matter and are far from being answered. The experiments presented in this manuscript rely on pulsed sources. As discussed throughout this manuscript, the interpretation of spectra in a transient regime and its comparison to steady-state is far from straightforward. Also, collecting new datasets raises interrogation regarding data treatment and their integration into material photoluminescence characterization workflow.

How can we compare steady-state and transient experiments?

In Chapter 4, experiments illustrate different trends in continuous wave and pulsed excitation experiments. However, in some cases, steady-state and transient regimes are comparable. When carrier diffusion is sufficient, the transient signal may return to an equilibrium carrier density similar to the one at steady-state. The experiment of pixel clustering on GaAs (Chapter 4, III.1) provides such an example. If quasi-equilibrium is reached fast enough, transient might be considered an intensity study. In this frame, Bleuse et al.¹ have demonstrated similar peak energies for transient spectra and power excitation study in steady-state on a kesterite sample. Otherwise, photoluminescence decay was successfully retrieved from RANdom Temporal Sampling (RATS)² by considering the collected intensity I_{PL} as the convolution of the uncontrolled excitation signal I_{exc} and the decay:

$$I_{PL} = I_{exc} * I_{decay}$$

Moreover, spectra could be influenced by slow mechanisms, such as carrier detrapping. Such dynamic can be well investigated with modulated photoluminescence (MPL)³. What about a characterization of photoluminescence spectra under similar conditions? It would link continuous and pulsed excitations and track potential spectral signatures of the traps. Changing the relative contribution of fast, slow, or quasi-equilibrium phenomena can disentangle their influence on the spectrum. MPL could also be combined with single-pixel imaging to obtain spatially resolved information.

Comparing steady-state and transient regimes is also important for ultrafast dynamics and carrier cooling, with a clear interest in hot carrier studies. Such investigation is necessary to compare temperatures and cooling rates achieved by the devices characterized in these two regimes. It could also lead to further insight into the phonon bottleneck effect seen as crucial for the obtention of temperatures above the lattice in a continuous regime.

What strategies can we implement to treat the 4D data?

Experiments such as 4D-PL provide data intricated in the dimensions of interest that are therefore challenging to analyze. Future works could deepen this aspect to have a broader view of what can be achieved with the setups. Simulations could greatly help at different levels, particularly to fit properties or target adapted observables.

To fit or not to fit?

The notion of observable (spectral peaks, characteristic time...) to describe a material always stems from a physical model. However, some are direct, and others require a hypothesis. It can be illustrated through the example of time-resolved photoluminescence decay, which is often fitted with exponential functions. As highlighted by Dordevic et al.⁴, the chosen functions imply different physical phenomena, and several kinds of fits can converge. Complete simulation can also be performed with optical drift-diffusion models, raising the same questions. Therefore, they involve many parameters and are difficult to realize for materials without prior knowledge. Alternatively, it is possible to find hypothesis-free ways of visualizing data. For PL decays, it can be done by extracting the distribution of decay times rather than setting a fixed number. This graph would provide an indication on the physical mechanisms at stake. The interpretation is postponed to keep the data analysis as free from bias as possible. Otherwise, it is ideal to rely on observables depending on a very low number of parameters, leading to direct fits. For instance, it is achieved with the scaling laws⁵ of short time derivative in TRFLIM, provided the assumption of low diffusion is verified.

What crossed correlations should we look for?

Multidimensional photoluminescence imaging gathers a huge amount of data leading to the possibility of investigating many different correlations. They potentially owe the key to disentangling the physical mechanisms and are also related to another crucial question: **what is the appropriate visualization for 4D data?** The challenge of interpreting the correlation is widespread in photovoltaics. Julien et al.⁶ explore how the correlation of different parameters of the I-V curve helps identify degradation pathways. Hundreds of optoelectronic parameters fitting a reference I-V and photoluminescence spectrum are first determined. Variations of properties associated with degradations are simulated for all configurations to extract

Conclusion and perspectives

correlations, as in Figure 6-1(a). In this example, HTL acceptor density, ETL donor density, and defects at the HTL/perovskite interface leads to similar signature in the (J_{SC}, V_{OC}) plane. The correlation between PL intensity and V_{OC} would allow to discriminate interface defects from the two others. This approach can support the interpretation of various problems, as the reference curve can be taken as the ideal I-V, a control sample among a batch where a parameter is optimized or even at a reference time.

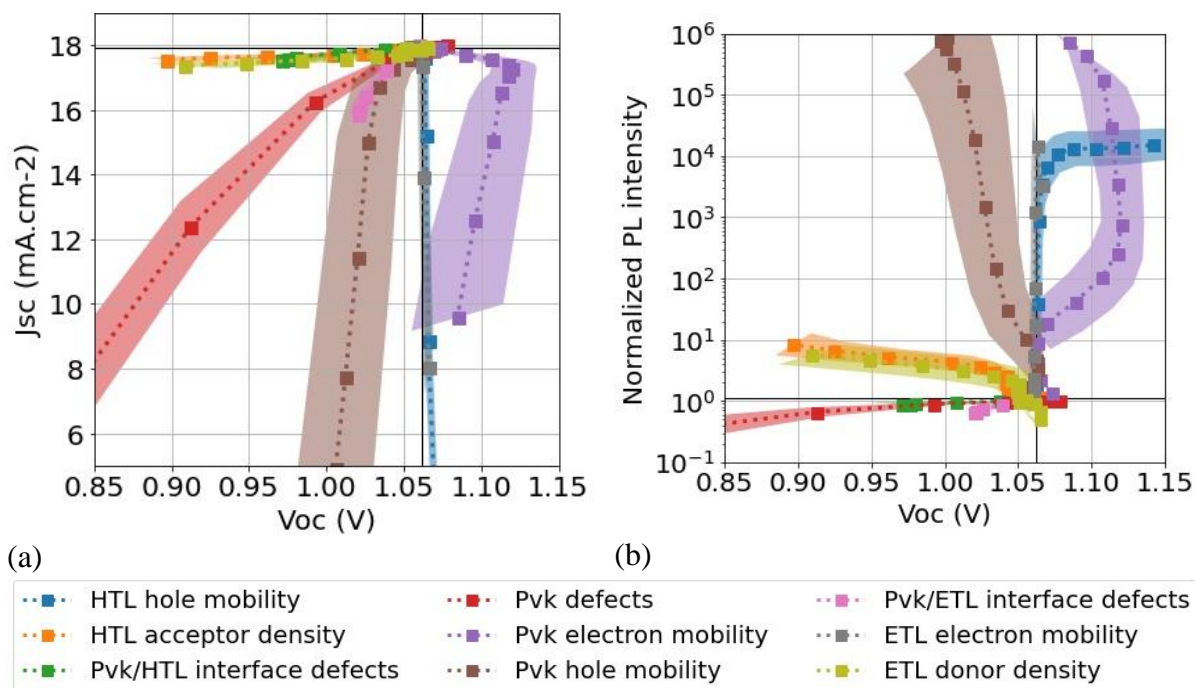


Figure 6-1: Correlations for different changes in the properties of a reference device (a) between short-circuit current J_{SC} and open-circuit voltage V_{OC} , (b) between photoluminescence intensity and open-circuit voltage. © Arthur Julien

We could imagine performing the same reasoning with 4D data. Firstly, the spectrum at $t = 0$ (or $t \rightarrow \infty$) could be modeled from sets of optoelectronic properties, and the incidence of their evolution in 4 dimensions could be deduced. It could help identify problems where 4D sampling would bring significant added value. Alternatively, this goal could be pursued by Bayesian inference, which was demonstrated with photoluminescence decays in the literature⁷. It is all the more tempting as a code to model the temporal evolution of the photoluminescence spectra is available³, as shown in the preceding paragraph. These statistical methods could also be extended to various experiments to identify their correlations and provide a qualitative analysis. It could be a way to identify a simple set of experiments to restrict the hypothesis easily to be made on an unknown sample.

How to obtain reliable visualizations of noisy data?

In this work, the collected signal is notably influenced by noise and requires many processing steps. The limit between over-smoothing and reliable data is not always easy to draw, especially with low-intensity photoluminescence. Monte Carlo simulation could be run to assess the number of photons necessary for a given data treatment. Moreover, machine learning could be interesting in that sense. As seen with the example of *LumiML*⁴ and *Spirit*⁸, algorithms can be trained on noisy data and still provide satisfactory results. It could be the key to obtaining exploitable data visualization with a confidence interval. They have the advantage of speed for treating huge datasets as maps.

What setup and experiment should we use?

This work provides insight into the diversity of approaches possible to characterize photovoltaic devices by photoluminescence. It also shows the variety of physical quantities upon which PL depends and inevitably raises the following question: what experiments should I perform to have reliable a given optoelectronic property assessment? Should I prefer a parametric study, multimodal or multidimensional setup? The first elements of answers appear in this manuscript through a literature review and interpretation of experiments. However, no clear scheme can be distinguished as PL is a multivariate problem and can be analyzed in many different ways. Numerical approaches presented above, i.e., drift-diffusion (PLPLP®), correlation analysis, or Bayesian inference, provide as many tools to investigate the information brought by new configurations or parameter study. It could guide toward the appropriate workflow to follow depending on the targeted properties and precision while limiting redundancies.

Conclusion's conclusion

The instrumental development has led to the creation of setups obtaining new datasets. Experimental results provide examples of photoluminescence signal variations in the spectral, temporal, and spatial dimensions. Such data offers promising information on mechanisms such as bandfilling, carrier cooling, optical transport, or transfers between layers or phases. So far, we have provided elements of interpretation for different samples. Ways to obtain a better understanding of 4D data remains an open question that simulation can help address.

Many more interrogations could be asked. Some are directly related to the photoluminescence of perovskites. Why are they shining so much when scratched? What could explain a blue shifting spectrum observed with the streak camera? Others have wider scopes: how could we link density functional theory calculations to our results to improve defects

Conclusion and perspectives

understanding, as demonstrated in the literature⁹? All these open questions suggest that exploring 4D sampling is just taking its first steps. They are closely related to works led by inspiring colleagues at IPVF (or further away!), highlighting a strong potential for collaborations. Thus, 4D offers an advanced characterization tool for addressing various challenges in different branches of research on photovoltaic materials.

Bibliography

References – Chapter 1

1. Look, D. C. & Leach, J. H. On the accurate determination of absorption coefficient from reflectance and transmittance measurements: Application to Fe-doped GaN. *Journal of Vacuum Science & Technology B, Nanotechnology and Microelectronics: Materials, Processing, Measurement, and Phenomena* **34**, 04J105 (2016).
2. Pearce, P. RayFlare: flexible optical modelling of solar cells. *JOSS* **6**, 3460 (2021).
3. Timò, G., Martinelli, A. & Andreani, L. C. A new theoretical approach for the performance simulation of multijunction solar cells. *Prog Photovolt Res Appl* **28**, 279–294 (2020).
4. Würfel, P. & Würfel, U. *Physics of solar cells: from basic principles to advanced concepts*. (Wiley-VCH Verlag GmbH & Co. KGaA, 2016).
5. Ahmed, I. *et al.* There is plenty of room at the top: generation of hot charge carriers and their applications in perovskite and other semiconductor-based optoelectronic devices. *Light Sci Appl* **10**, 174 (2021).
6. Mathieu, H. *Physique des semiconducteurs et des composants électroniques*. (Masson, 1997).
7. Sze, S. M. & Lee, M.-K. *Semiconductor devices: physics and technology ; international student version*. (Wiley, 2013).
8. van Roosbroeck, W. & Shockley, W. Photon-Radiative Recombination of Electrons and Holes in Germanium. *Phys. Rev.* **94**, 1558–1560 (1954).
9. Würfel, P., Finkbeiner, S. & Daub, E. Generalized Planck's radiation law for luminescence via indirect transitions. *Appl. Phys. A* **60**, 67–70 (1995).
10. Katahara, J. K. & Hillhouse, H. W. Quasi-Fermi level splitting and sub-bandgap absorptivity from semiconductor photoluminescence. *J. Appl. Phys.* **116**, 173504 (2014).
11. Jimenez, J. & Tamm, J. W. Photoluminescence (PL) Techniques. in *Spectroscopic Analysis of Optoelectronic Semiconductors* vol. 202 143–211 (Springer International Publishing, 2016).
12. Elliott, R. J. Intensity of Optical Absorption by Excitons. *Phys. Rev.* **108**, 1384–1389 (1957).
13. Fang, H.-H., Adjokatse, S., Shao, S., Even, J. & Loi, M. A. Long-lived hot-carrier light emission and large blue shift in formamidinium tin triiodide perovskites. *Nat Commun* **9**, 243 (2018).
14. Nguyen, D.-T. *et al.* Quantitative experimental assessment of hot carrier-enhanced solar cells at room temperature. *Nat Energy* **3**, 236–242 (2018).
15. Kirchartz, T., Helbig, A. & Rau, U. Note on the interpretation of electroluminescence images using their spectral information. *Solar Energy Materials and Solar Cells* **92**, 1621–1627 (2008).
16. Hinken, D., Bothe, K., Ramspeck, K., Herlufsen, S. & Brendel, R. Determination of the effective diffusion length of silicon solar cells from photoluminescence. *Journal of Applied Physics* **105**, 104516 (2009).
17. Zegrya, G., Gunko, N. & Polkovnikov, A. New Semiconductor Materials. Characteristics and Properties. <http://www.ioffe.ru/SVA/>.

18. Conibeer, G., Zhang, Y., Bremner, S. P. & Shrestha, S. Towards an understanding of hot carrier cooling mechanisms in multiple quantum wells. *Jpn. J. Appl. Phys.* **56**, 091201 (2017).
19. Kim, J. Y., Lee, J.-W., Jung, H. S., Shin, H. & Park, N.-G. High-Efficiency Perovskite Solar Cells. *Chem. Rev.* **120**, 7867–7918 (2020).
20. Delport, G., Macpherson, S. & Stranks, S. D. Imaging carrier transport properties in halide perovskites using time-resolved optical microscopy. *arXiv:1911.10615 [cond-mat, physics:physics]* (2019).
21. Krückemeier, L., Krogmeier, B., Liu, Z., Rau, U. & Kirchartz, T. Understanding Transient Photoluminescence in Halide Perovskite Layer Stacks and Solar Cells. *Adv. Energy Mater.* 2003489 (2021) doi:10.1002/aenm.202003489.
22. Maiberg, M. & Scheer, R. Theoretical study of time-resolved luminescence in semiconductors. II. Pulsed excitation. *Journal of Applied Physics* **116**, 123711 (2014).
23. Kirchartz, T., Márquez, J. A., Stolterfoht, M. & Unold, T. Photoluminescence-Based Characterization of Halide Perovskites for Photovoltaics. *Adv. Energy Mater.* **10**, 1904134 (2020).
24. Fraunhofer ISE. *Photovoltaic report*. <https://www.ise.fraunhofer.de/content/dam/ise/de/documents/publications/studies/Photovoltaics-Report.pdf>.
25. Guillemoles, J.-F., Kirchartz, T., Cahen, D. & Rau, U. Guide for the perplexed to the Shockley–Queisser model for solar cells. *Nat. Photonics* **13**, 501–505 (2019).
26. NREL. Best Research-Cell Efficiency Chart. at <https://www.nrel.gov/pv/cell-efficiency.html>.
27. Connolly, J. P. & Mencaraglia, D. III-V Solar Cells. at <http://arxiv.org/abs/1301.1278> (2013).
28. Celik, I. *et al.* Energy Payback Time (EPBT) and Energy Return on Energy Invested (EROI) of Perovskite Tandem Photovoltaic Solar Cells. *IEEE Journal of Photovoltaics* **8**, 305–309 (2018).
29. De Wolf, S. *et al.* Organometallic Halide Perovskites: Sharp Optical Absorption Edge and Its Relation to Photovoltaic Performance. *J. Phys. Chem. Lett.* **5**, 1035–1039 (2014).
30. Proise, F. Study and realisation of micro/nano photovoltaic cells and their concentration systems. (2015).

References – Chapter 2

1. Johnson, S. D., Moreau, P.-A., Gregory, T. & Padgett, M. J. How many photons does it take to form an image? *Appl. Phys. Lett.* **116**, 260504 (2020).
2. Gove, R. J. CMOS image sensor technology advances for mobile devices. in *High Performance Silicon Imaging* 185–240 (Elsevier, 2020). doi:10.1016/B978-0-08-102434-8.00007-6.
3. Hagen, N. & Kudenov, M. W. Review of snapshot spectral imaging technologies. *Opt. Eng.* **52**, 090901 (2013).
4. Gottlieb, P. A television scanning scheme for a detector-noise-limited system. *IEEE Trans. Inform. Theory* **14**, 428–433 (1968).
5. Streeter, L., Burling-Claridge, G. R., Cree, M. J. & Künnemeyer, R. Optical full Hadamard matrix multiplexing and noise effects. *Appl. Opt.* **48**, 2078 (2009).
6. Welsh, S. S. Applications of single-pixel imaging. in (2017).
7. Simpson, R. G. & Barrett, H. H. Coded-Aperture Imaging. in *Nuclear Medicine, Ultrasonics, and Thermography* (eds. Nudelman, S. & Patton, D. D.) 217–311 (Springer US, 1980). doi:10.1007/978-1-4684-3671-6_8.

8. Swift, R. D., Wattson, R. B., Decker, J. A., Paganetti, R. & Harwit, M. Hadamard transform imager and imaging spectrometer. *Appl. Opt.* **15**, 1595 (1976).
9. Golay, M. J. E. Multi-Slit Spectrometry*. *J. Opt. Soc. Am.* **39**, 437 (1949).
10. Hotelling, H. Some Improvements in Weighing and Other Experimental Techniques. *Ann. Math. Statist.* **15**, 297–306 (1944).
11. Gao, L. & Wang, L. V. A review of snapshot multidimensional optical imaging: Measuring photon tags in parallel. *Physics Reports* **616**, 1–37 (2016).
12. Schermelleh, L. *et al.* Super-resolution microscopy demystified. *Nat Cell Biol* **21**, 72–84 (2019).
13. Duarte, M. F. *et al.* Single-pixel imaging via compressive sampling. *IEEE Signal Process. Mag.* **25**, 83–91 (2008).
14. Rousset, F. Single-pixel Imaging: development and applications of adaptive methods. (2017).
15. Cuiling Gong & Hogan, T. CMOS Compatible Fabrication Processes for the Digital Micromirror Device. *IEEE J. Electron Devices Soc.* **2**, 27–32 (2014).
16. Gibson, G. M., Johnson, S. D. & Padgett, M. J. Single-pixel imaging 12 years on: a review. *Opt. Express* **28**, 28190 (2020).
17. Sun, M.-J. & Zhang, J.-M. Single-Pixel Imaging and Its Application in Three-Dimensional Reconstruction: A Brief Review. *Sensors* **19**, 732 (2019).
18. Xu, Z.-H., Chen, W., Penuelas, J., Padgett, M. & Sun, M.-J. 1000 fps computational ghost imaging using LED-based structured illumination. *Opt. Express* **26**, 2427 (2018).
19. Ferri, F., Magatti, D., Lugiato, L. A. & Gatti, A. Differential Ghost Imaging. *Phys. Rev. Lett.* **104**, 253603 (2010).
20. Bian, L., Suo, J., Dai, Q. & Chen, F. Experimental comparison of single-pixel imaging algorithms. *J. Opt. Soc. Am. A* **35**, 78 (2018).
21. Penrose, R. A generalized inverse for matrices. *Math. Proc. Camb. Phil. Soc.* **51**, 406–413 (1955).
22. Rousset, F. *et al.* Adaptive Basis Scan by Wavelet Prediction for Single-Pixel Imaging. *IEEE Trans. Comput. Imaging* **3**, 36–46 (2017).
23. Higham, C. F., Murray-Smith, R., Padgett, M. J. & Edgar, M. P. Deep learning for real-time single-pixel video. *Sci Rep* **8**, 2369 (2018).
24. Yao, R., Ochoa, M., Yan, P. & Intes, X. Net-FLICS: fast quantitative wide-field fluorescence lifetime imaging with compressed sensing – a deep learning approach. *Light Sci Appl* **8**, 26 (2019).
25. Mur, A. L., Peyrin, F. & Ducros, N. Recurrent Neural Networks for Compressive Video Reconstruction. in *2020 IEEE 17th International Symposium on Biomedical Imaging (ISBI)* 1651–1654 (IEEE, 2020). doi:10.1109/ISBI45749.2020.9098327.
26. Pronina, V. *et al.* 3D denoised completion network for deep single-pixel reconstruction of hyperspectral images. *Opt. Express* **29**, 39559 (2021).
27. Zhang, J. & Ghanem, B. ISTA-Net: Interpretable Optimization-Inspired Deep Network for Image Compressive Sensing. in *2018 IEEE/CVF Conference on Computer Vision and Pattern Recognition* 1828–1837 (IEEE, 2018). doi:10.1109/CVPR.2018.00196.
28. Crombez, S., Exbrayat-Heritier, C., Ruggiero, F., Ray, C. & Ducros, N. Hyperspectral compressive microscopy based on structured light sheet and deep convolutional neural network. in *Unconventional Optical Imaging III* (eds. Georges, M. P., Popescu, G. & Verrier, N.) 24 (SPIE, 2022). doi:10.1117/12.2616521.
29. Duarte, M. F. *et al.* Single-pixel imaging via compressive sampling. *IEEE Signal Processing Magazine* **25**, 83–91 (2008).
30. Czajkowski, K. M., Pastuszczyk, A. & Kotyński, R. Single-pixel imaging with Morlet wavelet correlated random patterns. *Scientific Reports* **8**, (2018).

31. Zhang, Z., Wang, X., Zheng, G. & Zhong, J. Hadamard single-pixel imaging versus Fourier single-pixel imaging. *Optics Express* **25**, 19619 (2017).
32. Zhang, Z., Wang, X., Zheng, G. & Zhong, J. Fast Fourier single-pixel imaging via binary illumination. *Scientific Reports* **7**, (2017).
33. Rousset, F., Peyrin, F. & Ducros, N. A Semi Nonnegative Matrix Factorization Technique for Pattern Generalization in Single-Pixel Imaging. *IEEE Trans. Comput. Imaging* **4**, 284–294 (2018).
34. Li, M. *et al.* Underwater Object Detection and Reconstruction Based on Active Single-Pixel Imaging and Super-Resolution Convolutional Neural Network. *Sensors* **21**, 313 (2021).
35. Rodríguez, A. D., Clemente, P., Tajahuerce, E. & Lancis, J. Dual-mode optical microscope based on single-pixel imaging. *Optics and Lasers in Engineering* **82**, 87–94 (2016).
36. Welsh, S. S. Applications of single-pixel imaging. (University of Glasgow, 2017).
37. Yu, W.-K. *et al.* Complementary compressive imaging for the telescopic system. *Sci Rep* **4**, 5834 (2015).
38. Radwell, N. *et al.* Single-pixel infrared and visible microscope. *Optica* **1**, 285 (2014).
39. Zhang, J., Wang, Q., Dai, J. & Cai, W. Demonstration of a cost-effective single-pixel UV camera for flame chemiluminescence imaging. *Appl. Opt.* **58**, 5248 (2019).
40. Schmitt, K. M. & Rahm, M. Evaluation of the impact of diffraction on image reconstruction in single-pixel imaging systems. *Opt. Express* **24**, 23863 (2016).
41. Ivanov, O. P., Sudarkin, A. N., Stepanov, V. E. & Urutskoev, L. I. Portable X-ray and gamma-ray imager with coded mask: performance characteristics and methods of image reconstruction. *Nuclear Instruments and Methods in Physics Research Section A: Accelerators, Spectrometers, Detectors and Associated Equipment* **422**, 729–734 (1999).
42. Cieślak, M. J., Gamage, K. A. A. & Glover, R. Coded-aperture imaging systems: Past, present and future development – A review. *Radiation Measurements* **92**, 59–71 (2016).
43. Vallés, A., He, J., Ohno, S., Omatsu, T. & Miyamoto, K. Broadband high-resolution terahertz single-pixel imaging. *Opt. Express* **28**, 28868 (2020).
44. Chan, W. L. *et al.* A single-pixel terahertz imaging system based on compressed sensing. *Appl. Phys. Lett.* **93**, 121105 (2008).
45. Studer, V. *et al.* Compressive fluorescence microscopy for biological and hyperspectral imaging. *Proc. Natl. Acad. Sci. U.S.A.* **109**, (2012).
46. Chen, W. *et al.* Hyperspectral imaging via a multiplexing digital micromirror device. *Optics and Lasers in Engineering* **151**, 106889 (2022).
47. Baltušis, A., Koutsourakis, G., Wood, S. & Sweeney, S. J. Imaging of Minority Charge Carrier Lifetimes of Semiconductors using Digital Light Processing and Compressed Sensing. in *Conference on Lasers and Electro-Optics JTu3A.11* (Optica Publishing Group, 2021). doi:10.1364/CLEO_AT.2021.JTu3A.11.
48. Pian, Q., Yao, R., Sinsuebphon, N. & Intes, X. Compressive hyperspectral time-resolved wide-field fluorescence lifetime imaging. *Nature Photon* **11**, 411–414 (2017).
49. Rousset, F. *et al.* Time-resolved multispectral imaging based on an adaptive single-pixel camera. *Opt. Express* **26**, 10550 (2018).
50. Zhang, Y. *et al.* 3D single-pixel video. *J. Opt.* **18**, 035203 (2016).
51. Yang, Z. *et al.* 3-D Computational Ghost Imaging With Extended Depth of Field for Measurement. *IEEE Trans. Instrum. Meas.* **68**, 4906–4912 (2019).
52. Li, M. *et al.* Single-pixel ptychography. *Opt. Lett.* **46**, 1624 (2021).
53. Musarra, G. *et al.* Non-line-of-sight 3D imaging with a single-pixel camera. *Phys. Rev. Applied* **12**, 011002 (2019).

54. Sun, M.-J. *et al.* Single-pixel three-dimensional imaging with time-based depth resolution. *Nature Communications* **7**, (2016).
55. Klein, L., Kristoffersen, A. S., Touš, J. & Židek, K. Versatile compressive microscope for hyperspectral transmission and fluorescence lifetime imaging. *Opt. Express* **30**, 15708 (2022).
56. Soldevila, F. *et al.* Giga-voxel multidimensional fluorescence imaging combining single-pixel detection and data fusion. *Opt. Lett.* **46**, 4312 (2021).
57. Cox, M. A., Toninelli, E., Cheng, L., Padgett, M. J. & Forbes, A. A High-Speed, Wavelength Invariant, Single-Pixel Wavefront Sensor With a Digital Micromirror Device. *IEEE Access* **7**, 85860–85866 (2019).
58. Zhang, Z. *et al.* Simultaneous spatial, spectral, and 3D compressive imaging via efficient Fourier single-pixel measurements. *Optica* **5**, 315 (2018).
59. Velsink, M. C., Lyu, Z., Pinkse, P. W. H. & Amitonova, L. V. Comparison of round- and square-core fibers for sensing, imaging, and spectroscopy. *Opt. Express* **29**, 6523 (2021).
60. Farley, K. *et al.* Optical fiber designs for beam shaping. in (ed. Ramachandran, S.) 89612U (2014). doi:10.1117/12.2041992.
61. Nie, S., Zhu, Y., Kunz, O., Trupke, T. & Hameiri, Z. Advanced photoluminescence imaging using non-uniform excitation. *Progress in Photovoltaics* **30**, 349–359 (2022).
62. Spatial Filters Tutorial.
https://www.thorlabs.com/newgrouppage9.cfm?objectgroup_id=10768.
63. Goetz, A. F. H. Three decades of hyperspectral remote sensing of the Earth: A personal view. *Remote Sensing of Environment* **113**, S5–S16 (2009).
64. Brunner, K., Abstreiter, G., Böhm, G., Tränkle, G. & Weimann, G. Sharp-line photoluminescence of excitons localized at GaAs/AlGaAs quantum well inhomogeneities. *Appl. Phys. Lett.* **64**, 3320–3322 (1994).
65. Wu, Q., Grober, R. D., Gammon, D. & Katzer, D. S. Imaging Spectroscopy of Two-Dimensional Excitons in a Narrow GaAs/AlGaAs Quantum Well. *Phys. Rev. Lett.* **83**, 2652–2655 (1999).
66. Johnson, W. R., Wilson, D. W., Fink, W., Humayun, M. & Bearman, G. Snapshot hyperspectral imaging in ophthalmology. *J. Biomed. Opt.* **12**, 014036 (2007).
67. Gat, N., Scriven, G., Garman, J., Li, M. D. & Zhang, J. Development of four-dimensional imaging spectrometers (4D-IS). in (eds. Shen, S. S. & Lewis, P. E.) 63020M (2006). doi:10.1117/12.678082.
68. Grusche, S. Basic slit spectroscope reveals three-dimensional scenes through diagonal slices of hyperspectral cubes. *Appl. Opt.* **53**, 4594 (2014).
69. Delamarre, A. Characterization of solar cells using electroluminescence and photoluminescence hyperspectral images. *J. Photon. Energy* **2**, 027004 (2012).
70. A Horse's Motion Scientifically Determined. *Scientific American* vol. 39 (1878).
71. Mach, E. & Salcher, P. Photographische Fixirung der durch Projectile in der Luft eingeleiteten Vorgänge. *Ann. Phys. Chem.* **268**, 277–291 (1887).
72. Gao, L., Liang, J., Li, C. & Wang, L. V. Single-shot compressed ultrafast photography at one hundred billion frames per second. *Nature* **516**, 74–77 (2014).
73. Greenstein, M., Tamor, M. A. & Wolfe, J. P. Time-resolved images of electron-hole droplets produced by intense pulsed-laser excitation of germanium. *Solid State Communications* **45**, 355–359 (1983).
74. Arnold, C. An ultrashort history of ultrafast imaging.
75. Datta, R., Heaster, T. M., Sharick, J. T., Gillette, A. A. & Skala, M. C. Fluorescence lifetime imaging microscopy: fundamentals and advances in instrumentation, analysis, and applications. *J. Biomed. Opt.* **25**, 1 (2020).

76. Zhao, W. *et al.* Coupled time resolved and high frequency modulated photoluminescence probing surface passivation of highly doped n-type InP samples. *Journal of Applied Physics* **129**, 215305 (2021).
77. Hirvonen, L. M. & Suhling, K. Wide-field TCSPC: methods and applications. *Meas. Sci. Technol.* **28**, 012003 (2017).
78. Delport, G., Macpherson, S. & Stranks, S. D. Imaging carrier transport properties in halide perovskites using time-resolved optical microscopy. *arXiv:1911.10615 [cond-mat, physics:physics]* (2019).
79. *PI-MAX4 Camera System Manual*. <https://www.princetoninstruments.com/wp-content/uploads/2020/04/PI-MAX4-System-Manual-Issue-10-4411-0139.pdf>.
80. Yang, C. *et al.* Hyperspectrally Compressed Ultrafast Photography. *Phys. Rev. Lett.* **124**, 023902 (2020).
81. Wang, P., Liang, J. & Wang, L. V. Single-shot ultrafast imaging attaining 70 trillion frames per second. *Nat Commun* **11**, 2091 (2020).
82. Ding, P. *et al.* Single-shot spectral-volumetric compressed ultrafast photography. *Adv. Photon.* **3**, (2021).
83. Krishnan, R. V., Saitoh, H., Terada, H., Centonze, V. E. & Herman, B. Development of a multiphoton fluorescence lifetime imaging microscopy system using a streak camera. *Review of Scientific Instruments* **74**, 2714–2721 (2003).
84. Kester, R. T., Bedard, N., Gao, L. & Tkaczyk, T. S. Real-time snapshot hyperspectral imaging endoscope. *J. Biomed. Opt.* **16**, 056005 (2011).
85. Heshmat, B., Satat, G., Barsi, C. & Raskar, R. Single-shot ultrafast imaging using parallax-free alignment with a tilted lenslet array. in *CLEO: 2014 STu3E.7* (OSA, 2014). doi:10.1364/CLEO_SI.2014.STu3E.7.
86. Bub, G., Tecza, M., Helmes, M., Lee, P. & Kohl, P. Temporal pixel multiplexing for simultaneous high-speed, high-resolution imaging. *Nat Methods* **7**, 209–211 (2010).
87. Scikit Learn Clustering Documentation. <https://scikit-learn.org/stable/modules/clustering.html>.
88. SHyLoc IP Core. https://www.esa.int/Enabling_Support/Space_Engineering_Technology/Microelectronics/SHyLoC_IP_Core.

References – Chapter 3

1. Bercegol, A. Transport de charge dans le photovoltaïque par imagerie multidimensionnelle de luminescence. (2019).
2. IMAGERIE MONO-PIXEL HYPER-SPECTRALE RÉVOLUE EN TEMPS.
3. Yang, C. *et al.* Hyperspectrally Compressed Ultrafast Photography. *Phys. Rev. Lett.* **124**, 023902 (2020).
4. Pian, Q., Yao, R., Sinsuebphon, N. & Intes, X. Compressive hyperspectral time-resolved wide-field fluorescence lifetime imaging. *Nature Photon* **11**, 411–414 (2017).
5. Rousset, F. *et al.* Time-resolved multispectral imaging based on an adaptive single-pixel camera. *Opt. Express* **26**, 10550 (2018).
6. Horn, A. *Ultra-fast material metrology*. (Wiley-VCH, 2009).
7. Uhring, W. & Zlatanski, M. Ultrafast Imaging in Standard (Bi)CMOS Technology. in *Photodetectors* (ed. Gateva, S.) (InTech, 2012). doi:10.5772/35767.
8. Hamamatsu. Guide to streak camera.
9. Gao, L., Liang, J., Li, C. & Wang, L. V. Single-shot compressed ultrafast photography at one hundred billion frames per second. *Nature* **516**, 74–77 (2014).

10. Meyzonnette, J. & L??pine, T. *Bases de radiom??trie optique*. (CEPADUES-Editions, 2001).
11. Andaji-Garmaroudi, Z. *et al.* A Highly Emissive Surface Layer in Mixed-Halide Multication Perovskites. *Adv. Mater.* **31**, 1902374 (2019).
12. Tokarev, S. *et al.* Electron injection effect in In₂O₃ and SnO₂ nanocrystals modified by ruthenium heteroleptic complexes. *Phys. Chem. Chem. Phys.* **22**, 8146–8156 (2020).
13. deQuilettes, D. W. *et al.* Slowed Recombination via Tunable Surface Energetics in Perovskite Solar Cells. *arXiv:2204.07642 [cond-mat, physics:physics]* (2022).
14. Arnaoutakis, G., Cazzanelli, M., Koura, Z. E. & Miotello, A. Charge Carrier Recombination Dynamics of Semiconductor Photocatalysts. **3**.
15. Seitz, M. *et al.* Mapping the Trap-State Landscape in 2D Metal-Halide Perovskites Using Transient Photoluminescence Microscopy. *Adv. Optical Mater.* 2001875 (2021) doi:10.1002/adom.202001875.
16. Li, Q. *et al.* Time-resolved photoluminescence studies of InGaN/GaN multi-quantum-wells blue and green light-emitting diodes at room temperature. *Optik* **127**, 1809–1813 (2016).
17. Bleuse, J., Ducroquet, F. & Mariette, H. Potential Fluctuations and Localization Effects in CZTS Single Crystals, as Revealed by Optical Spectroscopy. *Journal of Elec Materi* **47**, 4282–4288 (2018).
18. Yamada, T., Yamada, Y., Nakaike, Y., Wakamiya, A. & Kanemitsu, Y. Photon Emission and Reabsorption Processes in CH₃NH₃PbBr₃ Single Crystals Revealed by Time-Resolved Two-Photon-Excitation Photoluminescence Microscopy. *Phys. Rev. Applied* **7**, 014001 (2017).
19. Staub, F., Anusca, I., Lupascu, D. C., Rau, U. & Kirchartz, T. Effect of reabsorption and photon recycling on photoluminescence spectra and transients in lead-halide perovskite crystals. *J. Phys. Mater.* **3**, 025003 (2020).
20. Sridharan, A., Noel, N. K., Rand, B. P. & Kéna-Cohen, S. Role of Photon Recycling and Band Filling in Halide Perovskite Photoluminescence under Focussed Excitation Conditions. *J. Phys. Chem. C* acs.jpcc.0c09103 (2021) doi:10.1021/acs.jpcc.0c09103.
21. Snoke, D. W., Rühle, W. W., Lu, Y.-C. & Bauser, E. Evolution of a nonthermal electron energy distribution in GaAs. *Phys. Rev. B* **45**, 10979–10989 (1992).
22. Ryan, J. F. *et al.* Time-Resolved Photoluminescence of Two-Dimensional Hot Carriers in GaAs-AlGaAs Heterostructures. *Phys. Rev. Lett.* **53**, 1841–1844 (1984).
23. Pelouch, W. S. *et al.* Comparison of hot-carrier relaxation in quantum wells and bulk GaAs at high carrier densities. *Phys. Rev. B* **45**, 1450–1453 (1992).
24. Kahmann, S., Shao, S. & Loi, M. A. Cooling, Scattering, and Recombination—The Role of the Material Quality for the Physics of Tin Halide Perovskites. *Adv. Funct. Mater.* **29**, 1902963 (2019).
25. Li, M. *et al.* Slow cooling and highly efficient extraction of hot carriers in colloidal perovskite nanocrystals. *Nat Commun* **8**, 14350 (2017).
26. Fang, H.-H., Adjokatse, S., Shao, S., Even, J. & Loi, M. A. Long-lived hot-carrier light emission and large blue shift in formamidinium tin triiodide perovskites. *Nat Commun* **9**, 243 (2018).
27. Bleuse, J. *et al.* Optical determination of the band gap and band tail of epitaxial Ag₂ZnSnSe₄ at low temperature. *Phys. Rev. B* **102**, 195205 (2020).
28. Bhattacharya, R., Pal, B. & Bansal, B. On conversion of luminescence into absorption and the van Roosbroeck-Shockley relation. *Appl. Phys. Lett.* **100**, 222103 (2012).
29. Popoff, S. M., Shih, G., Dirk, B. & GustavePariente. *wavefrontshaping/ALP4lib: 1.0.1*. (Zenodo, 2022). doi:10.5281/ZENODO.6121191.

30. Klein, L. & Zidek, K. Collection of micromirror-modulated light in the single-pixel broadband hyperspectral microscope. *arXiv:2001.08804 [physics]* (2020).
31. Rice, J. P., Neira, J. E., Kehoe, M. & Swanson, R. DMD diffraction measurements to support design of projectors for test and evaluation of multispectral and hyperspectral imaging sensors. in (eds. Hornbeck, L. J. & Douglass, M. R.) 72100D (2009). doi:10.1117/12.808990.
32. Lorente Mur, A. Single-pixel imaging : compressed video acquisition and reconstruction using Deep learning. (INSA Lyon, 2021).
33. Streeter, L., Burling-Claridge, G. R., Cree, M. J. & Künnemeyer, R. Optical full Hadamard matrix multiplexing and noise effects. *Appl. Opt.* **48**, 2078 (2009).
34. Popoff, S. M. Setting up a DMD: Diffraction effects. <https://www.wavefrontshaping.net/post/id/21>.
35. Douet, B. *et al.* Digital micromirror device for holographic and Fourier optics applications. *Emergent Scientist* **5**, 4 (2021).
36. Soldevila, F. *et al.* Giga-voxel multidimensional fluorescence imaging combining single-pixel detection and data fusion. *Opt. Lett.* **46**, 4312 (2021).
37. He, C. *Compressive Sensing pour la 4D-photoluminescence*.

References – Chapter 4

1. Motti, S. G. *et al.* Controlling competing photochemical reactions stabilizes perovskite solar cells. *Nat. Photonics* **13**, 532–539 (2019).
2. Huang, Y. *et al.* Detrimental effects of ion migration in the perovskite and hole transport layers on the efficiency of inverted perovskite solar cells. *J. Photon. Energy* **10**, 1 (2020).
3. Deng, X. *et al.* Dynamic study of the light soaking effect on perovskite solar cells by in-situ photoluminescence microscopy. *Nano Energy* **46**, 356–364 (2018).
4. Mahon, N. S. *et al.* Photoluminescence kinetics for monitoring photoinduced processes in perovskite solar cells. *Solar Energy* **195**, 114–120 (2020).
5. Cacovich, S. *et al.* Light-Induced Passivation in Triple Cation Mixed Halide Perovskites: Interplay between Transport Properties and Surface Chemistry. *ACS Appl. Mater. Interfaces* **12**, 34784–34794 (2020).
6. Andaji-Garmaroudi, Z. *et al.* A Highly Emissive Surface Layer in Mixed-Halide Multication Perovskites. *Adv. Mater.* **31**, 1902374 (2019).
7. Motti, S. G. *et al.* Defect Activity in Lead Halide Perovskites. *Adv. Mater.* **31**, 1901183 (2019).
8. Kim, J. Y., Lee, J.-W., Jung, H. S., Shin, H. & Park, N.-G. High-Efficiency Perovskite Solar Cells. *Chem. Rev.* **120**, 7867–7918 (2020).
9. Longeaud, C., Ramos, F. J., Rebai, A. & Rousset, J. Impact of Environmental Stresses Onto Transport Properties of Hybrid Perovskite Investigated by Steady State Photocarrier Grating and Steady State Photocurrent Techniques. *Sol. RRL* **2**, 1800192 (2018).
10. Bercegol, A. *et al.* Quantitative optical assessment of photonic and electronic properties in halide perovskite. *Nat Commun* **10**, 1586 (2019).
11. Seitz, M. *et al.* Mapping the Trap-State Landscape in 2D Metal-Halide Perovskites Using Transient Photoluminescence Microscopy. *Adv. Optical Mater.* 2001875 (2021) doi:10.1002/adom.202001875.
12. Zegrya, G., Gunko, N. & Polkovnikov, A. New Semiconductor Materials. Characteristics and Properties. <http://www.ioffe.ru/SVA/>.
13. Streeter, L., Burling-Claridge, G. R., Cree, M. J. & Künnemeyer, R. Optical full Hadamard matrix multiplexing and noise effects. *Appl. Opt.* **48**, 2078 (2009).

14. Soldevila, F. *et al.* Giga-voxel multidimensional fluorescence imaging combining single-pixel detection and data fusion. *Opt. Lett.* **46**, 4312 (2021).
15. Aspnes, D. E., Kelso, S. M., Logan, R. A. & Bhat, R. Optical properties of $\text{Al}_x\text{Ga}_{1-x}\text{As}$. *Journal of Applied Physics* **60**, 754–767 (1986).
16. Dalal, V. L., Dreeben, A. B. & Triano, A. Temperature Dependence of Hole Velocity in p -GaAs. *Journal of Applied Physics* **42**, 2864–2867 (1971).
17. Apostolova, T. Self-limited ionization in bandgap renormalized GaAs at high femtosecond laser intensities. *Opt. Eng* **51**, 121808 (2012).
18. Snoke, D. W., Rühle, W. W., Lu, Y.-C. & Bauser, E. Evolution of a nonthermal electron energy distribution in GaAs. *Phys. Rev. B* **45**, 10979–10989 (1992).
19. Rosenwaks, Y. *et al.* Hot-carrier cooling in GaAs: Quantum wells versus bulk. *Phys. Rev. B* **48**, 14675–14678 (1993).
20. Gfroerer, T. H. Photoluminescence in Analysis of Surfaces and Interfaces. in *Encyclopedia of Analytical Chemistry* (ed. Meyers, R. A.) a2510 (John Wiley & Sons, Ltd, 2006). doi:10.1002/9780470027318.a2510.
21. Jimenez, J. & Tomm, J. W. Photoluminescence (PL) Techniques. in *Spectroscopic Analysis of Optoelectronic Semiconductors* vol. 202 143–211 (Springer International Publishing, 2016).
22. Proise, F. Study and realisation of micro/nano photovoltaic cells and their concentration systems. (2015).

References – Chapter 5

1. Katahara, J. K. & Hillhouse, H. W. Quasi-Fermi level splitting and sub-bandgap absorptivity from semiconductor photoluminescence. *J. Appl. Phys.* **116**, 173504 (2014).
2. Seitz, M. *et al.* Mapping the Trap-State Landscape in 2D Metal-Halide Perovskites Using Transient Photoluminescence Microscopy. *Adv. Optical Mater.* 2001875 (2021) doi:10.1002/adom.202001875.
3. Daub, E. & Würfel, P. Ultralow Values of the Absorption Coefficient of Si Obtained from Luminescence. *Phys. Rev. Lett.* **74**, 1020–1023 (1995).
4. Bhattacharya, R., Pal, B. & Bansal, B. On conversion of luminescence into absorption and the van Roosbroeck-Shockley relation. *Appl. Phys. Lett.* **100**, 222103 (2012).
5. Barugkin, C. *et al.* Ultralow Absorption Coefficient and Temperature Dependence of Radiative Recombination of $\text{CH}_3\text{NH}_3\text{PbI}_3$ Perovskite from Photoluminescence. *J. Phys. Chem. Lett.* **6**, 767–772 (2015).
6. Jimenez, J. & Tomm, J. W. Photoluminescence (PL) Techniques. in *Spectroscopic Analysis of Optoelectronic Semiconductors* vol. 202 143–211 (Springer International Publishing, 2016).
7. Grubbs, E. K., Moore, J. & Bermel, P. A. Photoluminescence Excitation Spectroscopy Characterization of Surface and Bulk Quality for Early-Stage Potential of Material Systems. in *2019 IEEE 46th Photovoltaic Specialists Conference (PVSC)* 0377–0381 (IEEE, 2019). doi:10.1109/PVSC40753.2019.8980637.
8. Berdebes, D. *et al.* Photoluminescence Excitation Spectroscopy for In-Line Optical Characterization of Crystalline Solar Cells. *IEEE J. Photovoltaics* **3**, 1342–1347 (2013).
9. Gfroerer, T. H. Photoluminescence in Analysis of Surfaces and Interfaces. in *Encyclopedia of Analytical Chemistry* (ed. Meyers, R. A.) a2510 (John Wiley & Sons, Ltd, 2006). doi:10.1002/9780470027318.a2510.

10. Zhu, Y., Ding, C., Ma, G. & Du, Z. Electronic State Characterization of TiO₂ Ultrafine Particles by Luminescence Spectroscopy. *Journal of Solid State Chemistry* **139**, 124–127 (1998).
11. Miller, R. C., Gossard, A. C., Sanders, G. D., Chang, Y.-C. & Schulman, J. N. New evidence of extensive valence-band mixing in GaAs quantum wells through excitation photoluminescence studies. *Phys. Rev. B* **32**, 8452–8454 (1985).
12. Wang, X. *et al.* Valence Band Splitting in Wurtzite InGaAs Nanoneedles Studied by Photoluminescence Excitation Spectroscopy. *ACS Nano* **8**, 11440–11446 (2014).
13. DeLong, M. C. *et al.* Photoluminescence, photoluminescence excitation, and resonant Raman spectroscopy of disordered and ordered Ga_{0.52}In_{0.48}P. *Journal of Applied Physics* **73**, 5163–5172 (1993).
14. García-García, J., González-Hernández, J., Mendoza-Alvarez, J. G., Cruz, E. L. & Contreras-Puente, G. Photoluminescence characterization of the surface layer of chemically etched CdTe. *Journal of Applied Physics* **67**, 3810–3814 (1990).
15. Bhosale, J. S., Moore, J. E., Wang, X., Bermel, P. & Lundstrom, M. S. Steady-state photoluminescent excitation characterization of semiconductor carrier recombination. *Review of Scientific Instruments* **87**, 013104 (2016).
16. Van Ryswyk, Hal. & Ellis, A. B. Optical coupling of surface chemistry. Photoluminescent properties of a derivatized gallium arsenide surface undergoing redox chemistry. *J. Am. Chem. Soc.* **108**, 2454–2455 (1986).
17. Wang, X. *et al.* Photovoltaic Material Characterization With Steady State and Transient Photoluminescence. *IEEE J. Photovoltaics* **5**, 282–287 (2015).
18. Corfdir, P., Van Hattem, B., Uccelli, E., Fontcuberta i Morral, A. & Phillips, R. T. Charge carrier generation, relaxation, and recombination in polytypic GaAs nanowires studied by photoluminescence excitation spectroscopy. *Appl. Phys. Lett.* **103**, 133109 (2013).
19. Michl, B., Giesecke, J. A., Warta, W. & Schubert, M. C. Separation of Front and Backside Surface Recombination by Photoluminescence Imaging on Both Wafer Sides. *IEEE J. Photovoltaics* **2**, 348–351 (2012).
20. Araújo, G. L. & Martí, A. Absolute limiting efficiencies for photovoltaic energy conversion. *Solar Energy Materials and Solar Cells* **33**, 213–240 (1994).
21. Cacovich, S. *et al.* Imaging and quantifying non-radiative losses at 23% efficient inverted perovskite solar cells interfaces. *Nat Commun* **13**, 2868 (2022).
22. van Roosbroeck, W. & Shockley, W. Photon-Radiative Recombination of Electrons and Holes in Germanium. *Phys. Rev.* **94**, 1558–1560 (1954).
23. Fassel, P. *et al.* Revealing the internal luminescence quantum efficiency of perovskite films via accurate quantification of photon recycling. *Matter* **4**, 1391–1412 (2021).
24. Raoult, E. *et al.* Optical Characterizations and Modelling of Semitransparent Perovskite Solar Cells for Tandem Applications. *36th European Photovoltaic Solar Energy Conference and Exhibition*; 757-763 7 pages, 6408 kb (2019) doi:10.4229/EUPVSEC20192019-3BV.2.53.
25. Merdasa, A. *et al.* Impact of Excess Lead Iodide on the Recombination Kinetics in Metal Halide Perovskites. *ACS Energy Lett.* **4**, 1370–1378 (2019).
26. Delamarre, A. Development of new methods of optoelectronic characterization of solar cells. (2013).
27. Burgelman, M., Nollet, P. & Degraeve, S. Modelling polycrystalline semiconductor solar cells. *Thin Solid Films* **361–362**, 527–532 (2000).
28. Zegrya, G., Gunko, N. & Polkovnikov, A. New Semiconductor Materials. Characteristics and Properties. <http://www.ioffe.ru/SVA/>.

References – Conclusion

1. Bleuse, J. *et al.* Optical determination of the band gap and band tail of epitaxial Ag₂ZnSnSe₄ at low temperature. *Phys. Rev. B* **102**, 195205 (2020).
2. Junek, J., Ondič, L. & Židek, K. Random temporal laser speckles for the robust measurement of sub-microsecond photoluminescence decay. *Opt. Express* **28**, 12363 (2020).
3. Béranguier, B. *et al.* Defects characterization in thin films photovoltaics materials by correlated high-frequency modulated and time resolved photoluminescence: An application to Cu(In,Ga)Se₂. *Thin Solid Films* **669**, 520–524 (2019).
4. Đorđević, N. *et al.* Machine Learning for Analysis of Time-Resolved Luminescence Data. *ACS Photonics* **5**, 4888–4895 (2018).
5. Vidon, G. *et al.* Mapping Transport Properties of Halide Perovskites via Short-Time-Dynamics Scaling Laws and Subnanosecond-Time-Resolution Imaging. *Phys. Rev. Applied* **16**, 044058 (2021).
6. Julien, A. Understanding Perovskite Experimental Degradation Pathways Combining Experimental Measurements and Simulations. (2022).
7. Hages, C. J. Machine Learning for Accelerated Analyses of Time-resolved Photoluminescence Data Via Bayesian Inference. (2022).
8. Pronina, V. *et al.* 3D denoised completion network for deep single-pixel reconstruction of hyperspectral images. *Opt. Express* **29**, 39559 (2021).
9. Motti, S. G. *et al.* Defect Activity in Lead Halide Perovskites. *Adv. Mater.* **31**, 1901183 (2019).

Appendices

A.	Consideration for calibrations	II
	From raw data to relative intensity	II
	From relative to absolute intensity	III
B.	Noise and artefacts consequences on basis scan with Hadamard.....	VI
C.	Generalization of diffraction artifact to 2D	XI
D.	Improvements for the pixel clustering setup	XIII
E.	Filtering out the laser reflection by polarization	XIV

A. Consideration for calibrations

From raw data to relative intensity

The raw signal from the different photodetectors needs processing to retrieve what is emitted by the sample (or to estimate it). Indeed, the electrons collected by sensors are produced by capturing photons from the device, the ambient light, and the sensor itself (thermal signal). Their extraction induces a read noise. Together with an offset added to avoid clipping values, they contribute to the dark (or background). The collected signal is further affected by the transmission of the setup. It can be assessed through a calibrated lamp (as discussed in the following paragraph) or compared to a reference sample.

In imaging, the transmission is not necessarily homogeneous spatially. Uniformity defects coming from the optical setup and detectors are corrected by estimating it with a flatfield acquisition. An example of classical data processing flow to take into account both the dark and the relative transmission is provided in Figure 1. Realizing this correction also increases the acquisition noise: the variance of the dark noise and the initial image add up. Furthermore, if the flatfield does not have a sufficient signal-to-noise ratio, it will induce fluctuations in the corrected image. These steps are not always relevant depending on the signal's desired precision and quality.

$$\text{corrected image} = (\text{initial image} - \text{dark}) / \text{dark corrected flatfield}$$

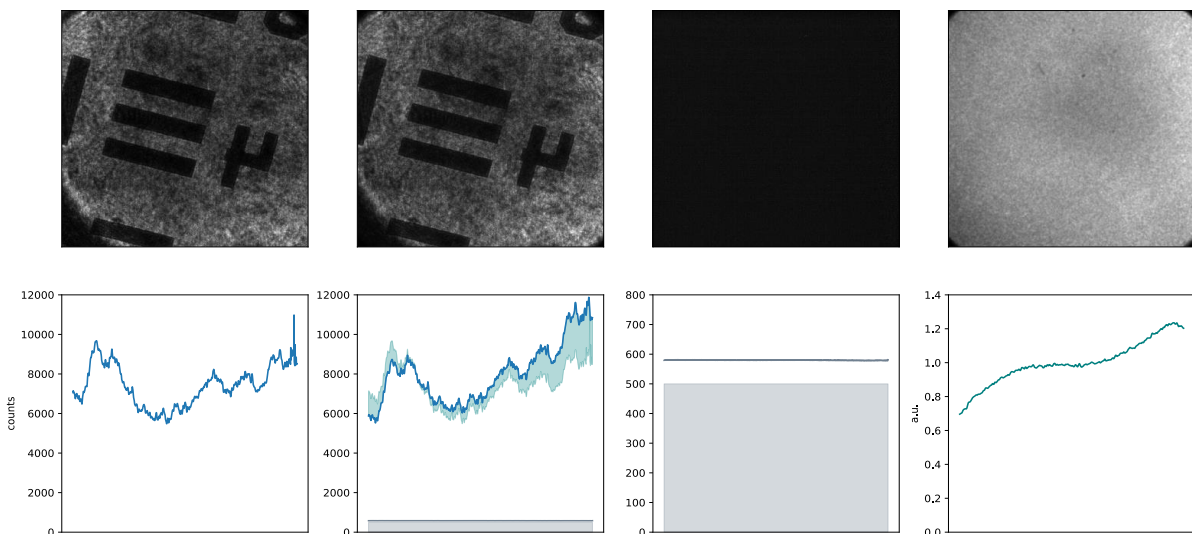


Figure 1: Classical correction of dark signal and uniformity defects for the TRFLIM setup. The top row presents different images, and the bottom corresponds to their spatial integration along the y-axis. Corrected data requires subtracting a dark reference and the division by a flatfield reference.

As with any streak camera acquisition, 4D-PL acquisitions require the subtraction of a dark measurement, performed with all mirrors in the "off" or shutter closed position. In SPI tests with the spectrometer, hyperspectral acquisitions of darks did not show any significant dependence on the position of the mirrors on the DMD while the laser was turned off. On the other hand, the Single Pixel Imaging acquisitions made with the spectrometer highlight the importance of spectral transmission calibration for the system. It can be combined with a flatfield correction by making an SPI acquisition using a calibrated lamp with a diffuse cosine, an integrating sphere, or a spectralon to image a homogeneous field. This extra step usually degrades the signal and is not applied for this setup.

From relative to absolute intensity

The absolute PL intensity emitted by the sample is pursued to compare different materials and to extract physical quantities as the quasi-Fermi level splitting or PLQY¹. Intensity calibration consists of estimating the photons flux emitted from the sample plane [$phot/s/sr/m^2$] from the number of analog-digital units (ADU, usually named as counts) provided by the camera.

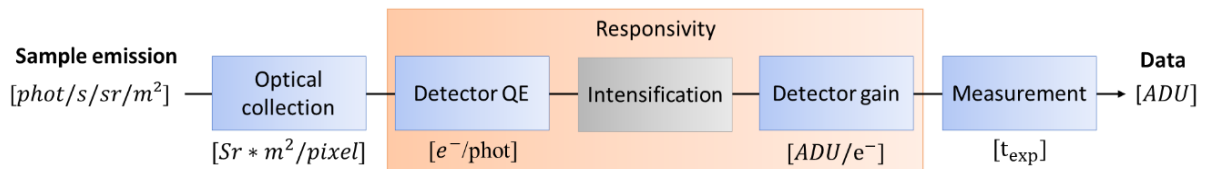


Figure 2: Scheme of the processes involved in the camera acquisition process. For intensified devices, the additional step in grey must be considered. Calibration is then performed for a certain intensification that is further calibrated.

This calibration depends on camera settings (acquisition time, intensification...) and optical setup (beam-splitter, filter...), as pictured in Figure 2. As the transmission of the optics is usually provided by the seller or can be measured, it can be corrected afterward. The collection of optics can be assessed through simple optical models generating approximation. For instance, the angular emission of the source must be known to evaluate the microscope objective collection. In this work, a Lambertian source is used, so the collected etendue is obtained by angular integration: $A_{sample} * \pi NA_{obj}^2$ where A_{sample} corresponds to the field of view and NA_{obj} denotes the numerical aperture of the objective. The camera's ability to detect photons also needs to be evaluated. The responsivity can describe a classical camera, the number of ADU per photon impinging on the detector. For an intensified camera, intensification

¹ Delamarre, A. Characterization of solar cells using electroluminescence and photoluminescence hyperspectral images. *J. Photon. Energy* **2**, 027004 (2012).

settings influence it and can be calibrated, as shown in G. Vidon's thesisⁱⁱ. For the example of the TRFLIM performed with an intensified camera, the number of ADU can be shown as a function of camera intensification and gate width and fit with classical parts. Indeed, for this model, the intensification gain increases the signal linearly by combining electron multiplication in the MCP and after the CCD.

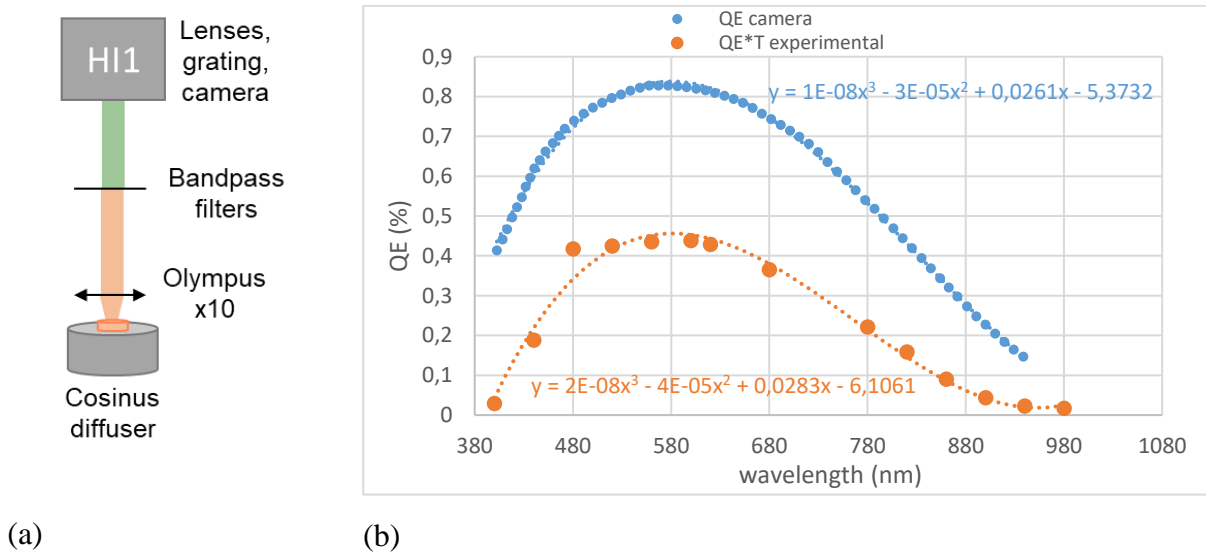


Figure 3 (a) Optical configuration used for zero order hyperspectral camera calibration (b) measured calibration curve in orange compared to the quantum efficiency provided by Hamamatsu in blue (dots: measurements, dashed line: polynomial fit).

When the detector is spectrally resolved, absolute calibration is directly obtained from the flatfield measurement with the calibrated lamp once the camera settings are considered. Otherwise, acquisition needs to be restricted to the wavelength of interest, as both transmissions of the optical setup and quantum efficiency of the detector vary spectrally. Doing so with a set of filters allows for extrapolating the spectral dependence. This approach was used to calibrate the hyperspectral zero-order camera and TRFLIM.

The estimated responsivity can be compared to the camera's quantum efficiency to have feedback on the calibration. Indeed, the former, once multiplied by the electronic gain, corresponds to the product of the QE and the transmission. Figure 3 b shows the photocathode quantum efficiency provided by Princeton compared to the experimental responsivity of the same order of magnitude. The experimental T*QE decreases faster, around 700-900nm, probably due to the optical transmission. The similarity in shape of these two curves suggests

ⁱⁱ Vidon, G. Why do decays decay? Transport and recombination dynamics of solar cells revealed via time resolved photoluminescence imaging: application to hybrid perovskites. (2022).

that the camera is the component that affects the spectral response more. One should note the QE from Hamamatsu is indicative and does not come from the test report of the lab camera. This plot tends to validate our calibration and our simple model of camera acquisition.

B. Noise and artifacts consequences on basis scan with Hadamard

This appendix presents the impact of different noises and artifacts on SPI reconstruction. If this imaging approach is told to improve the signal-to-noise ratio compared to raster scanning, multiplicative and additive noise propagates differently. In a second time, the influence of a constant offset and a linear drift in the illumination are studied.

A theoretical analysis of the influence of different noises in Hadamard basis scan is provided by Streeter et al.ⁱⁱⁱ Even though the information in each pixel is obtained from the linear combination of m measurements, the structure of the Hadamard matrix avoids the multiplication of noise by a factor of \sqrt{m} . Rather, it provides an additive noise reduction of factor $1/\sqrt{m}$ case because the Hadamard inverse introduces a multiplication of the variance by $1/m$. This case corresponds to a splitting approach in which the signal is indeed multiplied by the Hadamard inverse. Shifting leads to different weights in the reconstruction. It is comparable to the Hadamard S-matrix multiplexing, which employs a shift matrix whose first line and the first column are removed. It rather provides a reduction of a factor $m/2$ of additive noise. However, Hadamard multiplexing offers no improvement to multiplicative noise as photon noise.

The process is simulated on synthetic data to investigate the spatial reconstruction and the signal quality stake. A simulation with a Monte-Carlo algorithm used to add both additive and multiplicative noise allows for verifying the SNR boost of such an approach. The results are shown in Figure 4 and confirm the literature when excluding pixel 0. Indeed, because of the first line of the matrix, it is poorly conditioned.

Simulation of SPI

The impact of different factors is investigated, such as a background or a linear illumination drift. A constant offset in the measurement is completely suppressed on all pixels but the first. Shifted Hadamard matrix is thus robust to the background signal. Furthermore, a linear variation caused by temporal drift would influence the pixels $2^n - 1$, creating visible discontinuities in the reconstruction.

ⁱⁱⁱ Streeter, L., Burling-Claridge, G. R., Cree, M. J. & Künnemeyer, R. Optical full Hadamard matrix multiplexing and noise effects. *Appl. Opt.* **48**, 2078 (2009).

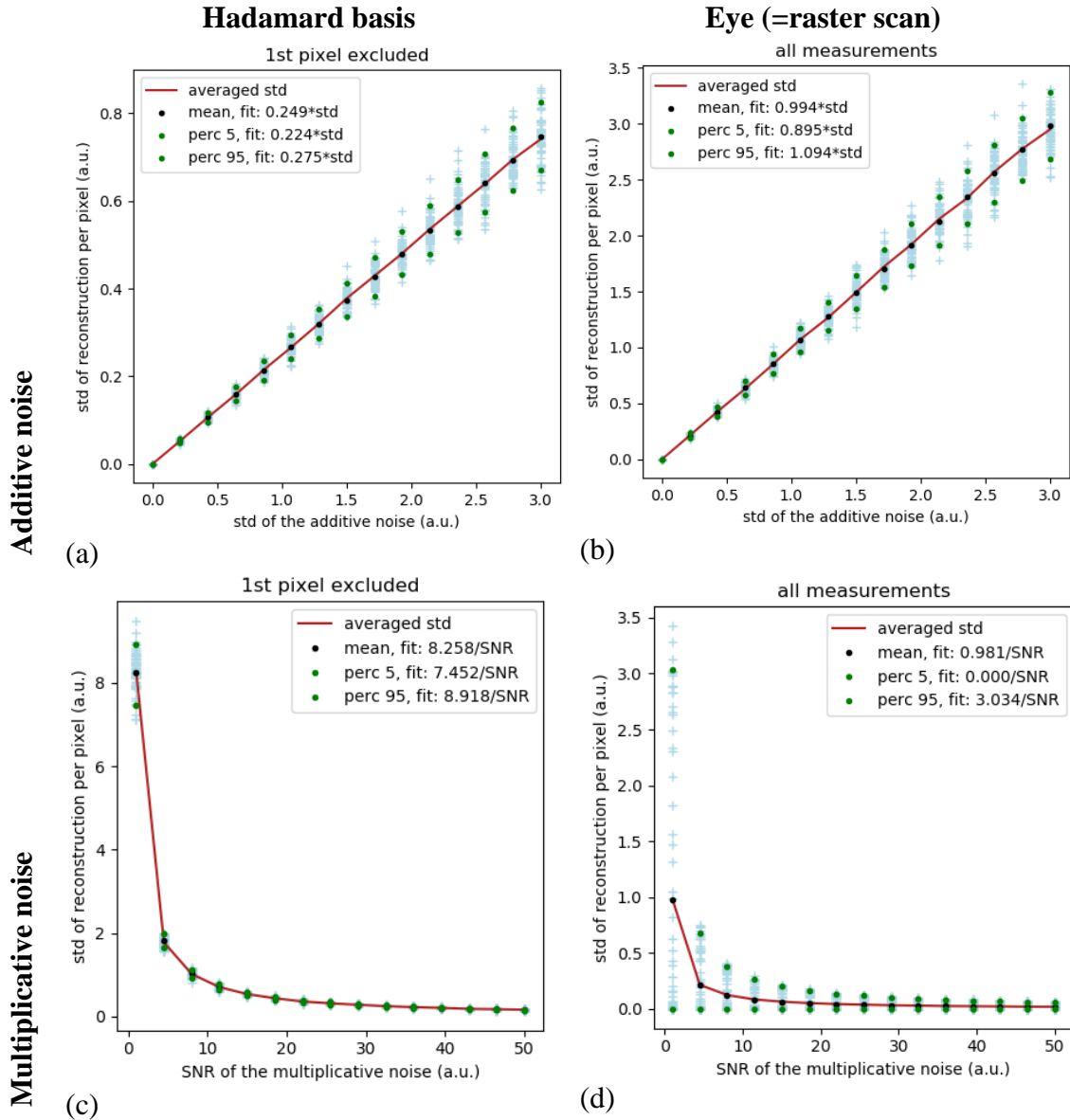


Figure 4: Influence of the additive (a-b) and multiplicative (c-d) noises on the reconstruction by assessing the standard deviation of the reconstruction as a function of a quantity representing the noise amplitude. In (a-c), the first pixel on the reconstruction is excluded in the STD calculation and included in (b-d).

SPI (with 64 patterns similar to the experiment of Chapter 4, section III.2) is modeled on a synthetic image corresponding to a dose-response function normalized by its mean value. We describe the measurement of an image intensity x with the set of patterns A in the presence of additive noise e and multiplicative noise e_p by the following equation:

$$Ax = e_p b + e \quad (1)$$

The influence of both additive and multiplicative noise is assessed by simulation by performing $N_{iter} = 120$ measurements with random noise following a gaussian distribution of standard deviation std of $1/SNR$.

In the presence of additive noise only:

$$\mathbf{x} = \mathbf{A}^{-1}\mathbf{b} + \mathbf{A}^{-1}\mathbf{e} \quad (2)$$

We note σ^2 the variance of the noise added to the measurement. In the case of Hadamard shifting, 1st pixel excluded

$$\mathbf{x} = \frac{2}{n}\mathbf{H}\mathbf{b} + \frac{2}{n}\mathbf{H}\mathbf{e} \quad (3)$$

The operation $\mathbf{H} * \mathbf{e}$ implies the linear combination of n terms of variance σ^2 ; hence $std\left(\frac{2}{n}\mathbf{H}\mathbf{e}\right) = \frac{2}{\sqrt{n}} * \sigma$. It corresponds to an SNR boost compared to the raster scan by $\sqrt{n}/2$. This calculation agrees with the Monte-Carlo simulation, which shows a reduction of the additive noise by a factor of 4 for 64 pixels.

Multiplicative noise

A noise increase of $8\sim\sqrt{n}$ is induced in the SPI simulation and compared to the raster scan approach. However, the collected light intensity is increased by a factor $n/2$, which provides an improvement by a factor $\sqrt{n/2}$. At equal source intensity, multiplicative noise is increased by a factor $\sqrt{2}$. Figure 4 shows that the multiplicative noise with Hadamard multiplexing is less dependent on the pixel intensity than on raster scanning, as the standard deviation distribution of pixels is much tighter.

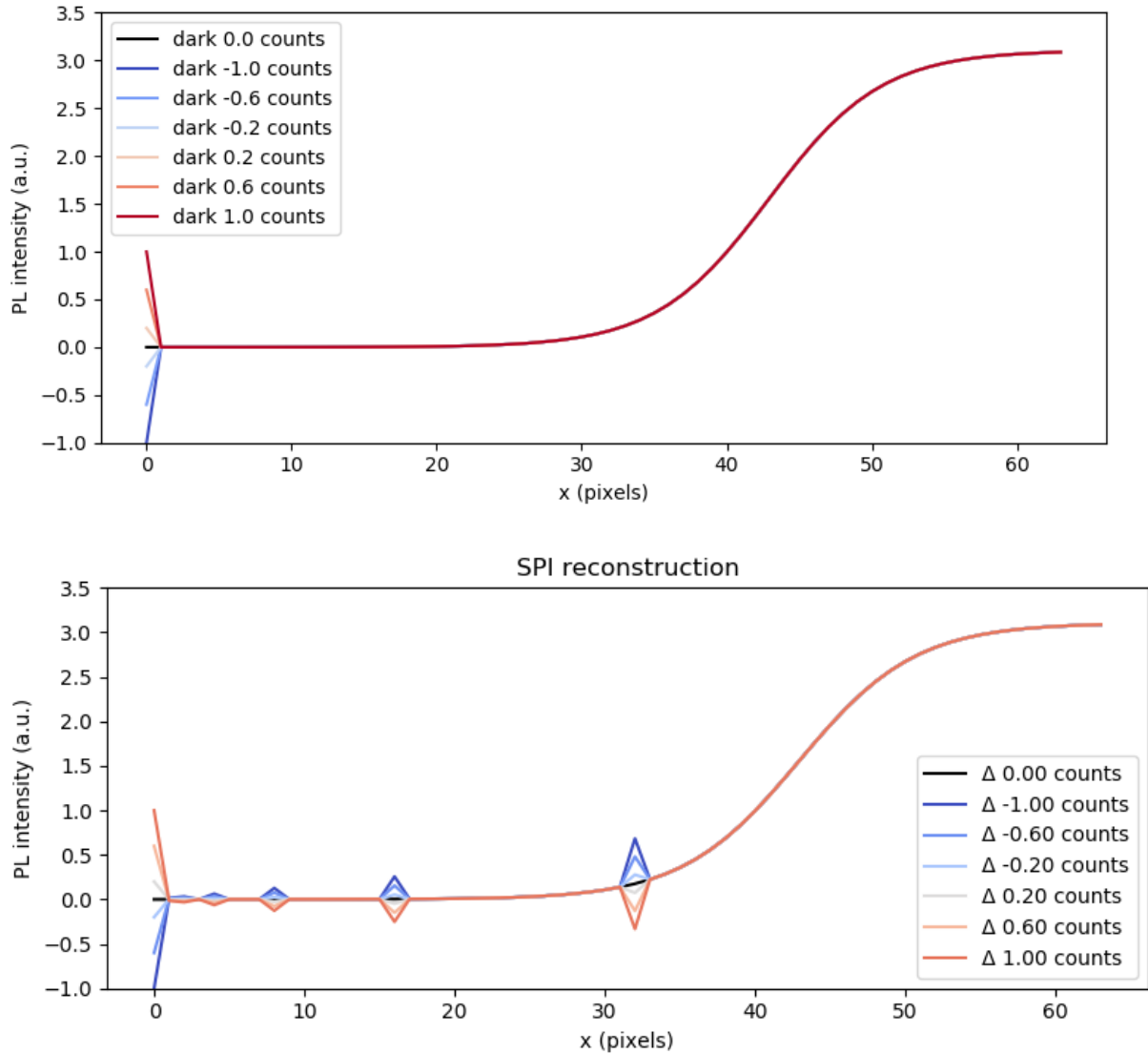


Figure 5: (a) Simulation of SPI reconstruction with various constant offsets. (b) Tests of reconstruction of a linear drift with multiple slopes.

Constant offset

The reconstruction of SPI with a constant offset and the initial image differs in the value of the first pixel, as shown in Figure 5(a). As the sum of the inverse pattern matrix is null in every other pixel, it offers a differential measurement. In pixel 0, this sum equals 1 and increases the reconstructed value by the offset intensity. Therefore, the incidence of constant background is very limited, almost null when the noise is neglected.

Linear drift

A value $i\delta = i * \Delta / (n - 1)$ is added to the pattern numbered i in the natural Hadamard order. Pixels numbered 2^n are changed by this process, while the others remain unaffected, as

illustrated in Figure 5(b). Indeed, 2^n pixels correspond to the only row that is not symmetric in the Hadamard inverse. Also, the overall sum of the image is not affected. A short calculation provides the value of added noise on the reconstruction on the pattern numbered $n/2$.

$$\delta \left(patt = \frac{n}{2} \right) = \frac{2}{n} \left(\sum_{i=0}^{\frac{n}{2}-1} i\delta - \sum_{i=\frac{n}{2}}^{n-1} i\delta \right) = -\frac{n\delta}{2} = -\frac{n}{2(n-1)} \quad (4)$$

C. Generalization of diffraction artifact to 2D

In the latter, the number of transition patterns is determined by summing them along the x and y axes. Similarly to Chapter 3, a correlation between the intensity and transition number is observed in Figure 6 and can be approximated by a linear function, though noisier than the 1D one.

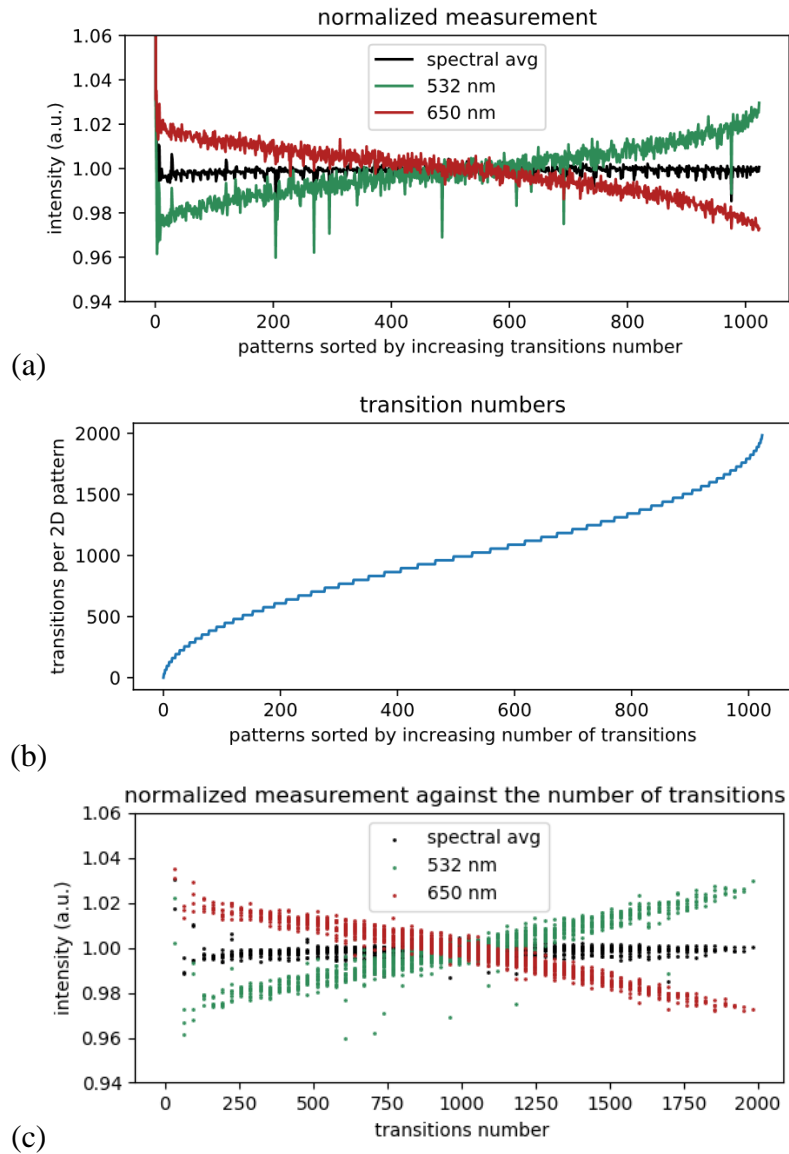


Figure 6: Intensity as a function of the transition number. (a) Measurements sorted by patterns with increasing numbers. (b) Transitions per patterns. (c) Intensity as a function of transition number.

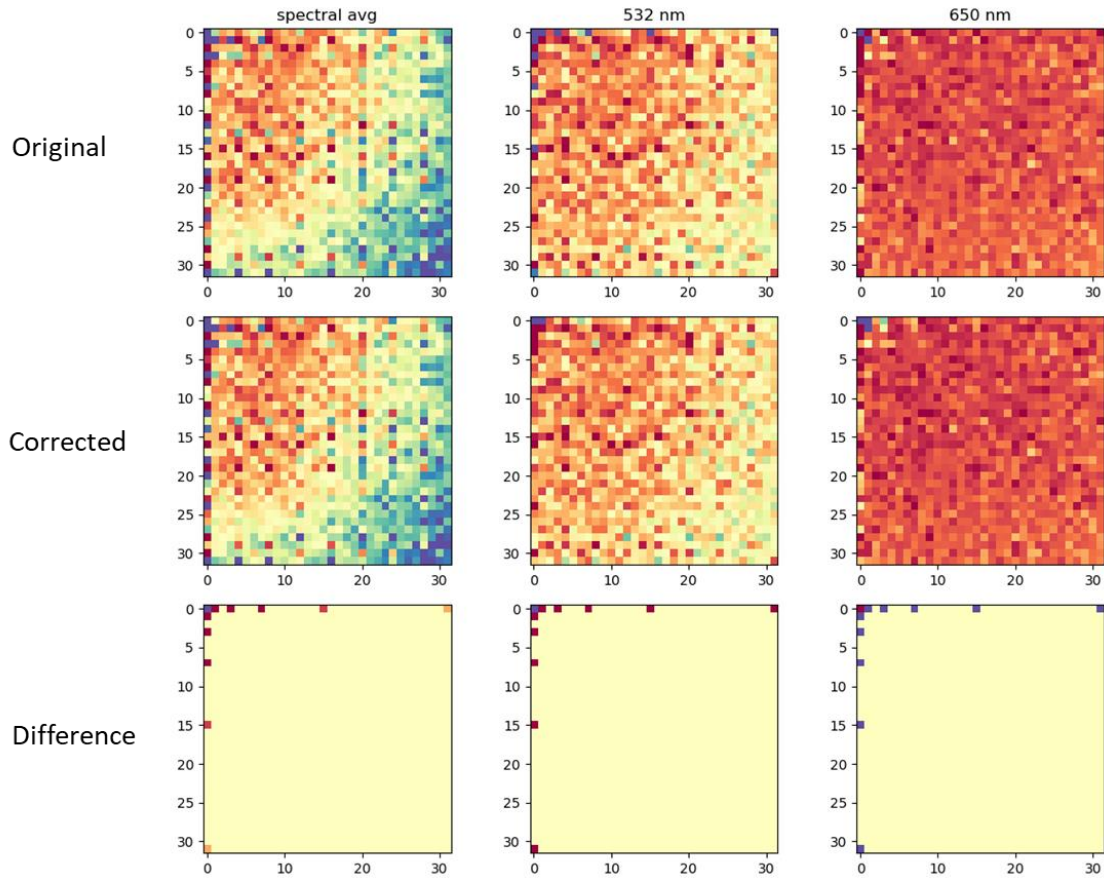


Figure 7: Comparison of SPI reconstructions with and without drift slope correction for different wavelengths. The edge pixels are mainly impacted.

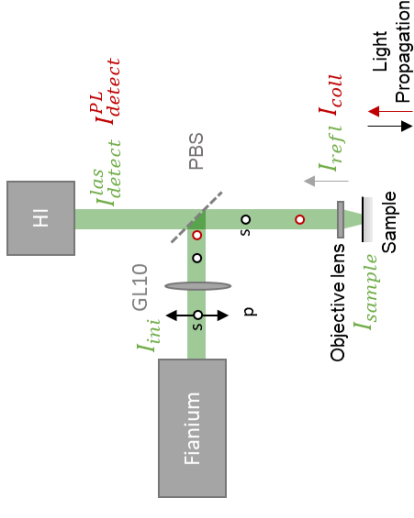
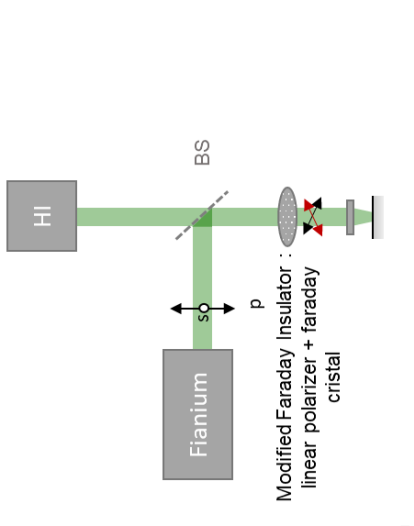
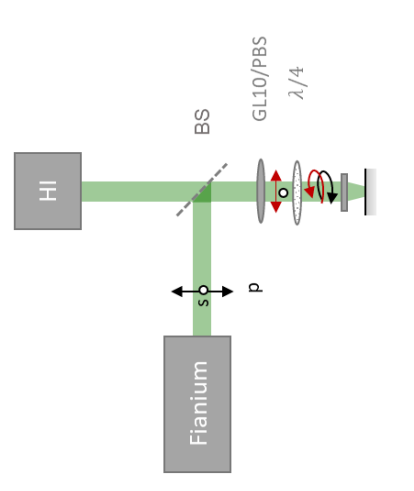
This approach was tried on experimental data. As displayed in Figure 7, the affected pixels are on the edge of the image and are less important for data analysis. However, some artifacts are still visible on columns multiple of 4. As the measurement takes longer than the 1D acquisitions, the chances of spectrometer synchronization dysfunctioning are higher. It is also possible that the generalization of the 1D correction to 2D needs refinement. A proper shading model could be extended to 2D, also considering diagonal-mirrors interaction. Also, the pattern drift is maybe more correlated with a representative spatial frequency of the patterns as the average/minimal or maximal one.

D. Improvements for the pixel clustering setup

This approach can be improved, and the following ideas are ranked from major to minor refinements.

- Synchronization with the spectrometer: to avoid any artifacts due to the timing of spectra acquisitions and changes in the DMD pattern, controlling both with Python would be the first solution. It requires buying several toolboxes from the provider. It might still be long, provided spectra capture is irregular while using a spectrometer without a buffer.
- Compressed sensing: optimization algorithms such as TVAL3 seem to perform well with sufficient pixels, which should be the case for the hyperspectral acquisition in the first step. In noisy conditions, machine learning has been demonstrated on this problem with impressive results². As the corresponding toolbox is available online, its implementation should be feasible in a reasonable time. It would also be possible to project the patterns in the cake-cutting order and regularly display the reconstruction obtained by the Moore-Penrose inverse, providing reconstructions with different numbers of pixels.
- Codes interfacing: Pattern parameters are transferred manually at the moment. Exporting their data as a structure and interface for the different codes at stake would make them more user-friendly.
- In the case of high dynamic range, optimized acquisitions would be obtained in pixel groups with various streak parameters, particularly with multiple acquisition times. They could be determined automatically from the intensity of the clustered areas.

E. Filtering out the laser reflection by polarization

Polarizing beam splitter	Faraday isolator	PBS+λ/4*
 <p>Objective lens I_{sample} Sample I_{refl} I_{coll} Light Propagation</p>	 <p>Modified Faraday Isolator : linear polarizer + Faraday cristal I_{det} I_{refl} I_{coll} I_{PL}</p>	 <p>BS GL10/PBS $\lambda/4$</p>
$GL + PBS \rightarrow \frac{I_{sample}}{I_{ini}} \sim 50\%$	$BS + FI \rightarrow \frac{I_{sample}}{I_{ini}} \sim 25\%$	$BS + GL \rightarrow \frac{I_{sample}}{I_{ini}} \sim 25\%$
$PBS \rightarrow \frac{I_{det}^{las}}{I_{refl}} \sim \frac{1}{20}, \frac{1}{100}$	$FI \rightarrow \frac{I_{det}^{las}}{I_{refl}} \sim \frac{1}{30}, \frac{1}{2000}$	$FI \rightarrow \frac{I_{det}^{las}}{I_{refl}} \sim \frac{1}{30}, \frac{1}{500}$
$PBS \rightarrow \frac{I_{det}^{PL}}{I_{coll}} \sim \frac{1}{2}$	$LP \text{ and } BS \rightarrow \frac{I_{det}^{PL}}{I_{coll}} \sim \frac{1}{4}$	$GL \text{ and } BS \rightarrow \frac{I_{det}^{PL}}{I_{coll}} \sim \frac{1}{4}$
<p>In practice, low attenuation due to a tilt in the HI alignment.</p>	<p>A lot of uncertainty on the attenuation capacity, wavelength dependence, and requires new components.</p>	<p>Important variations with wavelength</p>

GL10 = Glan-Laser Polarizer, PBS = polarizing beam-splitter, FI = Faraday Isolator

* <https://www.edmundoptics.fr/knowledge-center/application-notes/lasers/building-a-custom-optical-isolator-with-stock-components/>

Résumé étendu en français

Cette dernière décennie a vu une croissance exponentielle de la capacité solaire photovoltaïque installée, qui est passée de 63,8 TWh en 2011 pour finalement dépasser la valeur symbolique de 1000 TWh en 2021. Les scénarios d'émission nette zéro prévoient que cette tendance se poursuivra dans les années à venir. En effet, le solaire photovoltaïque constitue l'une des sources d'énergie dont l'empreinte carbone est la plus faible, avec le nucléaire, l'hydraulique et l'éolien. Cependant, le développement de nouvelles structures et de nouveaux matériaux est nécessaire pour améliorer les technologies actuellement employées. Des rendements plus élevés sont recherchés pour nécessiter moins de surface, de matériaux et d'infrastructures. Par ailleurs, le temps de retour énergétique des cellules en silicium est de l'ordre de l'année, et les technologies émergentes comme la pérovskite pourraient le ramener à l'échelle du mois. La dégradation des technologies matures comme le silicium doit être étudiée pour améliorer leur fiabilité. La caractérisation avancée peut jouer un rôle crucial pour répondre à chacun de ces enjeux.

Dans ce cadre, cette thèse aborde le développement de nouvelles méthodes d'imagerie par photoluminescence pour caractériser les dispositifs photovoltaïques et aider à leur amélioration. Nous étudions comment l'imagerie de photoluminescence résolue spectralement en illumination pulsée peut contribuer à la quantification des propriétés optoélectroniques tout en limitant les connaissances préalables nécessaires. De nouveaux systèmes d'imagerie sont développés, décrivant la lumière émise en quatre dimensions : 2D spatiale à l'échelle du micron, temporelle et spectrale avec des résolutions jusqu'à la 50ps et inférieures au nanomètre. Ce travail est complété une étude en longueur d'onde d'excitation sur un autre montage de luminescence, ce qui permet d'obtenir l'absorptivité locale de la couche mince.

Ce mémoire comprend cinq chapitres décrivant le contexte, les méthodes expérimentales et les résultats obtenus. Le chapitre 1 établit un cadre pour décrire l'absorption de la lumière, le transport électronique et la recombinaison. Les modèles classiques d'analyse de la photoluminescence spectrale et transitoire sont fournis, et les différents types de matériaux caractérisés sont présentés. Le chapitre 2 décrit les techniques d'imagerie pour les acquisitions multidimensionnelles à partir d'une revue de la littérature. Le développement du système dit 4D-PL et de ses variantes est expliqué dans le chapitre 3. Les défis que cette nouvelle architecture soulève et les moyens possibles de les relever sont discutés. Le chapitre 4 présente les résultats expérimentaux obtenus avec les différentes techniques mises en œuvre. Les échantillons d'arséniure de gallium et de pérovskite sont caractérisés simultanément dans les dimensions spectrale, temporelle et spatiale. Le chapitre 5 explore les informations supplémentaires apportées par la dépendance de la photoluminescence à la longueur d'onde d'excitation. Le lien de la photoluminescence avec les propriétés d'absorption et le profil des

porteurs de charge est illustré par des expériences sur un empilement de pérovskite et une cellule d'arséniure de gallium, respectivement. Enfin, les principaux résultats de ce travail sont résumés, ainsi que les questions soulevant des perspectives à court et à long terme pour les méthodes nouvellement développées.

Chapitre 1 – Luminescence des semiconducteurs

La luminescence constitue l'une des voies de recombinaison après la génération de porteurs de charge dans un matériau photovoltaïque, qui peut se faire par absorption de la lumière. Les recombinaisons radiatives témoignent de la qualité du matériau car elles sont d'autant plus importantes que les concentrations de porteurs de charge, et donc le potentiel chimique associé, sont élevés. Comme montré sur la Figure R 1, la luminescence s'oppose avec les recombinaisons non radiatives. En particulier, elle est en concurrence avec celles dites SRH (Shockley-Read-Hall), assistées par des défauts. Ces mécanismes ont lieu en même temps que le transport de charges de manière électronique ou optique, qui joue un rôle majeur sur les densités de porteurs.

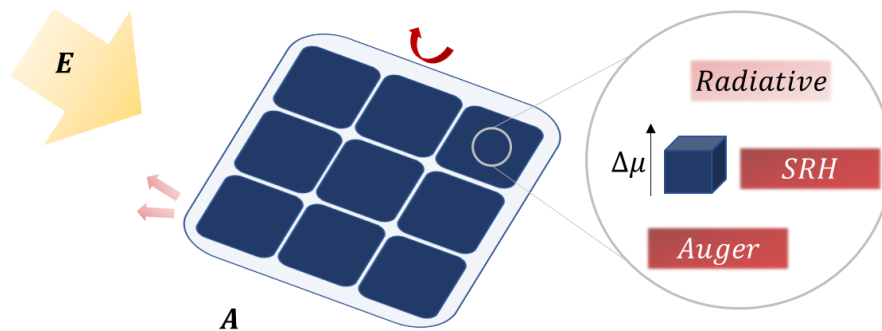


Figure R 1 : Schéma des échanges d'énergie entre l'irradiation solaire, l'absorbeur photovoltaïque, et son environnement. L'énergie absorbée peut être stockée sous forme de potentiel $\Delta\mu$, ou perdue par rayonnement ou thermiquement.

La description spectrale et temporelle de la luminescence permet de caractériser ces différents mécanismes de transport et de recombinaisons, donnant ainsi un moyen d'accéder aux propriétés optoélectroniques. En effet, les modèles correspondants basés sur la loi de Planck généralisée et des équations de continuité font intervenir l'absorption de la lumière et les densités de porteurs de charge. La Figure R 2 récapitule les grandeurs décrites à partir de ces deux dimensions de la luminescence. Cependant, son interprétation repose sur de nombreuses hypothèses et nécessite de fixer des paramètres pour extraire les propriétés optoélectroniques. Comme les différentes dimensions de la lumière émise dépendent différemment des propriétés en jeu, et leur acquisition simultanée peut favoriser leur séparation. Cette thèse explore comment l'acquisition de cartes spectralement résolues de photoluminescence en excitation pulsée peut contribuer à la caractérisation des matériaux tout en limitant les connaissances préalables nécessaires et en contrôlant les hypothèses et modèles sous-jacents.

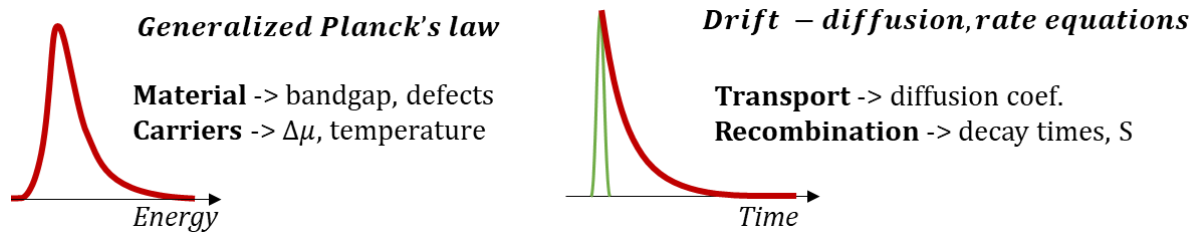


Figure R 2 : Schéma des modèles et propriétés optoélectroniques en jeu pour l'interprétation de la luminescence spectrale et temporelle.

Chapitre 2 – Techniques d'imagerie de caractérisation

Différentes stratégies peuvent être mises en place pour obtenir des cartographies de champs lumineux. Les matrices de photodétecteurs (réseau de plans focaux) tels que les capteurs d'appareil photo permettent d'acquérir une image instantanée. A l'inverse, le balayage ou l'imagerie monopixel (anciennement multiplexage optique), permettent d'utiliser des capteurs mono-pixel suivi d'une étape de reconstruction. Ces techniques peuvent toutes être appliquées à l'imagerie multidimensionnelle, qui fournit des informations supplémentaires sur les photons, telles que la longueur d'onde, le moment ou la profondeur d'émission, la polarisation ou les angles de propagation. En particulier, l'imagerie monopixel est avantageuse car elle peut employer un détecteur résolu dans une dimension et est moins sensible au bruit que le scan.

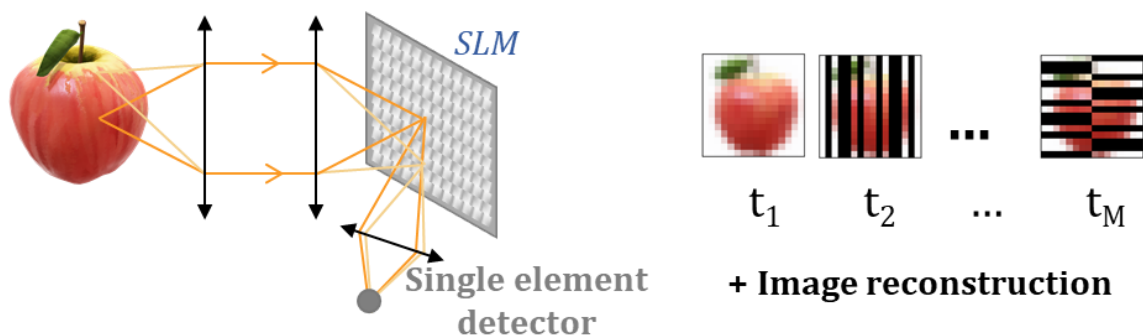


Figure R 3 : Principe de l'imagerie monopixel. L'image est focalisée sur un modulateur spatial de lumière (SLM) qui permet de varier la transmission locale est d'appliquer des masques sur celle-ci. Un photodétecteur détecte le flux ainsi modulé.

L'imagerie monopixel repose sur deux composants principaux : un photodétecteur non-imageant et un modulateur spatial de lumière, comme illustré en Figure R 3. La reconstruction spatiale est effectuée à partir d'acquisitions de l'image souhaitée modulée par un ensemble de masques. Mathématiquement, il s'agit d'un problème d'inversion et diverses approches sont disponibles pour le résoudre, associées à des nombres de mesures et exigences de complexité de calcul différents. Un état de l'art montre que l'imagerie monopixel a permis de réaliser des cartographies avec des capteurs non conventionnels, sensibles dans les micro-ondes ou les

rayons gamma par exemple. Elle a également servi la conception d'imageurs multidimensionnels, résolus en profondeur, temps ou spectre, ainsi que des systèmes multimodaux, notamment fournissant le signal en réflexion et en transmission.

L'imagerie hyperspectrale, qui fournit l'intensité locale résolue spectralement $I(x, y, \lambda)$ est particulièrement utile à la caractérisation de semiconducteurs. Il est possible d'obtenir le cube de données associé par une image instantanée, en répartissant les différentes dimensions spatialement sur une matrice de photodétecteur. Par ailleurs des scans spatiaux, spectraux ou spatio-spectraux sont également possibles. C'est cette dernière approche qui est employée dans le banc utilisé dans ce travail. De même, l'imagerie résolue en temps, en fournissant des films $I(x, y, \lambda)$ à des échelles de temps très courtes permet d'observer les phénomènes transitoires dans les matériaux photovoltaïques. Des détecteurs permettent de résoudre le moment d'émission d'un photon à la picoseconde, et peuvent encore une fois être intégrés sous formes de matrices pour obtenir de l'imagerie, ou utilisés en balayages.

Jusqu'à présent, des acquisitions séparées sont nécessaires pour obtenir des images résolues en temps et en longueur d'onde, de sorte qu'une étude complète de la dynamique est hors de portée. En particulier, le parallèle entre les expériences en régimes continu et transitoire soulève des interrogations. C'est pourquoi nous cherchons à obtenir une la photoluminescence en 4D : $I(x, y, \lambda, t)$, représenté schématiquement sur la Figure R 4.

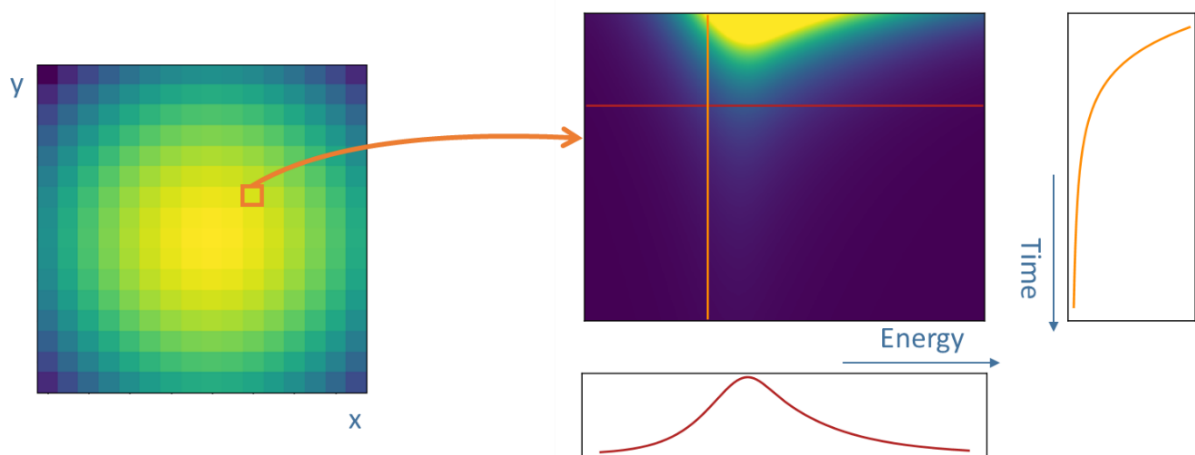


Figure R 4: Représentation schématique des données 4D. À gauche, une projection dans le domaine spatial est présentée. Chacun des pixels contient l'évolution temporelle locale du spectre sous la forme d'une image avec des colonnes représentant la décroissance à différentes énergies et des lignes correspondant au spectre émis à différents délais.

La littérature présente un banc permettant d'obtenir une telle information à partir d'une technique d'imagerie non-conventionnelle dite de *Compressed Ultrafast Photography* employant une caméra à balayage de fente avec une large surface de détection couplée à un spectromètre. Différentes approches seraient également possibles en scannant avec un tel

détecteur, en combinant les approches d'imagerie hyperspectrale instantanée avec une caméra résolue en temps, ou inversement. Le choix des approches alloue un « budget de photons » à un « budget de pixels », faisant l'arbitrage entre la sensibilité de l'instrument et les résolutions dans les différentes dimensions. Dans ce projet, nous choisissons de mettre en avant les dimensions spectrale et temporelle, à partir du design expliqué au chapitre 3.

Chapitre 3 – Développement du système de 4D-PL

Le banc de 4D-PL est basé sur une caméra à balayage de fentes couplée à un spectromètre, qui fournit le déclin du spectre $I(\lambda, t)$ avec des résolutions temporelles et spectrales pouvant aller jusqu'à 20ps et 0.5nm respectivement. Comme schématisé sur la Figure R 5, l'information spatiale est reconstruite par imagerie monopixel, tout en conservant les résolutions spectrales et temporelles. Par construction, ces dimensions sont donc largement favorisées par rapport aux dimensions spatiales. Le modulateur spatial employé ici est un *Digital Micromirror Device* (DMD), qui consiste en une matrice de micro-miroirs contrôlables par ordinateur. Ceux-ci peuvent réfléchir la lumière selon deux directions dites « on » et « off » suivant s'ils sont dirigés vers le détecteur ou non. Le système suit une architecture en collection structurée afin de pouvoir imager les phénomènes de diffusion et de ne pas imposer d'illumination. Les acquisitions se font à partir des matrices de Hadamard, qui sont une base binaire.

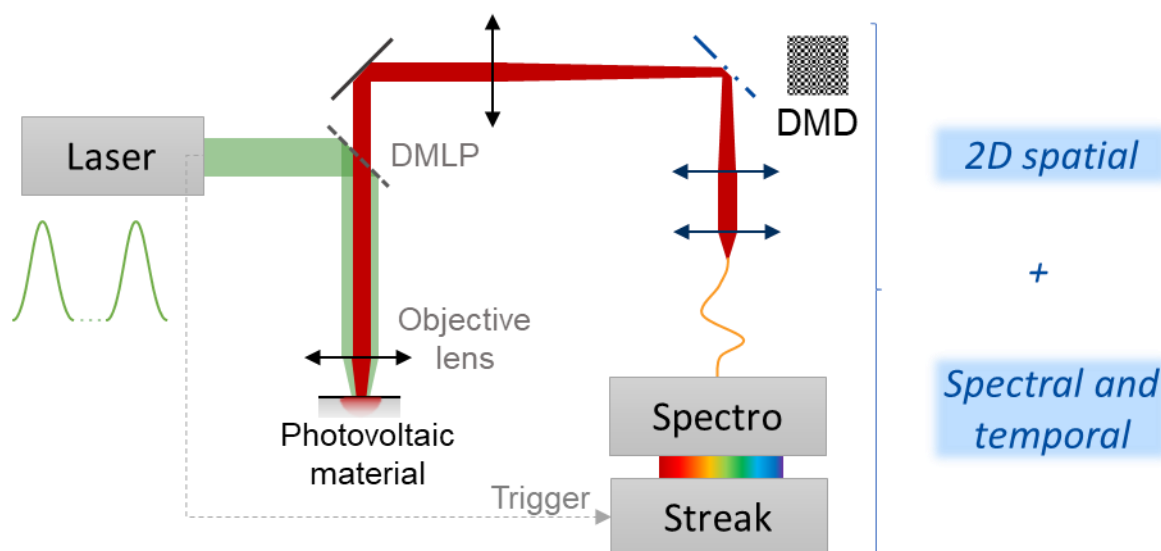


Figure R 5 : Schéma du banc de 4D-PL. Un laser pulsé excite l'échantillon dans une configuration de réflexion. L'illumination est ensuite filtrée par le miroir dichroïque long-pass (DMLP). L'émission PL est focalisée sur le DMD et analysée avec la caméra à balayage de fentes.

La mise en œuvre pratique de cette approche introduit des contraintes et des défis supplémentaires. Lorsqu'il s'agit de développer un système multidimensionnel, chaque

composante doit faire l'objet d'une attention particulière. Le système doit restituer toutes les dimensions au mieux, et un compromis entre elles émerge. En effet, l'information spatiale est codée par un DMD qui induit une diffraction, intriquant les dimensions spatiales et spectrales. Le dimensionnement optique, avec une large collection angulaire, permet de réduire les effets de la diffraction lorsque tous les miroirs sont « on ». En outre, les artefacts dus aux interférences variant en fonction des masques sont corrigés empiriquement.

En outre, en contrepartie des résolutions temporelle et spectrale exceptionnelles, le détecteur présente une faible sensibilité, même pour une collection optimisée. Étant donné la faible intensité lumineuse en jeu dans les mesures PL et les contraintes de temps qui y sont associées (pour des raisons de stabilité), le nombre de canaux dans la dimension spatiale doit être réduit. En pratique, jusqu'à 64 pixels ont été utilisés, ce qui correspond à une spatialisation de la spectroscopie résolue en temps plutôt que de l'imagerie. Deux variantes de la 4D-PL ont été proposées pour étendre son champ d'application à d'autres échantillons. Tout d'abord, en effectuant de l'imagerie monopixel avec un spectromètre en parallèle du banc de TRFLIM, un set-up $2x3D I(x, y, \lambda) + I(x, y, t)$ est mis en place. Également, en effectuant une première acquisition d'imagerie monopixel et en utilisant des algorithmes de segmentation d'images, il est possible d'obtenir le déclin spectral dans des zones d'intérêts. Cela fournit une information de la forme $I(x_i, \lambda, t)_{1 \leq x_i \leq p}$, avec typiquement $p=4$. Ces deux approches novatrices sont prometteuses pour la caractérisation d'un large éventail de phénomènes, du transport optoélectronique des porteurs aux transferts vers des états localisés.

Chapitre 4 - Démonstration de la 4D-PL et de ses variations sur des dispositifs photovoltaïques

Les résultats des trois schémas d'échantillonnage dans les domaines spatial, spectral et temporel sont présentés dans ce chapitre. Ils sont pertinents pour divers problèmes physiques en fonction des données d'intérêt. L'imagerie monopixel est la clé pour accéder à la dimension spatiale dans les différentes approches.

L'effet d'une illumination localisée dans les pérovskites à triple cations a été suivie par la configuration 2x3D à deux niveaux d'injection différents. Au niveau le plus bas, l'émission PL est améliorée sur une zone plus large que celle sur laquelle des porteurs en excès notables ont été générés par l'impulsion. Un décalage vers le rouge des spectres et une variation dynamique dépendante de l'emplacement l'accompagnent. A l'injection supérieure, les propriétés de l'échantillon sont dégradées, l'intensité PL diminue et des variations spectrales latérales sont observées. En perspective, la question de la comparaison des spectres acquis en régime continu et transitoire est discutée.

L'imagerie 4D-PL a permis la caractérisation d'une couche d'arséniure de gallium sous forte injection, où l'on observe un décalage vers le rouge au cours du déclin et en s'éloignant du centre de l'illumination. La vitesse caractéristique de la propagation de l'énergie en périphérie peut être estimée à partir de la ligne isoénergie montrée sur la Figure R 6(a). Elle est de 10^7 cm/s , ce qui correspond à la vitesse de saturation des trous, pour un régime associé à une interaction accrue entre les porteurs et le réseau. Dans des conditions qui ne modifient pas la forme de l'absorption, des variations de température et de séparation des niveaux de quasi-Fermi pourraient être obtenues localement et temporellement à partir de l'énergie moyenne et de l'intensité, qui sont des indicateurs statistiques relativement peu sensibles au bruit. Les modèles simples ne s'appliquent pas ici, comme le soulignent les variations conjointes de ces deux grandeurs montrées en Figure R 6(b) : dans le cas où seul le remplissage de bande joue un rôle on s'attend à des bijections entre le potentiel $\Delta\mu$, l'énergie moyenne et l'intensité. Des stratégies ont été proposées pour interpréter les données, qui indiquent que le remplissage de bande, le transport optique et probablement la température des porteurs contribuent à la tendance observée. Un modèle plus complexe pourrait être développé dans le cadre de travaux futurs pour évaluer les contributions de chacun de ces mécanismes.

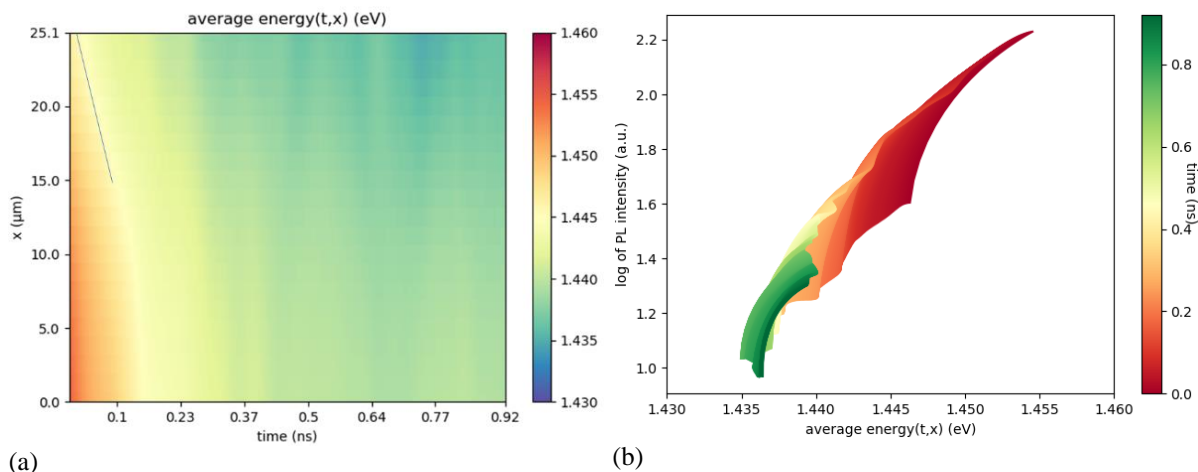


Figure R 6 : Évolution de l'énergie moyenne et de l'intensité spectrale en fonction du temps et de l'emplacement. (a) Énergie moyenne pendant le temps à différentes distances du centre. (b) Corrélation entre le logarithme de l'intensité PL et l'énergie PL moyenne. Le code couleur met en évidence les variations temporelles (d).

La variante de 4D-PL basée sur la segmentation d'images est illustrée en illumination ponctuelle. Son utilisation sur un nouvel échantillon d'arséniure de gallium à haute fluence illustre les promesses de cette approche pour le remplissage de bande et la caractérisation des porteurs chauds. Des mesures sur des fluorophores montrent la signature du transport optique et valident les dynamiques observées. La démonstration sur la pérovskite met en évidence la présence d'une dégradation qui ne peut être observée lorsque le spectre est moyenné. En

conclusion, cette méthode offre une généralisation réussie de la spatialisation des raies pour la caractérisation de divers échantillons et le suivi d'un large éventail de phénomènes physiques.

Chapitre 5 – Spectroscopie d'excitation de photoluminescence

Ce chapitre aborde un autre ensemble de données 4D : plutôt que d'analyser plus en profondeur la lumière émise lors d'une expérience, une étude paramétrique est réalisée. L'expérience de variation de la longueur d'onde d'excitation λ_{exc} , appelée spectroscopie par excitation de photoluminescence (PLE), est réalisée avec un imageur hyperspectral. Elle aboutit à l'obtention de la matrice $I(x, y, \lambda_{em}, \lambda_{exc})$ où les corrélations dépendent du système sondé.

Les expériences de PLE offrent un moyen d'accéder aux propriétés d'absorption des absorbeurs de lumière photovoltaïque, comme cela a été démontré principalement de manière qualitative dans la littérature. Elle est également illustrée comme un outil permettant d'évaluer la recombinaison de surface en faisant varier sa contribution au PL. Des modèles théoriques décrivant le lien entre le PL et les propriétés d'absorption sont présentés. Une méthodologie expérimentale a été mise en place pour réaliser de telles mesures.

Nous avons présenté une preuve de principe d'une mesure d'absorptivité locale bien résolue spatialement et spectralement. Nous avons confirmé par simulation que l'utilisation d'un laser pulsé ne devrait pas gêner l'absorptivité de la PLE dans notre cas. L'absorptivité obtenue près de l'énergie de la bande interdite par ajustement PL est compatible avec celle évaluée par PLE. Une mesure supplémentaire par spectroscopie est nécessaire pour mettre à l'échelle l'absorptivité mesurée localement, car le rendement quantique de photoluminescence et l'absorptivité ne peuvent être dissociées. Compléter la PLE par une mesure de réflexion spatiale donne un aperçu des propriétés optiques du dispositif et offre des informations utiles pour construire un modèle physique.

Une autre expérience sur une cellule GaAs complète illustre comment la longueur d'onde d'excitation peut modifier le spectre PL observé. Des spectres à décalage vers le rouge avec une longueur d'onde d'excitation croissante sont observés lorsque le produit des porteurs de charge est déplacé vers des profondeurs plus importantes. La simulation de la dérive-diffusion suggère que ce phénomène ne devrait pas se produire dans des conditions de circuit ouvert à l'état d'équilibre. Cependant, des profils de concentrations de porteurs de charge variables sont obtenus dans le modèle de court-circuit, et le calcul de la PLE pour différentes longueurs d'onde de réabsorption correspond qualitativement au comportement expérimental. Par conséquent, le choix de la longueur d'onde d'intégration permet l'obtention de PLE reflétant différentes épaisseurs de la cellule et pourrait être la clé pour atteindre l'information en profondeur.

Conclusion et perspectives

Cette thèse a porté sur le développement de nouvelles approches pour caractériser la photoluminescence des semi-conducteurs pour les applications photovoltaïques. Elle a exploré différentes manières d'acquérir des jeux de données de photoluminescence à résolution spectrale plus complets pour évaluer les propriétés optoélectroniques en limitant les connaissances préalables nécessaires et en contrôlant les hypothèses et les modèles.

Cette thèse a posé les bases d'un échantillonnage de la photoluminescence dans les dimensions spatiale, spectrale et temporelle en régime transitoire. À ce titre, elle a abordé des questions cruciales qui mériteraient d'être approfondies. En particulier se pose la problématique de la comparaison entre régime continu et transitoire de l'émission de photoluminescence qui est loin d'être directe en dehors des cas limites. Par ailleurs, plusieurs approches de simulation peuvent être envisagées pour aider au traitement des données 4D. Cela pourrait permettre de mieux cibler les observables d'intérêt et de déterminer des visualisations appropriées. Les outils numériques peuvent également identifier des conditions expérimentales et types d'échantillons pour lesquels la 4D-PL peut apporter des informations déterminantes.

Résumé :

Les méthodes de caractérisation de luminescence sont devenues la norme pour le développement de dispositifs photovoltaïques. Elles permettent d'accéder aux mécanismes de transport de charges et aux propriétés optoélectroniques clés à partir de modèles et de paramètres matériaux simplifiés, ce qui rend leur utilisation complexe pour les nouvelles compositions.

Cette thèse explore comment l'imagerie de photoluminescence résolue spectralement en illumination pulsée peut contribuer à la quantification des propriétés optoélectroniques tout en limitant les connaissances préalables nécessaires. Nous développons de nouveaux systèmes d'imagerie décrivant la lumière émise en quatre dimensions : 2D spatiale à l'échelle du micron, temporelle et spectrale avec des résolutions jusqu'à la 50ps et inférieures au nanomètre. Ce travail est complété une étude en longueur d'onde d'excitation sur un autre montage de luminescence, ce qui permet d'obtenir l'absorptivité locale de la couche mince.

Mots clés : Photoluminescence ; Imagerie mono-pixel ; Spectroscopie transitoire ; Spectroscopie d'excitation de photoluminescence ; Propriétés optiques de semiconducteurs ; Matériaux photovoltaïques

Advanced imaging of transient and spectral luminescence for optoelectronic characterization of photovoltaic materials

Abstract:

Luminescence-based characterization methods have become standard for the development of photovoltaic devices. They give access to performance-determining charge transport mechanisms and optoelectronic properties based on simplistic models and material parameters, making this technique challenging for new compositions.

This thesis explores how spectrally resolved photoluminescence imaging under pulsed excitation can contribute to quantifying optoelectronic properties while limiting the necessary prior knowledge. We develop new imaging systems describing the emitted light in four dimensions: 2D spatial, temporal and spectral, to observe micron-sized features with resolutions down to 50ps and below the nanometer, respectively. With another luminescence setup, the excitation wavelength is varied, allowing the obtention of the local absorptivity.

Keywords: Photoluminescence; Single-Pixel Imaging; Time-resolved spectroscopy; Photoluminescence excitation spectroscopy; Optical properties of semiconductors; Photovoltaic materials